Corrosion fatigue initiation in stainless steels : The scanning reference electrode technique.

GONZALEZ-SANCHEZ, Jorge A.

REFERENCE

Corrosion fatigue initiation in stainless steels: The scanning reference electrode technique.

Jorge A. Gonzalez-Sanchez

A thesis submitted in partial fulfilment of the requirements of Sheffield Hallam University for the degree of Doctor of Philosophy

March 2002

The Materials Research Institute, Sheffield Hallam University

Acknowledgements

Firstly I would like to thank my supervisor Dr. B Akid for his help and guidance during my studies at Sheffield Hallam University.
I would like to take this opportunity to gratefully acknowledge the National Council of Science and Technology of Mexico (CONACYT) for the financial support and advice given to me with which it has been possible to complete successfully my Ph.D. studies in Sheffield.

Thank you very much Father, Mother, Hector, Carolina, Mauricio, Luis, Emilio, Alejandra and Rodrigo you all are my greatest motivation and support.

Also I would like to thank the technical support I received from Mr. G. Robinson, B. Didsbury, R. Tingle from the School of Engineering.

Thanks a lot friends without whom this PhD thesis could have been completed several months before, but without whom I could not have the best time in my life when living in Sheffield, thanks again for giving me so many great moments.

Abstract.

The early stages of damage by corrosion fatigue in austenitic and duplex stainless steel were studied using a novel scanning reference electrode technique (SRET). Emphasis was made on the role played by corrosion pits, which can act as stress concentrators and promote fatigue crack nucleation.

SRET measurements conducted during the potentiostatic generation of pits on the austenitic stainless steels in artificial seawater showed that the pit current density increases with the time of application of anodic polarisation. The data of the volume of metal dissolved calculated from pit current density obtained by SRET agreed well with the measurements of pit profiles. The austenitic and duplex stainless steels showed high resistance to pitting corrosion in artificial seawater at free corrosion potential. The use of a 0.05 M $FeCl_3$ solution as the electrolyte promoted severe localised attack in 304 and 316L stainless steel specimens. SRET tests carried out simultaneously with the application of cyclic stress to the specimens permitted the evolution of the electrochemical activity of corrosion pits to be followed. Transformation from pitting to fatigue cracking was observed.

In this work it is proposed that a decrease of the pit electrochemical activity in terms of pit current density, is related to the nucleation of the corrosion fatigue crack. From SRET measurements a critical pit depth was calculated for the nucleation of the fatigue crack. A threshold stress intensity factor range was then calculated, which was found to be similar to the values reported in the literature.

It is suggested at the end of this thesis that parallel studies and measurements of the pit-to-crack transition can be conducted in order to corroborate the reliability of SRET measurements to assess semi-quantitatively the threshold conditions for the transition.

The scanning reference electrode technique showed advantages over other electrochemical methods used to assess the damage induced by localised corrosion in that it provides in-situ, spatially resolved, real-time electrochemical activity measurements.

CONTENTS

Nomenclature.

AC alternative current

a crack length, also the minor axis of a pit

$\mathbf{a_{th}}$ threshold crack length

bcc body centred cubic

C Coefficient in Paris law

c major axis of a pit

CF corrosion fatigue

DC direct current

d dominant microstructural barrier length, also diagonal of an indentation

E Young´s Modulus

$\mathbf{E_{corr}}$ open circuit potential (free corrosion potential)

$\mathbf{E_{MAX}}$ maximum potential

$\mathbf{E_P}$ pitting potential

EPFM Elastic-plastic fracture mechanics

fcc face centred cubic

h depth of the indentation from a diamond pyramid indenter

HAZ Heat Affected Zone

da/dN Crack growth rate per cycle

$\mathbf{\Delta K}$ stress intensity factor range

$\mathbf{\Delta K_p}$ stress intensity factor range for a critical pit condition

$\mathbf{\Delta K_{th}}$ threshold stress intensity factor range

$\mathbf{I_a}$ anodic current

$\mathbf{I_c}$ cathodic current

i current density

$\mathbf{i_a}$ anodic current density

$\mathbf{i_c}$ cathodic current density

$\mathbf{i_p}$ pit current density

IGA Intergranular attack

IGSCC Intergranular stress corrosion cracking

$\mathbf{K_{max}}$ maximum stress intensity factor

K_{min} minimum stress intensity factor

K_t stress concentration factor

LEFM Linear Elastic Fracture Mechanics

MDCS Micro Disk Calibration Source

MDS minimum detectable signal.

m Exponent in Paris law

m_{hd} half of the major pit mouth diameter

MSC Microstructural short cracks

N number of cycles

OCP open circuit potential

p applied pressure

p_{ar} pit aspect ratio

P_d pit depth

PIS Point in space specimen

PSC Physically short crack

PCF Pitting corrosion fatigue

R electric resistance, also stress ratio = $\sigma_{min}/\sigma_{max}$, also load ratio = K_{min}/K_{max}

R_p polarisation resistance

r inner radius

rpm revolutions per minute

r_p plastic zone size

S_a anode surface area

S_c cathode surface area

SCC Stress Corrosion Cracking

SCE Saturated calomel electrode

SRET Scanning reference electrode technique

SS stainless steel

SVET Scanning vibrating electrode technique

t time

x critical pit depth for stable pit propagation

UNS Unified numbering system

WHM potential distribution at half-maximum

α ferrite phase

γ austenite phase

$\Delta\sigma$ stress range = $\sigma_{max} - \sigma_{min}$

$\Delta\sigma_{th}$ threshold fatigue strength

δ delta ferrite

ε strain

κ solution conductivity

η_a anodic overpotential

η_c cathodic overpotential

ν Poisson´s ratio

Σ sum

σ_{cy} cyclic yield stress

σ_{ys} yield stress

σ_{uts} ultimate tensile stress

σ_C circumferential stress

σ_L longitudinal stress

τ_p life time of a pit

CHAPTER 1 – Introduction

The Gulf of Mexico is a large extension of territory that embraces the Mexican estates of Tamaulipas, Veracrúz, Tabasco, Campeche and Yucatán involving 5,100 km of coast. In this area and offshore, about 80% of Mexican petroleum is produced and exported. In addition there are other industries, such as seafood processing, manufacturing, chemical processing, metallurgical industries, textile, pulp and paper processing [1].

Stainless steels are an important group of materials for seawater applications. This kind of "more resistant material" was introduced with the aim of reducing maintenance costs involved with materials such as carbon steel having internal and external linings and coatings. However, there are several cases around the world, from the North Sea area [2], to the Gulf of Mexico [1], in which the failure frequency in seawater of stainless steel piping systems on offshore platforms is very high, resulting in unacceptable maintenance costs.

In seawater applications, the most widely used stainless steel grade, namely, 316L, suffers from localised corrosion and is frequently affected by pitting and crevice corrosion.

Even though there is a substantial amount of data published, which documents studies of localised corrosion of 316 and 316L stainless steels, the problem of structural failure in marine environments remains. Unfortunately the degradation process is more complex than just localised electrochemical reactions at the metal surface.

Failures of real structures in marine environments are induced by the effect of stresses and the corrosive environment. The stresses can be mechanically applied (constant or cyclic), residual, and in some cases, thermal which depend on the operation conditions of the component or structure.

Due to their higher strength and corrosion resistance when compared to the austenitic grades, duplex stainless steels have been employed in many applications, for example the petrochemical industry, to solve problems of localised corrosion, e.g. stress corrosion cracking, pitting, crevice and corrosion fatigue. Currently the largest application of duplex steels exists in the oil/offshore industry [3].

It is well documented [1,4-6,8] that the corrosion of stainless steels (SS) is more severe in natural seawater than in sterile or synthetic seawater and there is agreement among researchers that the increased corrosion is due to biofilm formation. Electrochemical reactions are influenced by the formation of biofilms and the chemical micro-environment generated at the metal-biofilm interface [1,7].

There is an increasing demand for an understanding of the effects of complex load history on fatigue lifetime of components subjected to variable amplitude loading. The accumulation of damage during the fatigue lifetime of a component depends not only on its load history, but also of the synergistic effects of stress and surrounding environment [9]. The total fatigue life of a structure or component is often evaluated in terms of two stages: crack initiation and propagation. A more detailed characterisation of fatigue life considers the process of failure as [10]: crack nucleation, small crack growth, macro-crack growth and final failure.

Corrosion fatigue is defined as a synergistic effect in which corrosion and fatigue occur simultaneously. The combined effect of an aggressive environment, such as seawater, with a cyclic stress or strain is invariably more severe than the sum of the two effects of

corrosion and fatigue acting separately. It has been shown that many corrosion fatigue failures of stainless steels in seawater are induced in the early stages of damage by corrosion pits [11].

Pitting corrosion is a form of localised corrosion, and is interesting and unusual because most of the material is in fact not corroding; i.e., it is passive and stable [12]. Temperature, pH, oxygen concentration and biological activity also play an important role on the pitting corrosion process and, as a consequence, in the corrosion fatigue lifetime of structures constructed using SS.

The localised nature of pitting corrosion and corrosion fatigue initiation make necessary the use of increasingly sensitive electrochemical techniques. The Scanning Reference Electrode Technique (SRET) has been applied successfully to study this phenomenon. Using this technique it has been possible to measure localised pitting current densities and potential profiles during pitting corrosion of 304 SS in natural seawater [13]. SRET methods provide spatially resolved measurements and therefore have the advantage of improving the quantitative characterisation and understanding of localised corrosion.

The present work was focused in relation to the synergism between localised corrosion and microstructural short crack initiation in the early stages of damage by corrosion fatigue of stainless steels. Attending specifically the transition from corrosion pit to short crack involved in the corrosion fatigue process of these steels in saline solution by carrying out SRET measurements during corrosion fatigue experiments.

CHAPTER 2 – Literature Review

2.1 Stainless Steels

2.1.1. General Overview

Stainless Steels (SS's) are iron alloys containing at least 11% chromium. This weight percentage of chromium avoids the formation of rust in benign aqueous environments. The corrosion resistance of stainless steels is provided by the formation of a thin surface film of corrosion products of the steel, which is stable and self-healing in the presence of O_2. The presence of this protective film results in a very low corrosion rate, despite the high thermodynamic tendency of the steel to react in aggressive environments. It is from this characteristic that the popular designation "stainless" is used for this kind of steels.

SS's were developed during the first decades of this century in Great Britain and Germany. The earliest stainless steel types were martensitic and ferritic iron-chromium alloys but quite soon austenitic iron-chromium-nickel steels became the largest group. This was mainly due to the ease of production and fabrication, particularly welding, of these types of steel. The minimum carbon concentration that could be reached with the production and refining processes existent in that time was 0.08%. This made the steels susceptible to grain boundary carbide precipitation during heat treatment and welding operations. This carbide precipitation and the consequent

formation of chromium depleted zones after welding, (the heat affected zone "HAZ"), could induce sensitisation of the alloy and susceptibility to localised attack [14,15]. Stress corrosion cracking (SCC), intergranular attack (IGA) and intergranular stress corrosion cracking (IGSCC) are the most common forms of localised attack of sensitised austenitic SS's in chloride environments.

More than 180 different alloys can be recognised as stainless steel and each steel-manufacturer continue to produce new alloys with small compositional changes. In some stainless steels the chromium content now approaches 30%, and many other elements are added to provide specific properties. For example, nickel, nitrogen and molybdenum are added to improve corrosion resistance; carbon, titanium, aluminium, molybdenum, nitrogen and copper for strength; sulphur and selenium for machinability; and nickel for formability and toughness [15].

2.1.2 General Characteristics

According to metallurgical structure stainless steels are divided into three groups: austenitic "γ" face centred cubic (fcc), ferritic "α" body centred cubic (bcc), and martensitic (body centred tetragonal or cubic). There is another stainless alloy, duplex ("γ - α"), which possesses a two-phase microstructure with approximately equal amounts of austenite and ferrite [16].

The initial solution-treated state of the 300 series austenitic SS's is thermodynamically unstable and, consequently, changes in their microstructure can be induced to occur by thermo-mechanical treatment. Rapid quenching in the leaner alloys can promote martensite formation whilst thermal ageing of all steels promotes precipitation of carbides and intermetallics which may continue for considerable periods of time.

Carbides are the precipitates predominantly formed at temperatures in the range of about 500 to 600°C. Intermetallic phases are formed at higher temperatures. There are about 30 phases that have been identified in austenitic SS's [16,17]. The predominant precipitates found in weld metals and in-service components at 500 °C are $M_{23}C_6$ and the MC carbides in which M represents the metal involved. At temperatures above 600 °C, phase sigma (σ) and Fe_2Mo are also formed [17]

To a first approximation, the high temperature constitution of austenitic SS's is predicted from relevant isothermal sections of the ternary Fe-Cr-Ni equilibrium diagram, which uses the chromium and nickel equivalents which are calculated as follows [16,17].

Cr equivalent (wt percent) = % Cr + 2.0% Si + 1.5% Mo + 5% Va + 5.5% Al + 1.75% Nb + 1.75% Ti + 0.75% W.

Ni equivalent (wt percent) = % Ni + % Co + 0.5% Mn + 30% C + 0.3% Cu + 25% N.

The relative tendency of the elements to promote or inhibit the formation of ferrite has been quantified by numerous equations involving chromium and nickel equivalents. The actual amount of ferrite present in a steel composed mainly for austenite depends not only on the overall chemical composition, but also on the solidification and cooling rates and any thermo-mechanical treatments.

Austenitic SS's are commonly used in different processes of the chemical industry. Their high ductility and good resistance to general corrosion make these kinds of steels one of the most used around the world. Unfortunately, the most conventional austenitic SS (ANSI 304) is susceptible to stress corrosion cracking failure in chloride containing environments as well as localised corrosion notably pitting and crevice corrosion in the same media even at room temperature.

It has been proposed [6,8] that commercial austenitic SS's are not safe in marine applications because of the presence of chloride ions and microbiological activity, which can lead to a bio-film formation in the surface. The bio-film activity promotes changes in the rest potential towards more noble values so pitting corrosion can occur more easily. On the other hand, when the passive film is mechanically, chemically or electrochemically ruptured in seawater localised corrosion starts and in some cases this results in the failure of the component. For marine applications, the use of higher Nickel, Chromium and Molybdenum austenitic SS, or even ferritic SS is recommended. The problem is that alloying austenitic SS makes them more expensive, while ferritic SS are not sufficiently ductile and are difficult to weld.

However there is also the Ferritic-Austenitic "Duplex" SS, which was introduced only a few decades after stainless steels were developed. It has been shown [17], that an increase in the ferrite content increases the tensile strength and proof stress of austenitic SS. A further advantage of the presence of ferrite is that it causes grain refinement of the austenite, which produces additional strengthening. These two effects can be combined and accentuated by further refining the grain size by a controlled-rolling treatment, using hot working in the range of 900 to 950 °C or at even lower temperatures. This causes a very fine dispersion of ferrite and austenite, in approximately equal proportions, which give proof stress values in excess of 450 MPa. In fact, the central qualities of the Duplex SS are due in part to their two-phased microstructure, containing approximately 50% α and 50% γ, which strongly depends on the chemical composition, and on the heat treatment.

There are however some disadvantages associated with the presence of ferrite in duplex SS's since numerous structural modifications occur in these types of steel during isothermal or anisothermal heat treatments.

The majority of these modifications concern to ferrite, due to the diffusion rates are much higher in the bcc structure than in the fcc austenite. Ferrite phase is enriched in chromium and molybdenum, which have a strong tendency to promote the formation of intermetallic compounds. The matrix surrounding these precipitates can thus become depleted in these two elements leading to local decrease in corrosion resistance [17,18].

The duplex alloys generally have a superior resistance to localised corrosion and higher corrosion fatigue strength as compared to austenitic alloys. As for the austenitic and ferritic grades, the corrosion resistance of Duplex SS's is based on the presence of a passive surface layer. The protective characteristics of this passive film are determined principally by the chemical composition of the underlying metal. The composition of the passive layer is quite different from that of the metal substrate, as a consequence of the various processes which can take place when the alloy is in contact with an aggressive environment. The interaction with the environment can produce enrichment in elements such as chromium, nickel, molybdenum, silicon and copper, or selective dissolution of other species like iron.

In the case of Duplex SS's, each phase may have a distinct behaviour, with passive films of different thickness. Selective dissolution of one of the two components is also viable, since the anodic and cathodic reactions can take place simultaneously on each of them, but at different rates. It has been shown that the precipitation of intermetallic compounds in the ferrite phase induce more active electrochemical behaviour of this phase and as a consequence decreases dramatically the corrosion resistance of the alloy [18]. Stainless steels with a duplex structure show another mode of localised corrosion with respect to that of austenitic steels. The pitting behaviour of Duplex SS's depends on their structure, and the fact that manganese sulphide resides at grain boundaries when it is present, makes the process very complicated.

In Duplex SS's, the corrosion pits initiate at the ferrite/austenite (α - γ) phase boundary [14]. Once pits have initiated at the manganese sulphide or other species residing at the ferrite - austenite boundaries, they can propagate into either the austenite or the ferrite. Several researchers [19-22] have studied both behaviour trends and found that the content of nitrogen in the duplex alloy is the factor that controls the direction of the propagation of pits. When nitrogen concentration is in the range of 0.01 to 0.02%, the preferential partitioning of chromium and molybdenum to the ferrite phase renders the ferrite more resistant to pitting with the consequent pit propagation, and selective phase attack, taking place at the austenite phase. Conversely, for duplex SS's with a significant nitrogen content (e.g., 0.14 %), the opposite effect was found.

The high strength and good localised corrosion and corrosion fatigue resistance of duplex SS's have been employed for down-hole tubular in corrosive wells since the early 1970's. Duplex SS's were also used quite early in many applications in oil refineries to solve problems with stress corrosion cracking. In fact, the largest application of duplex SS's exists in the oil and gas/offshore industry. Hundreds of kilometres of pipeline have been installed and are still being installed [3].

2.2 Corrosion and Localised Corrosion

2.2.1. Introduction

In this part of the literature survey the basic aspects of corrosion and localised corrosion are presented. Pitting corrosion is addressed with some detail in section 2.2.4 due to the implications that this type of localised attack can have in the early stages of damage by

corrosion fatigue of stainless steel, which study is the main objective of the present work.

Corrosion reactions taking place at the surface of a metal in contact with an aggressive environment affect its mechanical behaviour when subjected to cyclic or static stress. For example it has been reported that carbon steel does not present a fatigue limit when it is tested in a corrosive environment [9, 23]. Stainless steels which are susceptible to pitting corrosion in chloride containing environments, present failure by fatigue induced in the early stages of damage by corrosion pits as shown by Boukerrou et al. [11]. The same behaviour has been reported by Wu [24], in a high strength steel and by Akid [9], in a medium carbon steel in contact with chloride solutions.

2.2.2. Corrosion

In everyday life, civilisation depends upon components, structures and machines, which are built with metals. Metals and alloys in contact with moist atmospheres are in most cases unstable. The presence of oxygen and other oxidising agents in the atmosphere or media with which metals are in contact favour metal instability and consequently their degradation. It is recognised that metals are unstable because they show a thermodynamic tendency to revert to their oxide or other chemical species from which most of them were extracted. Excluding the noble metals such as gold and platinum, for example, (which are much more expensive), all other metals present some degree of instability under atmospheric conditions. The stability of metals depends upon the events taking place on their surface when they are in contact with an electrolyte [25].

Corrosion of metals and alloys is generally an electrochemical process, which involves complex mass and charge transfer taking place at the metal-electrolyte interface. These charge transfer reactions at the interface are the origin of the instability of metals.

The theoretical principles for corrosion as an electrochemical phenomenon were derived from the mixed potential theory, which is the basis for corrosion testing. The modern form of this theory is commonly accredited to Wagner and Traud [26,27].

The necessary condition for corrosion is that the metal dissolution reaction and some electronation reactions (reactions that consume the electric charge liberated during metal dissolution) proceed simultaneously at the electrode-electrolyte (metal-environment) interface.

For the anodic and the cathodic reactions to take place simultaneously, two conditions are necessary:

a) The potential difference across the interface must be more positive than the equilibrium potential of the anodic reaction, represented here in a simplified way as

$$\mathbf{M^{n+} + n}e^- \rightarrow \mathbf{M}$$

where, M represents any metal, n is the number of interchanged charges and e^- is the electron, and

b) The potential difference across the interface must be more negative than the equilibrium potential of the electronation reaction:

$$\mathbf{A + n}e \rightarrow \mathbf{D}$$

which involves electron acceptors (represented by A in this equation) contained in the electrolyte.

When the electron-sink site or cathode, and electron-source area or anode are stable in time but at different defined places in the corroding metallic surface, local-cell or localised corrosion takes place.

On the other hand, when the metal dissolution and electronation reactions occur randomly over the surface with regard to both, space and time, the Wagner and Traud mixed potential theory of homogeneous corrosion is considered to be operative.

Corrosion can range from highly uniform attack for some metals and alloys in not very aggressive environments, (chemical or electrochemical polishing) to highly localised attack, such as occurs during pitting and crevice corrosion, intergranular attack and stress corrosion cracking.

The selection of the techniques used to evaluate and study corrosion depends on the kind of corrosion taking place. The principal aim of the corrosion scientist is to determine the mechanism of the corrosion process including intermediate reactions and the kinetics of these processes. Sometimes it is necessary to use intrusive methods (electrochemical methods) in which the system is stimulated externally and the response of the system to that perturbation is measured. Other techniques are able to measure electrochemical activity without the necessity of any kind of external perturbation to the system, the scanning reference electrode technique (SRET) and scanning vibrating electrode technique (SVET) are examples of non-intrusive techniques.

The most important aspect of corrosion assessment on components and structures in real service is the prediction of their residual life when there is a risk of undergoing localised attack. In that respect the use of electrochemical methods for studying localised corrosion is an important part of the evaluation since the kinetics and thermodynamics of localised corrosion are different with respect to general (uniform) corrosion.

In the case of general corrosion several electrochemical methods have been developed and are applied to assess the corrosion rate. In laboratory experiments and in the field the method of Tafel extrapolation and the measurement of the polarisation resistance (R_p) are the DC techniques most frequently used. AC techniques like electrochemical impedance spectroscopy are used as well to measure corrosion rate and to study the mechanisms involved in the metallic dissolution process.

From a structural integrity point of view general corrosion does not represent a serious problem for the corrosion engineer due to the fact that stress concentrator defects are not generated. Therefore general corrosion can be assessed using basic electrochemistry concepts and techniques [26,27]. In the case of localised corrosion, the measurement of the corrosion rate becomes more complicated due to unequal anodic and cathodic area ratios and therefore the effects of this kind of damage on the structural integrity of structures are much more severe.

2.2.3. Localised Corrosion

Due to their recurrent nature, localised corrosion processes often cause major practical problems affecting the performance of technologically important metallic materials, like stainless steels, nickel, aluminium, and many others metals and their alloys in different environments, especially those containing chlorides.

It can be considered that the corrosion process results from changes in the nature and composition of metals exposed to environments of homogeneous composition. The point of interest is "what happens when metals with approximately uniform composition are exposed to electrolytic environments in which composition changes makes them

heterogeneous, e.g. differential aeration?" In this case we are dealing with concentration cells, i.e. localised corrosion.

One of the established essential principles of corrosion is that: The sum of the rates of the cathodic reactions must be equal to the sum of the rates of the anodic reactions, irrespective of whether the attack is uniform or localised [26], so the following equation must be satisfied:

$$\Sigma I_a = \Sigma I_c$$

where I_c and I_a denote the cathodic and anodic currents respectively which has a direct relation with the reaction rate of the electrochemical process.

If it is considered that the attack is uniform and assuming that there is only a single predominant anodic and cathodic reaction, then:

$$I_a/S_a = I_c/S_c \text{ or } i_a = i_c$$

where i_a and i_c are the anodic and cathodic current densities assuming the area of the cathode S_c equals the area of the anode S_a.

When the corrosion attack is localised the anode area is very small compared with the cathode area, $S_a < S_c$ and as a consequence $i_a > i_c$, and the larger the ratio $i_a : i_c$, the more intensive the attack. Thus localised attack usually involves a corrosion cell consisting of a large cathodic area and a small anodic area.

It is now known that many aqueous corrosion processes of great technical interest occur under conditions in which the access of electrolyte is restricted. This can be due to the special geometry of the corroding material e.g. structures with riveted plates, flange joints, gaskets; and also due to the existence of some deposits such as corrosion products or scales on the corroding surface.

In the cases where corrosion occurs under conditions of restricted diffusion, the chemical composition of the corroding environment inside the occluded cavity may be very different from that of the composition of the bulk solution.

One of the most important effects is that changes in oxygen or ionic concentration in the electrolyte give rise to changes in corrosion potential. Under normal circumstances where the aggressive environment is aerated, the surface of the corroding alloy outside the occluded cavities is often passive as a result of the formation of an oxide film of corrosion products. Passivation takes place at these sites because they are in direct contact with the oxygen dissolved within the electrolyte. These surfaces act as aerated cathodes where oxygen takes part in the reduction reaction of the corrosion process. In this reaction the oxygen is reduced with the consequent increase of pH according to the following reaction for the case of basic or neutral solutions [25]:

$$O_2 + 2H_2O + 4e^- \rightarrow 4OH^-$$

or in a solution of low pH [28]:

$$O_2 + 4H^+ + 4e^- \rightarrow 2H_2O$$

The surface, which is inside the occluded cavity, is active and acts as anode as a consequence of the very low concentration of oxygen in the solution inside the cavity. At these surfaces the metal undergoes dissolution. Additionally, the hydrolysis reaction takes place with a decrease in the pH of the solution according to the following reaction sequence:

For iron

$$Fe \rightarrow Fe^{++} + 2e^-$$

and

$$3Fe^{++} + 4H_2O \rightarrow Fe_3O_4 + 8H^+ + 2e^-$$

For aluminium

$$Al \rightarrow Al^{+++} + 3e^-$$

and

$$Al^{+++} + 3H_2O \rightarrow Al(OH)_3 + 3e^- + 6H^+$$

Much effort has been made in the last 40 years for a better understanding of the processes involved in localised corrosion, the majority of these studies being focused principally on aspects of the growth and stability of the sites undergoing localised attack. On the other hand, the mechanisms of nucleation and early stages of damage are not yet completely understood.

An important improvement on the present state of knowledge is achieved when the global process of localised corrosion can be partitioned into a nucleation stage (initiation), and a successive metastable growth stage, which eventually is followed either by rapid repassivation or stable pit growth. If the active condition inside a crevice or pit is stable over a longer period of time, rapid metal dissolution usually takes place. The rate controlling reaction during the localised corrosion processes such as activation, diffusion, or ohmic control, has a significant influence on the shape and geometry of the crevices or pits produced.

The theoretical models, that have been proposed to describe the initiation of the localised corrosion process, can be grouped into [29-32]:

1. Adsorption mechanisms
2. Ion migration and penetration models

3. Mechanical film breakdown theories.

Substantial research has been carried out to study the structural parameters involved in localised corrosion processes. From these, it has been demonstrated that defects in the metal structure, such as non metallic inclusions or dislocations [33,35] may generally act as sites for pit initiation on passive metal surfaces.

Böhni [29], and Dean et al [36], used photo-electrochemical methods to study the semiconducting characteristics of passive films of stainless steels, which results emphasised the importance of the "electronic structure" of passive films on the resistance to localised attack. Ferreira et al. [37], using capacitance (Mott-Schottky approach) and photocurrent measurements, showed that the electronic structure of passive films of 304 SS is comparable to that of a p-n heterojunction in which it is necessary to consider the space charges developed at the metal/film and film/electrolyte interfaces. There is evidence of the structure of passive films in SS's, that suggests a two-layer structure as pointed out by E. le Roy et. al [38].

The inner layer is mainly composed of chromium oxide mixed with other chromium phases such as $Cr(OH)_3$ or CrOOH which has a p-type semi-conductive behaviour.
The outer layer is composed of iron hydroxide FeOOH and γ-Fe_2O_3 (pseudo-spinel structure) and has an n-type semi-conductive behaviour. Figure 2.1 shows a representation of this model of passive film.

The same authors [38] suggested that the passive film formed on SS's has a structural amorphous nature due to the excellent bond flexibility of the chromium. Increasing the chromium content in the alloy enhances the amorphous degree of the structure. They also indicated that molybdenum alloyed with SS's enhances the passive film to be chemically more homogeneous and structurally amorphous.

There is also indication that the increase of chromium in the alloy decreases the thickness of the passive film and is also responsible for its amorphous character [34].

Komachi and Katada [39], by using Electrochemical Atomic Force Spectroscopy found that the thickness of passive film of 316LN SS formed in 0.5 M NaCl at open circuit potential (OCP) increases as the immersion time. For polarisation experiments they observed that the height of the passive film increased when the potential was increased from the OCP to potentials 500 and 800 mV more positive.

Their results were as follows:

- At OCP condition: $d \cong 18$ nm
- At OCP after 2 hours of immersion: $d \cong 28$ nm
- At 500 mV (anodic polarisation) for 1 hour: $d > 60$ nm
- At 800 mV (anodic polarisation) for 1 hour: $d \cong 80$ nm

SS's with higher concentrations of alloying elements were found to have an increased pitting resistance due to the formation of passive films containing fewer defects and greater stability.

Despite the efforts made to understand this phenomenon, localised corrosion is a non-predictable degradation process of metals and alloys in contact with aggressive environments. This characteristic applies particularly to pitting corrosion in which the location and distribution of the pits on the metal surface, as well as their size depend upon the structure of the alloy and environmental conditions.

Given that most of the information related to the stable stage of localised corrosion has been obtained throughout studies of pitting and crevice corrosion, this aspect of the localised attack will be presented in the next section dedicated to pitting corrosion.

2.2.4 Pitting Corrosion

Pitting corrosion can be considered as a case where only small areas of the metal surface undergo localised attack whilst the rest of the surface is largely unaffected and remains passive. Pitting is a particularly insidious form of corrosion because the extent of metal dissolution reaction is small but the attack is rapid and penetrates into the metal. The result is the rapid perforation of thin metal sections. This can induce leakage of fluid in one case, or on the other hand, crack nucleation leading to brittle catastrophic failure. The location of pits on metals that develop passive films is often unpredictable, and the pits tend to be randomly dispersed on the metal surface [40-44].

Pitting corrosion can occur when a local breakdown of the passive film takes place in an aqueous solution. Active dissolution of the freshly exposed metal takes place and a microscopic corrosion pit is formed. When the passive film does not recover sufficiently rapidly, the tiny pit continues to grow, leading to an active macroscopic pit. Nevertheless in most cases, regeneration of the passive film occurs far more often than formation of an active macropit [40]. This suggests that only under specific disadvantageous conditions, repassivation fails to occur.

The location of pits is to some extent defined by the microstructure of the alloy and the geometry of the system. In chloride containing aqueous solutions, the uniform corrosion rate of stainless steels in the passive state is insignificant, i.e. 0.15 to 15.0 μm per year [41]. However, pitting corrosion of this type of metals is very common in these environments [42], where the local dissolution rate of metal can be up to 12 mm per year [43].

According to Burstein and Pistorius [45,46], the initiation of pitting corrosion in stainless steels takes place in two successive steps.

The first step is nucleation: breakdown of the passive film on a microscopic scale. This process involves small and sudden increments of anodic current, which are characterised by current spikes, leading to oxidation and dissolution of less than 0.01 μm^3 of metal. The nucleation process is unstable and in most cases it will stop by the regeneration of the passive film. Another possibility is that a nucleation event develops into the second stage of initiation, i.e. the metastable pit growth.

During this step, a gradual and bigger increase of the anodic current takes place. This stage stops if repassivation of the micro-pit occurs. A volume of up to several μm^3 of metal can be dissolved in stainless steel during the metastable growth. In some cases the metastable pit growth precedes stable pitting.

If fast repassivation of the freshly exposed metal does not occur after passive film breakdown, the formation of stable pits can take place. It follows then that a lack of repassivation of metastable pits leads to stable pitting. A high repassivation capacity of metals and alloys is therefore fundamental for avoiding pitting. Results obtained by the same authors in stainless steel showed that corrosion pits nucleate by a microscopically violent event associated with a sharp tiny transient current that induces metastable pit growth. They also observed that many of such nucleation events did not achieve the metastability stage, and became inactive after nucleation, as also pointed out by Isaacs [40].

Emphasis has been given to the concept that repassivation depends greatly on microstructural features present in most of the metals and alloys. Sedriks [42,47] indicates the importance of different types of inhomogeneities at the material surface during pit initiation. Lattice defects at the surface, precipitates, intermetallic phases, second phases and non metallic inclusions are advantageous sites for the nucleation of

pitting corrosion due to their different electrochemical behaviour with respect the metal matrix.

Pit nucleation, which leads to the formation of a small area of bare, (non passive metal) is likely to be a probabilistic process but can itself be the result of elementary steps at the atomic scale. As far as nucleation is concerned, pits can nucleate directly on the passive film, far from any non-metallic inclusion. Pits can also arise from the dissolution of unstable inclusions such as MnS, leading to a small area of bare metal when the inclusion is entirely or partially dissolved.

The behaviour of different types of non-metallic inclusions as initiation sites for localised attack has been explained by Srivastava and Ives [48,49]. They suggest four types of inclusion that can act as sites for the initiation of pitting corrosion, depending on the electrochemical characteristics of the couple inclusion – metal matrix. The four ways of pitting corrosion nucleation in non-metallic inclusion are represented in figure 2.2.

1. Preferential dissolution of the inclusion with a passive metal matrix, this is the case of the chemically homogeneous MnS in stainless steels.
2. Selective dissolution of one phase of the multiphase inclusion while the metal matrix is passive. For example combined oxide – sulphide inclusions in stainless steels where the sulphide phase is attacked first.
3. In type 3, the metal matrix that is adjacent to the inclusion is dissolved due to its electrochemical anodic condition to the inclusion.
4. The matrix and the inclusion are inactive, but a cavity formed in the boundary between them acts as an occluded cell and the localised attack occurs via a crevice corrosion mechanism.

Sulphide inclusions are considered to be of paramount importance with respect to the susceptibility of stainless steels to the initiation of pitting. In commercial austenitic stainless steels two types of sulphides that lead to the initiation of pitting are normally found. Sulphides of the type $Cr_xFe_yMn_zS$ enriched in manganese are generally designated as MnS. One characteristic of this type of sulphide is that it is readily soluble in aqueous solutions. The second type is a complex inclusion consisting of oxides combined with MnS, e.g. the oxy-sulphides [50-53]. Pitting corrosion can be initiated by the selective dissolution of the sulphide inclusion itself or by the sulphide phase of the oxy-sulphide inclusion present at the surface when the metal is in contact with an aqueous environment.

Wranglen and Eklund [54,55] have described in more detail the mechanism of pit initiation at MnS inclusions in stainless steels. Their mechanism also applies for oxy-sulphide inclusions; this mechanism basically suggests that MnS inclusions act as local anodes in the metal matrix.

Regardless of the specific set of reactions involved in the mechanism for the dissolution of sulphide inclusions, these normally dissolve selectively if they are in contact with aqueous solutions and produce a localised aggressive environment. The dissolution takes place principally at the boundary between the metal matrix and the inclusion and in most cases this induces the formation of micro-crevices.

There are other aspects affecting the growth of metastable pits, most of them are related to the formation of a physical barrier for the transport of species in and out of the micro-cavity. If dilution of the aggressive environment within the micro-pit does not take place, metastable pitting is maintained.

Castle et al. [51,56] found that the deposition of non-soluble products (FeOOH, Al(OH), Mn(OH) and metal silicates) from the matrix, or from oxides if a complex

inclusion is involved, can lead to the formation of a cap over the mouth of a micro-pit, which is in fact a transport barrier. Therefore, if the aggressiveness of the local environment is maintained above a critical level as a consequence of this physical barrier, passivation of the fresh metal surface created will not take place. The formation of an aggressive environment is favoured by the hydrolysis process, which induces the decrease of pH in the micro-pit.

Complex sulphides consisting of an inner oxide, surrounded by MnS are more liable to act as initiation sites for corrosion pits than homogeneous sulphides. Due to the selective dissolution of the sulphide phase the oxide part of the inclusion remains in the cavity acting as a diffusion barrier, which also promotes the formation of an occluded cell and prevents passivation. The attack of the metal matrix during dissolution of a sulphide inclusion only takes place if the precipitation of the $MnCl_2$ salt film occurs in the micro-pit [57]. When the precipitation of a $MnCl_2$ film occurs, passivation of the bare matrix metal is prevented at the former boundary metal - inclusion, stabilising pit growth.

Pickering [58] gave emphasis on the importance of changes in the local potential within a micro-pit. An IR-drop between the bottom of the cavity and the passive exterior surface surrounding the pit can induce this potential shift which could move the local corrosion potential in the pit to values below the passivation potential. It can be considered that precipitation of metal salts might increase the IR-drop within the micro-cavity, however this phenomenon is not applicable to all systems and it can not be taken as a constant step for the pitting initiation mechanism.

After pit initiation the micropit often repassivates and the localised attack finishes. Alternatively, in certain cases metastable pitting develops and the process moves to the

stage of stable pit growth, e.g. pit propagation. During the pit propagation stage, active dissolution of the metal matrix takes place continuously in the pit. The necessary condition for an active pit is the presence of an aggressive environment inside of it. The aggressiveness of the environment is a function of the pit depth and the local dissolution current, which provide a saturated metal salt solution that prevents passivation.

The pH in the pit decreases due to hydrolysis induced by the metal ions produced during metal dissolution. Under this condition, the pit remains active, behaving as a small anode, while the surrounding surface acts as a large cathode. Pit growth continues by an autocatalytic mechanism. The rapid production of metal ions within the pit induces the diffusion and migration of anions towards the pit. Cl^- is the principal anion in marine environments and the commonest ion leading to passive film breakdown. Suzuki et al [59] determined the pH within artificial pits in different pure metals as well as in stainless steels immersed in chloride solution. Their results indicated that when chromium and molybdenum were present in an alloy these elements would have the greatest effect in lowering the pH within the pit. On the other hand, pit extension, in depth and area, is in some degree an autocatalytic process, which is favoured if the passive film remains partially covering the pits.

Several researchers have suggested that a critical concentration of ionic species must be exceeded for stable pit growth to occur. Galvele [60,61] considered localised acidification in the pit due to hydrolysis by metal ions as the principal precursor of stable pit growth. Acidification reduces the ability of OH^- to absorb and hydroxide layers to form at the metal surface during passivation. The same author establishes from a simulation using a mathematical model that a critical value of the product **ix** must be attained to allow stable propagation of pits, where (**i**) is the anodic current density and (**x**) is the pit depth.

The required degree of acidification to maintain the activity of the pit can be reached at the critical value of **ix**.

The effect of salt films formed within the pits during initiation or growth processes has been recognised and discussed by several authors. Beck and Chan [62] demonstrated that the presence of salt films on stainless steels is important for the stability of growing open pits. They concluded that repassivation takes place as soon as the salt film is destroyed or removed and that the salt film is more important in maintaining pitting than a low pH within the pit.

Further support of the importance of salt film formation was obtained by Frankel et al. from studies on metastable pitting of stainless steels where covered pits were formed during metastable growth [63]. From the evaluation of single current transients and assuming a hemispherical pit shape the same author showed that most of the pits grow at constant current density. The transition from metastable to stable pit growth occurs only when a critical value of the product $i_P\sqrt{\tau_P}$ is attained, where i_P is the pit current density and $\sqrt{\tau_P}$ is the life time of the pit.

Ohmic drops can not serve as an explanation for the formation of small pits with micrometre dimensions. However in the case of pits with widths of several millimetres at the latter stages of propagation the ohmic drop might become sufficiently high to satisfy this condition. pH shifts also cannot explain the stable pit growth for metals like Fe, Ni, and steels which are passive in strongly acidic electrolytes.

The requirement for aggressive anions and their influence on the repassivation kinetics demonstrates that their accumulation stabilises localised corrosion in the early stages. The autocatalytically enhanced dissolution of the passive layer by these anions prevents any repassivation once a pit has formed.

For sufficiently positive potentials the intense dissolution process leads to severe accumulation of corrosion products and finally, after a transition time, to the formation of a salt film which is a further stabilising factor for a pit.

Pits may also be stabilised by other complicated effects. In some cases precipitated corrosion products such as hydroxides cover the mouth of the pit or even a metal layer can cover it leading to irregular dissolution. Under these circumstances an ohmic drop can induce a potential shift of the pit surface below the passivation potential.
Finally, the presence of a gas bubble within a pit can cause a similar situation to that with a crevice with related ohmic drops. Hydrogen bubbles have been observed within pits and served as an explanation for stable pitting [64]. Apparently gas bubbles may be an important stabilising factor for some special systems particularly in the latter stages of pit growth.

Pickering [58] has shown that attached gas bubbles could be a factor in causing local dissolution of the passive film. When the metal surface containing an attached gas bubble is polarised into the passive region, the passive film is formed everywhere except where the bubble is attached to the surface. Although it is not physically possible to measure the potential difference in the micro-crevices formed by a gas bubble and the metal wall, its value needs to be large enough to cause the electrode potential in the micro-cavities to be below the passivation potential of the metal. Results of IR drop measurements in the micro-crevice support this hypothesis [58].

A specially damaging form of pitting occurs when a structure is subjected to static or cyclic loading while exposed to an aggressive environment in which it is passive. The applied strain breaks the oxide film, allowing fresh metal to corrode at the sites of film breakdown leading to pit nucleation and growth.

There are some models to explain the Pitting-Corrosion Fatigue damage in metals, which involve an initiation step where breakdown of the passive film has an important role, as will be presented in the literature survey dedicated to corrosion fatigue.

2.2.5 Crevice Corrosion

Crevice corrosion is another type of localised attack that is frequently found on stainless steels in contact with chloride containing electrolytes. This phenomenon is typically encountered in confined media, i.e. when the corrosion occurs in a limited volume of electrolyte, as a consequence of the presence of a geometrical heterogeneity in the corroding system. Thus, this form of localised attack starts at defects formed at the surface of the metal e.g. scratches, cracks or contact joints with other components or contaminant deposits.

Because of the nature and characteristics of this kind of localised attack, it can be considered that pitting and crevice corrosion are virtually the same, i.e., a pit is a form of crevice that is self initiating. Stainless steel equipment that undergoes pitting corrosion can be expected to also suffer crevice corrosion, but the reverse is not true. On a passive metal such as stainless steel, crevice corrosion occurs when the cathodic reaction, that sustains the dissolution in the passive state, becomes insufficient due to depletion of the oxidising species in solution inside a cavity [65].

In this kind of localised attack the cathodic reactant (dissolved oxygen in most cases) can readily gain access by convection and diffusion to the metal surface outside the crevice. In the next stage, only the metal dissolution reaction takes place in the crevice, which provokes an increase in cation concentration and acidification due to hydrolysis.

On the other hand, access to the layer of the stagnant solution within the cavity (crevice) is much more difficult and can be achieved only by a diffusion process through the small mouth of the crevice. When the local environment reaches a critical concentration, the third stage, permanent breakdown of the passive film takes place. This is a clear case of corrosion induced by differential concentration of the cathode reactant.

Crevice corrosion can range from a quasi-uniform attack to pitting at the metal surface within the crevice. It can occur with a variety of alloys, and it is especially prone to take place with metals and alloys that rely on passivity for their corrosion resistance, for example stainless steels.

One possible indicator of crevice corrosion activity is the "protection potential" as used in pitting corrosion studies. This protection potential is the potential below which crevice and pitting corrosion will not occur. Above the protection potential crevice corrosion will occur, but pits will supposedly not initiate, although if present they will grow. Above a second potential, (critical pitting potential or rupture potential), pits will initiate, and both pits and crevices will grow. Hubbell et al. [66], suggested that pitting corrosion, supposedly initiated by activating the metal surface at elevated potentials, and crevice corrosion can be prevented at the same " protection" potential. This is due to the fact that crevice attack normally takes place at more active potentials compared with the pitting potential.

Experiments carried out during the present research showed, for the case of stainless steel in artificial seawater subjected to anodic polarisation, that crevice corrosion was induced before or instead of pitting. In some cases crevice corrosion was the dominant form of attack with pits repassivated after being nucleated.

The chronoamperometries performed at anodic potential on SS samples undergoing crevice corrosion presented a higher increase of current with time when compared with that for stable pit growth.

Increasing attention has been paid to the effect of inclusions, specifically oxy-sulphides, on the initiation of crevice corrosion. The mechanism described above is extended with the dissolution of the oxy-sulphides in the crevice, which stimulates the formation of an aggressive solution of critical concentration. According to this mechanism, the initiation of crevice corrosion is similar to that for pitting, with the difference being the additional barrier formed at the former and also that crevice corrosion can occur under milder conditions than pitting.

2.3 Fatigue

2.3.1 Introduction

Fatigue phenomenon in engineering materials is a topic which involves several scientific disciplines and which provides a rich variety of phenomena for fundamental and applied research. In this part of the literature survey a basic introduction of the fatigue process is given. The intention is to gain a basis of the two aspects involved in the complex process of damage by corrosion fatigue (CF), the corrosion theory given in the previous section and fatigue damage of metals before presenting the theories developed to explain the CF phenomenon.

Metal fatigue has been studied for over 150 years, with the first study believed to have been conducted around 1829 by Albert who performed tests involving repeated loading on mine-hoist chains made of iron [67]. In a historical survey of the fatigue of metals Suresh [68] pointed out the work of Wöhler who conducted systematic investigations of fatigue failure in Berlin from 1852 to 1869. Wöhler observed that the strength of steel railway axles subjected to cyclic loads was appreciably lower than their static strength. His work led to the characterisation of the fatigue behaviour in terms of stress amplitude-life (S-N) curves and to the concept of the fatigue endurance limit. The work of Gerber in 1874 is also mentioned as he began developing methods for fatigue design such as fatigue life calculations for different mean levels of cyclic stresses.

During the last 4 decades many aspects of fatigue damage in materials has been studied and reported, such as fatigue crack initiation, fatigue crack propagation, the fatigue limit, fatigue resistance, the calculation of fatigue life and mathematical modelling of the fatigue process.

In 1961 Forsyth [69] recognised and proposed the existence of two different forms of cracks, a stage I crack driven by shear stresses, and a stage II crack driven by tensile stresses figure 2.3. The former occurs on a plane of maximum shear strain, the latter on a plane whose normal is the direction of the maximum tensile stress. Depending on the stress-state and its intensity, either Stage I or Stage II cracking will dominate the fatigue lifetime of specimens, components and structures.

As it will be seen later in this chapter, before, during and after the transition zone from stage I to stage II the description of the fatigue crack growth will depend on the current crack length, the stress state and the stress level. Once an initial crack is detected in a component or structure the next task is to determine and measure the crack growth rate for which the concepts of fracture mechanics are applied.

Figure 2.4 illustrates the three different forms of fracture mechanics applicable to the fatigue process. For long cracks propagating under low applied stresses, linear elastic fracture mechanics (LEFM) provides an adequate description of fatigue crack growth behaviour. But when the initial crack size is physically small, e.g. 500 microns, the stress level for propagation is necessarily high and the assumptions that were considered for LEFM analysis may be inappropriate.

Consequently an EPFM (elastic-plastic fracture mechanics) description of the crack growth is necessary. Finally, considering the extremely short cracks, these are influenced in their behaviour by the texture of the given material, therefore requiring the implementation of microstructural fracture mechanics (MFM) to describe their growth [67].

Some models have been reported recently for the study of short cracks, for example Hobson´s [70] and Navarro-de los Rios [71]. Also, it has been reported the use of a superposition term (da/dN_{diss}) in the Brown-Hobson and the Navarro-de los Rios models to predict the short crack growth under corrosion fatigue conditions [72].

It is well know that fatigue damage results in progressive localised and permanent structural change and may result in cracking and subsequent fracture of the structure or component after a sufficient number of loading cycles. Most of the work reported concerning fatigue research considers fatigue as a two-stage process. The first stage involves the development of a crack, i.e. crack initiation, and the second stage describes crack propagation.

Depending upon the level of a cyclic stress, a crack can be initiated at the surface of the component from pre-existing surface features such as grain boundaries, non-metallic inclusions or boundaries between two or more phases.

The presence of inclusions almost always has a deleterious effect on the fatigue and fracture resistance of materials subjected to loading in air as well as in corrosive environments. Inclusions introduce strain concentrations because of the mismatch of mechanical, physical and electrochemical properties with the matrix material. The vast majority of cracks associated with fatigue start at a free surface, so, the nature of that free surface is an important factor [73]. Wang and Miller [74,75] have shown the effect of inclusion orientation on fatigue resistance. The size and shape of non-metallic inclusions has an important effect on fatigue crack initiation.

It is not necessary for the bulk of the grains in a piece of metal to deform plastically for it to fail by fatigue. Continued cyclic plastic deformation in one localised surface region is sufficient for fatigue failure to occur. Depending on the characteristics of the applied stress and the crack length, once initiated, cracks may either continue to propagating or arrest [76]. The arrest of cracks at sub-fatigue limit stresses occurs because the mechanical driving force associated with the crack is not large enough to overcome the arresting microstructural feature, for example a grain boundary. Hence a fatigue limit can be defined as a limiting stress below which cracks once initiated are unable to propagate and produce failure, i.e. the crack growth rate being zero [77].

Structures subjected to cyclic loading may fail as a consequence of the growth of a single crack or as a result of the coalescence of several cracks, which depends upon the stress history-material strength relationship. It has been proposed that the fatigue fracture process can be divided in the following stages [78]:

1. Cyclic plastic deformation prior to fatigue crack initiation,
2. Initiation of one or more microcracks,
3. Propagation or coalescence of microcracks to form one or more macrocracks,

4. Propagation of one or more macrocracks and

5. Final failure.

The trend in recent evaluations has been to define a concept involving crack growth rates rather than to determine the "total life to failure". The new "fail safe criterion" generally assumes that either cracks are present in the material before service or that cracks are initiated very early in the service history, these assumptions suggest that the crack growth controls fatigue behaviour [68]. Therefore, crack initiation and crack growth measurement are very important parts of the material property studies.

2.3.2. Fatigue crack initiation

The initiation stage of fatigue cracks is an event whose definition depends upon the size scale of observation. Materials scientists are expected to consider the nucleation of flaws on persistent slip bands as the initiation stage of fatigue failure, whilst on the other hand designers and mechanical engineers normally associate the resolution of crack detection with the threshold for crack nucleation. Generally speaking it can be considered that crack initiation is strongly dependent on the ductility of the material, which is a function of the microstructure, and applied stress level. The fatigue failure can be considered as a mechanism of crack initiation and crack growth. As the time period spent in the initiation of a crack is usually significantly short with respect to the total life, Miller [76] has described fatigue as a mechanism dominated by crack propagation. From this point of view it is suggested, that in polycrystalline metals it can be safely assumed that the crack initiation phase does not exist.

When considering crack initiation, it is necessary to emphasise the stages that serve as the basis for the initiation and subsequent growth of cracks during mechanical fatigue conditions. Several researchers in this area have shown that pre-crack deformation is accompanied by considerable plastic deformation, which generates a highly localised dislocation density on slip plans [79]. It is normally accepted that fatigue crack initiation occurs at the surface, although sub-surface nucleation has also been reported [79,80].

It is clear that cracks generally initiate where a stress concentration exists, sometimes due to the surface roughness or from persistent slip bands (PSBs) in which minute extrusions and intrusions form as illustrated in figure 2.5. Fatigue tests of carbon steel showed the formation of slip bands and their role as sites for crack initiation [81].
Defects present in metals and alloys can induce the initiation and growth of fatigue cracks if they act as stress concentrator, which depends on their shape, size, orientation, the stress state and applied stress level. Cracks can also initiate within large grains, at relatively weak grain boundaries or at soft regions such as the precipitate free zones adjacent to grain boundaries.

Initiation can take place at second phase particles due to incompatible deformation paths within the matrix and from non-metallic inclusions as consequence of:

a) Cracking of the metal matrix adjacent to the inclusion.
b) Separation or de-bonding at the inclusion/metal matrix interface, or
c) Cracking of the inclusion itself.

In general the presence of inclusions can have a harmful effect on the fatigue and fracture resistance of components and structures. The number, size, and position of the inclusion have been found to be of paramount importance in determining their effects on the subsequent fatigue behaviour.

Inclusions induce localised strain concentrations due to the mismatch of physical and mechanical properties with the surrounding metal. Differences in thermal conductivity and thermal expansion coefficients between metal and inclusions can introduce either tensile or compressive residual stress fields, which are frequently the sites of crack initiation on the surface. The effect of the inclusion size, grain size, inclusion orientation and inclusion shape factors on the fatigue crack behaviour is represented schematically in figure 2.6(a),(b),(c) and (d) respectively .

From a scientific point of view, the development of a quantitative understanding of the crack initiation process must be regarded as one of the most important tasks in the study of fracture by fatigue. A number of models for fatigue crack initiation have been proposed and can be generally classified into:

1. Single slip system model.
2. Alternating parallel slip system model and
3. Two intersecting slips line models.

Due to a confusion of data and theories, it is considered that the theory of crack initiation is still at a formative stage and so will not be discussed further.

2.3.3 Fatigue crack propagation

Following crack initiation the crack enters the propagation stage. It has been established that the change of the crack length **a** with the number of loading cycles **N** (fatigue crack propagation rate da/dN) in metals generally varies with the stress intensity factor range $\Delta K = (K_{max} - K_{min})$ where $K = \beta\sqrt{\pi a}$ [82,83]. In most metals crack growth rates vary over a wide range, typically between 10^{-8} to 10^{-2} mm/cycle and can be divided into three different stages:

Stage I Crack Propagation

Regime I: Low crack growth rates below 10^{-6} mm/cycle are strongly sensitive to microstructure, load ratio $R = K_{min}/K_{max}$ and environment. The threshold stress intensity factor range below which, no cracking occurs is termed ΔK_{th}. Cracks in the stage I of propagation lie along the active slip planes, which coincide with the maximum shear plane. This stage of growth can continue for a few grain diameters, usually one or three until the crack changes its propagation direction onto the tensile plane, at which point stage II starts.

Stage II Crack Propagation

When the crack grows in a plane that is perpendicular to the direction of the nominal stress it is considered to have entered the second stage. The transition from stage I to stage II depends upon the stress level, the material microstructure, the environment and stress state and is due to strain incompatibility at grain boundaries or phase boundaries. Cracks in stage II are frequently classed as long cracks because their growth can be quantified using Linear Elastic Fracture Mechanics (LEFM) as shown in figure 2.7. The Paris law established that crack growth rate is proportional to the stress intensity factor range, i.e., $da/dN = C\Delta K^m$, where C and m are constants obtained experimentally [68,83]. Where crack growth rates are between 10^{-6} and 10^{-3} mm/cycle, cracking proceeds by a transgranular ductile striation mechanism and there is little influence of microstructure and load ratio on the propagation rates.

Stage III Crack Propagation

Stage III of the fatigue process corresponds to growth rates above 10^{-3} mm/cycle, inducing instability before final failure and the crack growth rate is faster than that predicted by the Paris equation. Crack growth in this stage is influenced by the microstructure, mean stress and thickness, but not affected by the environment. This stage of propagation is known as final rupture and ductile tearing of the material takes place as a consequence of the nucleation of voids.

2.3.4. Short Crack Behaviour

LEFM has been a valuable tool in the analysis of long crack growth. However, when this approach is extended to the short crack regime it is found that short cracks tend to grow more rapidly than long cracks (as predicted by LEFM) when subject to the same nominal driving force. As a result of the interaction between small cracks and microstructural features, the underlying similitude concept in LEFM analysis which links ΔK and the crack growth rate is known to break down [84,85].

From the studies of short fatigue cracks in the last 20 years a new perspective of the concept of fatigue limit has been introduced [86-88]. This limit is now seen as one associated with the inability of very small cracks to propagate beyond microstructural barriers, which are inherent within the material.

Miller [76] has proposed the following definition for a short fatigue crack:

The upper limit of a short crack is the length from which the crack growth can be evaluated from LEFM concepts. In this case the stress intensity factor is the threshold value and the maximum value of the cyclic stress is approximately equal to two - thirds of the cyclic yield stress of the material.

Three types of short cracks have been defined [76]:

1. Microstructural short cracks (MSC): include those that are of the same order of size as the microstructural features such as grains or inclusions. Plastic deformation near the crack tip is very much influenced by material microstructure, and the grain boundaries will block or retard crack growth. The assumption of a macroscopic continuum in fracture mechanics is violated because of the non-homogeneous microstructure.

2. Physically short cracks (PSC): The length of this kind of crack could be comparable to the plastic zone size; PSC are longer than the dominant microstructural barrier length (d), but are of a length less than the minimum length for which LEFM is valid. As the growth rate of these cracks is not affected by the microstructure, their growth rate increases linearly with crack length.

3. Highly stressed cracks: The behaviour of these cracks can be analysed applying the LEFM concepts, but the applied stress level is greater than $2\sigma_{cy}/3$.

Brown [89] also proposed that short and long cracks can be differentiated if the extent of plasticity ahead of the crack tip is considered, i.e. a crack is considered as short if its length "a" is smaller than the plastic zone size at its tip (r_p). It is generally accepted that when the ratio $a/r_p >> 1$, a crack is considered long LEFM - Mode I (Stage II) tensile crack.

For intermediate values of the ratio a/r_p the crack is considered physically short, in this case the crack growth rate is assessed by the use of EPFM. If the situation is that $a/r_p << 1$, a crack is considered microstructurally short MFM - Mode II (Stage I) shear crack. It has been shown that short cracks grow at faster rates in the beginning of their growth but then slow down and sometimes arrest.

This behaviour depends on the applied stress level, as they approach a barrier to their growth, which can be a grain or phase boundary.

When the applied stress is higher than the fatigue limit, the crack growth decelerates for a while and then accelerates until failure occurs. If the applied stress is equal to the fatigue limit the crack growth shows again a deceleration with longer periods of time spent at the microstructural barriers before the development of a long crack. For the case of a stress level below the fatigue limit an initiated crack will arrest at every microstructural barrier appearing during its growth and depending upon the stress level the crack will become non-propagating. Even though a crack can be non-propagating it can induce failure if the barrier is overcome by the imposition of an overload or by dissolution process acting in the crack tip [90]. Under these conditions the crack length can attain the threshold value (a_{th}) for the corresponding stress level and produce failure.

It has been reported by Lankford [91] that deceleration of short cracks happens as a consequence of blockage of the plastic zone and pointed out that the grain size and the size of the plastic zone are parameters which affect short crack growth. If the size of the plastic zone is greater than that of the grain, the grain boundaries do not represent a significant influence on the growth and then no deceleration is observed.

Brown [92] reported that the increase or decrease of crack growth in a titanium alloy was associated with the orientation of grains ahead of a growing crack. Favourable orientations will avoid deceleration during crack growth; the opposite case might induce retardation or even, crack arrest.

From the results presented by several researchers as quoted above it is clear that microstructural aspects must be considered and incorporated during the analysis of short crack growth behaviour.

Several models have been developed to predict the behaviour of short fatigue crack growth. These models which, in general deal with fatigue in air of different metals and alloys do not consider the crack initiation stage. The objective of the present research project is however the study of the transition of a corrosion pit to a short crack during corrosion fatigue damage of stainless steels, for that reason no emphasis is made in describing these models.

In the next section of the literature survey some models of pitting corrosion fatigue are presented as the final aspect of the corrosion fatigue phenomenon.

2.4 Corrosion Fatigue

2.4.1 General overview

Corrosion fatigue (CF) is a degradation process, which involves the synergistic effect of electrochemical reactions (reactions in which charge transfer takes place at the metal - electrolyte interface), and mechanical cyclic loading (fatigue). The combined effect of an aggressive environment, such as seawater, with a cyclic stress, or strain, is invariably more severe than the sum of the two effects of corrosion and fatigue acting separately.

CF is the successive stages of metal damage that evolve with accumulated cycling loading, in an aggressive environment compared to inert or benign media, and resulting from the interaction of irreversible cyclic plastic deformation with localised chemical and electrochemical reactions. The most complicated aspect of CF is the "combined" nature of the process, as it has been shown by Gangloff [93] that neither cyclic stress in

air nor environmental attack applied separately produces the same damaging results as that of the simultaneous action.

It is generally suggested that the presence of an aggressive environment enhances both crack initiation and crack growth for a number of specific metal-environment systems when subjected to cyclic loading [94].

Corrosion fatigue has been recognised since the beginning of this century as a principal mechanism for material damage during service. The emphasis of much of the earlier work was placed upon the S-N behaviour, which is dominated by the initiation phase [95].

The majority of observed fatigue failures are in fact CF failures, since only fatigue occurring in an absolute vacuum could be termed as "pure fatigue." The study the fatigue damage of machines and structures operating in corrosive environments is imperative, as it is known that such environments reduce the fatigue strength far below the typical fatigue strength determined in air. In some cases the environment eliminates the fatigue limit associated with air fatigue performance as represented schematically in figure 2.8 [96-99].

The analysis of the fatigue behaviour of metals and alloys in aggressive environments is much more complicated than that of the (in-air) fatigue damage process. An interesting result obtained by Cowley et al [100], shown in figure 2.9, indicates that for high cyclic stresses, a solution of 10% sulphuric acid promotes a longer fatigue life for a stainless steel at open circuit potential when compared with its fatigue life in air. When the cyclic stress was decreased they observed failure for corrosion fatigue while the fatigue test in air did not show failure after 10^8 cycles. That behaviour can be due to retarded crack initiation as a consequence of the tip crack blunting [82].

In some metal-environment systems the combined effect of corrosion and cyclic loading has been shown to produce cracks from corrosion pits and pits have frequently been the source of cracks, for example on aircraft components operating in fleets. Once a pit or group of pits is formed, the rate of pit growth is dependent mainly on the material, environment, and on the type and state of stress. Therefore, to estimate the total corrosion fatigue life of a component, it is of great importance to develop realistic models which take into account the early stages of damage, including corrosion dominated processes, i.e., pitting. These models can be used to formulate methods by which designers can know and assess the effect of pitting corrosion on the fatigue life of components and structures, and apply that information for the design.

With the intention of understanding and controlling the phenomenon of corrosion fatigue failure, some models based on pitting corrosion fatigue (PCF) mechanisms have been proposed in the past and some others are emerging which will be presented later in this chapter.

While it has frequently been stated that any metal or alloy that presents corrosion in a particular environment will also exhibit corrosion fatigue, such a behaviour, although supportable, can not be generalised. It is not possible to establish a simple correlation between the extent to which different environments provoke different amounts of corrosion upon a given material and their relative influence upon the fatigue lifetime. Corrosion reactions may enhance crack growth if they produce metal dissolution at the crack tip maintaining crack sharpness or promoting the easy transport of hydrogen into the metal for those metals that are susceptible to hydrogen induced damage [101]. The aggressive environment acting simultaneously with cyclic loading promotes an increase in the density of cracks when compared to that observed in air.

The corrosion fatigue phenomenon is also considered to consist of two principal stages like the process of air fatigue, namely crack initiation and crack propagation. The initiation stage, the period required for the nucleation of cracks has been estimated to be 10 per cent of the total lifetime, whereas it is around 90 per cent for the case of air fatigue [102]. The term 'initiation stage', is in someway an ambiguous concept as in fact such term refers to a period that a defect takes to attain a detectable size. The minimum detectable size, and as a consequence the duration of this period as a fraction of total life, is a function of the method used to detect the defect. The second stage, which corresponds to crack propagation, presents perturbations in the growth of short cracks due to microstructural obstacles such as grain and phase boundaries.

This anomalous behaviour only continues to a certain crack length after which the crack growth rate may have a linear relationship with the crack length.

In both air fatigue and corrosion fatigue fracture processes, macroscopic cracks are termed long cracks and the initiation and growth of microscopic cracks in the sub-millimetre range precedes their formation. The latter are termed short cracks and their growth can occupy the major percentage of the fatigue life.

During the CF process, the damage accumulates with increasing the number of load cycles (N) in the following stages [103]:

1. Cyclic plastic deformation
2. Microcrack initiation

   2.1 Corrosion fatigue crack initiation can be the result of pitting.
3. Short crack growth to link and coalescence, and
4. Macrocrack propagation.
5. Failure of the component.

The mechanisms for CF may involve hydrogen embrittlement; film rupture, dissolution and repassivation; enhanced localised plasticity; interactions of dislocations with surface dissolution, films or adsorbed atoms; and complex combinations of these processes [103, 104]. The contribution of each mechanism is controversial and depends on metallurgical, environmental and chemical conditions.

Theories of corrosion fatigue have generally relied on one or more of the following mechanisms [104-109]:

1. Stress concentration at the base of hemispherical corrosion pits created by the interaction with the aggressive environment.

2. Electrochemical attack of plastically deformed areas of metal with non-deformed areas acting as cathode.

3. Dissolution of the metal due to the rupture of the protective surface film.

4. Surface energy reduction of the metal produced by adsorption of species (principally atomic hydrogen).

Fatigue crack initiation of components in an aggressive environment can take place as a result of diverse electrochemical phenomena such as localised corrosion processes. Pitting corrosion, preferential dissolution, film rupture and the lowering of the surface energy are the most studied mechanisms suggested to explain the phenomenon.

2.4.2. Pitting Mechanism

Pitting is considered as a major mechanism for crack initiation in CF. Many researchers [9-11, 23, 94-106] have studied corrosion fatigue of metals in a variety of environments and surface conditions. It has been proposed that for damage at smooth surfaces the

process can involve the generation and growth of corrosion pits, the wedge action of corrosion products, dissolution and passivation of crack surfaces, as well as the interaction and coalescence of multiple cracks. As it was described in the section dedicated to corrosion fatigue, the presence of corrosion pits is not necessary to promote cracking on some alloys undergoing corrosion fatigue damage.

Congleton et al [101] provided evidence of crack initiation associated with the pitting corrosion process where corrosion pits were seen very easily on the surface of the metal when this is subjected to CF conditions.

Corrosion pit formation in metals and alloys in aggressive environments undoubtedly does lead to a reduction in fatigue life. Akid [81] demonstrated the effect of pH on the CF crack initiation, he showed that CF cracking arose from pitting in pH 6 solutions and from the dissolution of slip bands in solutions with pH 2. However, it is important to note that the corrosion fatigue phenomenon also occurs in environments where pitting corrosion does not occur. For example Duquete et al. [110] showed that carbon steels are highly susceptible to CF in acidic solutions, where pits are not detected, and additionally they observed that, reduced fatigue lives could be induced be the application of small anodic currents in de-aerated solutions where corrosion pits do not form.

On the other hand, fatigue tests carried out in 3% NaCl solution adjusted to pH 12 with NaOH, where only a few randomly distributed pits were found, showed fatigue limits very similar with those observed in air [108]. This behaviour is perhaps expected since corrosion pits formed in carbon steel in these conditions tend to have a hemispherical geometry and the stress concentration they induce is not very high.

Akid et al. [111] observed that during the early stages of defect development in carbon steel in chloride solutions, pit development and stress assisted dissolution speeded up the transfer of a stage I shear crack to a stage II tensile fatigue crack.

In stainless steels, corrosion fatigue crack initiation is promoted by any surface defect that has the characteristics of a real stress concentrator. Mechanical notches are more dangerous in corrosive environments than in air fatigue, and the development of corrosion pits is particularly deleterious.

Quian and Cahoon [112] demonstrated that cyclic plastic deformation accelerated both the dissolution of slip steps and the pit initiation in 316L SS in chloride containing solution. The same authors suggested the mechanism of pitting corrosion and preferential dissolution of slip steps, in which groups of small crystallographic pits form and coalesce resulting in the creation of small cracks. However, it is clear today that the presence of surface defects or pits is not necessary, as indicated by Magnin [113] who shown how the environment promotes CF crack initiation by enhancing the localisation of plastic strain.

For 'defect' free surfaces of metallic components susceptible to pitting corrosion subjected to cyclic stresses in aggressive environments a very important aspect of the corrosion fatigue damage process is the transition: corrosion pit $\rightarrow$ short crack. This transition step, which can be considered as the moment at which a crack is completely established at a pit site, is believed to have a marked effect on the resulting fatigue lifetime. The transition point depends on the applied stress level, the nature of the environment, the pit depth and on the loading frequency as demonstrated by Akid [111]. The same author suggested that a model to determine the time for a pit to develop into a crack must incorporate both frequency and stress terms.

For a given metal - electrolyte system that develops corrosion fatigue cracks from pits, the stress-assisted dissolution enhances the crack development and reduces the influence of the microstructure on crack growth. On the other hand, much of the investigations carried out on fatigue and CF have focused on the behaviour of long cracks, though it is now well known that under specific circumstances fatigue lifetime is controlled by the nucleation and growth of microscopic defects [114, 115].

More recent investigations [11, 116, 117] have shown that non-metallic inclusions play a very important role in the corrosion fatigue process during the initiation stage of cracks. Pits develop from electrochemical-active sulphide containing inclusions in the metal, whereas during the growth stage, corrosion tends to overcome the inherent resistance of the microstructural barriers, which in the absence of corrosion retard crack growth.

2.4.3. Preferential dissolution mechanism

Evans [118] suggested that deformed areas in metals and alloys, such as regions of intense slip, are anodic with respect to non-deformed areas. Due to the application of cyclic stresses, atoms at the crack tip are in a higher energy state than atoms in the specimen body, and consequently electrochemically more active. The material at the crack tip that has been cyclically deformed dissolves preferentially and the CF crack growth is accelerated. This mechanism has been used to explain early crack initiation in corrosion fatigue. The same principle can be applied to atoms in cyclically deformed metal, which develop slip bands at the metal surface. It can be said that preferential dissolution takes place as a result of electrochemical inhomogenity promoted by deformation.

Several CF mechanisms were proposed based on interactions between dislocations and environment-based processes at initiation sites or crack tip surfaces [93].

The cyclic deformation can promote precipitation of impurities on slip bands, which increases their electrochemical activity. Whitwham and Evans [119] reported that preliminary dry fatigue had little or no effect on corrosion fatigue life of annealed and cold drawn wires. The authors concluded that failure due to corrosion fatigue is caused by the deformed metal acting as anode with the undistorted metal acting as cathode; short cracks then grow by the combination of electrochemical and mechanical action.

2.4.4. Film rupture mechanism

Many metals and alloys become covered with oxide films on exposure to aqueous environments. Surface film breakdown is dependent upon the nature of the film, which in fact must be insoluble, the characteristics of the electrolyte, the electrochemical activity developed at the interface metal - electrolyte and the application of stresses. Copper, aluminium or tin and their alloys develop thick films, while metals which exhibit passive behaviour like stainless steels have a very thin film of the order of 9 to 20 nm. These films are cathodic to the metal matrix.

When the metal is subjected to cyclic loading the film is damaged mechanically due to the creation of slip steps from beneath. The breakdown of the film causes dissolution of the non-covered active metal in contact with the electrolyte, which acts as a small anode against the large cathodic film. This mechanism does not apply for all metal-electrolyte systems undergoing CF, as is the case for acid solutions where oxide films can be soluble.

It is also possible that even where passive films are present, the stresses generated in high cycle fatigue experiments are either not high enough to break the surface films or slip band emergence is so slow that film repair takes place more rapidly than the possible corrosion damage [108]. This shows the important effect of the test frequency on the CF lifetime. Retardation in the formation of corrosion pits as a consequence of a delay in film rupture results in the increasing of corrosion fatigue life of the metal.

2.5 Pitting Corrosion Fatigue Models

Linear Elastic Fracture Mechanics (LEFM) concepts are widely used to assess the crack growth behaviour of pre-cracked components undergoing cyclic deformation in different environmental conditions. The pit growth rate theory is combined with the fatigue crack growth concepts to develop CF models. The number of cycles to nucleate a Mode I crack from a pit (subjected to cyclic loading) could be modelled using LEFM concepts and in this respect some models have been proposed [120-123]. All of the models consider pits with hemispherical geometry and the corresponding stress intensity relation is used to assess the critical pit depth using the crack growth threshold (ΔK_{th}), which is found empirically [124]. These models provide a reasonable estimate for total corrosion fatigue life.

Hoeppner [120] proposed a model, which determines the critical pit depth to nucleate a mode I crack. This model applies to metal-environment systems susceptible to pitting corrosion fatigue. The number of cycles needed to develop a critical pit size that will produce a mode I crack is obtained by combining calculations of pit growth rate and the fatigue crack growth curve fit in the specific corrosive environment.

The stress intensity relation for a surface discontinuity is used to simulate hemispherical pits and with the fatigue crack growth threshold determined empirically, critical pit depth is obtained.

Even though the model proposed by Hoeppner provides reasonable estimates for hemispherical pits and is useful to predict total corrosion fatigue life, it does not propose mechanisms for crack nucleation from corrosion pits. Another disadvantage of this model is that it is only valid for conditions where LEFM concepts are applicable.

Lindley et al [121] proposed a model similar to Hoeppner's for determining the threshold at which fatigue cracks would grow from corrosion pits. Lindley considered corrosion pits as semi-elliptical shaped cracks. The threshold stress intensity can be calculated from assessments of pit geometry i.e. the a/c ratio where a is the minor axis and c the major axis of the pit and for the corresponding a/c ratio, the critical pit depth can be estimated. The limitation of this model is the same as Hoepnner's model i.e. it is only valid for conditions in which LEFM concepts are applicable.

The model of Kawai and Kasai [122] is based on the assessment of allowable stress under corrosion fatigue conditions making emphasis on pitting corrosion. They considered corrosion pits as elliptical cracks and the important parameter for their calculations was the pit depth. From experimental data of allowable stress intensity thresholds the allowable stresses were proposed. With this model it is possible to estimate the allowable stress in relation to corrosion fatigue threshold as a function of time. The model, as the previous two, depends on the material and is valid only for LEFM conditions.

Kondo [123] proposed a model to determine the corrosion fatigue life of a component based on calculations for the critical pit condition which, is estimated by using relations

of the stress intensity factor as well as pit growth rate. The model relies on intermittent measurements of pit diameter during corrosion fatigue tests in order to establish a corrosion pit growth law. A critical pit condition in terms of a stress intensity factor (ΔK_p) was proposed by assuming pits to be cracks. The relationship between the pit growth rate theory and fatigue crack growth rate is then used to determine the critical pit condition. Finally, the critical pit size was calculated from a stress intensity factor relation. This model has the same limitations as the three previous models mentioned above.

2.6 The Scanning Reference Electrode Technique (SRET)

As mentioned in section 2.2.3, the electrochemical dissolution of metals during localised corrosion takes place at permanently separated sites from the cathodic areas, a schematic drawing of a local corrosion cell is shown in figure 2.10. This gives the possibility of direct measurements of the cathodic and anodic reactions through *in situ* non-intrusive studies. Measurements of the physical separation of anodic and cathodic areas, the currents flowing between them as well as the mapping of potentials in electrolytic solutions have been successfully used for the study of the processes of localised corrosion of different systems [13,40,44,118,125 - 132].

Evans in 1960 [118] was the first in detecting and measuring small potential variations close to the surface of a zinc specimen corroding in a sodium chloride solution. In 1966, with the aim of determining the velocity of metal dissolution directly in the operating pits during pitting corrosion, Rosenfeld and Danilov [44] designed an apparatus to measure the field strength in the electrolyte directly above an active pit. They employed

a twin probe method by using two reference electrodes, which makes it possible to measure the potential difference ΔE in any direction between two points in the electrolyte with the aid of two non-polarisable electrodes, for example calomel electrodes.

With the measurement of the electric field strength in the electrolyte over the pits it was possible to determine the current flowing from the anode points, based on a well-known fact. This fact establishes that, the vector of the normal component of the current density at a pre-determined point (i') in a uniform field is equal to the product of the electric field strength E and the specific conductivity of the medium κ.

The method used by these workers was a real scanning reference electrode technique but at that stage of development the method had some limitations. From the electrochemical point of view the use of reference electrodes with porous membranes like the saturated calomel electrode (SCE) involved the contamination of the electrolyte particularly for measurements involving very diluted solutions. Under this circumstances the scanning signal showed instability due to leakage of saturated solution from the reference electrode to the electrolyte.

One of the most successful promoters of this technique is Isaacs who in 1971 explained in detail the characteristics and performance of the Scanning Reference Electrode Technique (SRET) [125] and after gave a review of the technique [126]. Currents flowing from cracks in freely corroding stainless steel surfaces in LiCl solution were observed *in situ* by using the scanning reference electrode by Isaacs and Vyas. In this paper they also gave a review of the developments in both flat and cylindrical specimens variants on the SRET [126]. The aim of their work was to separate, as clear as possible, the anodic and cathodic reactions during localised corrosion without interfering with the processes taking place.

They indicated that the resolution of the SRET is dependent on the proximity of the corroding sites and the magnitude of the corrosion currents from each site. As shall be shown later, the distance between the probe and specimen surface and the conductivity of the solution governs the sensitivity of the technique.

Isaacs et al in 1972 applied the technique to measure the number of active pits on 304 stainless steels in ferric chloride solution with time [127]. They showed that the propagation of active pits is dependent on the surface preparation of specimens, which reflects the properties of the oxide film on the surface. By performing potential scans at different times after the immersion of the specimen within the electrolyte they were able to identify the de-activation of pits with time. Through their work with SRET measurements of localised attack in stainless steels these authors did not intent to determine the shape or dimensions of the localised anodes. What they were able to measure was the local current densities associated with the localised metal dissolution. They reported the capability of the SRET to identify the position of localised activity in the metal surface however did not report any assessment of pit size or shape from the performed SRET measurements.

Tuck [128] evaluated the usefulness of reference microelectrodes in identifying local anodic and cathodic sites on aluminium alloys as they were scanned mechanically over a polished surface. The electrolyte in which the specimens were immersed for the study was shown to have a critical effect on the detectability of sites undergoing localised activity. He demonstrated that a solution of low conductivity is indispensable if the electrodes were microscopic in size. This is obviously a limitation in the application of microelectrodes because they can not be used for real systems undergoing localised corrosion in electrolytes of high conductivity, e.g. seawater.

Bates et al. [129] working with the design and development of SRET showed that this technique relates directly to the instantaneous electrochemical activity within pits and avoids the necessity of perturbing the pitting process by the removal of the material from the corroding medium. The apparatus they designed could detect and monitor small potential variations associated with active pitting in FV 448 gas turbine disc steel. They reiterated that the reliability of the method depends upon the electrochemical activity associated with the pits, rather than the size or depth of pits.

Sargeant et al. [130] showed that the use of a commercial microcomputer to control and process data collected from SRET measurements resulted in improvements in several aspects, mainly the ability to handle large amounts of online data in a controlled way. For the same material studied in their previous work, the FV 448 gas turbine disc steel [129] they showed the advantages of using cylindrical specimens. The recording of rapid potential changes in very active systems was possible with the apparatus they designed. They demonstrated that microscopic pitting could be detected at a very early stage, and the possibility to resolve and display individual pits by using a software control.

Trethewey et al. [13] obtained pit life history at specific points in a 304 stainless steel specimen immersed in seawater. They showed that the measured current density adjacent to an active pit exceeded 300 times that obtained from a conventional pitting scan which was a maximum current density of 0.8 mA/cm^2. In another paper Trethewey et al [131] showed the advantages that in theory should give the use of a differential probe configuration over the conventional single ended system. The same authors indicated that with the use of SRET it is possible to study pit initiation and development, surface coating behaviour, inhibitor performance, battery performance,

corrosion under hydrodynamic conditions as well as microbiological induced corrosion and stress corrosion cracking.

In 1996 Trethewey et al. [132] also obtained the pit life history on a martensitic stainless steel at different applied potentials using an area mapping technique. With the use of a calibration factor obtained from measurements of the ohmic potential generated by a point current density source (point in space specimen, PIS) they were able to report localised current densities associated pitting. However they emphasised the fact that in all the measurements carried out, there seems to be no direct relationship between measured current density and pit size and geometry which supported the results previously reported by Isaacs [127] and by Bates et al [129].

Recently SRET measurements have been applied to the study of environmental assisted fracture of stainless steels paying particular attention to the early stages of damage. Akid [133] evaluated the effect of stress on pit propagation of stainless steel in NaCl solution. He demonstrated that the application of a stress below that of the yield stress induced the initiation of pitting activity on a specimen subjected to a potential below that of the pitting potential. He showed that the magnitude of the corrosion activity increases with each application of stress, and when the cyclic stress was stopped, pitting continued.

In the present work the rotating cylinder electrode version of SRET was used for the study of corrosion fatigue initiation of stainless steel. The method showed the capability of detecting changes on localised activity during crack initiation from sites in which localised attack was detected previously in specimens immersed within a very aggressive electrolyte (0.05 M $FeCl_3$).

The principles of operation of the SRET are based on the following:

During the localised corrosion of a metal the electronic charge generated by the dissolution reaction flows from the localised anode to the cathodic sites through the metal. The high electronic conductivity of the metal induces a negligible ohmic potential difference in the metal, thus the surface of the corroding metal can be considered as a plane of constant potential. However within the aqueous electrolyte in contact with the corroding metal the ionic flow that develops to complete the corrosion cell produces ohmic potential gradients owing to the low electric conductivity of the electrolyte. As shown in figure 2.10, these potential gradients may be described as a series of iso-potential lines lying in perpendicular direction to the lines of ionic current flux. In order to study the kinetics of localised corrosion in its various forms it is necessary to use electrochemical techniques, which measure variations in electrochemical activity at the metal surface, originated by localised attack. The activity can be assessed in terms of the current emanating from the sites undergoing local dissolution. By scanning a non-polarizable reference probe containing a fine capillary tip parallel and very close to the metal surface, the ohmic potential gradients generated in the electrolyte by localised anodic currents can be measured.

It must be emphasised that the SRET does not directly measure the potential variations in the surface of the metal, but it responds to the ohmic potential gradients originated by ionic fluxes in the solution. Improvements and sophistication of the SRET due to recent major advances in computing and microelectronics make the technique able to measure micro-galvanic potentials existing local to the surface of materials undergoing localised attack. SRET is a powerful system allowing real-time localised electrochemical activity to be managed and fully quantified. From the Laplace equation and Ohm's law the theoretical distribution of ionic current and potential in the electrolyte can be determined.

$$\nabla^2 E = 0 \tag{2.1}$$

$$i = -\kappa \nabla E \tag{2.2}$$

where i is the current, κ is the solution conductivity and E is the electrical potential.

The analytical solutions to this problem are not possible except for the very simplest cases in which some specific conditions are assumed. For example be the case of a point current source which is situated at height z = 0 in a non-conducting plane (x, y) in a rectangular co-ordinate system and with a current drain to infinity. Under these conditions, it may be shown that the potential at the point (x, y, z) in the electrolyte is inversely proportional to the distance from the point current source [134,135] and is given by equation (2.3).

$$E = \frac{i}{2\kappa\pi\left(x^2 + y^2 + z^2\right)^{0.5}} \tag{2.3}$$

The maximum potential of a point in the electrolyte in the position (z, 0, 0), i.e., directly above the point current source and at height z from the plane is given by:

$$E_{MAX} = \frac{i}{2\kappa\pi z} \tag{2.4}$$

Equation (2.4) shows the effect of the electrolyte conductivity on the SRET response to highly localised forms of current sources. Furthermore it is the theoretical basis of what has been termed the point in space calibration (PIS).

From equation (2.4) and Ohm's law it is possible to determine theoretically the width of the potential distribution at half maximum peak height (whm), i.e. when $E = 0.5\ E_{MAX}$, which is given by equation (2.5).

$$WHM = 3.46z \quad (2.5)$$

Equation (2.5) implies the theoretical maximum resolution of the SRET, which establishes that it will be difficult to resolve two point current sources if the separation between them is less than the value of the WHM. In most cases during SRET measurements the microtip electrode is scanned at distances above the corroding surface of around 100 μm implying a theoretical spatial resolution of 346 μm.

Trethewey et al [13] performed measurements of localised corrosion densities in 304 SS with a commercially designed SRET instrument, in which the microelectrode tip of the twin platinum-scanning probe was positioned at a distance of 20 μm from the corroding surface. Considering that the presence of the microelectrode positioned at that short distance from the current supply does not perturb the potential distribution in the electrolyte, it can be expected a theoretical spatial resolution of 69.2 μm.

A SRET measurement with minimum resolution of the order of 70 μm could give the possibility of assessing electrochemical changes during the transition from corrosion pit to short fatigue crack if the activity involved is sufficient high to be detected.

The other important parameter in SRET measurements is the sensitivity of the equipment, which is significantly determined by the probe design.

New improvements on the SRET technique make it a promising tool for the study of localised corrosion processes, and in the present work it was used to study the early stages of damage by corrosion fatigue in stainless steels.

It has been reported that an important improvement on sensitivity and resolution of the scanning techniques has been achieved by the use of a vibrating microelectrode. The use of vibrating probes has been reported since the early 70's for studies in the field of

cellular biology for measuring relatively steady electrical current densities near individual living cells [136].

The modern version of the scanning vibrating electrode technique involves a pseudo-reference microtip electrode which, as the name suggests, is vibrated relative to the scanned surface. McMurray et al. [135], gave a basic description of the SVET principles and compare the two techniques SRET and SVET for the study of localised corrosion.

It should be noted that the theoretical improvement in resolution of the SVET is a factor of 2 compared with that of the SRET. Isaacs [137], determined the relation between potential fluctuations and the initiation of stress corrosion cracking on sensitised type 304 stainless steel by using SVET. He reported the detection of currents coming from growing stress corrosion cracks on sensitised stainless steel.

The initiation and crack passivation of the 304 SS in thiosulfate solutions could be determined by monitoring the potential.

Xiang-chun Jiang et al. [138] identified local variations in the chromium concentration in the Fe-rich region in some tens of microns scale by using the scanning vibrating electrode technique (SVET) during the study of the electrochemical behaviour of aged steel in H_2SO_4 containing KSCN. They used electrochemical potentiokinetic reactivation and SVET and observed the reactivation behaviour. The reactivation ratio was obtained by deconvolution of the active dissolution peaks based on SVET measurements.

CHAPTER 3 – Experimental Work

3.1 Introduction

As previously stated, the aim of this research project was to conduct an electrochemical study in the regard to further understanding the transition from a corrosion pit to a short fatigue crack which occurs during the early stages of damage arising from corrosion fatigue. The materials used in this study were austenitic stainless steel grades 304L and 316L and a duplex stainless steel. Emphasis was given to the novel use of the Scanning Reference Electrode Technique (SRET) as a tool to quantitatively assess the localised electrochemical activity involved in the early stages of CF failure. In order to achieve this objective several activities were carried out in the experimental programme. These included; characterisation of the microstructure, electrochemical tests, SRET measurements, electrochemical generation of pits on SRET specimens, modifications of the SRET equipment in order to perform CF tests, and finally CF-SRET tests.

The characterisation of microstructures was performed using an optical microscope and associated image analysis system. Different methods of etching were used to develop the microstructure of each stainless steel. Electrochemical tests were performed on samples to assess the electrochemical parameters associated with the pitting corrosion performance of these steels in synthetic seawater.

Modifications were made to the SRET instrument, which was not designed a priori to perform corrosion fatigue tests. The SRET equipment used was the model SR100, which involves a rotating working electrode as described in the following sections. Due to this experimental configuration special SRET-CF specimens were made in order to perform CF tests whilst simultaneously conducting SRET measurements.

Measurement of the stress-strain behaviour of the stainless steels under internal pressure and the calibration of the hydraulic system used to apply the cyclic loading were performed.

Preliminary SRET tests were carried out using solid bar specimens of the three SS's in seawater at free corrosion potential and under anodic polarisation. CF-SRET tests were performed on CF-SRET specimens of S31603 and S30400 steel for a number of cycles at different stress levels and under anodic polarisation. SEM analysis of the corroded surface was carried out at different stages of the CF test.

Results of the preliminary SRET tests showed a limited sensitivity of the SRET instrument to detect the initiation and propagation of corrosion pits in the SS - artificial seawater system at free corrosion potential.

With the intention of creating a crack nucleation site on the CF-SRET specimens for which electrochemical activity could be followed by SRET measurements, corrosion pits of pre-defined depth were induced electrochemically. The "pre-pitting" process was performed on samples of S31603 and S30400 steels in order to determine an empirical pit growth law for the two austenitic SS's. Additionally, pre-pitting tests were carried out on cylindrical specimens rotating at 100 rpm within the electrolyte. SRET measurements were carried out simultaneously whilst electrochemically pre-pitting the samples in order to assess the localised activity associated with the potentiostatic growth of pits.

The electrochemical generation of pits was not performed on specimens of S31803 steel due to the high pitting corrosion resistance of this steel. The anodic potential levels required to nucleate pits in samples of S31803 steel promoted the formation of crevices and in some cases oxygen evolution also occurred.

A second electrolyte, a solution 0.05 M $FeCl_3$, pH 2.1 ± .1 was used for SRET and CF-SRET tests as this environment has been reported to induce localised attack (pitting and crevice corrosion) on stainless steels [127]. The greater electrochemical activity induced by the ferric chloride solution was observed in the present work where UNS S30400 and S31603 steel samples developed localised corrosion at free corrosion potential within a few seconds after the immersion of the specimens. The localised activity was easily followed by SRET measurements.

3.2 Materials

As stated the materials used in the experimental work were two different austenitic stainless steels, the UNS S30400 (304 SS) and UNS S31603 (316L SS), and one austenitic-ferritic stainless steel the UNS S31803 (Duplex SS), all three are 'corrosion resistant' steels. The steel manufacturer and supplier indicated a hot rolled, softened and descaled (as received) condition for the three steels.

3.2.1 Chemical Composition

The actual chemical composition of the steels is shown in table 1 as reported by the manufacturer.

3.2.2 Characterisation of the Microstructure

The microstructure of the UNS S30400, S31603 and S31803 stainless steels in the as-received condition was investigated by metallographic studies. An Olympus Vanox optical microscope and an image analysis system were used to measure the average grain size of the austenitic steels and the percentage of ferrite and austenite phases present in the duplex stainless steel.

Grinding of specimens was performed using water-cooled silicon carbide papers of 240, 320, 400, and 600-grit size. Polishing was performed in three steps, starting with rough polishing with 6-μm diamond abrasive paste followed by a second polish step using 1-μm and finally with silico-colloidal solution.

The selected etching method for all steels was electrolytic, which gave the best results when compared with non-electrolytic methods proposed in the literature [139, 140]. The etching of the samples was carried out immediately after the surface preparation was completed (polishing to 1 μm surface finish) as follows:

For the UNS S31803 (Duplex SS)

Etching agent composition: 60 ml HNO_3 - 40 ml H_2O

In order to develop the microstructure it was necessary to use a potentiostat and a three-electrode cell with a Platinum mesh as the auxiliary electrode and saturated calomel electrode (SCE) as a reference. The specimen was subjected to anodic polarisation, 400 mV above the open circuit potential for periods of 20 sec until the microstructure was completely developed.

For the UNS S3Q4Q0 (304 SS)

Etching agent composition: 15 ml HC1, 10 ml HN03, 100 ml H_20.

A platinum mesh was used as the cathode and the application of 1.5 V dc for periods of 30 seconds gave the optimum microstructure developing for a total etching time of 1.5 minutes.

For the UNS S31603 (316LSS)

Etching agent composition: 60 ml HNO_3, 40 ml H_20.

A platinum electrode was used as the cathode, the applied voltage was 0.80 V DC for periods of 30 seconds, until good resolution was obtained, that is, avoiding pit formation. The maximum time used was 2 min.

In order to develop the possible presence of intermetallic compounds, e.g., delta ferrite (8) and sigma phase (a) in the austenitic grades, samples of (UNS S30400) and (UNS S31603) steel were subjected to electrolytic etching in 10 % aqueous NaOH for periods of 15 seconds until the phase was clearly distinguishable. X ray diffraction analysis was carried out in order to determine the presence of intermetallic compounds, which were observed on the austenitic SS's after etching.

An optical microscope and image analysis system was used to study the microstructure, and the average grain size of the three stainless steels was obtained following the ASTM standard E1 12-95 [141].

3.2.3 Mechanical Properties

The mechanical tests performed on the austenitic and duplex SS's were carried out using specimens in the as received condition (hot rolled, softened and descaled). The mechanical properties of the three materials are presented in table 2.

3.3 Test Facilities

3.3.1 Test Specimen

In order to study the electrochemical activity involved in the transition from corrosion pit to short crack transition during the early stages of corrosion fatigue, a cylindrical tube SRET-CF specimen, figure 3.1, was used for this research. This type of specimen was previously designed and used by Akid [133] during SRET measurements on different steels subjected to mechanical stresses.

This present specimen was designed to make possible the application of cyclic or static load during SRET measurements, without interfering with the rotation of the working electrode. The cylindrical specimens had a section with reduced wall thickness in order to concentrate the stress in this area. The 20-millimetre length of this section had a wall thickness of 200 to 250 microns, which acted as a thin wall-pressure vessel.

For the present research all the specimens were machined in the rolling direction (L-T). The dimensions and configuration of the specimen are shown in figure 3.2 An adaptor of non-conducting material was constructed in order to eliminate galvanic coupling

between the specimen and the base frame of the SRET equipment through which the hydraulic pressure was applied by pumping oil from a reservoir, figure 3.2.

3.3.2 Fatigue Test Machine

The fatigue testing facility coupled to the SRET base frame used in this study, shown in figure 3.3, is a load controlled hydraulic system which provides facilities for high stress low-cycle and low stress high-cycle fatigue testing. The hydraulic system applies an internal pressure to the cylindrical SRET specimen, which undergoes bi-axial circumferential and longitudinal strains. The configuration and dimensions of the SRET specimens, figure 3.2, make easy for the hydraulic system to induce circumferential stresses higher than the σ_{ys} for S30400 and S31603 steels.

The system is able to apply a minimum pressure of 1.0 bar and a maximum of 230 bar. This range of applied pressure corresponds, for the specimen configuration used in this work to circumferential stresses of a minimum of 2 MPa and a maximum of 500 MPa, being that of twice the longitudinal stress. This range of induced stresses is sufficient to attain up to 85 % of the ultimate tensile stress (σ_{uts}) of the two austenitic SS's, as reported in table 2. On the other hand, the maximum induced circumferential stress is just below the yield stress (σ_{ys}) of the S31803 steel, which is 504 MPa. A reduction of the wall thickness of SRET specimens of this steel was performed in order to increase the induced circumferential and longitudinal stresses.

Using a signal generator connected directly to the control unit of the hydraulic system the frequency and load wave of the hydraulic system can be varied. For this study a frequency of 0.27 Hz and a positive saw tooth load wave was used in all CF tests.

The number of loading cycles was determined by recording the time of the application of the cyclic load since no instrument was used to automatically count up the number of cycles. The response of the hydraulic machine to the load frequency imposed by the control unit was stable with time. The value of 0.27 Hz reported as the frequency used for the CF tests corresponds to 16 cycles per minute. A variation of (+) 4 cycles every 3 hours was observed, which represents 0.14 % deviation from the actual and theoretical number of cycles.

3.3.3 Calibration of the applied pressure - induced stress

The calibration of the hydraulic system used to apply cyclic loading to the cylindrical SRET specimens was conducted with the aim of assessing the stresses generated in the thin walled section of the SRET samples by the application of cyclic internal pressure during CF-SRET tests.

Strain-gauged dummy specimens and a digital strain indicator model P-3500 were used to evaluate the applied load - strain behaviour of S30400, S31603 and S31803 steels. Two specimens of the three steels were gauged in both, circumferential and longitudinal directions as shown in figure 3.4. The values of the circumferential and longitudinal strains obtained from the measurements were used to determine the circumferential and longitudinal stresses induced on the SRET specimens.

The calibration tests were conducted at room temperature. The hydraulic component test rig was used under manual control, which permitted the application of pressure to the gauged specimen to a pre-established value entered as the limiting pressure condition. Once the strain measurement was stable (no changes in the strain value), the pressure

was released from the specimen and dropped back to 0 bar. The applied pressure was then increased in steps of 5 bar and the induced strain was measured. The sequence was repeated until the value of the applied pressure induced a circumferential stress approximately equal to the yield stress of the UNS S30400, UNS S31603 and UNS S31803 steels. Three sequences of strain measurements, as a function of the applied pressure, were performed to each gauged specimen.

The value of the maximum pressure applicable to the dummy specimens during the calibration to ensure elastic behaviour was obtained based upon the pressure vessel equations (3.1) and (3.2) [142] for the longitudinal and circumferential stresses respectively. The equations are:

Longitudinal stress: $\sigma_L = p*r/2t$ (3.1)

Circumferential stress: $\sigma_C = p*r/t$ (3.2)

where:

p: applied pressure

r: inner radius of the cylinder, and

t: wall thickness

The sizes of r and t for the gauged specimens were as follows:

Material	Wall thickness (mm)	Internal radius (mm)
S30400	0.229 (± .005 mm)	5.005 (± .005 mm)
S31603	0.231 (± .005 mm)	5.006 (± .005 mm)
S31803	0.231 (± .005 mm)	5.005 (± .005 mm)

In the case of the gauged specimen of S30400 steel the maximum applied pressure was 110 bar (11.0 MPa), which from equation (3.2) equates to a circumferential stress of 240 MPa. For the S31603 steel the maximum applied pressure was 110 bar (11.0 MPa), which corresponded to a theoretical circumferential stress of 238 MPa. For the S31803 steel dummy specimen the maximum pressure applied was 230 bar, (23.0 MPa), which from equation (3.2) corresponds to a circumferential stress of 500 MPa.

The applied load was measured directly from the control unit of the hydraulic system which gives the value of applied pressure in bar with a variation of ± 1 bar. The circumferential and longitudinal stresses generated in the specimens were calculated from the experimental strains measured during the calibration.

For a thin-walled tube loaded by internal pressure, equations (3.3) and (3.4) apply and were used for the calculation of stresses from elastic strains. For this case it is considered that plain stress conditions apply [143,144].

The equations are:

$$\text{Circumferential stress: } \sigma_1 = (\varepsilon_1 + \nu\varepsilon_2)^* E/(1-\nu^2) \qquad (3.3)$$

$$\text{Longitudinal stress: } \sigma_2 = (\varepsilon_2 + \nu\varepsilon_1)^* E/(1-\nu^2) \qquad (3.4)$$

where:

E: Modulus of elasticity

ν: Poisson's ratio

and

ε: the strain measured.

The parameters E and ν for the three SS's used for the calculations were assumed to have the values presented in table 2, which were taken from the literature [16,17,142,145].

From the calibration tests performed using the gauged specimens two equations were obtained for each steel, one for the circumferential and one for the longitudinal stress as a function of the applied pressure (P) in bar. These equations will be presented in section 4.3 in chapter four.

3.4 Electrochemical tests:

3.4.1 Polarisation Studies

Electrochemical experiments were carried out in order to determine the susceptibility of the three stainless steels to pitting corrosion in synthetic seawater, the value of the pitting potential (E_p) was the most important parameter to be determined from potentiokinetic experiments. Its value was used to determine the level of anodic polarisation applied during SRET, CF-SRET and pre-pitting tests as indicated in the following sections.

Specimens of 1.44 cm^2 surface area were embedded in non-conducting Bakelite. Electrical contact between the specimen and the electrochemical equipment was made using a brass bar screwed on the backside of the Bakelite. The brass bar was isolated with a polymeric coating to avoid contact with the electrolyte.

Sample surfaces were prepared prior to testing as follows: Grinding with 320, 400 and finally with 600 grit SiC papers.

After grinding the steel surface was polished to 1 μm with diamond past and finally washed with de-ionised water, and dried using acetone and hot air.

The experimental cell consisted of a glass container of 1500 ml. of capacity. The electrolyte was synthetic seawater prepared with de-ionised water and 39 g/l of sea salts. The chemical composition of the sea salts is given in table 6.

A saturated calomel reference electrode (SCE) and Platinum counter electrode were used along with the stainless steel specimen (working electrode) in a conventional 3-electrode test cell arrangement as shown schematically in figure 3.5.

Electrochemical tests of the three SS's were performed using a computer controlled Potentiostat (Radiometer model PGP 201). Test data was processed using a commercial software.

The temperature of the electrolyte was controlled at 26° C ± 1° C, and the pH was 8.2. During the tests the electrochemical cell was open to the atmosphere and after each of the potentiokinetic tests the cell was filled with fresh solution.

Electrochemical tests included potentiokinetic polarisation at potentials more negative and more positive than the corrosion potential of the three steels in artificial seawater. The intention was to evaluate the cathodic and anodic behaviour of the steels. Prior to potentiokinetic polarisation the samples, once immersed, were subjected to potentiostatic cathodic polarisation for 3 minutes at a potential 600 mV more negative than the open circuit potential.

The electrochemical system was then left at free corrosion potential for 60 to 120 minutes to allow the corrosion potential (E_{corr}) to stabilise. Once the E_{corr} value for each specimen had stabilised (potential drifts < 1 mV/min), potentiokinetic polarisation was commenced from a potential 450 mV below E_{corr} at a potential sweep rate of 10 mV/minute in the anodic direction.

Polarisation was continued until breakdown of passivity occurred. An anodic current density of 30 $\mu A/cm^2$ was considered as the breakdown limit in order to avoid the formation and growth of large, deep pits in the surface of the specimen. The measuring frequency of the applied potential and the induced current was one second in the potentiokinetic polarisation experiments. For the evaluation of the pitting potential 5 tests were carried out, each one on a different sample of the three grades of SS.

The samples for the electrochemical tests were subjected to the surface preparation mentioned above before every test, which gave a sample with a 1-μm surface finish. The tests in which crevices developed during the anodic polarisation were discarded.

3.5 Scanning Reference Electrode Technique (SRET) Tests

3.5.1 Introduction

Once the polarisation studies were completed and the electrochemical parameters for the three stainless steels in seawater were obtained, measurements of localised corrosion using the rotating electrode model of SRET were performed. The equipment utilised was the EG&G Instruments SRET model SR100 which measures micro-galvanic potentials existing local to the surface of materials under examination using a pseudo reference electrode probe that scans the surface under micro-computer control. The spatially displaced probe scan is synchronised with a VDU display and the resultant data is shown in the form of line scans and 2D area maps. A schematic representation of the SRET SR100 is shown in figure 3.6 [146].

3.5.2 Current density measurements and system calibration

One of the major objectives of the use of the SRET in the present work was to quantify the degree of localised electrochemical activity involved in the nucleation of cracks from corrosion pits in terms of current density. In order to determine localised current densities directly from SRET measurements a reliable calibration routine was followed [13]. The procedure takes into account the principal electrochemical conditions of the system and other variables that affect the level of the SRET output [137].

The calibration was performed by means of an 'active' micro-disk electrode of known surface area through which a known current was driven. The golden disk specimen acted as the working electrode in a three-electrode corrosion cell.

The micro disk calibration source (MDCS) specimen consisted of a gold wire of 200 μm of diameter mounted in insulating polymer. The area of the micro disk was the flat circular cross section of the gold wire with a surface area of 3.27e-4 cm^2. The MDCS which, is surrounded by an insulator was positioned face to face to the probe platinum tip as shown in figure 3.7. Some researchers [13,131], use the name Point in Space (PIS) specimen to describe this microscopic electrode used for calibration purposes. When the micro disk electrode is subjected to galvanostatic polarisation and rotation within the electrolyte simulates a single micro-current dipole. Despite the micro disk electrode is not a true point in space current supply it was used to perform the calibration of the system.

An important factor controlling the spatial resolution of the SRET system is the dimensions and profile of the platinum probe tips. The SRET model SR100 utilised in the present work involves the use of a twin platinum probe as shown in figure 3.8 which, consists of two 200 μm diameter platinum pseudo reference electrodes, separated approximately 0.2 mm vertically and spaced 2.0 mm horizontally.

The external platinum microelectrode of the probes was sharpened by using an ac electrolytic method to attain a conical shape with a diameter of the tip in the range of 10 - 25 microns. After sharpened the microelectrode tip was platinised using a dc electrolytic method. In order to achieve a reliable calibration for the current sensed in solution, identical experimental conditions of that used in the calibration prevailed during the SRET and CF-SRET measurements.

The calibration measurements using the PIS specimen were carried out in synthetic seawater and in ferric chloride solution at a temperature of 26 °C. The concentration, pH and conductivity of the two electrolytes were as listed in table 8.

The first calibration test was carried out in order to establish the relation between the detected signal level and the specimen to probe distance.

The test consisted on the application of a constant anodic current of 25 μA (equivalent to 78 mA/cm^2) between the golden micro disk electrode and the auxiliary electrode with the aid of a galvanostat. The scanning probe was positioned initially at 50 μm from the surface of the golden disk specimen, which was rotated at 100 revolutions per minute (rpm). When the electric current was driven through the PIS the output signal was recorded. The scanning probe was then moved away from the surface of the micro disk in steps of 50 μm and the detected output signal (in millivolts) was recorded at each new probe position.

To test the relationship between probe output signal and the current density emanating from the active golden micro disk specimen a second calibration test was carried out. In this experiment the separation between the Pt probe tip and the micro disk surface was maintained constant at 100 μm and different currents were applied to the rotating micro disk electrode. The output signal in millivolts was recorded as a function of the applied

current. From this second calibration test a multiplication factor for the probe output was obtained, which was used to assess localised currents from SRET measurements in a semi-quantitative base.

3.5.3 The SRET experiments

SRET experiments were carried out on specimens of 316L, 304 and duplex SS's in two different electrolytes, synthetic seawater and 0.05 M $FeCl_3$ solution with the conductivity and concentration of that used in the calibration tests. The SRET measurements involved two kinds of specimens firstly; tests were performed using solid bar samples of 20-millimetre diameter, 100-millimetre length. The surface of the bars was covered with a thin film of coating (50 to 100 μm) leaving a circumferential band of 10-mm height of uncovered metal. The second type of specimen was the thin walled tube described in section 3.3.1, which was used to perform SRET measurements under corrosion fatigue conditions. The same coating was applied to the tubes leaving an uncovered metal area of approximately 3 cm^2. Before the application of the coating the surface of the specimens was polished to 1 μm surface finish following the procedure used for the preparation of samples for microstructure analysis and polarisation tests.

The SRET measurements in artificial seawater were carried out on samples of the three stainless steels at free corrosion potential (E_{corr}), and a potentials more positive and more negative than the pitting potential (E_p); the values of the anodic potential applied during SRET test were as follows:

Steel type	316L	304	Duplex
SRET measurement at: (E (mV) vs SCE).	E_p = 350 to 380 E = 290 (< E_p) E = 390 (> E_p)	E_p = 300 to 360 E = 280 (< E_p) E = 370 (> E_p)	E_p = 1060 to 1110 E = 1050 (< E_p) E = 1170 (> E_p)

The system used to perform the SRET tests under potentiostatic polarisation consisted of the SRET test cell arranged with an auxiliary electrode (Pt) and a reference electrode (SCE) to form a three-electrode electrochemical cell. The three electrodes were connected to a potentiostat as shown in figure 3.6. The cylindrical specimens of the three stainless steels acted as the working electrode and rotated at 100 rpm during the measurement. The SRET probe was then positioned by computer control to approximately 100 μm of the specimen surface using the software of the SRET equipment.

The distance between the platinum microtip and the surface of the working electrode was measured with a CCD video camera coupled to an optical microscope. Care was taken during the performance of the SRET tests in order to avoid damaging of the specimen surface and of the platinum probe tip, which may affect the output signal response.

3.6 Electrochemical generation of pits

Corrosion pits can promote fatigue crack development, in general, by acting as stress concentrators. CF lifetime prediction is complex because of the need to account for pit initiation, pit growth, crack initiation, short crack growth and long crack growth.

Several models have been proposed for life prediction of fatigue cracking initiated from corrosion pits, based in the kinetics of pit and crack growth [73,95,111]. The condition for the transition of cracks from pits is generally defined phenomenologically using a LEFM approach. A major concern is that the threshold stress intensity range for corrosion fatigue determined from long cracks can not be applied to short cracks initiated from pits. For this reason, there is considerable high merit in pre-pitting fatigue tests specimens in a controlled manner to the relevance depths.

The objective of this part of the experimental work was to develop an electrochemical method to generate corrosion pits with controlled depth and number on SRET-CF specimens and to obtain the pit growth law for the induced corrosion pits. Pits were induced on stationary (non-rotating) samples of 316L and 304 SS's immersed in artificial seawater. The depth of the induced pits was measured using a metallographic grinding technique. Using the same method corrosion pits were also generated in cylindrical specimens under the hydrodynamic conditions imposed by the simultaneous SRET measurements during which the specimens was rotating at 100 rpm.

SRET measurements have been used in the past to monitor the life of corrosion pits on stainless steels [127], however no attempt was made to assess the pit growth rate through SRET measurements. For the present work, after the pit growth law under potentiostatic controlled conditions was determined, the aim was to establish a relationship between this and the localised activity measured by SRET. With these results it can be possible to determine approximately the size of a growing pit without removing the specimen from the electrolyte for pit depth measurement.

Once the pit growth law for the two austenitic SS's was determined, corrosion pits of known depth were induced in the cylindrical specimens used for SRET-CF tests.

SRET measurements were then performed on specimens under CF conditions with the intention of evaluating the changes in localised activity during the transition corrosion pit - short crack. Due to the high resistance to pitting corrosion in seawater presented by the duplex SS, the method for pit generation was not applied to specimens of this steel.
The first pit generation (pre-pitting) tests were conducted on cylindrical specimens of 10 mm diameter and 45 mm length with a longitudinal flat section initially of 5 mm width. The exposed area of the electrode was 1 cm^2. The area subjected to corrosion was limited by applying an organic coating.

The exposed surface of the specimens used for pre-pitting under non-rotating and rotating conditions was wet ground to a 600 SiC grit finish, rinsed in distilled water, polished to 1 μm using diamond paste and finally polished with silica emulsion.
For the two kinds of specimens, it was of paramount importance to ensure a uniform state of surface over the whole exposed area to control the sites for pit initiation.
In order to control the spread of pitting over the CF specimens and SRET specimens, the platinum counter electrode and the reference electrode were positioned close to the centre of the specimen.

The solution used was artificial seawater with the same characteristics to that used for the previous electrochemical tests. The temperature was controlled at 26 ± 1°C.
A three - electrode electrochemical cell was used to generate the pits using the same potentiostat with which the previous electrochemical tests were carried out.
In this work a method was established to generate corrosion pits having a controlled density and depth. By controlling the applied anodic potential at values above the pitting potential, followed by reduction in potential to values below the pitting potential, it was possible to generate pits of different depth as reported by Zhou and Turnbull [147,148].

Using this method a pit growth law of the form $P_d = Ct^b$ was obtained for S31603 and S30400 steels. In this empirical equation P_d represents the pit depth (in μm), t is the time of anodic polarisation (in minutes) and C and b are empirical constants obtained from the regression analysis of the experimental data.

As shown in table 7 the corrosion potentials (E_{corr}) in synthetic seawater of the UNS S30400 and UNS S31603 SS's were –230 and –220 mV Vs SCE respectively. The pitting potentials (E_p) in mV Vs SCE were in the range of 290 to 340 mV for UNS S30400 and 350 to 380 mV for the UNS S31603. From the results of preliminary pre-pitting tests in which different combinations of anodic potentials were applied, the combination of applied anodic potentials that induced controlled pit nucleation and stable pit growth was chosen.

The following sequence of potentiostatic polarisation was applied for the electrochemical generation of pits of both grades of steel, which is shown schematically in figure 3.9 as a plot of potential Vs time:

a. Cathodic polarisation at –700 mV SCE (η_c = 500 mV) for 2 min.
b. Specimens left immersed at open circuit potential for 40 min, at which time the corrosion potential (E_{corr}) was approximately –210 mV for 316L and –205 mV for 304.
c. Anodic polarisation at 500 mV SCE (η_a = 700 mV) for 30 seconds to induce pit initiation.
d. The potential was then stepped down to 280 mV (SCE) on samples of S31603 steel and to 290 mV (SCE) on samples of S30400 steel in order to promote pit growth without the initiation of new pits.

The anodic polarisation at the potential level below the pitting potential was maintained for different periods of time, which varied from 6 to 60 minutes after which the samples were removed from the electrolyte.

During the anodic polarisation the current generated at the specimen surface was recorded every 2 seconds in order to determine the quantity of electric charge, which can be associated, via Faraday's law, to the amount of metal dissolved from the pits.

After each polarisation sequence, the specimens were removed from the electrochemical cell in order to determine the depth of the induced pits. A method involving material removal was used to measure the depth and determine the morphology of the induced pits. This involved grinding the surface with emery papers, 340, 400, and 600 grit, which were chosen as a function of the polarisation time and the diameter of the pits induced. For small pits induced (short polarisation time) the material removal was carried out using 600 grit emery paper.

In order to assess the depth of the biggest pit induced at the different polarisation times, a hardness indentation was made near each pit, (1 to 3 pits).

The indenter was a square pyramid diamond with an angle of 136° between faces, figure 3.10. The geometry of the indentation gives the possibility of determining its depth "h" from the measurement of the length of its diagonals "d" [149]. The relationship between these two parameters is:

$$h = 0.142845*d \qquad (3.5)$$

The difference in the diagonal length of the indentation due to grinding of the surface until the pit disappeared gave the depth of the pit. In order to avoid the accidental complete removal of the pits, the last stages of the material removal procedure involved the polishing of the surface with diamond paste of 6 μm.

For polarisation times of 30 minutes and longer, the complete removal of two or three consecutive indentations was necessary in order to measure the depth of the big pits induced.

Samples of S31603 steel were polarised for periods of 6, 12, 18, 24, 30, 36, 48 and 60 minutes. Samples of S30400 steel were polarised for periods of 6, 12, 18, 30, 42 and 54 minutes. The pre-pitting tests carried out to generate pits of different depth corresponding to different periods of polarisation were performed 4 or 5 times.

The measurements of the thickness of metal required for the complete removal of the deepest pit (the actual pit depth) gave a variation of ± 6 % in four measurements.

3.7 CF-SRET tests

SRET measurements were carried out on S30400, S31603 and S31803 SS specimens whilst simultaneously being subject to corrosion fatigue conditions in artificial seawater and in ferric chloride solution.

A modified corrosion cell was designed and used to perform the CF-SRET test. The cell must permit the free rotation of the specimen during the SRET measurements and the simultaneous application of the cyclic pressure. During the tests the CF-SRET cell was open to the air. Figure 3.11 shows the whole corrosion cell arrangement used during the CF tests in the two electrolytes.

SRET area map and line scans were performed at room temperature, with the Pt scanning probe distanced 100 microns from the cylindrical specimens as shown schematically in figure 3.12. For the initial tests the surface of the cylindrical specimens of S31603, S31803 and S30400 steels were free from corrosion pits.

In each of the tests performed the specimen was immersed in the electrolyte for one hour at free corrosion potential without application of load. After that period, the first SRET measurements were carried out in order to determine the presence of any site undergoing localised activity before the application of load.

The SRET measurements started with line scans at different positions (vertical direction) and finally complete area map scans were performed.

After the initial SRET measurements in synthetic seawater at free corrosion potential and in the absence of applied pressure the SRET specimens were subjected to CF conditions for different number of cycles, and at different stress levels.

All the CF-SRET tests were performed at room temperature using a loading frequency (f) of 0.27 Hz, and a stress ratio (R) of 0.

The CF-SRET tests started with low applied stress amplitude (45% σ_{ys}) at free corrosion potential with the intention of evaluating the general performance of the SRET equipment when measuring localised activity on the surface of rotating specimens subjected to cyclic internal pressure. The circumferential stress induced in the specimens was increased sequentially in order to determine a stress level that promotes localised corrosion in artificial seawater at free corrosion potential that could be detected by SRET measurements.

SRET measurements were carried out continuously on the specimens during the period they were subjected to CF conditions. For the tests in synthetic seawater at free corrosion potential fresh electrolyte was added to the CF-SRET cell every 24 hours.

CF-SRET experiments were also conducted on SRET specimens in artificial seawater under anodic polarisation during which fresh electrolyte was added to the cell at the end of each polarisation. The tests were carried out on specimens of the three SS's at different stress levels.

The objective was to promote stress enhanced localised electrochemical activity in the surface of the specimens, which could be assessed by SRET measurements.

Using the pit growth law obtained for the two austenitic SS's, pits of approximately 90 μm depth (40 % the wall thickness of the cylindrical SRET specimens), were generated on specimens of both the S30400 and the S31603 SS in seawater. The specimens were subjected to CF conditions at high stress level and SRET measurements were carried out in order to assess the electrochemical activity of the induced pits.

SRET-CF tests were conducted in 0.05 M ferric chloride solution in specimens of 304 and 316L SS at free corrosion potential and at stress levels above 80 % σ_{ys}. This electrolyte induced intense localised attack at open circuit potential on specimens of both austenitic SS's. The localised activity occurring at the surface of the specimens was easily detected by SRET map and line scan measurements.

On the other hand, due to the high resistance to pitting corrosion of the UNS S31803 steel (duplex SS) in synthetic seawater and in 0.05 M $FeCl_3$, the CF-SRET tests were carried out on specimens of this material in 0.1 M $FeCl_3$ solution. The applied stress level was above 80 % σ_{ys} of the respective steel specimen used. The objective of this change in electrolyte concentration was to induce localised activity in the surface of the specimens however, even in this more concentrated solution the duplex SS showed high resistance to localised attack. Due to this behaviour some CF-SRET tests were carried out on specimens subjected to potentiostatic anodic polarisation.

CHAPTER 4 – Results

4.1 Introduction

This chapter presents the results obtained from the experiments carried out on UNS S31603, S30400 and S31803 during the present investigation. The metallurgical microstructure and the grain size of the three SS's is described. The results of the stress - strain calibration of the hydraulic system which shows the relationship between applied pressure and the stress generated in the cylindrical SRET specimens are presented in section 4.3. Results of electrochemical tests for the evaluation of the corrosion potential (E_{corr}) and pitting corrosion potential (E_p) and passive behaviour of the Austenitic and Duplex SS's are shown in section 4.4. The results of the electrochemically induced pits on S31603 and S30400 SS's are given in section 4.5. In addition, section 4.5 describes the empirical pit growth law obtained for the two steels.

The results obtained from the SRET system calibration are presented in section 4.6. Section 4.7 is dedicated to the presentation of the results of SRET measurements in seawater of the three SS's at open circuit potential (E_{corr}), at anodic potentials above and below the pitting potential (E_p) and the results of SRET measurements in ferric chloride solution at free corrosion potential. Finally section 4.8 is dedicated to the results obtained from the corrosion fatigue - SRET (CF - SRET) tests conducted in synthetic seawater and in ferric chloride solution.

4.2 Materials characterisation

To determine the microstructure of the steels, metallographic analysis was carried out using an optical microscope.

The ASTM 112-95 standard intercept method was used for determining grain size on all the three steels. An image analysis system was used to evaluate the percentage of ferrite and austenite phases in the duplex stainless steel.

The UNS S31603 steel presented an equiaxed austenitic microstructure, the average grain size was found to be 39 μm. Shallow non-metallic inclusions were observed lying in the rolling direction and some inclusions were present as spots of 5 to 10 microns in average diameter. Electrolytic etching in NaOH revealed the presence of delta ferrite (δ) distributed in the rolling direction. Figure 4.1(a) shows the microstructure of this steel in the L-T plane orientation, which is parallel to the rolling and transverse directions. The delta ferrite phase is shown in figure 4.1(b). The non-metallic inclusions as found in the surface of a non-etched specimen are shown in figure 4.1(c).

The microstructure of the UNS S30400 austenitic steel also consisted of equiaxed grains, figure 4.2(a). The average grain size for this steel was found to be 34 μm. The presence of delta ferrite was also evident as shown in Figure 4.2(b). Non-metallic inclusions which had a long shallow shape were found lying in the rolling direction of the steel, figure 4.2(c). The quantity of inclusions in this steel was less than in the S31603.

Figure 4.3 shows the two-phase microstructure with approximately equal amounts of austenite and ferrite of the UNS S31803 steel. The amount of ferrite phase in this steel

was found to be approximately 51 % and the balance corresponded to the austenite phase.

The continuous phase is the ferrite (α), and the austenite (γ) is distributed as islands as shown in the figure 4.3(a), which presents the ferrite-austenite phase boundaries well defined. The average grain size was found to be 14 μm. Figures 4.3(b) and 4.3(c) show the grain boundaries within the ferrite and the austenite phases respectively.

4.3 Applied pressure-induced stress calibration

The values of the applied pressure, the experimental data of the induced strains on the gauged specimens and the corresponding theoretical (σ_C, σ_L) and experimental (σ_1, σ_2) stresses (circumferential and longitudinal) are shown in tables 3, 4 and 5 for UNS S31603, S30400 and S31803 SS's respectively.

Figure 4.4 shows the plots of the induced strain and the experimental stress as a function of the applied pressure obtained form calibration tests for steel S31603. The same set of results obtained from tests on the dummy specimen of the steel S30400 are shown in figure 4.5, and in figure 4.6 for the case of the steel S31803.

In all curves shown in figures 4.4, 4.5 and 4.6 there is a linear relationship between the applied pressure and the induced stress and strain, which allowed the direct determination of the stress induced from the value of the applied pressure in bar.

The calibration of the hydraulic system gave the relation between the applied pressure, p (in bar) and the induced circumferential and longitudinal stresses in the cylindrical specimens. The equations obtained from the calibration for each stainless steel are as follows:

For UNS S31603 (316L SS).

Circumferential stress: $\sigma_1 = -4.54 + 2.22p$ (MPa)

Longitudinal stress: $\sigma_2 = -4.5 + 0.91p$ (MPa) (4.1)

For UNS S30400 (304 SS).

Circumferential stress: $\sigma_1 = -2.43 + 2.04p$ (MPa)

Longitudinal stress: $\sigma_2 = -0.67 + 0.92p$ (MPa) (4.2)

For UNS S31803 (Duplex SS)

Circumferential stress: $\sigma_1 = -8.51 + 3.28p$ (MPa)

Longitudinal stress: $\sigma_2 = -3.64 + 1.35p$ (MPa) (4.3)

4.4 Electrochemical Tests

Experiments were carried out to evaluate the electrochemical behaviour of the three SS's in synthetic seawater. Polarisation curves for the UNS S31603, S30400 and S31803 steels are shown in figures 4.7, 4.8 and 4.9 respectively. The polarisation curves represent an average of 5 potentiodynamic polarisations performed on different samples of the three SS's under the same experimental conditions.

The values of E_{corr} and E_P for each material are listed in table 7 as a range of potential versus the Saturated Calomel Electrode (SCE). From the polarisation curves it is possible to see that the steel S31803 presented the highest pitting potential in artificial seawater.

The pitting potential "E_P" was determined as the potential value at which the current density increased abruptly for one order of magnitude or more.

The polarisation curve for the steel S31603 presented in the figure 4.7 shows that this steel undergoes active dissolution during anodic polarisation up to a potential of around 0 mV. This is followed by a transition to passive behaviour. The steel passive region is stable over the potential range of E = 60 to E = 320 mV (ΔE = 310 mV). The passive current density was in the range 0.01 to 0.03 $\mu A/cm^2$. Once the pitting potential was reached the anodic current increase rapidly as a consequence of the nucleation and growth of corrosion pits.

The polarisation curve in the figure 4.8 shows that the surface of the steel S30400 was active during the anodic polarisation in the range of E = -230 to approximately E = 0 mV, after which the surface of the steel became passive. The steel remained passive through a potential range of E = 0 to E = 350 mV (ΔE = 350 mV), during which the anodic current remained approximately constant.

The steel S31803 in artificial seawater presented the highest pitting potential of all the stainless steels, as shown in figure 4.9 where E_P = 1060 to 1140 mV Vs SCE. This material also exhibited the highest passive potential range, which was from E = 40 to around 900 mV Vs SCE, (ΔE = 940 mV). At potential levels more positive than 900 mV the passive behaviour was not stable and a more gradual transition to pitting was observed as the current increased two orders of magnitude in a potential range of 200 mV after which pitting was initiated. The pits found in the S31803 following the polarisation test presented a shallow shape and were smaller than the pits formed in S30400 and S31603 SS's.

The electrochemical parameters of the three stainless steels obtained from these experiments are presented in table 7. The values of the E_p of the three steels in artificial seawater were the basis for the test conditions used for the CF-SRET tests using the tubular SRET specimens.

4.5 Electrochemical generation of pits

4.5.1 Pit growth laws

The results from the electrochemical generation of pits on S31603 and S30400 stainless steels are shown in figures 4.10 and 4.11 respectively, as plots of maximum pit depth versus polarisation time.

Regression analysis applied to the data of the pre-pitting tests on specimens of steel S31603 gave the following empirical equation for the pit growth law.

$$\mathbf{P_d = 26t^{0.60}} \qquad (4.4)$$

where P_d represents the pit depth (in μm), and t is the time (in minutes) of anodic polarisation.

The empirical equation that represents the pit growth law for pits induced electrochemically in specimens of steel S30400 was found to be:

$$\mathbf{P_d = 27.9t^{0.67}} \qquad (4.5)$$

The pits induced in samples of steel S30400 were in general, greater in depth and diameter than the pits induced in samples of steel S31603.

In both SS's the generated pits had a semi-elliptical morphology as revealed during the pit depth measurements, which involved material removal. During pit depth measurements layers of metal were removed in several steps and the major diameters of the pit mouth were measured and the thickness of removed metal was quantified.

4.5.2 Pit profile measurements

From the measurements of material removed and pit mouth diameters, the profiles of induced pits in the two SS's were determined for the different times of anodic polarisation. Pit profiles for pits induced in both, S31603 and S30400 for different polarisation times in artificial seawater are shown in figure 4.12 and 4.13 respectively. In these graphics the pit depth was plotted as a function of the pit width.

The mouth of the generated pits was quasi-circular, however some of them presented an elliptical geometry. In was also found that the profile of the induced pits was semi-elliptical with pit depths less than half of the pith mouth diameter. The length of the two major diameters of the pit mouth was measured and used as the pit width. The values of the pit width are represented with a red circle for the minor axis and with a black circle for the major axis in the plots of figures 4.12 to 4.15.

Pit profile plots for the pits generated on specimens rotating at 100 rpm are presented in figure 4.14 for the S31603 steel and in figure 4.15 for the S30400 steel. Using the data of the pit profiles a pit aspect ratio ($\mathbf{p_{ar}}$) can be defined as: $p_{ar} = m_{hd}/P_d$, where m_{hd} is half of the major pit mouth diameter and P_d is the pit depth. It is observed that the pits generated in both stainless steels under hydrodynamic conditions present a higher p_{ar} than that for pits generated on non-rotating specimens.

Table 9 presents the values of pit aspect ratio for pits generated under rotating and non-rotating conditions for different polarisation times.

Figure 4.16 presents photographs of the pit mouth taken during the sequence of material removal on samples of steel S31603. Photographs for a similar sequence of material removal and measurement of the pit depth and mouth size on samples of steel S30400 is presented in figure 4.17. In these photographs also shown are the diamond indentations made near the pits to assess the quantity of material removed.

4.5.3 Pit current measurements

The electric currents generated by the anodic polarisation of the specimens for different periods of time during the electrochemical formation of pits were recorded. The chronoamperometries obtained from the pit generation tests on samples of S31603 steel in stationary (non-rotating) conditions are shown in the figure 4.18.

The chronoamperometry obtained from the pit generation on S31603 steel specimens polarised for 60 minutes at 280 mV Vs SCE in both stationary and rotating conditions are presented in figure 4.19. The hydrodynamic condition induced by the rotation of the cylindrical specimen had the effect of decreasing the current generated during active dissolution of pits at a given anodic potential.

Current Vs time records, corresponding to the pit generation tests on samples of S30400 steel in the non-rotating condition at different periods of anodic polarisation, are presented in figure 4.20. The chronoamperometry representing the generation of pits on cylindrical specimens of S30400 steel polarised for 60 minutes and subjected simultaneously to SRET measurements (rotating at 100 rpm) is shown in figure 4.21.

In all the current records it was possible to see a rapid increase of current during the first 30 seconds of polarisation which corresponds to the period of pit nucleation and accelerated growth at a potential level above the pitting potential. The current dropped down dramatically when the potential of the sample was decreased to levels below the pitting potential. After a period of 30 seconds at high potential the current increased slowly from values of 10 to 50 μA's to a few mA's at the end of the polarisation period. The increase of current with time may be associated with two processes taking place under potentiostatic polarisation, mainly the active dissolution of the nucleated pits (one to three pits) and the simultaneous dissolution of approximately 1 cm^2 of metal surface in the passive state. For polarisation periods longer than 12 minutes only one or two pits were actively dissolving.

The anodic polarisation of specimens of S31603 and S30400 steels during which no pits were nucleated, or if nucleated did not grow, provided a record of the anodic current for the metal in the passive state. The chronoamperometries for these tests are presented in figure 4.22. The anodic currents generated were in the order of 10^{-9} to 10^{-7} A with initial high values that decreased as the period of polarisation increased.

The integration of the current Vs time curves obtained from the pit generation tests gave the quantity of charge generated during the active dissolution of pits. The electric charge (in coulombs) presented in the plots of figure 4.23(a) is the total charge generated during the active pit growth divided by the number of pits generated, which was 1 or 2 maximum. The presence of small pits formed during the 30 seconds period of polarisation at 500 mV Vs SCE, which repasssivated after nucleation was disregarded. It is important to note that the charge generated during the 30 seconds of polarisation at 500 mV Vs SCE is associated with the dissolution of metal due to the nucleation of several pits, most of which repassivated and did not propagate.

This charge and that associated with the anodic current in the passive state were not taken into account for the calculation of the electric charge per pit. In this way all the charge is associated with the metal dissolved from the pits (1 or 2) that grew actively under potentiostatic control. Figure 4.23(a) presents the quantity of charge per pit as a function of the polarisation time, and figure 4.23(b) presents the current density per pit also as function of the time of polarisation obtained from the pre-pitting tests on the steels S31603 and S30400. The current densities were calculated by using the values of DC current at different times as measured from the chronoamperometries and the pit surface area calculated from the pit profiles obtained experimentally.

The electric charge involved in the dissolution of the two steels in the passive state was also calculated by integration of the chronoamperometry curves shown in figure 4.22. For the S31603 steel polarised for 48 minutes at 280 mV Vs SCE the electric charge was found to be around 2.22×10^{-4} coulomb, which corresponds to 6.4236×10^{-8} grams of dissolved metal. In the case of the S30400 steel polarised 60 min at 290 mV Vs SCE the charge was approximately 9.87×10^{-4} coulomb equal to 5.71×10^{-7} grams of dissolved metal. The charge per pit at different times of anodic polarisation was 4 orders of magnitude bigger that the charge generated for the steels in the passive state.

4.6 Current density calibration of the SRET system

Current density measurements and SRET system calibrations were carried out as a primary activity before the SRET and CF-SRET tests. The same experimental conditions were used in both, the calibration and the SRET tests.

The rotation rate of the gold micro disk calibration source (MDCS) was 100 rpm for calibrations conducted in both synthetic seawater and ferric chloride solution.

When the tip of the SRET Pt pseudo reference electrode suffered damage this was re-sharpened in order to attain the same conical shape and tip diameter, after which a new calibration was performed.

In order to determine a calibration factor relating the SRET measurement (mV) with the current emanating from a site undergoing localised attack, different currents were applied galvanostatically to the MDCS specimen and the measured signal was recorded. The results presented in figure 4.24 show the relation between the SRET output signal measured (in mV) and the current density emanating from the MDCS specimen immersed in synthetic seawater. The relationship between the applied current and output signal was found to be linear over the range of applied currents tested. From this calibration test a conversion factor of 115 mA/cm^2 per millivolt was obtained.

To establish the relationship between the detected signal level and the specimen-to-probe distance, SRET measurements were carried out by applying a constant current of 25 μA to the MDCS specimen. The distance of the scanning probe from the MDCS was varied and the detected signal at each different probe position was recorded. The results shown in figure 4.25 indicate that for distances up to 250 μm there is a linear relation between probe output (potential in mV) and probe to MDCS distance. For probe-to-MDCS separation greater than 250 μm an asymptotic behaviour of the output signal with distance was observed. At an operating distance of 100 μm, a current of 25 μA applied to the MDCS specimen produced a probe output of 0.770 mV. At 600 μm of separation the same current produced a maximum output signal of 0.1 mV.

Area map scans conducted on the MDCS when subjected to different applied currents during the calibration experiments are shown in figures 4.26 to 4.34.

Each map scan is accompanied by a line scan, which represent the maximum output signal detected from the SRET area map for the particular applied current. It was considered here that the maximum output signal corresponded to a position of the scanning probe exactly in the middle of the circular surface of the MDCS specimen.

The second set of calibration tests was carried out using a 0.05 M $FeCl_3$ solution as the electrolyte. The results of the output signal as a function of the applied current are shown in figure 4.35. The lineal relationship between the applied current and the maximum output signal gave a calibration factor of 70.4 mA/cm^2 per mV.

The results of the calibration for the output signal as a function of the specimen to probe distance are shown in figure 4.36. The output signal was found to have a linear relationship with the separation between the SRET probe and specimen for distances up to 350 microns. For probe-to-MDCS separations greater than 350 μm the output signal decreases asymptotically towards a constant value in a similar way as that found during the calibration tests in artificial seawater. Line scans of the calibration experiments in $FeCl_3$ for different applied currents are shown in figures 4.37(a) and 4.37(b). For these tests 5 line scans were performed with the Pt probe at fixed position facing approximately the middle of the MDCS surface area.

4.7 SRET measurements

4.7.1 SRET measurements in synthetic seawater

Figure 4.38 presents the area map scans of steel S31603 in seawater at different potentials. Colours in the more positive end of the palette (red) represent relatively cathodic potentials, whereas those at the negative end (blue) represent anodic areas.

Figure 4.38(a) is an example of an area map scan performed on specimens at free corrosion potential E_{corr}, which does not show any localised corrosion on the surface. For the SRET measurements on specimens under anodic polarisation at 350 mV, as shown in figure 4.38(b) localised attack could be seen in the area maps, the sites with high localised activity produced a very high output signal which correspond to high current densities. Finally figure 4.38c shows a SRET area scan which represents the results obtained on specimens polarised to 290 mV Vs SCE. The specimens presented a passive behaviour during the period of anodic polarisation and no localised attack was registered under this condition by the SRET line and map scans. For the SRET measurements on specimens at anodic potentials the complete polarisation period was approximately 15 minutes. The specimens were polarised for 10 minutes before the SRET measurements started, and continued during the SRET tests, which lasted between 5 and 6 minutes.

The two SRET maps shown in figure 4.39 correspond to the measurements conducted on specimens of steel S30400 in synthetic seawater. The map scans conducted on specimens at open circuit potential did not detect any localised electrochemical activity in the metal surface. The map scans obtained for the specimens at an anodic potential level of 280 mV Vs SCE are shown in figure 4.39a. When the specimen was polarised at 350 mV Vs SCE, the SRET measurements showed the development of intense localised activity, as shown in figure 4.39b. The surface of the specimens after completion of the area scans showed intense attack in zones near to the metal- coating boundary. Pits were also formed on the metal surface.

In figure 4.40 (a, b and c) area map scans are shown for specimens of steel S 31803 in synthetic seawater at free corrosion potential, 1170 mV and 1050 mV Vs SCE, respectively.

At free corrosion potential the specimens of steel S31803 were passive, as expected due to its high pitting corrosion resistance. The area scan did not register any localised activity during the period this stainless steel was immersed in the electrolyte. When the specimen was polarised to 1050 mV Vs SCE the non-coated surface presented some localised activity, which was not intense and did not promote pit nucleation. When the material was anodically polarised above the pitting potential, i.e., 1170 mV Vs SCE, localised attack was detected on the steel. The localised activity was severe at the metal/coating boundary, where crevice corrosion developed. It is common for the duplex SS to develop crevice attack instead of pitting corrosion in artificial seawater when subjected to anodic polarisation.

4.7.2 SRET measurements in 0.05 M $FeCl_3$ solution

The results of the SRET measurements on specimens of each stainless steel in ferric chloride solution are presented in this section. The SRET tests conducted on the two Austenitic SS's were for short periods of time, (maximum 2 hours) due to the aggressiveness of the electrolyte, which induced highly localised attack.

In the case of specimens of Duplex SS the immersion time was longer (12 hours), as this stainless steel presented a higher resistance to localised attack. The area maps presented in this section also used colours in the more positive end of the palette to represent relatively cathodic potentials and those at the negative end to represent anodic areas.

The results of the SRET measurements on samples of steel S31603 at free corrosion potential without cyclic loading are presented in figure 4.41 as time-dependant area map scans.

The results of SRET measurements on samples of steel S30400 at free corrosion potential without the application of cyclic loading are presented in figure 4.42 as time-dependant area map scans.

For the tests on samples of steel S31803 the concentration of the $FeCl_3$ solution used was 0.1 M due to the preliminary results in a solution 0.05 M, which showed a high resistance of the duplex SS to localised corrosion. The SRET area maps presented in figure 4.43 show very low localised activity at open circuit potential for specimens free from cyclic loading after 10 hours immersion.

4.7.3 SRET measurements during electrochemical generation of pits

The area map scans obtained from SRET measurements performed on samples of steel S31603 and S30400, during electrochemical generation of pits in artificial seawater, are presented in figures 4.44 and 4.45 respectively. The map scans were conducted continuously throughout the total period of anodic polarisation, during which the nucleated pits were growing actively on the specimen surface. The map scans consisted of 384 lines with 512 samples per line, which took 5 minutes to be completed. Line scans representing the maximum output signal of the complete area map are shown as well for different polarisation times.

The calibration factor obtained in artificial seawater was used to assess semi-quantitatively the activity of the pits generated potentiostatically in the two Austenitic SS's in terms of current density, which was plotted as a function of the polarisation time, figure 4.46.

4.8 CF-SRET measurements.

4.8.1 CF-SRET tests in synthetic seawater

- **Tests on specimens of steel S31603**

The first set of Corrosion Fatigue (CF) tests was carried out on specimens of steel S31603. The surface of the specimens was polished and free from corrosion pits or any other visible surface defects that could act as a stress concentrator.

The SRET measurements at free corrosion potential were conducted during the CF test at different numbers of cycles, with the specimens subjected to a circumferential stress range $\Delta\sigma$ = 106 MPa ($\sigma_{MAX} = 0.45\sigma_{ys}$), at a frequency of 0.27 Hz (16 cycles/min).

The SRET area map scans and line scans obtained from this first set of CF tests on samples of steel S31603 in artificial seawater did not show any signal associated with localised attack and for that reason are not presented in this section. In addition no visible evidence of pitting was observed. If the map or line scans do not detect localised activity, then no information of the electrochemistry of the system can be obtained from SRET measurements.

After the tests at free corrosion potential, CF experiments were conducted involving SRET measurements on specimens subjected to potentiodynamic polarisation. The applied circumferential stress range ($\Delta\sigma$) was 106 MPa. The specimens were polarised from –200 to 300 mV Vs SCE with a scan rate of 50 mV/min. Polarisation was conducted at different numbers of cycles.

Figure 4.47 shows two polarisation curves for a SRET specimen of steel S31603 obtained at different number of CF cycles.

After 266000 cycles the behaviour of the specimen is passive during anodic polarisation however some instability can be seen in current density within the passive region. For the potentiodynamic polarisation curve after 308700 cycles it can be seen that the passivity breaks down at a potential of 100 mV Vs SCE. Also the current density in the passive region is higher after 308700 cycles when compared with that obtained after 266000 CF cycles.

The specimens were further subjected to CF cycling at free corrosion potential until completion of 326500 cycles, after which they were subjected to a sequence of potentiostatic polarisations. The circumferential stress range was the same, 106 MPa ($\sigma_{MAX} = 0.45\sigma_{ys}$), the specimens were polarised at –200 mV vs SCE (50 mV cathodic overpotential) for 20 minutes followed by anodic polarisation at 200 mV Vs SCE, also for 20 minutes.

Figure 4.48 shows the chronoamperometry records for two consecutive polarisations performed on one of the specimens of steel S31603 which had previously been subjected to potentiodynamic polarisation. It was normally observed that during the first potentiostatic polarisation at 200 mV Vs SCE the area of the specimen was more active.

For example the case presented in figure 4.48(a) in which the chronoamperometry plot shows 2 spikes (i) after 3 and (ii) after 8 minutes of polarisation. This may be associated with metastable pit formation. After 12 minutes of anodic polarisation the current increased dramatically with time which can be associated with the kind of behaviour that is characteristic of the active dissolution of nucleated pits. The chronoamperometry plot in figure 4.48(b), which was conducted 30 minutes after the chronoamperometry (a), showed a more stable behaviour of the surface of the steel, with no spikes of current. SRET measurements on specimens of steel 31603 in seawater subjected to cyclic loading showed localised activity during the application of anodic polarisation.

When the anodic polarisation stopped, the localised activity decreased and vanished in all cases as could be seen from SRET line and map scans. The surface of the specimens presented sites of localised corrosion in the form of micropits aligned and forming crack-like flaws following the rolling direction of the steel, see below. Despite the presence of these sites of localised attack the SRET measurements did not detect any electrochemical activity associated to them.

After the potentiostatic polarisation, the circumferential stress range applied to the specimen was increased from 106 to 172 MPa ($\sigma_{MAX} = 0.73\sigma_{ys}$) with R=0. The cyclic loading continued with the specimens immersed in the solution at free corrosion potential for 93800 cycles. The SRET line and area map scans conducted at different numbers of cycles did not show evidence of localised attack despite the presence of pits of different sizes and crack-like surface flaws generated in the surface of the specimens. The flaws developed at the surface of the specimens did not provoke failure. After this sequence of CF-SRET tests specimens were removed from the corrosion cell and prepared for SEM examination.

The photographs from the SEM analyse conducted on specimens of steel S31603 are presented in figure 4.49. In images 1 and 2 several flaws can be seen which look like cracks and micro-pits of about 5 μm of diameter. These defects grew in a direction perpendicular to the circumferential stress. In photographs 3 and 4 it is possible to observe that the flaws are formed by the coalescence of micropits. Photographs 5 and 6 show higher magnification views of the flaws where it is possible to distinguish pits inside the surface imperfections. These microscopic pits had a diameter of approximately 2 μm. The same kind of damage was observed in 4 specimens of steel S31603 subject to similar experimental conditions.

CF tests on specimens of steel S31603 were also carried out at open circuit potential under an applied stresses range ($\Delta\sigma$) of 260 MPa ($\sigma_{MAX} = 1.10\sigma_{ys}$) and R = 0. The surface of the specimens did not show signs of localised attack (micro pitting) when analysed after failure. The SRET line scans conducted at different periods during the CF tests did not detect any localised activity.

Figure 4.50 shows the SEM analysis images of a specimen subjected to these experimental conditions, which presented failure after 48300 cycles.

- **Tests on specimens of steel S30400**

SRET measurements were conducted on specimens of steel S30400 subjected to CF conditions with an applied $\Delta\sigma$ = 197 MPa ($\sigma_{MAX} = 0.80\sigma_{ys}$), and R = 0 at free corrosion potential for 15000 cycles. SRET line and map scans performed after different numbers of cycles did not show evidence of localised attack. When the specimens were subjected to anodic polarisation at 350 mV Vs SCE, the SRET line and map scans performed identified the position of sites undergoing localised attack. SRET measurements showed that the activity of the nucleated pits ceased when the anodic polarisation was stopped and that the cyclic loading did not reactivate the pits. The surface of the specimens of steel S30400 showed imperfections that look like cracks and corrosion pits with the same pattern as that found in specimens of steel S31603.

SEM images shown in figure 4.51 present the surface of one of the SRET specimens of steel S30400 after 28400 cycles at a circumferential $\Delta\sigma$ = 197 MPa.

- **Tests on specimens of steel S31803**

SRET line and map scans conducted on specimens of steel S31803 after 46000 cycles at free corrosion potential subjected to a circumferential stress of 474 MPa (σ_{MAX} = $0.93\sigma_{ys}$) did not show sites of localised activity. This result was expected due to the well-known pitting corrosion and CF resistance of this grade of SS.

On the other hand, the specimens of steel S31803 developed crevice attack when polarised to anodic potential levels near its pitting potential (1020 mV Vs SCE) for periods of 20 minutes. SRET line and map scans showed that the localised attack induced by the anodic polarisation ceased at the same time the polarisation was stopped.

SRET measurements showed that the application of cyclic stress to the SRET specimens of steel S31803 did not promote any detectable reactivation of the pits or crevices formed during the previously applied anodic polarisation. The applied stress range was then increased from 470 to 547 MPa ($\sigma_{MAX} = 1.1\sigma_{ys}$), which is the limiting pressure of the hydraulic system (230 bar) and the CF test was continued for 2400 cycles. SRET line and map scans showed that the behaviour of the metallic surface in contact with the electrolyte was not altered.

Figure 4.52 shows a series of area map scans conducted on a duplex SS specimen when subjected to the conditions stated above. The visual examination of the specimen revealed the presence of shallow pits and crevices formed in the surface during anodic polarisation, but no cracks were found in the specimen.

4.8.2 CF-SRET tests in ferric chloride solution.

- **Tests on specimens of steel S31603**

A set of SRET area map scans representing the behaviour of specimens of UNS S31603 steel immersed in 0.05 M $FeCl_3$ solution are presented in figure 4.53(a) and (b).
Area map scans were performed at free corrosion potential at different immersion times. The first area maps were carried out after 5 and 15 minutes of immersion without the application of cyclic loading.
After 25 minutes of immersion within the electrolyte cyclic loading was introduced and continued for another 135 minutes. The stress range ($\Delta\sigma$) was 182 MPa (σ_{MAX} = $0.77\sigma_{ys}$) and the stress ratio (R) of 0. In all the experiments conducted under these conditions specimens developed active localised attack (pitting) at several sites on the surface.

SRET line and map scans showed that the electrochemical activity of the pits varied as a function of time (number of cycles) with a general tendency to increase until failure of the specimen occurred. The behaviour of the active pits in the specimens was assessed and recorded. Table 10 presents the information from SRET measurements of the activity, in terms of maximum output signal and localised current density, of one pit (pit **a** in figure 4.53). The corrosion potential of the specimen as a function of the number of stress cycles is also reported in table 10. Figure 4.54 shows the variation of the open circuit potential of the specimen with immersion time (number of cycles). The electrochemical activity of the pit **a** (in fig. 4.53) in terms of localised current density was plotted as a function of the number of cycles, figure 4.55. There was a decrease of current density after approximately 750 cycles, at the same time it was possible to see

short cracks growing from pit **a,** this "transition point" may be associated with the nucleation of a short fatigue crack from the pit.

- **Tests on specimens of steel S30400**

Results of SRET measurements on specimens of UNS S30400 steel subjected to cyclic loading in 0.05 M ferric chloride at free corrosion potential are presented (as time-dependant area map scans) in figure 4.56(a) and (b). The specimens were subjected to a circumferential stress range ($\Delta\sigma$) of 200 MPa ($\sigma_{MAX} = 0.81\sigma_{ys}$) and stress ratio R = 0. The total number of cycles to failure was 2570. The reason for this short period under CF conditions was that the specimens presented active pitting corrosion attack at different sites as revealed by the SRET measurements. The highly localised metal dissolution at the pit induced a rapid decrease in wall thickness of the specimen, which favoured the early nucleation of fatigue cracks. CF tests were stopped when specimens presented oil leaking from the nucleated cracks due to the internal hydraulic pressure. Some pits penetrated through the wall of the specimens without developing cracks. However the majority of pits eventually nucleated cracks.

High levels of localised attack (current densities of 20 to 50 mA/cm^2) took place on the surface of the specimens after a few seconds of immersion, as was the case for the SRET tests without cyclic loading. The localised activity of several sites was assessed by SRET measurements performed continuously throughout the period the specimens were subjected to CF conditions. By using the calibration factor obtained in 0.05 M $FeCl_3$ (70 mA/cm^2 per mV), localised current densities of 70 and 80 mA/cm^2 were measured after 17 minutes of immersion and 112 load cycles as shown by the map scans in figure 4.56(a). A maximum in localised current density (i = 202 mA/cm^2) was

detected after 68 minutes of immersion, (708 cycles), following which the activity decreased, figure 4.56(b). From the SRET map and line scans the localised activity, in terms of current density, was measured as function of time. Figure 4.57 presents a plot of the localised current density Vs time (number of cycles) of different sites undergoing localised attack on specimens of 304 SS subjected to CF in a solution 0.05 M$FeCl_3$.

- **Tests on specimens of steel S31803**

The set of CF-SRET tests on specimens of UNS S31803 steel again showed a high resistance of this steel to localised attack even in the 0.1 M $FeCl_3$ solution. Results obtained from SRET measurements indicated that at free corrosion potential the duplex stainless steel did not suffered from localised attack. The free corrosion potential of this steel was stable in the range 609 to 614 mV Vs SCE during 8 hours immersion under stress-free condition.

The application of cyclic stress ($\Delta\sigma$ = 474 MPa, $\sigma_{MAX} = 0.94\sigma_{ys}$) R = 0, did not induce changes in the electrochemical activity of the metallic surface in contact with the aggressive solution as shown in figures 4.58(a), 4.58(b) and 4.58(c) carried out after 0, 5000 and 9600 cycles respectively. The corrosion potential increased from 614 to 640 mV Vs SCE after 56 hours of immersion, (48 hours under cyclic loading = 46000 cycles). For this set of experiments the cyclic loading had to be stopped each time a SRET measurement was carried out.

The CF test continued at the lower applied stress level of 320 MPa ($\sigma_{MAX} = 0.63\sigma_{ys}$) for 5000 cycles after which SRET measurements were carried out on the specimen subjected to anodic polarisation at a potential 470 mV more positive than the E_{corr}. Figure 4.59(a) and (b) present the SRET area maps conducted at 1100 mV Vs SCE and

a free corrosion potential, (630 mV Vs SCE) respectively. The application of anodic potentials also induced localised attack in the form of crevices formed at the metal-coating boundary.

The localised activity ceased completely when the anodic polarisation was removed. SRET measurements carried out after the anodic polarisation did not detect any localised activity even at sites where crevices had previously been induced.

CHAPTER 5 – Discussion

5.1 Introduction

As stated in chapter 1, the main aim of this work was to conduct an electrochemical study in regard to further understanding the transition from a corrosion pit to a short fatigue crack which occurs during the early stages of damage arising from corrosion fatigue.

The system "stainless steel – seawater" was chosen to conduct the experimental work due to the industrial importance of this system and the large amount of information available related to the pitting corrosion and corrosion fatigue of this metal-environment combination. Although there has been much research on the generation and growth behaviour of cracks during corrosion fatigue process, relatively little work has been reported on the transition from corrosion pit to short fatigue crack.Emphasis was given to the novel use of The Scanning Reference Electrode Technique (SRET) to conduct a semi-quantitative assessment of this transition from an electrochemical point of view.

The results of the SRET measurements carried out in artificial seawater showed that the localised activity developed in the SS specimens at free corrosion potential was not sufficiently intense to be detected by SRET line and map scans. Better results were obtained with the use of $FeCl_3$ solution, which induced intense localised attack in the two austenitic stainless steels.

Changes in this localised activity as a function of time on specimens under stress free conditions and during CF tests were detected by SRET measurements.

5.2 Materials characterisation

The microstructural characterisation of the steels used in the present work, indicated the presence of delta ferrite in the two Austenitic stainless steels, S31603 and S30400. In the present case the delta ferrite phase was found as isolated elongated grains with the major axis parallel to the rolling direction in both Austenitic SS's, as shown in figures 4.1b and 4.2b. The delta ferrite (δ) phase is ferrite formed on solidification and is a phase rich in chromium and other ferrite-stabilising elements and lean in nickel and other austenite-stabilising elements. The presence of delta ferrite is known to decrease the pitting corrosion resistance of the steels and when present as a continuous grain boundary network it can decrease the resistance to sensitisation. The main problem with the presence of delta ferrite in austenitic SS's is that long-term exposure at elevated temperatures can lead to its transformation to sigma phase, which is hard and brittle and can reduce the ductility of the steel.

The major effect of the presence of delta ferrite in the steels S31603 and S30400 was that during the anodic polarisation of specimens in artificial seawater localised attack took place preferentially in this phase. This point will be discussed in more detail in the section of CF-SRET tests. The approximate amount of delta ferrite in the steel S31603 was found to be 6.75 % and 9 % in the steel S30400. Both SS's revealed the presence of non-metallic inclusions and although the steel S31603 contains more sulphur than the S30400 the steel S31603 appears to be more resistant to pitting corrosion.

This behaviour can be associated to the presence of Molybdenum (2.09 wt %) in the steel S31603. It is well documented that the addition of Mo increases the resistance to pitting and crevice corrosion of stainless steels [17,38]. This is primarily due to the fact that molybdenum improves the stability of the passive film. These improvements are visualised through the reduction of the critical anodic current density, the increase of the passive range and a decrease in the passive current density.

The same superiority of the steel S31603 was observed during the electrolytic etching of the two austenitic stainless steels for the metallographic preparation used for revealing the microstructure. In that experiments the specimens of steel S31603 showed minimum localised attack when compared to the steel S30400 which easily developed severe pitting.

In the steel S31603 the non-metallic inclusions were found to be approximately 3 μm wide, and varied in length from 5 to 30 μm. For the steel S30400 the non-metallic inclusions were stringers of 3 to 5 μm wide and up to approximately 90 μm long.

Chromium carbides did not appear to be present along the grain boundaries of the austenitic SS's and therefore, in the as-received condition, these two steels can be considered to be non-sensitised. This condition is due to the low carbon content in this SS (0.02 weight %). It is well known that austenite containing less than about 0.03 weight % carbon should be stable while austenite containing carbon in excess of 0.03 weight % can precipitate $M_{23}C_6$ on cooling below the solubility line.

The UNS S31803 (Duplex SS) presented a microstructure of 51% ferrite and the remainder being austenite, which is the expected microstructure for this grade of SS, (50% α, 50% γ) see figure 4.3a, 4.3b and 4.3c. No σ phase was present, as expected from the composition range of chromium (22-26 %) and molybdenum (2-5 %) as reported in the table 1.

The two phases were distributed along the rolling direction with the grains in each phase following the same direction. This stainless steel did not develop pitting during the electrolytic etching and in general the etching of the Duplex SS was easy compared with the steel S31603 and S30400. The microstructure of the steel S31803 in general presented a low volume-fraction of non-metallic inclusions providing the material with high resistance to general and localised corrosion.

As for the austenitic grades, the corrosion resistance of the duplex stainless steels is based on the formation of a passive surface layer. The resistance of duplex stainless steels to localised attack by pitting or crevice corrosion in chloride containing media is determined by their chemical composition and by the non-metallic inclusion content, (particularly sulphides), and depends relatively little on their microstructure.

5.3 Stress-strain calibration

As a part of the experimental work, SRET measurements were carried out using specimens subjected simultaneously to corrosion and cyclic stress. It was necessary therefore to conduct calibration tests using the hydraulic system. The relationship between applied pressure, the strain generated in the specimen and the resultant stresses was determined quantitatively.

As was expected, the elastic circumferential and longitudinal strains and stresses generated in the gauged specimens exhibited a linear behaviour when plotted as a function of the applied pressure, see figs. 4.4 to 4.6.

The calibration tests proved good reproducibility of the state of strain/stress imposed on the thin-walled specimens by the application of internal pressure. This condition was required to ensure that the fatigue tests were conducted under constant stress amplitude cycling.

From calculations based on the measurements of strain, it was found that the maximum elastic deformation in the radial direction of the SRET specimens induced by a circumferential stress equal to 95% σ_{ys} was as follows:

5 ± 2 μm for specimens of steel S31603,

6 ± 2 μm on specimens of steel S30400 and

15 ± 2 μm on specimens of steel S31803.

These radial deformations of the specimens did not represent a risk of contact between the specimen surface and the tip of the Pt probe during SRET measurements as the separation between them during the CF-SRET tests was 100 μm.

An important aspect of the elastic deformation of the specimens during the CF-SRET tests is in terms of the disturbance of the SRET signal level due to the variation in the probe-to-specimen separation.

The elastic deformation in the radial direction of the specimens due to the cyclic loading will induce a minimum variation on the SRET output signal. From the calibration tests it was found that:

a) In seawater

- A variation of ± 1.2 % in the E_{MAX} for measurements on specimens of steel S31603.
- A variation of ± 1.9 % in the E_{MAX} for measurements on specimens of steel S30400.
- A variation of ± 3.8 % in the E_{MAX} for measurements on specimens of steel S31803.

b) in 0.05 M. $FeCl_3$.

- A variation of ± 1.7 % in the E_{MAX} for measurements on specimens of steel S31603.
- A variation of ± 2.7 % in the E_{MAX} for measurements on specimens of steel S30400.
- A variation of ± 5.4 % in the E_{MAX} for measurements on specimens of steel S31803.

It was assumed that the rotation of the specimens during the CF-SRET measurements did not modify the state of stresses generated by the application of the internal pressure.

5.4 Electrochemical Tests

The pitting corrosion resistance and electrochemical behaviour of the stainless steels UNS S31603, S30400 and S31803 in chloride containing solutions has been extensively studied and reported [2,3,6-8,12,15,29-35,40-46,59]. Additionally the superiority of duplex SS in terms of localised corrosion resistance and mechanical properties when compared with the austenitic grades is well known [15-18].

The electrochemical tests conducted in the present work were carried out in order to determine the pitting potential of the steels S31603, S30400 and S31803 in artificial seawater under specific conditions in terms of concentration, pH and temperature of the electrolyte and metal surface condition.

The values of the E_p determined for the three SS's were used as a reference point for the SRET tests, for which measurements were performed at potential levels above, at and below the pitting potential.

It is known that studies of pitting corrosion behaviour of stainless steels by electrochemical methods are mainly influenced by the following factors:

i) Incubation time of pit nucleation

ii) Aggressive ion concentration and temperature of the environment

iii) Passive film properties on the stainless steels, e.g. alloying components

iv) Manufacturing and microstructure, and

v) in many cases by crevice corrosion attack developed during the measurement.

The conventional technique of polarisation curve measurements for pitting corrosion determination was used in the present work with a low scan rate (10 mV/min). However it has been suggested that this method is not appropriate for pitting potential determination of stainless steels, mostly due to the effects of crevice corrosion attack during potentiostatic or potentiodynamic polarisation [150]. In the present work the surface area of the specimens subjected to potentiodynamic polarisation was limited by the application of a coating, which showed good performance during pitting potential determinations. When the coating was removed from the specimen after the tests no signs of crevice attack were observed.

The range of pitting potential values obtained for repeat tests conducted using the 3 different stainless steels was not greater than 70 mV. It was assumed that the values of pitting potential obtained in the present investigation were not affected by crevice events taking place simultaneously with pitting attack during the polarisation curves measurements.

As was expected, the experimental results of the electrochemical tests showed that the steel S31803 posses the highest pitting potential of the three stainless steels and the steel S30400 the lowest in artificial seawater at 26 °C and pH 8.2 as shown in figures 4.7 to 4.9. The steel S31603 in artificial seawater showed superior electrochemical behaviour than that of the S30400.

This result was also expected, as it is known that the steel S3160 posses an improved resistance to general and localised corrosion when compared to its S30400 counterpart. The E_{corr} of the steel S31603 was found to be from -220 to -240 mV vs SCE, being more positive than the E_{corr} for the steel S30400. The current density in the passive condition for the steel S31603 was between 0.01 to 0.03 $\mu A/cm^2$ which represents a corrosion rate of $1.14x10^{-4}$ to $3.4x10^{-4}$ mm/year. The pitting potential, E_P for the steel S31603 in artificial seawater was found to be between 350 to 380 mV Vs SCE.

Using a scan rate of 10 mV/min Saricimen [151], reported a E_{corr} = -190 mV and a E_p = 348 mV Vs SCE for steel S31603 in deoxygenated 5 % NaCl solution at 25 °C. The pitting potential obtained in the present study for the 316L SS is more positive than that reported by Saricimen mainly for two reasons: a) the lower concentration of the electrolyte used in the present experiments; and b) the surface condition of the specimens which was 1 μm surface finish. Smialowska [152] on the other hand reported values of pitting potential around 300 mV vs SCE for 316L SS in 30 g/l NaCl solution at 25°C.

Specimens of steel S30400 were left immersed in artificial seawater at open circuit potential after the application of cathodic polarisation, after two hours the corrosion potential reached a stable value of –210 mV vs SCE.

For longer periods of immersion (15 days) the E_{corr} of the steel S30400 in artificial sweater stabilised at a value around –130 mV vs SCE. When the specimens of this steel were subjected to anodic potentiodynamic polarisation it was observed showed an active dissolution region (ΔE = 60 mV) before a passive region was observed.

The passive condition of the steel S30400 was found over the potential range from 0 to 340 mV Vs SCE.

At this potential range (ΔE = 340 mV), the passive current density value was found to be between 0.3 to 0.4 $\mu A/cm^2$ which represents, for the case of uniform corrosion, a dissolution rate of $3.4x10^{-3}$ mm/year.

The breakdown of passivity of steel S30400 occurs at a pitting potential E_P, which was found to be in the range of 300 to 360 mV vs SCE. These values are in good agreement with those obtained by Sedriks [15] who reported a E_P value of 290 mV Vs SCE for this steel in 3.5 % NaCl, at 24 °C.

The polarisation curve representing the electrochemical behaviour of the steel S31803 (Duplex) SS in artificial seawater, fig. 4.9 indicates that under the experimental conditions used in the present work this steel will pit at potential levels higher than 1000 mV vs SCE. Capobianco et al [153] have reported similar values of pitting potential (1.1 V vs SCE) for the S31803 steel at temperatures below 30°C. The same authors indicated that for the same range of temperatures the absence of the hysteresis loop allows a fast and effective repassivation of pits nucleated in the alloy surface. In the present work, when samples of steel S31803 were immersed in the electrolyte at open circuit potential for periods of 36 hours the measured E_{corr} was between -280 to -310 mV vs SCE being more active than both Austenitic steels the S30400 and S31603. The anodic current density of the steel S31803 in the passive state was around 0.01 $\mu A/cm^2$. During the anodic polarisation the passive condition of the Duplex SS was maintained over a large potential range, (ΔE = 940 mV) which was approximately from 40 to 1060 mV vs SCE, i.e., the (E_p) of this steel.

This result clearly shows that it is necessary to induce high anodic potentials in order to promote pitting corrosion in the S31803 (Duplex) SS in artificial seawater.

The corrosion pits generated on specimens of S31803 steel at the end of the potentiodynamic polarisation nucleated at the α–γ boundary. Pits propagated preferentially within the ferrite phase with no localised dissolution of the austenite as shown in figure 5.1.

The high pitting potential of the steel S31803 steel in artificial seawater as found in the present investigation made the electrochemical generation of pits on this steel very difficult when using the same method applied to promote pitting on steels S30400 and S31603. The high anodic potentials required to nucleate pits on specimens of S31803 steel induced oxygen evolution on the surface and the development of crevices at the metal-coating boundary. In most cases the presence of crevices with high activity hindered the propagation of the nucleated pits. After polarisation at 1300 mV vs SCE for 30 seconds small and shallow pits were observed in the surface of the specimens which repassivated when the potential was stepped down to 950 mV vs SCE. At this potential level the localised activity of crevices was maintained instead of the active growth of pits.

5.5 Electrochemical generation of pits.

As stated in chapter section 3.6 the objective of this part of the present study was to establish an electrochemical procedure for growing pits in stainless steels to a controlled depth. The assessment of the active pit growth was conducted by using both, the DC and SRET measurements.

The growth of pits has received less attention than their initiation, but it has been studied sporadically for many years. The kinetics of pit growth are generally measured by electrochemical or metallographic methods. However, a combination of the two methods is usually preferred. A wide variety of pit growth laws has been reported for different metal-electrolyte systems, but the theory of pit growth remains unclear [154,155].

Although the steels S31603 and S30400 are very widely used alloys, they have not been amenable to reproducible pit growth measurements in neutral NaCl solutions at open circuit potential. This is essentially because of the tendency for spontaneous repassivation of the pits when the steels are at open circuit potential [127].

This is the reason for the kinetic studies of potentiostatic controlled pit growth in diverse metal-electrolyte systems.

The pit growth laws reported in the present work, equations 4.4 and 4.5, do not represent the pitting behaviour of the steels S30400 and S31603 in artificial seawater at open circuit potential. They give the relationship of pit depth as a function of time for pits growing under severe (but controlled) potentiostatic conditions. It has been reported that the rate of pit growth is characterised by a gradual increase in current at constant potential, which is proportional to t^2 or t^3 [156].

For experiments at constant applied anodic potential, the pit growth in terms of the pit radius as a function of time of polarisation has been described for a power equation of the form: $r = \kappa t^b$ where κ and b are experimentally derived empirical constants [157].

Zhou et al. [147] generated pits on 12 Cr martensitic stainless steel in 0.1 M NaCl solution by applying the same electrochemical procedure used in the present study.

From linear regression analysis, these authors reported a pit growth law that can be expressed by: $a = 48t^{0.53}$, where a is the maximum pit depth in μm and t is the time in minutes.

In figure 5.2 the results of pit growth as a function of polarisation time obtained in the present work are plotted along with the results reported by Zhou.

In the present study the pits were generated at a high anodic potential (120 mV above the E_p) and the pit growth was conducted at a lower potential (60 to 70 mV below the E_p) immediately after the nucleation. The generated pits grew at a potential at which the induction time for the nucleation of a secondary (stable) pit was greater than the required duration of the whole experiment. However in some experiments a secondary pit was induced very close to the first pit generated. When secondary pits were initiated, they momentarily had a separate existence but then coalesced rapidly with the main pit, figure 4. 17. It was observed that the pit generated first was the dominating pit and its depth (P_d) was very similar to that for single pits generated after the same period of anodic polarisation.

During the potentiostatically controlled pit growth it was observed with the aid of an optical microscope that in most of the cases only one pit grew actively. In some of the experiments however two or three pits maximum were detected growing actively.
The measurement of the depth and width of the pits by material removal focused on the deepest pit in each one of the three or four tests carried out for the same period of anodic polarisation. It was observed that in general the deepest pit generated on the specimens subjected to the same time of anodic polarisation had approximately the same P_d with a variation of ± 5 %. As shown in figures 4.10 and 4.11, the size of the pits generated increased with the time of polarisation.

The shape of the pit mouth generated in both steels was approximately elliptical and the shape of the pits was semi-elliptical with an average width twice that of the pit depth as shown by the pit profiles in figures 4.12 and 4.13. For pits generated under hydrodynamic flowing conditions imposed by the rotation of the specimen during simultaneous SRET measurements it was found that the pit shape was also semi-elliptical. However, these pits presented a slightly greater aspect ratio than pits generated on non-rotating specimens as shown in table 9. A greater pit aspect ratio indicates that the pits generated under hydrodynamic conditions are less deep.

The chronoamperometries recorded for the different periods of anodic polarisation on stationary (non-rotating) specimens, figures 4.18 to 4.20 showed that the pit growth kinetics are essentially parabolic but are distorted by random and sudden variations in current. For polarisation periods greater than 12 minutes the perturbations in current were more evident. These may be associated to the nucleation of secondary pits, which in most cases did not reach a stable growth stage and repassivated after nucleation. It has been suggested [158] that metastable pit growth is initially established by the presence of a pit cover which helps to maintain the aggressive local chemistry within the pit. This cover will eventually collapse and a pit must survive this experience in order to become stable.

The chronoamperometries for pits induced on rotating specimens of the two austenitic SS's, showed a lower increase of electric current with the time of polarisation when compared with the results obtained from pit generation on "non-rotating" specimens as shown in figures 5.3(a) and (b).

It has been observed that pitting generally occurs more readily in stagnant conditions than in flowing electrolytes [27].

A number of workers have investigated flow parameters, not only with a view to understanding their effects on the pitting process but also to simulate plant conditions. Beck and Chan [62] have described a series of tests in flowing sodium chloride solutions for 304 SS and iron. Their main conclusions were related to the existence of a critical flow velocity, inversely proportional to the pit radius, above which convection determines the current density. Their tests involving the removal of the salt film covering the pits on specimens of steel S30400 resulted in repassivation at the ohmic-limited current density at the critical velocity. The rotation of cylindrical specimens of the same SS in 3.5 % NaCl solution revealed no effect of rotation on the pitting potential.

The data demonstrated the importance of local solution composition variations, both in the pit initiation and propagation stages.
Any disturbances that reduce or destroy local composition reduce the severity of the pitting attack.

In the present study it was found that under rotating conditions the nucleation of pits on specimens of both stainless steels took more time when compared with the pre-pitting tests on non-rotating specimens. The rotating specimens had to be subjected to anodic polarisation at 500 mV vs SCE for 40 to 50 seconds (10 to 20 seconds more than for non-rotating specimens) in order to nucleate pits that did not repassivate when the potential was decreased. Once the pits were nucleated they actively grew with polarisation time, which is supported by the SRET results that indicate an increase of pit current density with time. During the generation of pits on rotating specimens it was observed that only one pit was nucleated.

The surface area of the pits generated in the two austenitic steels increased as a function of polarisation time, as indicated by calculations based on the data of the pit profiles and pit growth law. The pit current density was calculated by using the values of the DC current at different times of polarisation and the surface area of the pits. It can be seen from figure 4.23(b) that the current density decreased noticeably for polarisation times from 6 to 20 minutes. After this period the current density decreased asymptotically with time attaining values in the range of 80 mA/cm^2 in the case of steel S31603 and 70 mA/cm^2 for specimens of steel S30400. The pit current density for pits generated in specimens of steel S31603 is higher than that for pits in specimens of steel S30400. This is because the surface area of the pits generated in the steel S31603 were smaller compared to the pits generated on specimens of steel S30400 after the same time of polarisation.

5.6 Current density calibration of SRET system

The calibration experiments in artificial seawater indicate that the relationship between the current density emanating from the MDCS specimen and the output signal is linear over the range of applied currents, figure 4.24. This means that the equipment responds directly to localised variations in ohmic potential gradients within the solution. Linear regression analysis of the data gave the equation that best describes this relation, which was found to be

$$V_{OS} = -0.0195 + 0.0087i.$$

in which V_{OS} is the SRET output signal (in mV), and i is the current density (in mA/cm^2) emanating from the MDCS specimen.

From this equation a calibration factor of 115 mA/cm^2 per millivolt was obtained. Trethewey [13, 131,132] and Isaacs [126] have previously shown a linear relationship between SRET output signal across a PIS specimen and the applied current.

It should be noted that the trendline in figure 4.24 does not pass through the origin, it intercepts the axis of current density at a value that in theory represents the minimum detectable signal (MDS) of the equipment. For this particular electrochemical system the intercept of the trendline was at a value of 2.24 mA/cm^2. This point corresponds to an applied current of 0.73 μA, however the smallest signal distinguishable from the map scans presented in figures 4.26 to 4.34 is for an applied current of 2.1 μA which corresponds to a current density of 6.4 mA/cm^2. The real MDS for the present electrochemical system was almost 3 times bigger that the predicted from the calibration analysis.

Much smaller MDS of the order of 10^{-4} mA/cm^2 have been reported by Sargeant et al. [159] which were achieved using the same "rotating electrode" model of the SRET as used in this study. Their results are based on the use of very diluted electrolytes and a small probe - sample separation (20 μm), compared to 100 μm used in the present study. Trethewey et al. [131] reported MDS of approximately 4 mA/cm^2 for calibrations in natural seawater. The same authors experimentally demonstrated that the sensitivity of the SRET equipment is significantly improved in diluted electrolytes, which have lower conductivity. This effect is theoretically predicted by equation 2.4, which establishes that the maximum output signal is inversely proportional to the electrolyte conductivity.

From figure 4.25 it can be seen that if the probe-to-MDCS separation is decreased form 100 to 20 μm the output signal increases 24.3 % in artificial seawater.

Data reported by Trethewey et al. [131], presented in figure 5.4 for the change in output signal as a function of the conductivity indicates that a decrease in the conductivity of NaCl solution from 80 to 1.8 mS/cm increases the output signal approximately 50 times. If these results are applied to the data obtained from the calibration tests carried out in the present study, in theory the MDS for calibrations in artificial seawater with conductivity κ= 1.8 mS/cm using a probe-to-MDCS specimen separation of 20 μm, should be 0.413 mA/cm^2.

The SRET line scans presented instability of the baseline at low signal values, from which it is difficult to categorically establish the values of MDS for the experimental conditions used in this study. Also, the base line showed an unexpected increase after the peak of maximum output signal in some of the maps, indicating the presence of a cathodic area immediately next to the anodic point source. Physically this phenomenon was not possible, as the gold MDCS specimen does not have any conducting material adjacent to it on which a cathodic reaction could take place.

This phenomenon of signal shadowing has been explained by Badger [160, 161] for the case of the planar version of the SRET as to be a consequence of the low time constant of the RC filter used for the AC coupling which also reduces the signal magnitude. It must be emphasised the fact that the commercial SRET equipment used in the present work uses twin pseudo reference platinum probes. The detection method involves faradic charging of the Pt relative to Pt reference. In the absence of a stable redox couple e.g. Fe^{2+}/Fe^{3+}, this can occur ratter slowly. The discharging process of the Pt pseudo electrode produces the shadow. To avoid this effect one could use Ag/AgCl probes, which are true reference electrodes.

Control of probe to specimen distance is a critical aspect as the signal level falls off drastically with a linear tendency from 50 to 250 μm of distance between sample and SRET probe as indicated by the calibration shown in figure 4.25.

In that range of probe-to-MDCS distance, increments of separation in 50 μm steps induces the maximum output signal to decrease in 12% for each step. During the SRET and CF-SRET tests carried out here the distance between the Pt probe and the specimen was keep constant although the rotation of the specimen involved a minor eccentric movement up to 25 μm, which could induce variations up to 6% in the signal. Careful experimental conditions for the CF SRET tests were therefore necessary to achieve accurate results.

The conductivity of the artificial seawater (39 g/l sea salt) at 26 °C was 80.1 mS/cm as reported in table 8. When this value was substituted into equation 2.4 ($E_{MAX} = i / 2\pi\kappa z$) which applies for a true point source, the theoretical maximum output signal resulted to be $E_{MAX} = 198i$ at a height of z = 100 μm.

The relationship obtained experimentally using the MDCS establishes a $E_{MAX} = 26.6i$ which is 7.5 times smaller that the theoretical value.

On the other hand, equation 2.5 (WHM = 3.46z) indicates that, at z = 100 μm, the WHM = 346 μm. The experimental value of the WHM determined from the lines scans in figures 4.26 to 4.34 is however 1.1 mm, which is three times greater than the theoretical value. The possible reasons for this discrepancy can be associated with the electrochemical characteristics of the calibration cell including the gold MDCS specimen.

The theoretical formulation of the equations that determine the electrostatic potential E(x,y,z) at any point in the electrolyte assume that:

(*i*) there are not concentration gradients in solution, (*ii*) the solution is electroneutral, (*iii*) there are not sources or sinks of ions in the electrolyte. The equations relating the local current with the electrostatic potential require the potential to satisfy the boundary conditions of no current flow across the planes at the centre and at the edge of the surface local cell [162]. Experimentally it is difficult to meet these requirements as ionic concentration gradients occur during the polarisation of the MDCS specimen. It was also observed that at the end of the calibration tests up to 1.63×10^{-2} mm^3 of gold were dissolved in both electrolytes. This had the effect of changing the geometry of the planar MDCS to a cavity shaped anodic source, which could contribute to peak broadening.

The rotation of the PIS specimen and the presence of the scanning Pt microprobe, may also affect the peak shape.

The experimental value of WHM obtained at a z = 100 μm is much greater than the diameter (200 μm) of the gold MDCS such that the MDCS surface area size is unlikely to contribute noticeably to the experimental WHM value. Despite this difference on size the MDCS can not be considered as a point current source.

For the calibration tests in 0.05M $FeCl_3$ the relationship of the output signal - applied current was linear, as indicated in figure 4.35. Regression analysis of the data gave the following equation:

$$V_{OS} = -0.0113 + 0.0142i$$

The slope of this relation was found to be 43.2 V/A, which indicates an experimental value for the maximum output signal at height z = 100 μm of $E_{MAX} = 43.42i$.

On the other hand, the theoretical value of E_{MAX} obtained by substituting the conductivity of the 0.05 M $FeCl_3$ solution at 26°C (16.5 mS/cm) and the value of z (100 μm) in equation 2.4 is E_{MAX} = 965i. The calibration factor for the system in this electrolyte was found to be of 70 mA/cm^2 per millivolt. This value was used to quantitatively assess the localised activity during the SRET and CF-SRET tests performed in this solution.

The line that describes the relationship between the output signal and the applied current, (figure 4.35) touches the X-axis at 0.807 mA/cm^2. However the MDS detected during the calibration tests as shown in figure 4.37 was for an applied current of 2.0 μA which in terms of current density is 6.12 mA/cm^2.

The calibration tests to determine the relation between the detected signal level and the specimen-to-probe distance indicated that for distances up to 350 μm, the relationship was linear. In this region, an increment of 50 μm in the specimen-to-probe separation resulted in a reduction of 17 % in the maximum output signal.

The results reported by Trethewey [131], indicate that a decrease in the conductivity of $FeCl_3$ solution from 16.5 to 1.5 mS/cm, increases the output signal 6.25 times. From the results of the calibration tests in 0.05 M $FeCl_3$ carried out in the present study it can be observed that the maximum output signal increases 24.8 % when the probe-to-PIS separation decreases from 100 to 20 μm.

Using the factors for the variation of output signal as a function of electrolyte conductivity and probe-to-PIS separation, in theory the MDS obtained from calibrations in $FeCl_3$ with conductivity κ= 1.5 mS/cm and probe-to-PIS separation of 20 μm the MDS should be 0.149 mA/cm^2.

The WHM determined from the line scans in figure 4.37 is 1.2 mm which, is also 3 times greater than the value predicted by equation 2.5 as in the case of the calibration in artificial seawater. The reason for this discrepancy is associated to the point discussed previously for the calibration in artificial seawater. The values reported for the WHM obtained from the calibration tests in both electrolytes considered the fact that the baseline was not at zero.

5.7 SRET measurements.

As stated before from the results of the electrochemical tests, the three grades of stainless steel presented high resistance to pitting corrosion in artificial seawater at free corrosion potential. The possible events of pit nucleation and metastable pit growth at open circuit potential could not be detected by the SRET measurements. It is known that nucleation of pits in stainless steels is a very fast process and involves current transients of the order of nA [45]. The spatial resolution and the MDS of the equipment are contributory factors which limit the detection of pitting activity. This means that the equipment can only detect the presence of active pits having a current density higher than 6.4 mA/cm^2. Under this condition, a pit that emanates a current of 1.0 μA involves a pit area of $1.56x10^{-3}$ cm^2, which corresponds a pit diameter of 446 μm.

When the specimens were polarised to levels above their pitting potential, highly localised activity was induced in the form of pits and sometimes crevices. The high current densities generated at these sites could be detected clearly by SRET measurements.

For the experimental conditions used in this study, the SRET equipment is not sufficiently sensitive to detect sites undergoing localised corrosion, i.e., pits and crevices on SS's in artificial seawater at open circuit potential. Trethewey el al. [13] have reported data of the activity of corrosion pits in 304 SS obtained by using the rotating version of the SRET instrument. In order to follow the active history of pits i.e. nucleation, growth and repassivation, these authors had to induce localised dissolution by applying anodic polarisation to the specimens, although they did not report the anodic potential applied.

The results obtained in the present study corroborate the limitations of the commercial equipment as shown in figure 4.38(a), which is an example of an area map scan performed on specimens at free corrosion potential E_{corr}, which does not show any detected localised corrosion on the surface. For SRET measurements on specimens under anodic polarisation at 350 mV (vs SCE) as shown in figure 4.38(b) localised attack could be clearly seen in the area maps. The sites with highly localised activity produced a very high output signal which correspond with high current densities, in all cases higher than 6.4 mA/cm^2. It has been reported that the sensitivity of the SRET equipment is considerably enhanced when is used in diluted electrolytes when a current is driven through a PIS specimen during calibration tests [131]. This apparent advantage does not apply for real systems were concentrated electrolytes are present, as the case of structural steels in natural seawater. In the present case a dilution of the artificial seawater made the nucleation of corrosion pits even more difficult in the stainless steels under study.

SRET measurements during the generation of pits.

Important information was obtained from SRET measurements during the electrochemical generation of pits in artificial seawater.

The SRET map scans performed on specimens of steel S31603 and S30400 presented in figures 4.44 and 4.45 respectively show the tendency of increasing pit current density with time of polarisation. Pit current densities greater than 700 mA/cm^2 were measured for polarisation times of 54 and 60 minutes as shown in figure 4.46. Measurements of the depth and diameter of the generated pits indicated that effectively the pits grew with the time of polarisation. SRET measurements gave the instantaneous current density emanating from a pit after a specific period of polarisation, however neither the pit current density or the pit size was constant during the time of polarisation, as both increased with time. Thus the best way to assess the amount of dissolved metal from SRET measurements requires the integration of the area of pit current density-time for a specific period of anodic polarisation. The calculation of pit depth from the measured current density by SRET for a polarisation period of 6 minutes in steel S30400 gives a value of 70 μm, which is in good agreement with the 110 μm of the real pit depth measured.

Strehblow [163] has reported extremely high dissolution current densities of several tens of mA/cm^2 up to more than 100 mA/cm^2 which were deduced from the growth of the corrosion pits using Faraday's law taking into account the size and form of the pits. Rosenfield et al. [44] reported anodic current densities in the solution over a pit of the order of 170 mA/cm^2 for 304 SS in chloride containing solution at free corrosion potential by using a scanning reference electrode technique. The same authors indicated that the current flowing from the active centres increased with time according to a parabolic law, which indicated the slowing down of the process.

Thus, if the behaviour of the current density emanating form a pit as a function of time is known from consecutive SRET measurements, it is possible to calculate the approximated pit depth by assuming a specific pit shape. The calculation is indirect and uses Faraday's law along with a pit mouth diameter from data of the pit profile Vs polarisation time. It is important to note that even if it is possible to relate the electrochemical activity of pits from SRET measurements with volume of metal removed, there seems to be no direct relationship between the information of area or line scans and pit size or geometry.

For the conditions used to generate the corrosion pits it was expected that active pits would be observed when the anodic polarisation was stopped. This was not the case and the induced pits repassivate almost immediately when the anodic polarisation ceased. This could be observed from SRET map and line scans, which did not detect any localised activity from the sites that were undergoing localised attack prior to open circuit condition.

SRET-CF tests in artificial seawater.

It seems that the SRET instrument was not sufficiently sensitive to directly detect short-lived events like pit nucleation and pit-to-short crack transition during the CF tests in artificial seawater at open circuit potential. The initiation of localised corrosion, i.e. pitting in SS's is favoured by the action of constant or cyclic stress. It has been reported that the application of stress on austenitic SS immersed in chloride containing solutions shifted the pitting potential to values 100 to 200 mV more negative [164]. In this study it was expected to detect from SRET measurements the electrochemical activity associated to the nucleation of localised attack enhanced by the applied cyclic stress.

However it is very probable that once initiated, corrosion pits repassivated before attaining the minimum localised electrochemical activity detectable for the SRET instrument. Consequently repassivated pits did not reach the minimum size to act as a crack initiators under the stress state imposed during the CF tests. The effect of the cyclic stress on the electrochemical behaviour of the steel S31603 was demonstrated from the results of potentiodynamic polarisation at different number of cycles as shown in figure 4.47. The pitting potential of the steel after 308700 cycles decreased from 320 to nearly 100 mV vs SCE indicating a higher susceptibility of this steel to suffer pitting corrosion. A greater stress level could induce a constant active condition of the corrosion pits by overcoming the transition of metastable-to-stable pit growth, which could be detected by SRET measurements. In order to attain this condition the stress should induce localised current densities greater than the experimental MDS of the equipment.

The potentiostatic polarisations performed on specimens of 316L SS under CF conditions, (figure 4.48), show that localised corrosion was induced in specimens, however the pits or crevices nucleated did not reach the condition of stable growth. SRET map and line scans conducted on the specimens after potentiostatic polarisation did not detect localised activity. It is possible that the current density emanating from the sites undergoing localised attack was lower than the MDS of the instrument. Qian et al. [112] for example, have indicated that small groups of crystallographic pits formed and coalesced creating small cracks in Austenitic SS in sodium chloride solution at open circuit potential. The same author stated that plastic deformation apparently accelerated pit initiation within the slip bands at stress levels higher than the yield stress but no information was given about the electrochemical activity of the corrosion pits involved.

Photographs 1, 2 in figure 4.49 show some flaw-like cracks in the surface of the specimen of steel S31603. These flaws were observed after the application of anodic potentials during the CF test in artificial seawater. Photos 3 and 4 show evidence of the presence of corrosion pits. Higher magnification shows that these are micro-pits, less than 5 μm in diameter. A similar pattern was observed for specimens of steel S30400 when subjected to analogous CF conditions as shown in figure 4.51. It is therefore considered that the flaws were initiated by localised corrosion promoted by the anodic polarisation applied. Corrosion pits are formed and coalesce in a direction perpendicular to the induced circumferential stress. The trend followed by the flaws in the two austenitic stainless steels coincided with the distribution of the δ ferrite phase in these steels as shown if figures 5.5a and 5.5b.

It has been reported that in austenitic stainless steels with a duplex structure, corrosion pits initiate almost exclusively at the ferrite/austenite (δ/γ) interfaces and propagate preferentially in the ferrite phase [165,166]. This was the behaviour observed in the present work when anodic polarisation was applied to specimens of the two Austenitic SS's subjected to CF conditions. This kind of attack was not observed during the pre-pitting tests on samples free from stress. Cyclic stress seems to promote preferential attack at the (δ/γ) boundary on specimens subjected to anodic polarisation.

On the other hand, when CF tests were conducted on a specimen of steel S31603 in artificial seawater at free corrosion potential with a circumferential stress of 260 MPa ($\sigma_{MAX} = 1.1\sigma_{ys}$), a crack developed and produced failure after just 48000 cycles. At that stress level the failure of the specimen took place after much fewer stress cycles than expected. Qian et al. [112] reported a maximum stress for failure of 316L SS in 0.5 M NaCl at 10^7 cycles of 250 MPa. Sedriks [15] reported values of 260 MPa also for 316L SS in 3% NaCl solution.

The SEM images in figure 4.50 of the crack that produced the failure of the specimen of steel S31603 show that the crack grew following pits possibly originated along a non-metallic inclusion. It is important to note that the same images do not show evidence of localised attack in the form found in specimens subjected to anodic polarisation. SRET measurements carried out at different periods during the CF tests did not detect localised activity that could be associated with the nucleation or propagation of the crack. From the results of the present study it is suggested that the localised events taking part in the nucleation of corrosion fatigue cracks involve very low current densities; at least too low to be detected by the SRET instrument used here.

Magnin et al. [167] proposed a method to detect corrosion fatigue crack initiation from measurements of current density as a function of cyclic plastic strain of specimens under potentiostatic control. These authors did not consider the effect of corrosion pits as they measured the global current emanating from a large area (1.5 cm^2) but the local dissolution of microcracks which, favours grain boundary crossing and the microcoalescence of the cracks.

Very little data about localised attack was provided by SRET tests on specimens of Duplex SS in artificial seawater. This material showed a very high resistance to localised corrosion in this media and the analysis of possible events related to the nucleation of sites undergoing localised corrosion was not possible from SRET measurements. By applying a high anodic potential to specimens of steel S31803 in artificial seawater, severe crevice attack was induced, but the nucleated crevices did not sustain an active condition when the anodic polarisation was stopped. The sites undergoing crevice attack repassivated and the localised activity ceased completely or at least to a level below the MDS of the instrument.

SRET measurements in 0.05 M $FeCl_3$ solution.

In order to attain the objective of measuring the electrochemical activity during the pit-to-short crack transition by using the SRET instrument, CF tests were carried out in ferric chloride solution with a pH = 2 ± 0.1 which induced severe localised attack on the two austenitic stainless steels at free corrosion potential.

SRET measurements carried out on a solid bar specimens of the two austenitic SS's in 0.05 M $FeCl_3$ solution showed intense localised activity at free corrosion potential. The pit growth law on the 304 and 316L steels in this electrolyte was not determined but the activity of corrosion pits in both SS's in terms of current density was followed through SRET measurements. The SRET maps exhibited a large degree of baseline instability and the presence of an apparent cathodic site next to the main anodic area. This made the quantitative assessment of the localised current density difficult. However as a first approximation, the values of current density (obtained by using the calibration factor) were considered from the maximum output signal detected and used to characterise the pit activity.

Several intense local anodes developed almost immediately following contact with the ferric chloride solution. Thus it was possible to assess semi-quantitatively by SRET measurements the activity of these localised anodes (pits) as a function of time when they attained a stable growth stage. The pits formed on samples of the two austenitic stainless steels had a semi-elliptical shape. The local anodes are indicated by areas of high negative SRET output signals, which are visualised as dark blue or black regions in the map scans.

It was observed that small pits repassivated after nucleation and some others continued growing actively up the moment the specimen was removed from the electrolyte. Optical analysis of the surface of the specimens after the CF tests showed that the pits that presented the highest activity in the SRET map scans, had a maximum diameter in the range of 300 to 450 μm.

The change of activity with time of four pits formed in a specimen of steel S31603 is shown in figure 4.41. These results indicate that the metal dissolution in each pit takes place at different rate as a function of time. The pits were at positions separated more than 1.2 mm to each other, which made possible their clear detection and the subsequent assessment of their electrochemical activity. In this case no pits of comparable size/activity were found in between the four major sites undergoing localised attack, with the exception of a few small pits (20 μm diameter), which after nucleation became passive.

Similar results were found for pitting corrosion in specimens of steel S30400 as shown in figure 4.42. Although more pits near the single anode shown were observed in the surface of the specimens during the SRET tests, their electrochemical activity was not detected through SRET measurements, therefore it was not possible to monitor their lives in terms of nucleation, subsequent growth and repassivation. The possible reason for this minimal information obtained from the SRET measurements may in this case be due to the limited resolution of the instrument. The SRET presented limitations to detect localised events separated by less than 1.2 mm as indicated by the results of the calibration tests, which also indicated that pits emanating current densities lower than 6.2 mA/cm^2 could not be detected. This situation represents a serious limitation of this technique as localised dissolution can take place form pits emanating current densities lower that 6.2 mA/cm^2, which presence can not be detected from SRET measurements.

For this study it can be assumed that the localised activity detected by the SRET map and line scans correspond to the pits having the highest metal dissolution over the area tested. It is worth mentioning that the SRET method depends basically on the electrochemical activity associated with the sites undergoing localised attack, rather than their size.

Isaacs et al. [127] used a more concentrated $FeCl_3$ solution (0.4 M) to evaluate the pit propagation in 304 SS. They found through SRET measurements that the number of active pits decreased with time and that the activity of the remaining pits apparently increased. These authors did not report any quantitative analysis of the activity of the pits observed in terms of current density or potential.

As stated in chapter 3, for the case of specimens of steel S31803 the concentration of the $FeCl_3$ solution used was 0.1 M due to the preliminary results in a 0.05 M solution showed a high resistance of this Duplex SS to localised corrosion. However even in the more concentrated electrolyte the steel S31803 offered a high resistance to localised corrosion. When a more concentrated solution (0.4 M $FeCl_3$) was used for this material, intense crevice attack was produced at the metal-coating boundary which, extended for large regions and it was difficult to assess quantitatively by SRET measurements. This higher concentration of the ferric chloride solution could induce severe instability of the Pt microelectrodes, which resulted in very noisy output signal. The same behaviour was observed when specimens of Duplex SS were polarised in the 0.1 M solution. Even in these conditions the activity of the anodic sites ceased when the polarisation was stopped. A more sensitive instrument with better spatial resolution is required for the study of localised corrosion of steel S31803, which possess inherently a high resistance to localised corrosion.

CF-SRET tests in ferric chloride solution.

Because the development of corrosion fatigue damage in some components with a smooth surface includes (1) localised corrosion damage (pitting, crevice), (2) transition from a pit to fatigue crack growth (crack nucleation), (3) early stages of fatigue crack growth (short corrosion fatigue regime), and (4) long corrosion fatigue crack growth, a reliable prediction would largely depend upon the quantitative understanding, characterisation and modelling of these elemental processes of damage. This study is focused on the process of corrosion fatigue crack nucleation, which is considered as the transition from pitting to corrosion fatigue crack growth.

The results of SRET tests performed in the 0.05 M ferric chloride solution showed that specimens of steel S31603 under stress-free condition at open circuit potential exhibited localised activity upon initial immersion in the electrolyte. Before the application of cyclic stress, the sites undergoing localised attack were well defined as indicated by black and purple spots in the area maps of fig. 4.53a. When the cyclic stress was applied, the activity of several corrosion pits was monitored with time, an example is pit (**a**) in figure 4.53. It was also noted that the activity of some pits decreased after reaching a certain size (electrochemical condition), whereas other pits continued to grow and serve as nuclei for fatigue cracks. In the present case it can be assumed that only the most stable pits sustained an active propagation with the number of cycles, which made possible the evaluation of the behaviour of these pits through SRET measurements.

The measurement of the electrochemical activity of the most active pits, in terms of current density as a function of the number of cycles was the method used here to determine the pit-to-crack transition.

In the cases monitored here the active crack-nucleating pits showed a reduction in current density after a number of cycles at which stage cracks were observed at the pit mouth. The moment at which these two events are observed to take place almost simultaneously is suggested here as the pit-to-crack transition point. The reduction of local current density may be associated with the formation of bare crack surfaces, which modify the current distribution. At the instant of crack formation, the crack enclave may not have the same electrolyte concentration and pH as the initial pit, but as soon the same conditions are reached localised activity starts to increase. Models for crack chemistry development proposed by Turnbull [168], consider that before the breakdown of passivity the metal dissolution rate in the cavity is controlled by the passive current.

In the present case the passive state only lasts for a few seconds due to the aggressiveness of the electrolyte and active dissolution take places after the critical chemistry in the crack is re-established. That promoted active dissolution of the crack surfaces plus dissolution of the pit surface area, which did not repassivate after crack nucleation. This behaviour is based on the values and tendency (slope) of the local current density, which increases with the number of cycles (N) after the transition point. It is also possible that the net imbalance of the total anodic and cathodic currents in the crack resulted in a outflow of anodic current which is detected by SRET.

It is important to note that for the case of pits on specimens of steel S31603 the change of current density associated with the nucleation of cracks was in the range of 80 to 100 mA/cm^2. Similar behaviour was observed for pit-to-crack transitions on specimens of steel S30400 in the same electrolyte. Figure 4.57 shows the change of current density for two different pits in a specimen of steel S30400. Pit 2 developed cracks after 400 cycles with a decrease of current density of about 80 mA/cm^2.

Pit 1 did not develop cracks and continued growing until through-wall perforation of the specimen occurred after 2000 cycles, where the activity of both pits started to decrease due to oil leaking which covered the active surface and prevented contact with the electrolyte.

As mentioned previously, even though the size of the local anodes can not be determined directly from SRET measurements, the change in electrochemical activity of pits, as a function of number of cycles may be used to define the pit-to-crack transition.

A reduction in current was observed when a crack initiated from a pit. This observation was made for cracks initiating from pits having different electrochemical activity i.e., current density. The data of SRET for the current density of the active pits can be used to calculate the pit depth at the transition to a fatigue crack.

The pit depth P_d, at which the pit-to-crack transition occurs, can be obtained by the following equation proposed in the literature [169,170].

$$a = \left[\left(\frac{3MI_{PO}}{2\pi nF\rho}\right)\exp\left(-\frac{\Delta H}{RT}\right)t + a_0^3\right]^{\frac{1}{3}};\ a \le a_{tr} \qquad (5.1)$$

in which:

a = P_d, pit depth at pit-to-crack transition (cm)

M = atomic weight (55.845 g/mol, for Fe)

n = number of transferred electrons (2 formation of Fe^{2+})

ρ = density (8 g/cm^3 for SS)

ΔH = activation enthalpy (-342 J/mol)

F = Faraday's constant (96500 C/mol)

T = absolute temperature (299 K)

R = the universal gas constant (8.3143 J/mol-K

I_{OP} = pit current (A)

t = time for a pit to reach the size (sec)

a_0 = initial pit depth (0.0001 cm)

If the value of the pit current obtained from the SRET measurement associated with the pit-to-crack transition (figure 4.55) for 316L SS is used in the equation 5.1, the depth of pit (**a**) P_d at the moment of transition is found to be 200 μm.

The stress intensity factor range ΔK_1 has been used [95,147], to account for the role of pitting in defining threshold conditions for cracking using LEFM in the context of fatigue-limit based propagation, using equation 5.2.

$$\Delta K_{th} = \alpha \Delta \sigma_{th} \sqrt{\pi a} \qquad (5.2)$$

where a is the pit depth (P_d), $\Delta\sigma_{th}$ is the threshold fatigue strength, α is a geometric factor and a is the pit depth. For semi-circular surface cracks, α is approximated by 0.67 [122,147] and $\Delta\sigma_{th}$ = 220 MPa for 316L SS in Cl^- containing solution, pH 3 [15].

Using equation 5.2 and the pit depth (P_d at transition) obtained from equation 5.1, the threshold stress intensity factor range was found to be: ΔK_{th} = 3.69 MPa$\sqrt{m}$.

The range of localised current density (at the pit-to-crack transition) for 316L SS specimens was from 200 to 350 mA/cm^2. From these values of localised current and using equation 5.1 it is possible to establish a range of pit depths at which the pit-to-crack transition occurs during CF tests of 316L SS in 0.05 M $FeCl_3$ at a $\sigma_{MAX} = 0.77\sigma_{ys}$.

$P_{d,316L}$ at transition = 175 to 210 μm.

The values of threshold stress intensity factor range vary according to these pit depths for the pit-to-crack transition and were found to be: ΔK_{th} = 3.45 to 3.78 MPa$\sqrt{m}$.

The results from SRET measurements on 304 SS specimens under CF conditions in 0.05 M $FeCl_3$ at a stress range of 200 MPa ($\sigma_{MAX} = 0.81\sigma_{ys}$), indicated that the values of pit current density at the pit-to-crack transition were in the range of 180 to 250 mA/cm^2. The application of equation 5.1 to the values of current density stated above gave the following range of pit depths at the transition: $P_{d,304}$ at transition = 130 to 175 μm.

These pit depth values for the pit-to-crack transition are used in equation 5.2 to determine the threshold stress intensity factor range for the 304 SS.

The value of the $\Delta\sigma_{th}$ for 304 SS in Cl^- containing solution, pH 3 used for this calculation was 200 MPa, [15]. The results showed that the threshold stress intensity factor was: ΔK_{th} = 2.7 to 3.14 MPa√m.

From studies of the effect of pitting on the CF crack nucleation, Zhou et al. [147] reported values of 5.06 to 6.16 MPa√m for the threshold stress intensity factor range for cracks nucleated from pits of 110 μm depth in 12 Cr martensitic steel in 0.1 M NaCl solution. Acuña [172], reported a ΔK_{th} = 2.5 MPa√m for cracks nucleating at pits of 120 μm depth in 316L SS flat specimens subjected to bending CF conditions in natural seawater at free corrosion potential. Result from CF tests on open-hole specimens of 2024 T3 (bare) alloy in 0.5 M NaCl solution conducted by Chen et al. [173] showed that the ΔK_{th} was of the order of 2.23 to 3.63 MPa√m for pits with aspect ratio (c/a) of 0.12 and 0.33 respectively.

Calculation of pit growth has been conducted in the past by using indirect methods or probabilistic models, [169]. SRET measurements on the other hand can provide direct assessment of localised current densities emanating from pits.

This technique used during the early stages of damage by CF can also overcome the uncertainty of intrusive methods for assessing the pit-to-crack transition.

Murtaza [90] and Akid [171] defined the pit-to-crack transition as the point at which deviation from hemispherical pitting occurred to the point where no effect of corrosion on the crack was observed. For this assessment these authors used an acetate replication method. From an electrochemical point of view, for different metals the effects of removal of the specimen from the electrolyte can modify completely its corrosion fatigue behaviour and consequently its lifetime.

An example being SS's which have a high repassivation capacity in chloride containing solutions.

CHAPTER 6 – Conclusions

6.1 Electrochemical tests.

Polarisation tests carried out on specimens of UNS S30400, S31603 and S31803 in artificial seawater (39 g/l seasalts, pH 8.2, T = 26° C), showed that the duplex SS has the highest resistance to pitting corrosion as indicated by the value of its pitting potential, E_p = 1060 to 1110 mV Vs SCE.

The 304 SS showed the lowest resistance to pitting corrosion indicated by its pitting potential E_p = 300 to 360 mV Vs SCE.

6.2 Calibration tests with the SRET equipment.

Initial SRET experiments using a micro disk calibration source (MDCS) specimen as a localised current source in artificial seawater and 0.05 M $FeCl_3$ solution have shown that the equipment exhibits a linear response of measured potential to applied current at source. The minimum detectable signal in artificial seawater was 2.24 mA/cm^2, which is 4 orders of magnitude higher than the MDS reported by other workers in the literature. The MDS obtained in the 0.05 M $FeCl_3$ was 0.807 mA/cm^2. This discrepancy is due to experimental conditions such as probe to sample distance and solution conductivity. One significant limitation of the SRET equipment used in this study, is the difficulty in solving the current-potential distribution for local current sources of finite size.

The resolution of individual active sites is not better than 1 mm, with which it was difficult to detect localised attack events taking place at distances less than 1 mm between each other.

The SRET output signal showed a linear behaviour as a function of the probe-to-MDCS distance for separations up to 250 μm in artificial seawater and up to 350 μm in 0.05 M $FeCl_3$ solution. It has been indicated in the literature that using electrolytes with very low conductivity increases the SRET output signal. However for alloys with high resistance to general and localised corrosion as is the case of SS's in seawater, a dilution of the electrolyte will reduce its aggressiveness and localised attack will be more difficult.

6.3 Potentiostatic generation of pits.

A pit generation procedure has been established for austenitic stainless steels in artificial seawater with which pits can be generated to a controlled depth with limited density (1 to 2 pits). The generated pits have semi-elliptical shape with pit mouth width twice the pit depth. Pits generated under hydrodynamic conditions (rotating specimen), present smaller depths when compared with pits generated on static (non-rotating) specimens. For studies of fatigue crack initiation from corrosion pits, a higher stress concentration is induced from pits generated under stationary (non-rotating) conditions.

6.4 SRET measurements during the generation of pits.

The SRET was used in this work for the study of the localised dissolution process taking place during the potentiostatic generation of pits in 304 and 316L SS specimens.

Besides the capability of this technique to determine the position of the active pits, it is able to assess semi-quantitatively the dissolution rate in terms of localised current density. Calculations of the pit depth from the values of current density obtained from SRET agree well with the physical pit depth determined by material removal.

SRET measurements showed that under potentiostatic control, active pit growth on 316L and 304 SS stainless steel in artificial seawater takes place with an increase of localised current with time.

Pit current densities obtained from SRET measurements were found to be up to three orders of magnitude higher than those obtained from DC measurements. From this point of view, localised current densities obtained form SRET tests are more reliable than DC measurements to assess metal dissolution rate during localised attack.

6.5 CF-SRET measurements in artificial seawater.

SRET tests performed on specimens of the three SS's subjected to CF conditions at free corrosion potential did not show evidence of localised attack. It is possible that the localised activity promoted by the applied cyclic stress was lower than the MDS of the equipment and for that reason it was not detected. Only when the specimens were subjected to high anodic polarisation $E \geq E_p$, it was possible to detect localised activity from SRET measurements. This means that the SRET presents limitations to the study of localised corrosion of metals with high resistance to this kind of attack for which the localised activity generated is too low to be detected by the SRET.

Anodic polarisation applied to specimens of the two austenitic SS's during CF tests promoted localised attack in the δ-γ boundary as shown by SEM analysis.

6.6 CF-SRET measurements in 0.05 M $FeCl_3$.

Despite the inability to spatially resolve either the pit or crack size from SRET measurements in $FeCl_3$, the change detected in electrochemical activity can be related to the transition from localised metal dissolution to crack nucleation; which may involve a redistribution of current over the new crack surfaces.

The semi-quantitative assessment of pit-to-crack transition in terms of localised current density proposed in this study may be conservative, as the SRET method presents limitations. However, the use of more stable scanning electrodes, SRET calibration factors together with the measurement of pit depth in a set of parallel tests can give a more reliable assessment of the pit-to-crack transition in a semi-quantitative and non-intrusive basis.

Pit depths are often measured using mechanical probes or optical methods where a microscope is focused onto the bottom of the pit and the depth calculated from the position of the focusing knob. Clearly these methods are only applicable to pits where undercutting has not occurred. Furthermore; the method is time consuming and offers no assurance that the deepest pit has been selected. Additionally, it is often difficult to remove corrosion products from the pits and this can lead to errors in the pit depth measurements. Mechanical machining and optical observation of the exposed layers of the sample can give more reliable information on pit depth but is tedious.

By using the values of pit current density obtained from SRET measurements, a critical pit depth for the pit-to-crack transition was determined from which, the threshold stress intensity factor range was calculated for the 304 and 316L SS's subjected to CF conditions in 0.05 M $FeCl_3$ solution. The values were, for 316L SS: ΔK_{th} = 3.45 to 3.78 MPa$\sqrt{m}$, and for 304 SS ΔK_{th} = 2.7 to 3.14 MPa$\sqrt{m}$.

6.7 Suggestions for Future Work

- Calibration tests involving SRET measurement during pitting corrosion of stainless steel in seawater as function of the probe-to-sample distance in order to determine the best fit between the localised current density and the volume of metal dissolved.

- Conduct SRET measurements during the electrochemical generation of pits on specimens subjected simultaneously to cyclic stress and compare the pit growth law as a function of the applied stress obtained from SRET, and DC measurements and the material removal method.

- To perform CF-SRET tests using a metal-electrolyte system with high tendency to develop pitting corrosion from which localised electrochemical activity can be more easily assessed from SRET measurements. The results obtained may be used to corroborate the semi-quantitative approach used in the present work to determine the pit-to-crack transition from an electrochemical point of view.

- To perform CF tests in artificial seawater using the SVET technique, which in theory has greater sensitivity and spatial resolution than SRET.

- Determine a pit growth law for 304 and 316L SS's in $FeCl_3$ at open circuit potential and at a stress free condition and compare with the pit depth obtained from the material removal method.

- To conduct CF tests in $FeCl_3$ using hourglass specimens and assess, via acetate replication, the pit-to-crack transition pit depths at the same stress level of that applied to the SRET specimens and compare the results obtained.

- The use of a true reference electrode to avoid the problem of shadowing. For example the Ag/AgCl reference electrode

REFERENCES.

1. N. Acuña & G. Hernandez-Duque (1998); "Effect of exposure time on corrosion resistance of prepassivated UNS S31603 SS in the Gulf of Mexico.". CORROSION-NACE 98, paper No. 698.
2. O. Hagerup & O. Strandmyr (1998); " Field experience with stainless steel materials in seawater systems ". CORROSION-NACE 98, paper No. 707.
3. J.Olsson & M. Liljas; "60 Years of Duplex stainless steel applications". CORROSION-NACE94, paper No. 395.
4. K.G. Compton, (1970), Corrosion-NACE, Vol. 26, p.448
5. F.L.Laque, (1982), Materials Performance, Vol.21, April, p.13
6. F..Mansfeld, R. Tsai, H. Shih, B. Little, R. Ray & P. Wagner (1990); " Results of exposure of stainless steels and titanium to natural seawater " CORROSION-NACE 90, paper No. 190
7. B. Little, P.Wagner & F. Mansfeld (1990); "Electrochemical Behaviour of Stainless Steels in Natural Seawater ". CORROSION-NACE 90, paper No. 150
8. O.P. Gartland, (1991), "Aspects of testing stainless steels for seawater applications", Marine and Microbial Corrosion, (Stockholm, Sweden), p. 134
9. R. Akid; (1996) "The influence of environment upon the accumulation of damage under corrosion fatigue conditions ". Fatigue Fract. Engng. Mater. Struct. Vol. 19, No.-3, p. 277.
10. K. Kim & W.H. Hartt; (1995) "Response of short cracks in high-strength steels to fatigue loading --Part I: Behaviour in air and freely corroding in seawater". Journal of Offshore Mechanics and Artic Engineering, Vol. 117, pp. 183.
11. A. Boukerrou & R.A. Cottis; (1993) "Crack initiation in the corrosion fatigue of structural steel in salt solution", Corrosion Science, Vol.35, No. 1-4, p. 577.
12. D.E. Williams, C. Westcott & M. Fleischmann; (1985) "Stochastic models of pitting corrosion of stainless steels ". Journal of Electrochemical Society, Vol. 132, No.8, p 1796.
13. K.R. Trethewey, D.A. Sargeant, D. Marsh & A. Tamimi; (1993) "Application of the Scanning Reference Electrode Technique to localised corrosion", Corrosion Science, Vol.35, Nos. 1-4, p.127.
14. Hronsky,C.W., Duquette, D.J. (1982); Corrosion-NACE, Vol. 38, p. 63 .

15. A.J. Sedriks, (1996), "Corrosion of Stainless Steels", second edition, John Wiley & Sons, Inc., USA.
16. P. Marshall, (1984), "AUSTENITIC STAINLESS STEELS, Microstructure and Mechanical Properties", Elsevier Applied Science Publishers LTD, England.
17. P. Lacombe, B. Baroux and G. Beranger, (1993), " Stainless steels", Les editions de physique, France.
18. J. Charles, J.P. Auduard, F. Dupoiron, J.M. Lardon, D. Catelin, (1989), "Duplex Stainless Steels for Marine Applications ". CORROSION-NACE 89, paper No. 116.
19. R. Sriram and D. Tromans, (1989), Corrosion-NACE, Vol. 45, p. 804.
20. N. Sridhar and J. Kolts, (1987), Corrosion-NACE, Vol. 43, p. 646.
21. A. Pozabsky, C.S. Nalbone, and J.D. Crawford, (1983) in "Duplex Stainless Steels", R.A. Lula, ed. ASM international, p. 431.
22. F.B. Pickering; (1976). Int. Met. Rev., Vol. 21, p. 227.
23. M. Goto; (1992), "Corrosion Fatigue Behaviour of a Heat-Treated Carbon Steel and its Statistical Characteristics", Engineering Fracture Mechanics, Vol.42, No.6, p.893.
24. X.D. Wu (1995) "Experimental and Theoretical Studies of Corrosion Fatigue in a High Strength Steel", Ph.D. Thesis, University of Sheffield.
25. J.O'M. Bockris and A.K. Reddy, (1970), "Modern Electrochemistry Vol. 2" Plenum Press, USA.
26. L.L Shreir, (1976), "CORROSION Volume 1" second edition, Newnes-Butterworths, London U.K.
27. M.G. Fontana and N.D. Greene, (1978) "Corrosion Engineering", McGraw Hill, New York.
28. M. Pourbaix, (1984), "On the Mechanisms, Teaching, and Research in Localised Corrosion", Journal of Electrochemical Society, Vol.131, No. 8
29. H. Böhni; (1992), "Localised corrosion- Mechanisms and methods", Materials Science Forum Vols. 111-112, p. 401,Trans Tech Publications Switzerland.
30. J. Kruger; (1976), In "Passivity and its breakdown on iron base alloys", USA_Japan Seminar, p.91, R.W. Staehle and H. Okuda editors,NACE.
31. J.R. Galvele; (1978), "Present state of understanding of the breakdown of passivity and repassivation", In Passivity of metals, p. 285, Frankenthal and Kruger Eds, Electrochemical Society.
32. H. Böhni; (1987) " Localised corrosion in corrosion mechanisms", p. 285, Mansfeld and Dekker Eds.

33. N.D. Tomashov, (1964), Corrosion NACE, Vol. 20, p. 1667
34. Szklarska-Smialowska and M. Janik-Czachor, (1967), Corrosion Science, Vol. 7, p. 65
35. I. Graz, H. Worch and W.Schatt, (1969), Corrosion Science, Vol.9, p. 71
36. M.H. Dean and U. Stimming, (1989), Corrosion Science, Vol. 29, p. 199
37. Ferreira, Hakaki, Simões and Da Cunha Belo, (2000) Paper No. 08 In 7th International Symposium on Electrochemical Methods in Corrosion Science.
38. Erwan le Roy, EunAe Cho (2000), Paper No. 140, In 7th International Symposium on Electrochemical Methods in Corrosion Science.
39. Komachi U. and Y. Katada (2000) Paper No. 106, In 7th International Symposium on Electrochemical Methods in Corrosion Science.
40. H.S. Isaacs, (1989), "The localised Breakdown and Repair of Passive Surfaces during Pitting", Corrosion Science, Vol. 29, No. 2/3, p. 313.
41. D.D. Macdonald, (1992), J. Electrochem. Soc., Vol. 139, p.3434.
42. A.J. Sedriks, (1989), Corrosion - NACE, Vol. 45, p. 510.
43. R. Djoudjou, C.Lemaitre, G. Beranger, (1993), Corrosion Reviews, Vol. 11, p. 157.
44. I.L. Rosenfeld and I.S. Danilov; (1967), "Electrochemical Aspects of Pitting Corrosion" , Corrosion Science, Vol.7, p.129.
45. G.T. Burstein, P.C. Pistorius and S.P. Mattin, (1993), " The Nucleation and Growth of Corrosion Pits on Stainless Steel" , Corrosion Science, Vol. 35, No. 1-4, p. 57
46. P.C. Pistorius, G.T. Burstein, (1992), "Detailed investigation of current transients from metastable pitting events on stainless steel – the transition to stability", Materials Science Forum, Vols. 111 – 112, p. 429
47. A.J. Sedriks, (1990), in Advances in Localised Corrosion (NACE-9), H.S. Isaacs, U. Bertocci, J. Kruger Eds. p. 253.
48. M.B. Ives, S.C. Srivastava, (1990) in Advances in Localised Corrosion (NACE-9), H.S. Isaacs, U. Bertocci, J. Kruger Eds. p. 295
49. S.C. Srivastava, M.B. Ives, (1987), Corrosion-NACE, Vol. 43, p. 687.
50. B. Baroux, D. Gorse, (1994), in Modelling Aqueous Corrosion, K.R. Tretheway, P.R. Roberge Eds., Kluwer Academic Publishers, The Netherlands, p. 161.
51. J.E. Castle, R. Ke, (1990), Corrosion Science, Vol. 30, p. 409
52. V. Scotto, G. Ventura, E. Traverso, (1979), Corrosion Science, Vol. 19, p. 237.
53. J. Stewart, , D.E. Williams, (1992), Corrosion Science, Vol. 33, p. 457.
54. G. Wranglén, (1974), Corrosion Science, Vol. 14, p. 331.
55. G.S. Eklund, (1974), J. Electrochem. Soc., Vol. 121, p. 467.

56. M..A. Baker, J.E. Castle, (1992), Corrosion Science, Vol. 33, p. 1295.
57. M..A. Baker, J.E. Castle, (1993), Corrosion Science, Vol. 34, p. 667
58. H.W. Pickering, (1989), "The significance of the local electrode potential within pits, crevices and cracks", Corrosion Science, Vol. 29, No. 2/3, p. 325.
59. T. Suzuki, M. Yamabe and Y. Kitamura, (1973), "Composition of an Anolyte Pit Anode of Austenitic Stainless Steel in Chloride Solution" Corrosion-NACE, Vol. 29, No. 1, p.18
60. J.R. Galvele, (1976), J. Electrochem. Soc. Vol. 123, p. 464.
61. J.R. Galvele, (1981), Corrosion Science, Vol. 21, p. 551.
62. T.R Beck and S.G. Chan, (1981), Corrosion-NACE, Vol. 37, p. 665
63. G.S. Frankel, L. Stockert, F. Hunkeler, (1987), Corrosion-NACE, Vol. 43, p. 429.
64. H.W. Pickering and R.P. Frankenthal, (1974), in Localised Corrosion, NACE Houston, p. 252.
65. J.W. Oldfield and W.H. Sutton, (1978), "Crevice corrosion of stainless steels. 1. A mathematical model", British Corrosion J., Vol. 13, No. 1, p. 13.
66. M. Hubbell, C. Price and R. Heidersbach, (1985), "Crevice and pitting corrosion tests for stainless steels: A comparison of short-term tests with longer exposures", Laboratory Corrosion Test and Standards, ASTM STP 866, p. 324, G.S. Haynes and R. Baboian, Eds., Philadelphia.
67. K.J. Miller, (1993) "Materials Science Perspective of Metal Fatigue Resistance", Materials Science and Technology, Vol. 9, p. 453.
68. S. Suresh, (1998), "Fatigue of Materials", second edition, Cambridge University Press, U.K.
69. P.J. Forsyth, (1961), "Two stage process of fatigue crack growth", Proc. Crack Propagation Symp., Cranfield, Vol. 1, p.76
70. P.D. Hobson, (1982), "The formulation of a Crack Growth Equation for Short Cracks", Fat. Fract. Engng. Mater. Struct. Vol. 5, No. 4, p. 323
71. A. Navarro and E.R. de los Rios, (1988), "A Microstructurally Short Fatigue Crack Growth Equation", Fat. Fract. Engng. Mater. Struct. Vol. 11, No. 5, p. 383
72. C.M. Wignall, (1997), "Torsional Fatigue of three 316L Stainless Steels in Air and Artificial Sea Water", Ph.D. Thesis, The University of Sheffield.
73. K.J. Miller and R. Akid, (1996), "The Application of Microstructural Fracture Mechanics to various Metal Surface States.", Proc. R. Soc. Lond. A, 452, p. 1411.
74. C.H. Wang and K.J. Miller, (1992), Fatigue Fract. Engng. Mater. Struct., Vol. 15, No. 12, p. 1223.

75. C.H. Wang and K.J. Miller, (1993), Fatigue Fract. Engng. Mater. Struct., Vol. 16, No. 2, p. 181.

76. K.J. Miller, (1987), "The Behaviour of Short Fatigue Cracks and their Initiation., part II", Fatigue Fract. Engng. Mater. Struct., Vol. 10, No. 2, p. 93.

77. B.N. Cox, W. J. Pardee and W. L. Morris, (1986) , "A Statistical Model of Intermittent Short Fatigue Crack Growth.", Fatigue Fract. Engng. Mater. Struct., Vol. 9, p. 435.

78. M.E. Fine, (1980), " Fatigue resistance of metals", Metall. Trans. A, 11, pp.365

79. H. Mughrabi, R. Wang, K. Differt, (1983), "Fatigue crack initiation by cyclic irreversible in high cycle fatigue", in Fatigue mechanisms: Advances in quantitative measurements of physical damage; J. Lankford and D. Davison Eds., ASTM publication, p. 5

80. A. Plumtree and S. Schafer, (1986), "Initiation and Short Crack Behaviour in Aluminium Alloy Castings", Fatigue Fract. Engng. Mater. Struct., Vol. 9, p 215.

81. R. Akid, (1987), "The Initiation and Growth of Short Fatigue cracks in Aqueous saline Environment", Ph.D. Thesis, University of Sheffield.

82. D. Broek, (1991), "Elementary Engineering Fracture Mechanics" 4th edition, Kluwer Academic Publishers, Dordrecht, The Netherlands.

83. T.L. Anderson, (1992), "Fracture Mechanics, fundamentals and applications", CRC Press, USA.

84. K.J. Miller and E.R. de los Rios, (1986), "The Behaviour of Short Cracks", EGF 1, p. 3.

85. S. Suresh and R.O. Ritchie, (1984), "Propagation of Short Fatigue Cracks", Int. Met. Rev., 29 (6), p. 445.

86. R. Akid and K.J. Miller, (1991), "Short Fatigue Crack Behaviour of a low Carbon Steel under Corrosion Fatigue Conditions", Fatigue Fract. Engng. Mater. Struct. Vol. 14, No. 6, p. 237.

87. Y. Murakami and M. Endo, (1986), "Effects of Hardness and Crack Geometry on ΔK_{th} of Small Cracks Emanating from Small Defects", The Behaviour of Short Fatigue Cracks. EGF Publication 1, (Edited by Miller K.J. and de los Rios E.R.), p. 275, London.

88. K.J. Miller, (1987), "The Behaviour of Short Fatigue Cracks and their Initiation., part I", Fatigue Fract. Engng. Mater. Struct., Vol. 10, No. 1, p. 75.

89. M.W. Brown, (1986), "Interfaces between short, long and non-propagating cracks", The Behaviour of Short Fatigue Cracks. EGF Publication 1, (Edited by Miller K.J. and de los Rios E.R.), p. 423, London.

90. G. Murtaza, (1992), "Corrosion Fatigue Short Crack behaviour in a High Strength Steel", Ph.D Thesis, University of Sheffield.

91. J. Lankford, (1985), "The Influence of microstructure on the Growth of Small Fatigue Cracks", Fatigue Fract. Engng. Mater. Struct., Vol. 8, p. 161.

92. C.W Brown and M.A. Hicks, (1983), "A Study of Short Fatigue Crack Growth Behaviour in Titanium Alloy IMI 658", Fatigue Fract. Engng. Mater. Struct., Vol. 6, p. 67.

93. R.P. Gangloff, (1990), "Environmental Cracking-Corrosion Fatigue" in Corrosion Tests and Standards Manual, p.253.

94. P.M. Scott., (1983), "Chemistry Effects in Corrosion Fatigue", Corrosion Fatigue: Mechanics, Metallurgy, Electrochemistry and Engineering, ASTM STP 801, p 319.

95. R.P. Wei, (1997), "Corrosion Fatigue - Science and Engineering.", Keynote Paper for the conference on Recent Advances in Corrosion Fatigue, Sheffield U.K.

96. H.H. Lee and H. Uhlig, (1972), Metallurgical Transactions, Vol.3, p. 2949.

97. M.E. Taylor and J..M. Barsom, (1981), in "Fracture Mechanics (Thirteenth Conference)", ASTM STP 743, R. Roberts Ed., p. 599.

98. S. Rajpathak and W.H. Hartt, (1990), in "Environmentally Assisted Cracking: Science and Engineering, ASTM STP 1049, W.B. Lisagor, T. Crooker , Eds., p. 425.

99. S.R. Novak, (1978), in "Corrosion Fatigue Technology" , ASTM STP 642, H.L. Craig, T.W. Crooker and W. Hoeppner Eds., p. 26

100. W.E. Cowley and F. Robinson, (1968) British Corrosion Journal, Vol. 3, p. 223.

101. J. Congleton, R.A Oleih and R.N. Parkins, (1983), "Some electrochemical and microstructural aspects of corrosion fatigue", in Corrosion Fatigue: Mechanics, Metallurgy, Electrochemistry and Engineering, ASTM STP 801, p 368.

102. T.S. Sudarshan, T.S. Srivatsan and D.P. Harveyii, (1990), "Fatigue process in metals - role of aqueous environments", Engng. Fract. Mech., 36, 6 p. 827.

103. D.J. Duquette, (1990), in Environment Induced Cracking of Metals, R.P Gangloff and M.B Ives, Eds. NACE, Houston, p. 45

104. R.P Gangloff, (1990), in Environment Induced Cracking of Metals, R.P Gangloff and M.B Ives, Eds. NACE, Houston, p.55

105. R. Murakami and W.G. Ferguson, (1987), "The Effects of Cathodic Potential and Calcareous Deposits on Corrosion Fatigue Crack Growth rate in Seawater for two Offshore Structural Steels." , Fatigue Fract. Engng. Mater. Struct. Vol. 9, p. 477.

106. A. Ragab, H. Alawi and K. Sorein, (1989), "Corrosion Fatigue of Steel in various Aqueous Environments", Fatigue Fract. Engng. Mater. Struct. Vol. 12, p. 469.

107. D. J. Duquette, (1972), "A review of aqueous corrosion fatigue", Corrosion Fatigue: chemistry, mechanics and microstructure, (eds. O. Devereux et al.), p.12, Houston, Tex., NACE.

108. C. Laird and D. J. Duquette, (1972), "Mechanisms of Fatigue Crack Nucleation", Corrosion Fatigue: chemistry, mechanics and microstructure, (eds. O. Devereux et al.), p. 88:, Houston, Tex., NACE.

109. H. Hu, (1997), "Fatigue and Corrosion Fatigue Crack Growth Resistance of RTQ501 Steel", Ph.D. Thesis, The University of Sheffield.

110. D. J. Duquette and H. Uhlig , (1969), Transactions ASM, Vol. 62, p. 839.

111. R. Akid, (1997), "The role of Stress-Assisted Localised Corrosion in the Development of Short Fatigue Cracks", Effects of the environment on the initiation of crack growth, ASTM STP 1298, p. 3, W. A. Van Der Sluys, R. S. Piascik and R. Zawierucha, Eds.

112. Y.R. Quian and J.R. Cahoon, (1997), "Crack Initiation Mechanisms for Corrosion Fatigue of Austenitic Stainless Steel", Corrosion-NACE, Vol. 53, No. 2, p. 129

113. T. Magnin , L. Coudreuse and J. Lardon, (1985), "A quantitative approach to fatigue damage evolution in FCC and BCC stainless steels", Scripta Metall, Vol. 19, p 1486

114. R.P. Gangloff, (1985), "Crack-size Effects on the Driving Force for Aqueous Corrosion fatigue", Metallurgical Transactions 16A, p. 953.

115. I. M. Dmytrakh, R. Akid and K. Miller, (1997), "Electrochemistry of Deformed Smooth Surfaces and Short Corrosion fatigue Crack Growth Behaviour", British Corrosion Journal, Vol. 32, No. 2, p. 138

116. Y. Wang and R. Akid, (1996), "Role of Nonmetallic Inclusions in Fatigue, Pitting and Corrosion Fatigue", Corrosion-NACE, Vol.52, No. 2, p. 92

117. Y-Z. Wang, R. Akid and K.J. Miller, (1995), "The Effect of Cathodic Polarisation on Corrosion Fatigue of a High Strength Steel in Salt water", Fatigue Fract. Engng. Mater. Struct. Vol. 18, No. 3, p. 293.

118. U.R. Evans, (1960), "The corrosion and oxidation of metals", 862; London, Edward Arnold.

119. D. Whitwham and U.R. Evans, (1950), J. Iron and Steel Inst, Vol. 165, p.72

120. D.W. Hoeppner, (1979), "Model for Prediction of Fatigue lives Based upon a Pitting Corrosion Fatigue Process", Fatigue mechanisms, Proceedings ASTM STP 675, p. 841, J.T. Fong, Ed.

121. T.C. Lindley, P. McIntyre and P.J. Trant, (1982), "Fatigue Crack Initiation at Corrosion Pits", Metals technology, Vol. 9, p. 135

122. S. Kawai and K. Kasai, (1985), "Considerations of Allowable Stress of Corrosion Fatigue (focused on the influence of Pitting)" Fatigue Fract. Engng. Mater. Struct. Vol. 8, No. 2, p. 115

123. Y. Kondo, (1989) "Prediction of Fatigue Crack Initiation Life based on Pit Growth", Corrosion Science Vol. 45, No. 1, p. 7

124. D.W. Hoeppner, V. Chandrasekaran and A.M. Taylor, (200), "Review of Pitting Corrosion Fatigue Models", The corrosion doctors Journal 2000.

125. H.S. Isaacs, (1971), Int. Conf. on Localised Corrosion, Williamsburg, Virginia.

126. H.S. Isaacs and B. Vyas, (1981), "Scanning Reference Electrode Techniques in Localised Corrosion", Electrochemical Corrosion testing, ASTM STP 727, p. 3, F. Mansfeld and U. Bertocci eds.

127. H.S. Isaacs and G. Kissel, (1972), "Surface Preparation and Pit Propagation in Stainless Steels", J. Electrochem. Soc., Vol. 119, No. 12, p. 1628.

128. C.D.S. Tuck, (1983), "The Use of Micro-electrodes in the Study of Localised Corrosion in Aluminium Alloys ", Corrosion Science, Vol. 23, No. 4, p. 379

129. S.J. Bates, S.R. Gosden and D.A. Sargeant, (1989), "Design and development of Scanning Reference Electrode Technique for investigation of pitting corrosion in FV 448 turbine disc steel", Materials Science and Technology, Vol. 5, p. 356

130. D.A. Sargeant, J.G.C. Hainse and S. Bates, (1989), " Microcomputer controlled scanning reference electrode apparatus developed to study pitting corrosion of gas turbine disc materials ", Materials Science and Technology, Vol. 5, p. 487

131. K.R. Trethewey, D.A Sargeant, D.J. Marsh and S. Haines, (1994), "New Methods on Quantitative Analysis of Localised Corrosion using Scanning electrochemical Probes", in Modelling Aqueous Corrosion: From individual Pits to

System management, p. 417, eds. K.R. Trethewey and P.R. Roberge, Kluwer Academic Press.

132. K.R. Trethewey, D.J. Marsh and D.A. Sargeant, (1996), "Quantitative Measurements of Localised Corrosion Using SRET", CORROSION-NACE 94, Paper no. 317.

133. R. Akid (1995), "Localised Corrosion: A new evaluation approach ", Materials World, November, p. 522

134. H.N. McMurray, S.R. Magill, and B.D. Jeffs (1996), "Scanning Reference Electrode Technique as a tool for investigating localised corrosion phenomena in galvanised steels", Iron and Steelmaking, Vol. 23, No.2, p 183

135. H.N. McMurray and D.A. Worsley (1997), "Scanning Electrochemical Techniques for the Study of Localised Metallic Corrosion", in Research in Chemical Kinetics, Vol. 4, p. 149, Compton & Hancock eds. Blackwell Science Ltd.

136. L.F. Jaffe and R. Nuccitelli, (1974), "An Ultrasensitive Vibrating Probe for Measuring Steady Extracellular Currents" The Journal o Cell Biology, Vol.63, p. 614

137. H.S. Isaacs, (1988), "Initiation of Stress Corrosion Cracking of sensitised type 304 Stainless Steel in Dilute Thiosulfate Solution", J. Electrochem. Soc., Vol. 135, No. 9, p. 2180.

138. Xiang-chun Jiang, T. Yoshimura, and Y. Ishikawa, (1992), "Investigation of Alpha Prime Precipitation in Aged Duplex Stainless Steel", J. Electrochem. Soc., Vol. 139, No. 4, p. 1001.

139. G.F. Vander Voort, (1989), "The Metallography of Stainless Steels", Journal of Metals, Vol. 41, No.3, March, p. 6

140. Metallography and Microstructures, Vol. 9, ASM Handbook, ASM international, (1985), p. 439.

141. ASTM standard E 112 - 95, "Standard Test Methods for Determining Average Grain Size", Annual book of ASTM Standards (1995), p.226

142. J.M. Gere and S.P. Timoshenko, (1985), Mechanics of Materials, Second SI Edition, Wadsworth International, USA.

143. G.E. Dieter, (1988), Mechanical Metallurgy, SI Metric Edition, McGraw-Hill Book Company (UK).

144. J.F. Harvey, (1974), "Theory and Design of Modern Pressure Vessels", 2nd edition, Van Nostrand Reinhold, Company.

145. ASM Specialty Handbook, Stainless Steels, (1994), edited by J.R. Davis, p. 495

146. SRET Model SR100, Operators manual version 1.71 EG&G Instruments.

147. S. Zhou and A. Turnbull, (1999), "Influence of pitting on Fatigue life of Turbine Steel", Fatigue Fract. Engng. Mater. Struct., Vol. 22, p. 1083.

148. S. Zhou and A. Turnbull, (1999), "Development of a Pre-pitting procedure for Turbine disc Steel", NPL Report.

149. Metals Handbook Vol. 8 Mechanical Testing, Ninth Edition, p.91

150. P. Eskelinen, O. Forsén, H. Hänninen, J. Onnela and S. Yläsaari, (1992), "The use of different techniques for determination of pitting corrosion potential of austenitic stainless steel", Materials Science Forum Vols. 111-112, p 515.

151. Saricimen, N.R. Jarrah and I.M. Allam; "Investigation of Corrosion of Commercial Grade AISI 316L SS Liner Plates in Desalination Plant Conditions", CORROSION-NACE94, paper No. 505.

152. Szklarska-Smialowska, (1971), Corrosion-NACE, Vol. 27, p.223.

153. G. Capobianco, G. Moretti, G. Quartarone and G. Sandona, (2000), "Pitting Corrosion Behaviour of Alloy UNS S31803 in Water containing Chlorides" , 7th International Symposium on Electrochemical Methods in Corrosion Research, EMCR, Butapest, Hungary, Paper No. 176.

154. Z. Szklarska-Smialowska, (1974), "The Pitting of Iron-Chromium-Nickel Alloys," in Localised corrosion, NACE, Houston Texas, p.312.

155. R. Newman and E. Franz, (1984), "Growth and Repassivation of Single Corrosion Pits in Stainless Steel", Corrosion-NACE, Vol. 40, No. 7, p. 325

156. Szklarska-Smialowska, (1971), Pitting Corrosion of metals, p.114

157. H.P. Godard, (1960), Canadian J. of Chemical Eng., No. 38, p. 167.

158. N.J. Laycock and R.C. Newman, (1997), "Localised dissolution kinetics, salt films and pitting potentials". Corrosion Science, Vol. 39, No. 10-11, p. 1790.

159. D.A. Sargeant, K. R. Trethewey, D. Marsh and N.X. Randall, (1991), "Experimentally Derived Correction Factors for the Quantification of Results from the Scanning Reference Electrode Technique aparatus", RNEC, Manadon, Plymouth, Report No. RNEC-RR-91019.

160. S.J. Badger, (1999), "Application of the Scanning Reference Electrode Technique to Localised Corrosion", Ph.D. Thesis, University of Manchester Institute of Science and Technology.

161. S.J. Badger, S.B. Lyon and S. Turgoose, (1998), "Modeling the Twin Platinum Probe Scanning Electrode Response", J. Electrochem. Soc., Vol. 154, No. 12, p. 4074.

162. E. McCafferty, (1977), "Distribution of potential and Current in Circular Corrosion Cells Having Unequal Polarisation Parameters", J. Electrochem. Soc., Vol. 124, No. 12, p. 1869.

163. H. Strehblow, (1995), "Mechanisms of Pitting Corrosion", in Corrosion, mechanisms in Theory and Practice, P. Marcus and J. Ordar editors, p. 201.

164. T. Suter, E.G. Webb, H. Böhni and R.C. Alkire, (2001), " Pit initiation on Stainless Steels in 1 M NaCl With and Without Mechanical Stress", J. Electrochem. Soc., Vol. 148, No. 5, B174.

165. P.E. Manning, D.J. Duquette and W. Savage, (1979), Corrosion-NACE, Vol. 35 P.151

166. P.E. Manning and D.J. Duquette, (1980), "The effect of temperature (25°-289°C) on pit initiation in single phase and duplex 304L stainless steels in 100 ppm Cl^- solution.", Corrosion Science, Vol. 20, p. 597.

167. T. Magnin and J.M. Lardon, (1985), "The influence of a 3.5% NaCl solution on the fatigue damage evolution in a planar slip f.c.c. stainless steel", Materials Science and Engineering, 76, L7-L10.

168. A. Turnbull, (1999), "Importance of Internal Cathodic Reactions for Crevice and Crack Chemistry", in, International conference on Engineering Materials, Environmental Degradation of. Poland. p.73

169. R.P. Wei, (1998), "A probability model for the growth of corrosion pits in aluminium alloys induced by constituent particles", Engineering Fracture Mechanics, Vol. 59, No. 3, p. 305.

170. R. Wei, (2000), "Material ageing and reliability of engineering systems. Predictive Methods for Risk Assessment and Evaluation of Materials, Equipment and structures", ASTM, STP 1401, R. Kane editor, p.

171. R. Akid, "Corrosion fatigue Resistance: Material, Environmental and Loading Variables During the Stage I and Stage I/II Transition Regimes. ", in proceedings of ICF-10, Hawaii. USA Dec. 2-6, 2001, Elsevier.

172. N. Acuña-González, (2001), " The effect of Micro-organisms on the Corrosion Fatigue Performance of Stainless Steel in Natural Seawater " Ph.D. Thesis, National University of Mexico, Mexico.

173. G.S. Chen, C.M. Liao, K.C. Wan, M. Gao and R.P. Wei, (1997), " Pitting Corrosion and Fatigue Crack Nucleation," Effects of the environment on the initiation of crack growth , ASTM STP 1298, W.A. Van Der Sluys, R.S. Piascik, and R. Zawierucha, Eds., p.18

TABLES

Material	C	Si	Mn	P	S	Cr	Mo	Ni	Co	N
S30400	.019	.39	1.40	.025	.001	18.30	_	9.07	.12	.054
S31603	.020	.49	1.28	.029	.003	17.13	2.09	11.19	.16	.032
S31803	.015	.36	.88	.021	.001	22.66	3.20	5.93	.12	.154

Table 1. Chemical composition (wt%) of 304, 316L and Duplex Stainless Steels used in this study.

Material	Orientation *	σ_{ys} (MPa)	σ_{uts} (MPa)	El %	Hardness Hv	E (GPa)	ν
S30400	T	246	583	56	147	193	0.30
	ST	246	574	54	140		
S31603	T	235	564	54	136	193	0.28
S31803	T	504	760	37	239	200	0.33

*T; Transverse, ST: Short-Transverse

Table 2. Mechanical properties at 20°C of 304, 316L and Duplex Stainless Steels used in this study.

		Circumferential			Longitudinal		
Applied Pressure		Strain	Stress		Strain	Stress	
(Bar)	(MPa)	(με)	(MPa) σ_C	(MPa) σ_1	(με)	(MPa) σ_L	(MPa) σ_2
10	1.0	89	21.67	18.99	6	10.84	6.48
15	1.5	136	32.51	29.00	9	16.25	9.86
20	2.0	187	43.34	40.00	14	21.67	13.90
25	2.5	238	54.17	50.95	19	27.10	17.93
30	3.0	287	65.0	61.57	25	32.5	22.06
35	3.5	335	75.85	72.03	32	37.92	26.34
40	4.0	387	86.68	83.40	40	43.34	31.01
45	4.5	439	97.52	94.75	48	48.76	35.8
50	5.0	491	108.35	106.2	57	54.18	40.73
55	5.5	544	119.19	117.9	67	59.60	45.93
60	6.0	590	130.0	128.1	77	65.00	50.72
65	6.5	643	140.86	139.6	84	70.43	55.29
70	7.0	696	151.69	151.2	93	75.84	60.29
75	7.5	749	162.53	162.8	101	81.27	65.1
80	8.0	793	173.37	172.3	107	86.68	69.33
85	8.5	846	184.6	183.8	113	92.30	73.7
90	9.0	898	195.0	195	118	97.52	77.58
95	9.5	950	206.6	206.2	124	103.3	81.88
100	10.0	1002	216.71	217.7	134	108.35	87.1
105	10.5	1052	228.0	228.6	141	114.00	91.42
110	11.0	1102	238.38	239.5	148	119.19	96.03
120	12.0						
130	13.0						

Table 3. Values of applied pressure, theoretical and experimental stress and experimental strain for the UNS S31603 steel obtained from the calibration of the hydraulic system.

		Circumferential			Longitudinal		
Applied Pressure		Strain	Stress		Strain	Stress	
(Bar)	(MPa)	(με)	(MPa) σ_C	(MPa) σ_1	(με)	(MPa) σ_L	(MPa) σ_2
10	1.0	86	21.85	19.32	17	10.93	9.08
15	1.5	128	32.78	28.61	23	16.39	13.02
20	2.0	175	43.71	39.08	31	21.86	17.71
25	2.5	217	54.64	48.5	39	27.32	22.08
30	3.0	262	65.57	58.62	48	32.79	26.85
35	3.5	305	76.50	68.24	56	38.25	31.28
40	4.0	356	87.42	79.64	65	43.71	36.44
45	4.5	397	98.35	88.91	74	49.18	40.95
50	5.0	445	109.23	99.60	82	54.62	45.70
55	5.5	491	120.21	109.86	90	60.1	50.32
60	6.0	533	131.14	119.15	96	65.57	54.27
65	6.5	579	142.10	129.41	104	71.1	58.89
70	7.0	629	153.00	140.59	113	76.5	63.98
75	7.5	671	163.92	150.00	121	81.96	68.36
80	8.0	722	174.85	161.4	130	87.43	73.51
85	8.5	770	185.78	172.28	141	92.88	78.89
90	9.0	810	196.7	181.33	150	98.35	83.35
95	9.5	860	207.63	192.44	158	103.82	88.23
100	10.0	903	218.56	201.88	163	109.28	92.02
105	10.5	950	229.49	212.36	171	114.75	96.71
110	11.0	1002	240.40	223.84	178	120.20	101.5
120	12.0	1086	262.27	242.61	193	131.12	110.03
130	13.0	1179	284.13	262.90	202	142.1	117.86

Table 4. Values of applied pressure, theoretical and experimental stress and experimental strain for the UNS S30400 steel obtained from the calibration of the hydraulic system.

		Circumferential			Longitudinal		
Applied Pressure		Strain	Stress		Strain	Stress	
(Bar)	(MPa)	(με)	(MPa) σ_C	(MPa) σ_1	(με)	(MPa) σ_L	(MPa) σ_2
70	7.0	952	151.67	170.5	89	75.83	91.2
75	7.5	1026	162.5	181.6	96	81.25	98.2
80	8.0	1100	173.23	193.7	103	86.67	105
85	8.5	1172	184.17	203.2	109	92.1	111.5
90	9.0	1232	195.0	215.3	116	97.5	117.7
95	9.5	1303	205.83	226.7	123	102.92	124.6
100	10.0	1374	216.67	238.2	131	108.33	131.4
105	10.5	1446	227.5	249.8	138	113.75	138.3
110	11.0	1517	238.33	261.3	145	119.17	145.1
115	11.5	1589	249.17	272.0	152	124.58	152.0
120	12.0	1659	260.0	284.2	159	130.0	158.8
125	12.5	1729	270.83	297.4	166	135.42	165.3
130	13.0	1800	281.67	309.7	173	140.83	171.9
135	13.5	1873	292.5	321.6	180	146.28	178.9
140	14.0	1940	303.33	332.2	186	151.67	185.4
145	14.5	2011	314.17	343.7	194	157.1	192.5
150	15.0	2082	325.2	356.2	201	162.5	199.3
155	15.5	2154	335.83	367.8	207	167.92	206.0
160	16.0	2230	346.67	378.4	214	173.3	213.4
165	16.5	2310	357.5	389.8	221	178.75	220.7
170	17.0	2385	368.3	403.6	229	184.17	201.3
180	18.0	2535	390.0	425.3	242	195	208.7
190	19.0	2670	411.67	450.2	256	205.83	219.8
200	20.0	2825	433.33	473.8	272	216.67	230.3
210	21	2974	455.0	498.2	286	227.5	244.5
220	22	3120	476.67	523.1	301	238.33	258.4
230	23	3269	498.33	547.3	315	249.17	272.7

Table 5. Values of applied pressure, theoretical and experimental stress and experimental strain for the UNS S31803 steel obtained from the calibration of the hydraulic system.

Ionic species	Ionic Composition (% total weight)
Chloride	49.943
Sodium	26.047
Sulphate	6.44
Magnesium	3.16
Calcium	0.996
Potassium	0.927
Bicarbonate	0.362
Borate	0.072
Strontium	0.016
Phosphate	—
Total solids	84.963
Water	14.987
Total	99.957

Table 6. Chemical Composition of the Sea Salt used to prepare the artificial seawater.

Material	(E_{corr})* (mV vs SCE)	(E_P)* (mV vs SCE)	($i_{passive}$)* ($\mu A/cm^2$)
304 SS	- 230 to - 250	300 to 360	0.3 to 0.4
316L SS	-220 to -240	350 to 380	0.01 to 0.03
Duplex SS:	-260 to -290	1060 to 1110	0.01 to 0.02

* Range of values for E_P, E_{corr} and $i_{passive}$ were obtained from five tests under identical experimental conditions.

Table 7. Values of electrochemical parameters.

Electrolyte	Concentration (g/l)	PH	Conductivity (mS/cm)
Synthetic seawater	39 (seasalts)*	8.2 ± .1	80.1
$FeCl_3$	16.22	1.9 ± .1	16.5

*The composition is given in table 6.

Table 8. Physical and chemical properties of the electrolytes used for SRET-CF tests.

304 SS			316L SS		
polarisation time (min)	p_{ar} non-rotating	p_{ar} rotating	polarisation time (min)	p_{ar} non-rotating	p_{ar} rotating
6	1.42	-	6	1.23	-
12	1.43	1.45	12	1.17	1.32
18	1.48	-	30	1.20	1.30
42	1.40	1.44	42	-	-
54	1.20	-	48	1.25	-
60	-	1.45	60	1.21	1.35

Table 9. Pit aspect ratio (p_{as}) of pits generated under hydrodynamic and stationary (non-rotating) conditions on 304 and 316L stainless steels.

E_{corr} (mV vs SCE)	**Time of immersion.** (min)	**Number of cycles**	**Maximum SRET signal from pit a*** (mV)	**Localised current density from pit a*** (mA/cm^2)
290	2	0	---------	---------
405	5	0	-1.04	73.24
355	15	0	-1.27	89.43
340	31	100	-1.35	95.1
335	37	188	-1.47	103.52
340	53	440	-2.55	179.57
354	58	520	-3.02	212.67
340	69	700**	-4.17	293.65**
335	78	830	-3.11	219.0
318	90	1020	-4.13	290.83
320	102	1250	-5.84	411.53
328	117	1860	-6.49	457.03
315	152	2450	-2.96	208.44

* See figure 4.53

** Crack nucleation from an active corrosion pit.

Table 10. Information from SRET measurements of the activity of the pit (a) in a specimen of 316L SS in $FeCl_3$ and the corrosion potential of the specimen as function of the number of stress cycles.

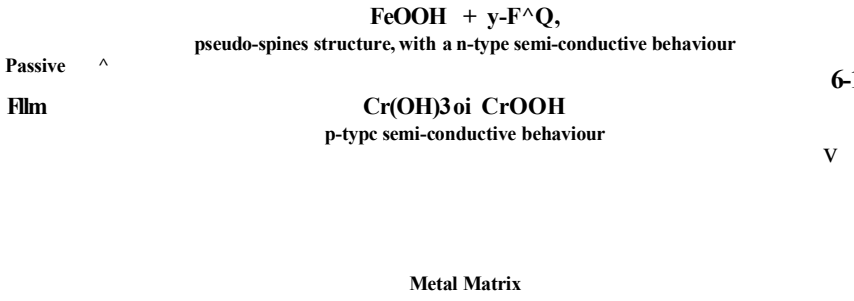

Figure 2.1 Representation of the hypothetical structure of passive films in stainless steels [38].

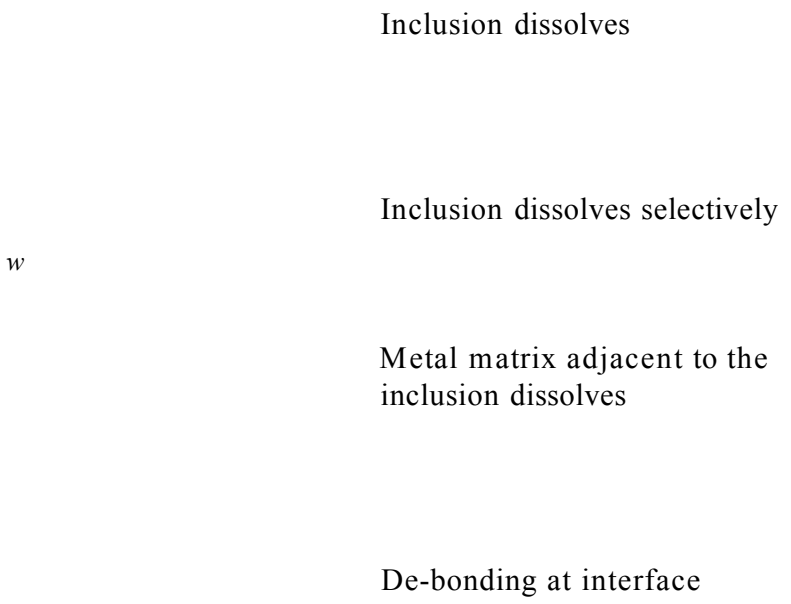

Figure 2.2 Classification of the non-metallic inclusion behaviour for the initiation of pitting corrosion |49|.

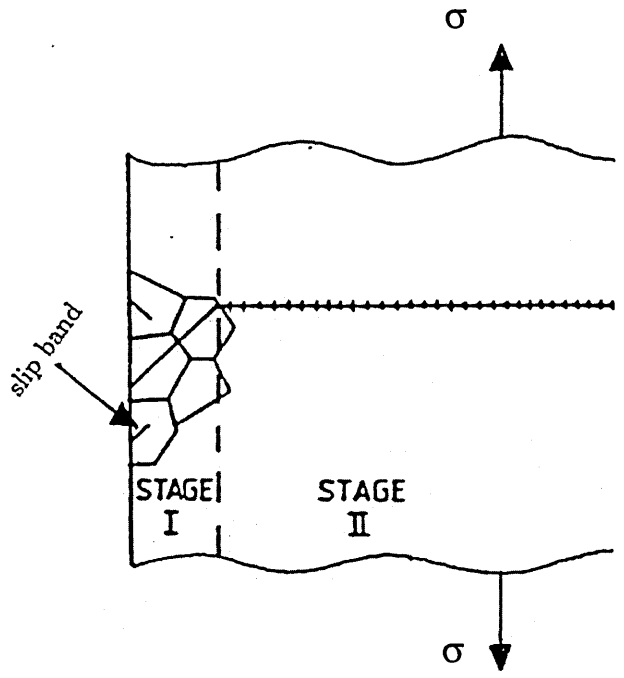

Figure 2.3. The different forms of crack behaviour as a function of the crack size [69].

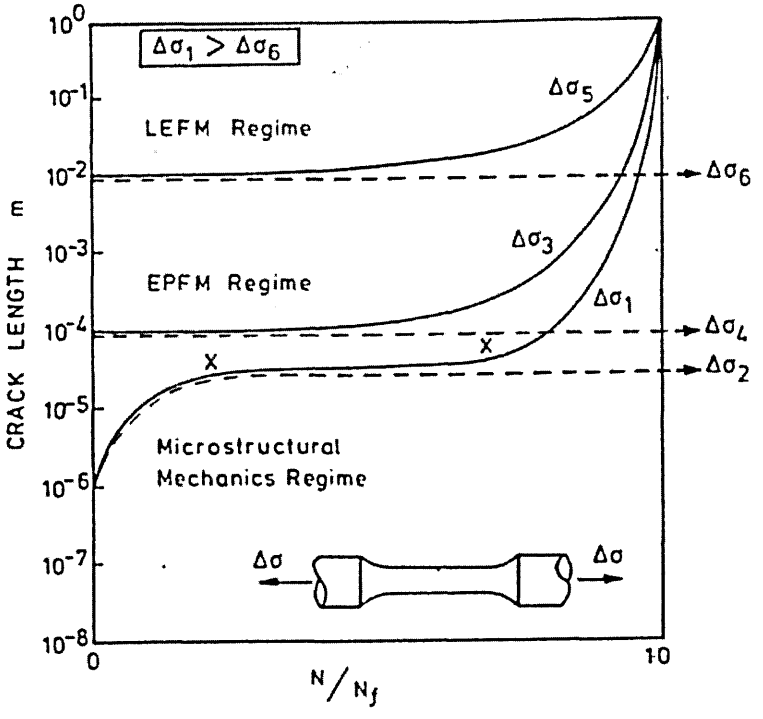

Figure 2.4. The different fracture mechanics approaches for describing crack behaviour as a function of the crack size and stress [67].

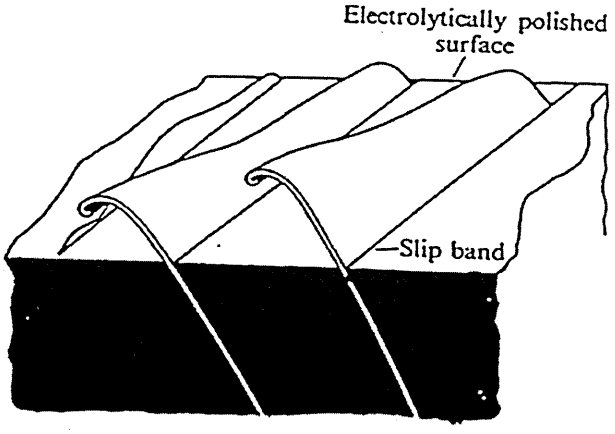

Figure 2.5. Extrusions formed at persistent slip bands (PSB's), which can act as stress concentrators for fatigue crack initiation.

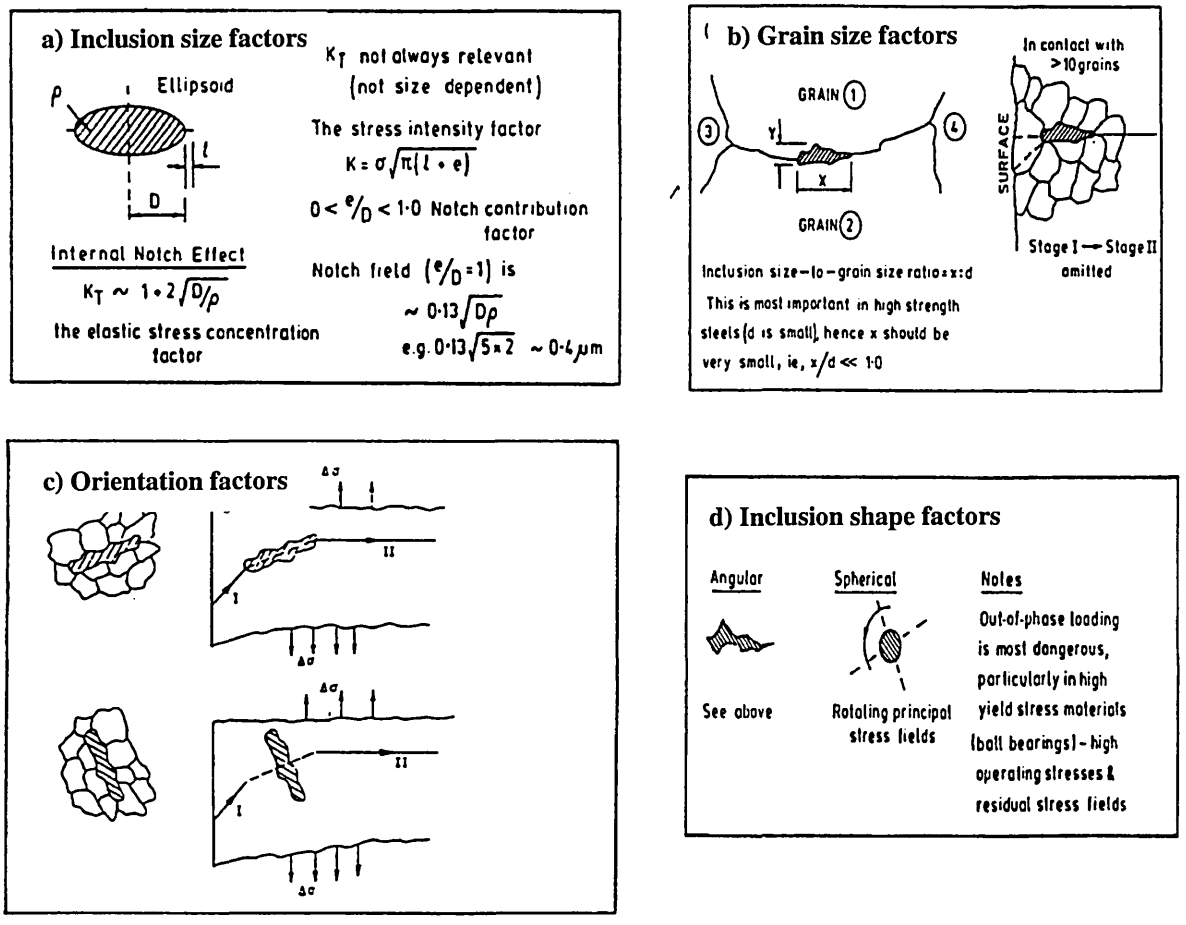

Figure 2.6. Effect of the size, shape, and orientation of the inclusions and the grain size of the metal matrix on the fatigue behaviour [67].

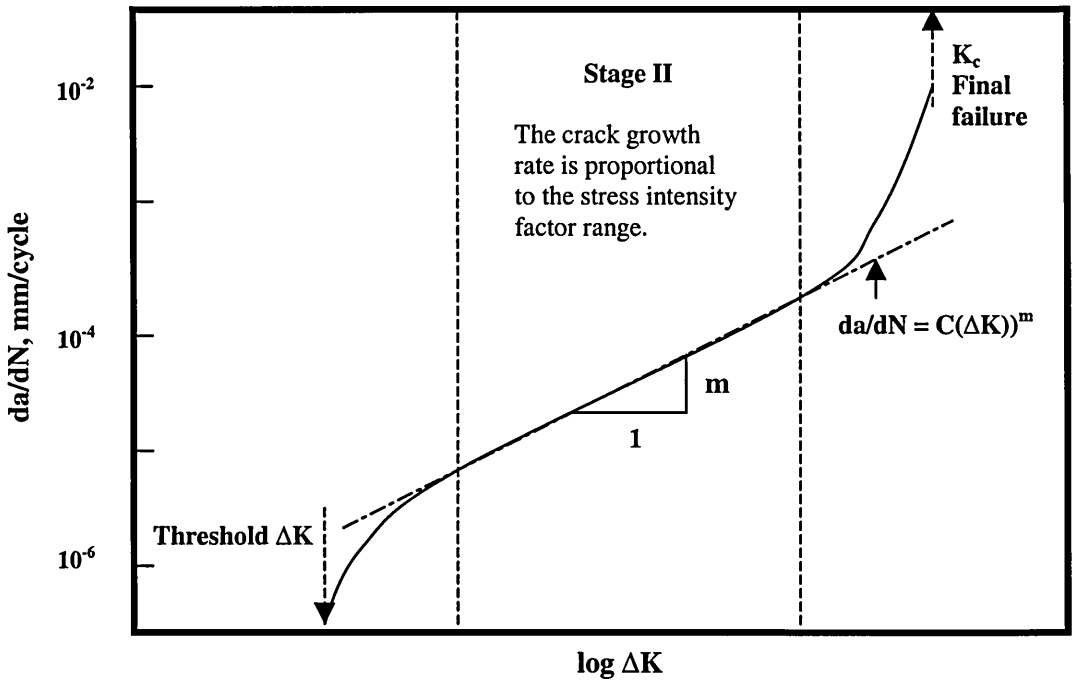

Figure 2.7. Cracks in stage II are frequently classed as long cracks because their growth can be quantified using Linear Elastic Fracture Mechanics (LEFM).

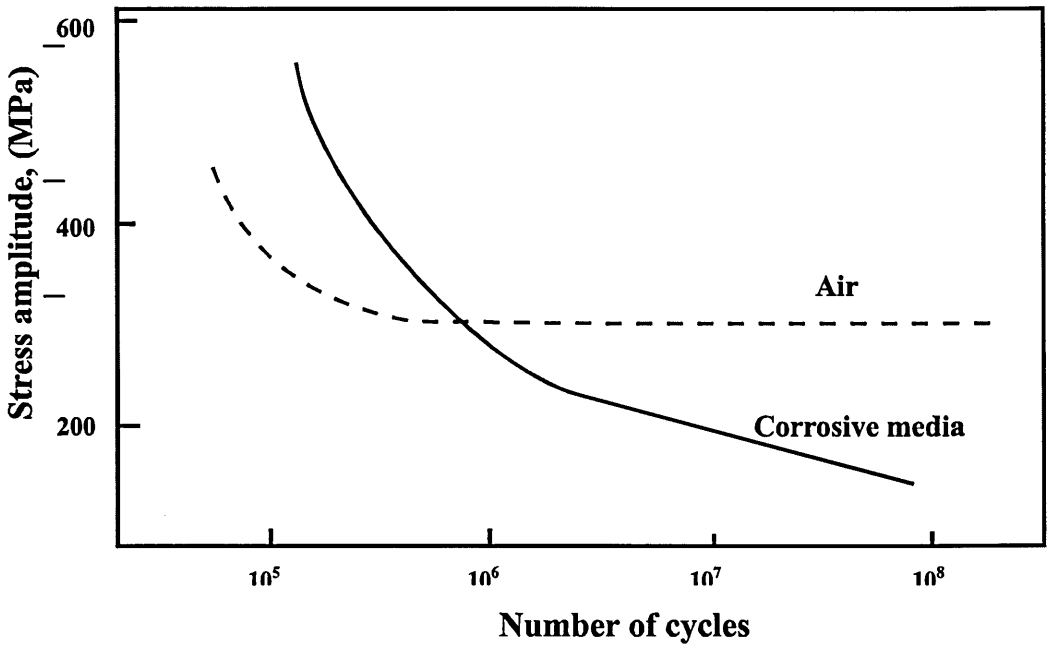

Figure 2.8. Schematic representation of air fatigue and corrosion fatigue behaviour.

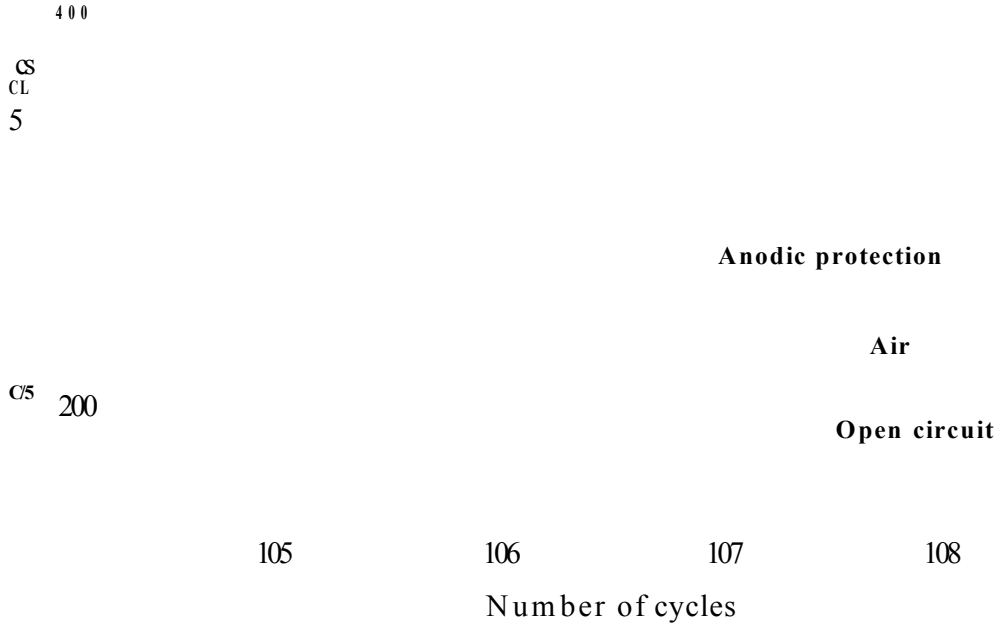

Figure 2.9. Air and corrosion fatigue S-N curves for 18Cr-10Ni-Fe alloy in 10% H2S04 under different environmental conditions [100]

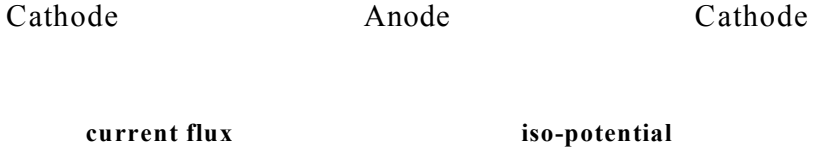

Figure 2.10 Schematic representation of the current and potential distribution in solution during localised corrosion.

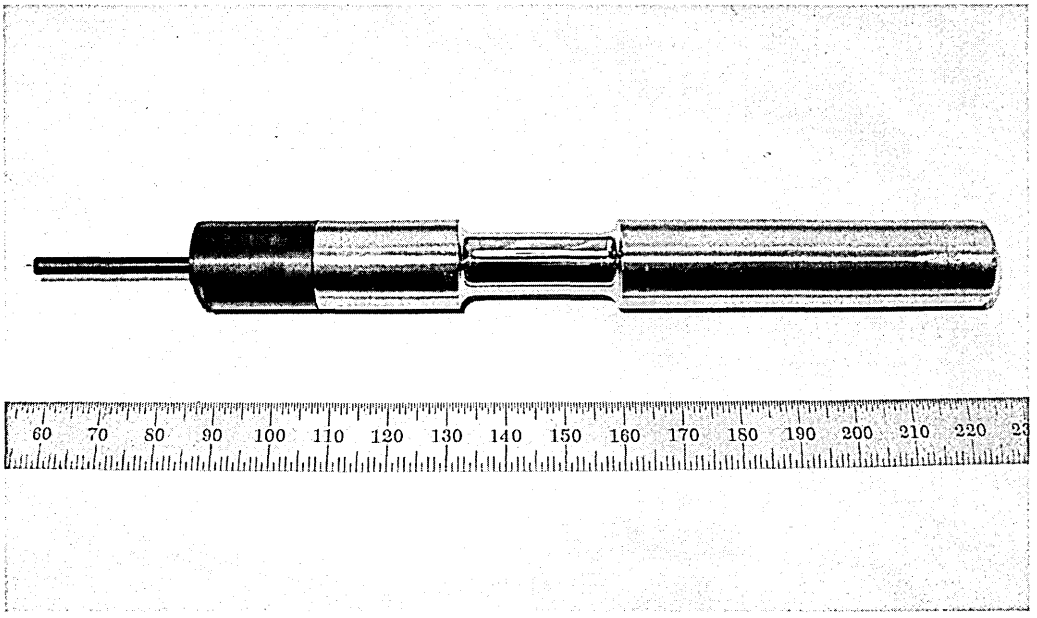

Figure 3.1. Tubular SRET specimen used to perform simultaneous corrosion fatigue - SRET tests .

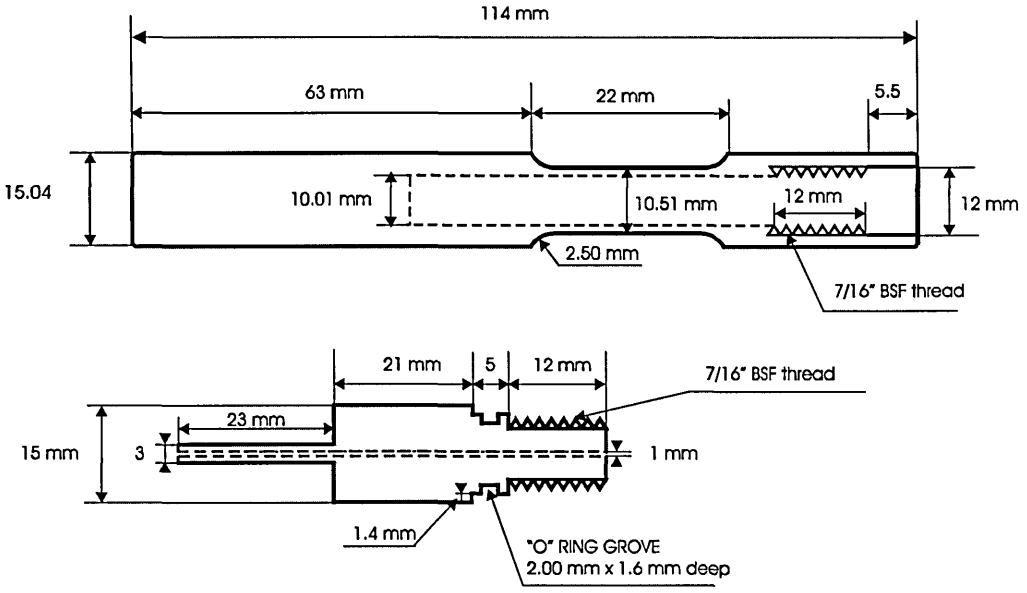

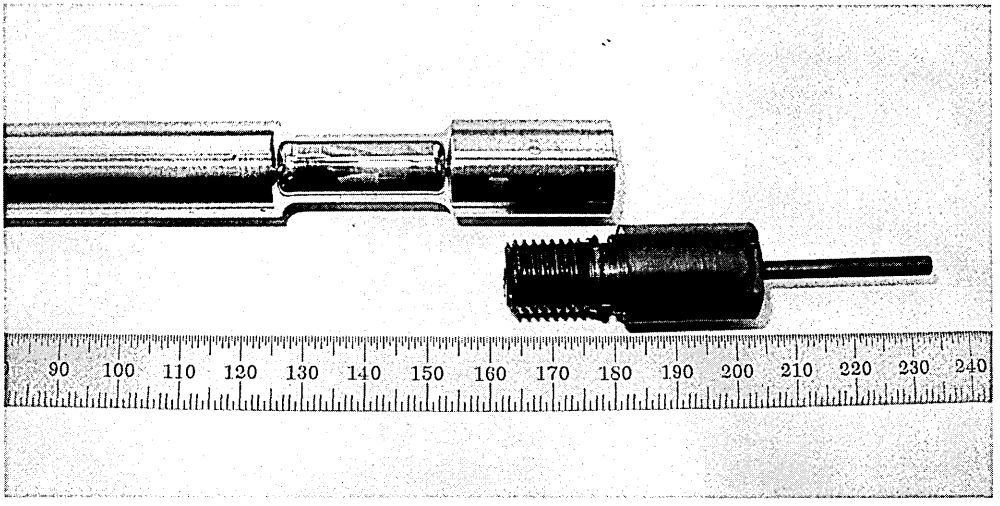

Figure 3.2. Dimensions of the tubular SRET specimen used to perform simultaneous corrosion fatigue - SRET tests .

Figure 3.3 The hydraulic system coupled to the SRET equipment used to perform CF-SRET tests

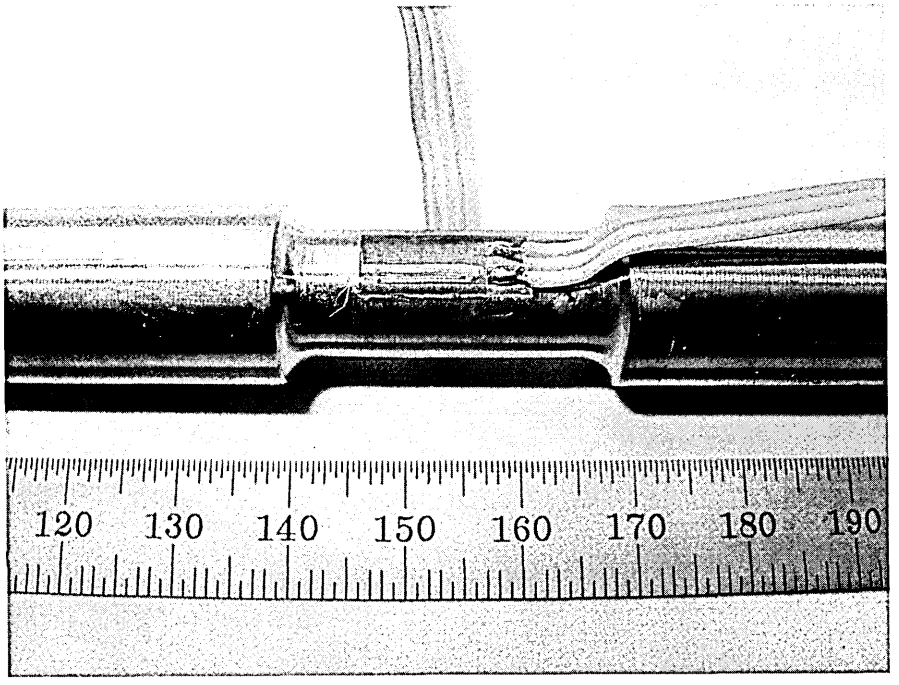

a) Strain gauge in the longitudinal direction

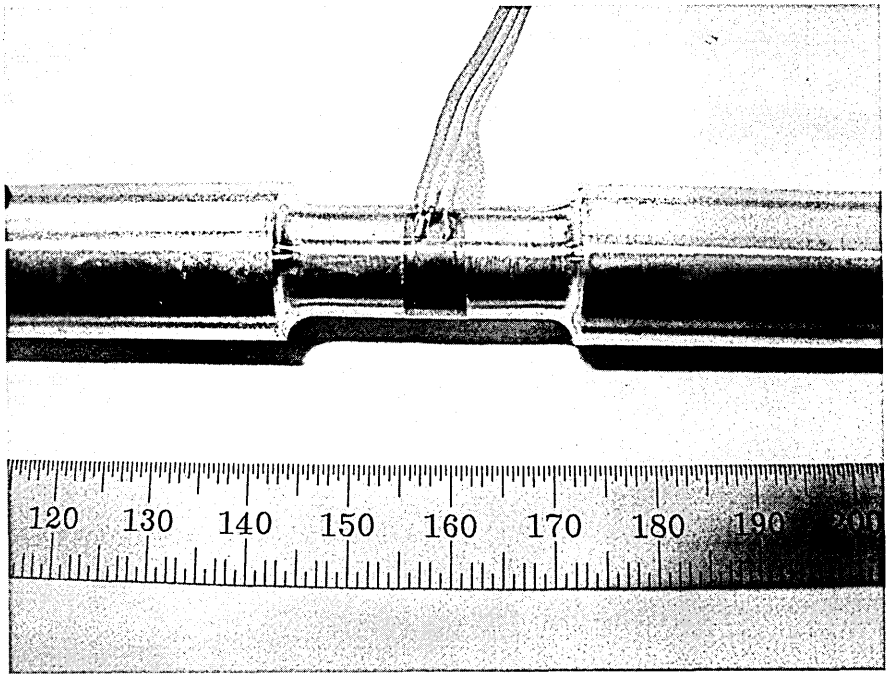

b) Strain gauge in the circumferential direction

Figure 3.4. SRET specimens strain-gauged in a) longitudinal and b) circumferential directions used to perform the calibration of the hydraulic system .

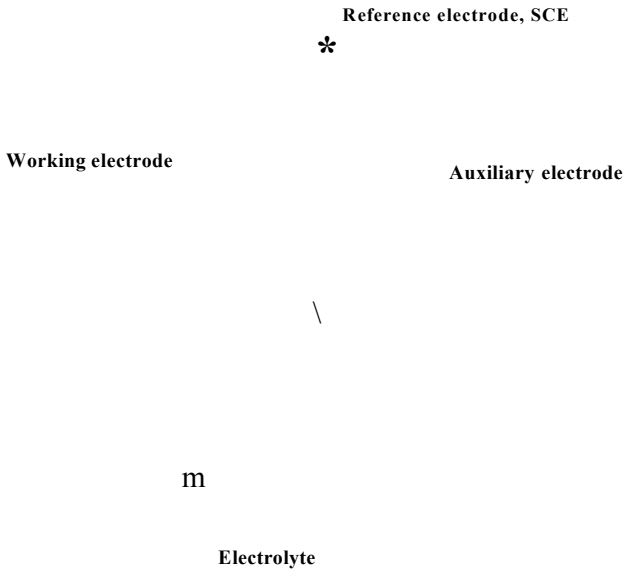

Figure 3. 5 Schematic of the three-electrode conventional corrosion cell used for the electrochemical tests.

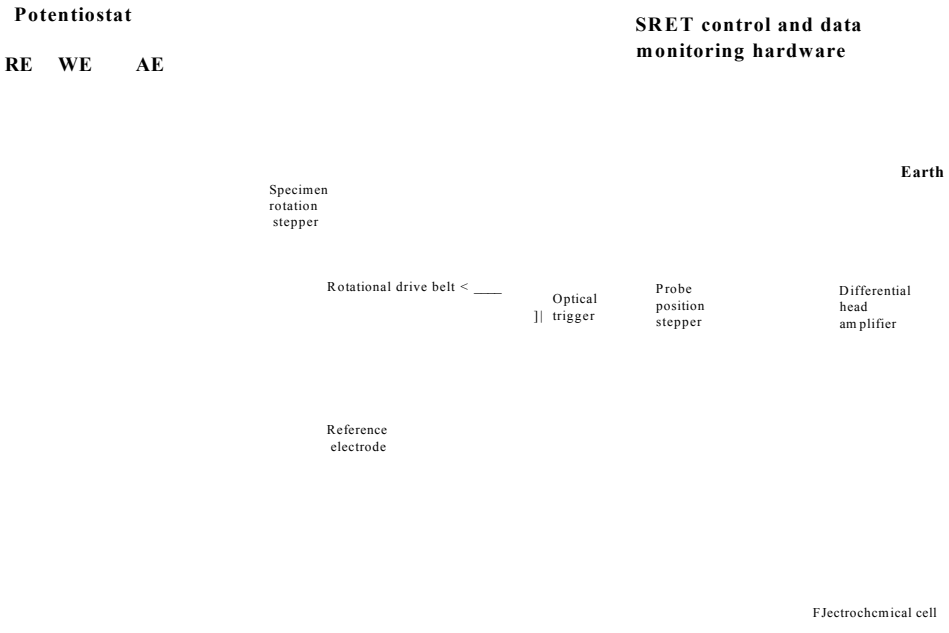

3.6 Schematic representation of the SRET SRI 00

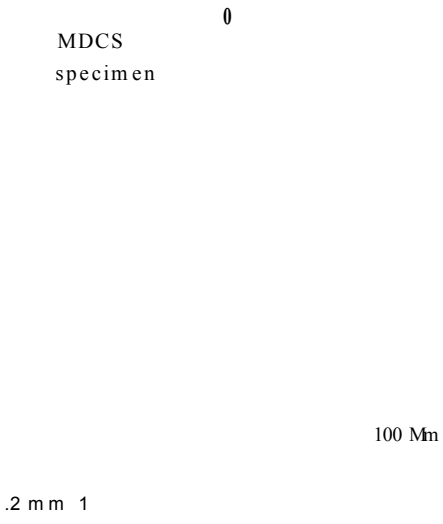

Figure 3.7. Configuration used for the calibration of the SRET equipment using the micro disk calibration source (MDCS) specimen, (not in scale).

Figure 3. 8 Twin platinum scanning probe used with the SRI 00

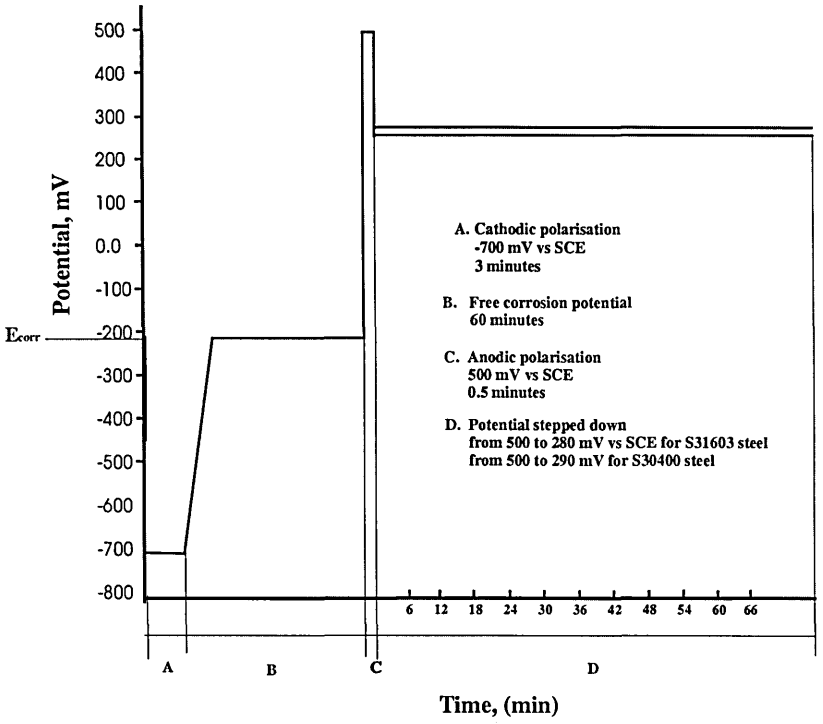

Figure 3.9. Schematic of the potentiostatic polarisation sequence used for the generation of pits, (potential in mV vs SCE).

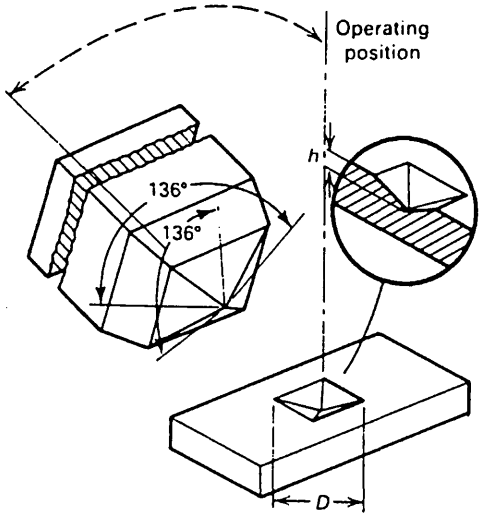

Figure 3.10. Diamond indenter and indentation geometry used to measure the pit depth by removing material [149].

Figure 3.11 Corrosion cell arrangement used for the CF-SRET tests.

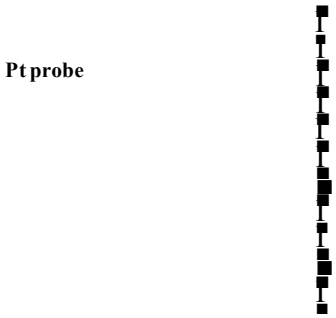

Figure 3.12 Pt probe to cylindrical specimen separation used for the CF-SRET tests.

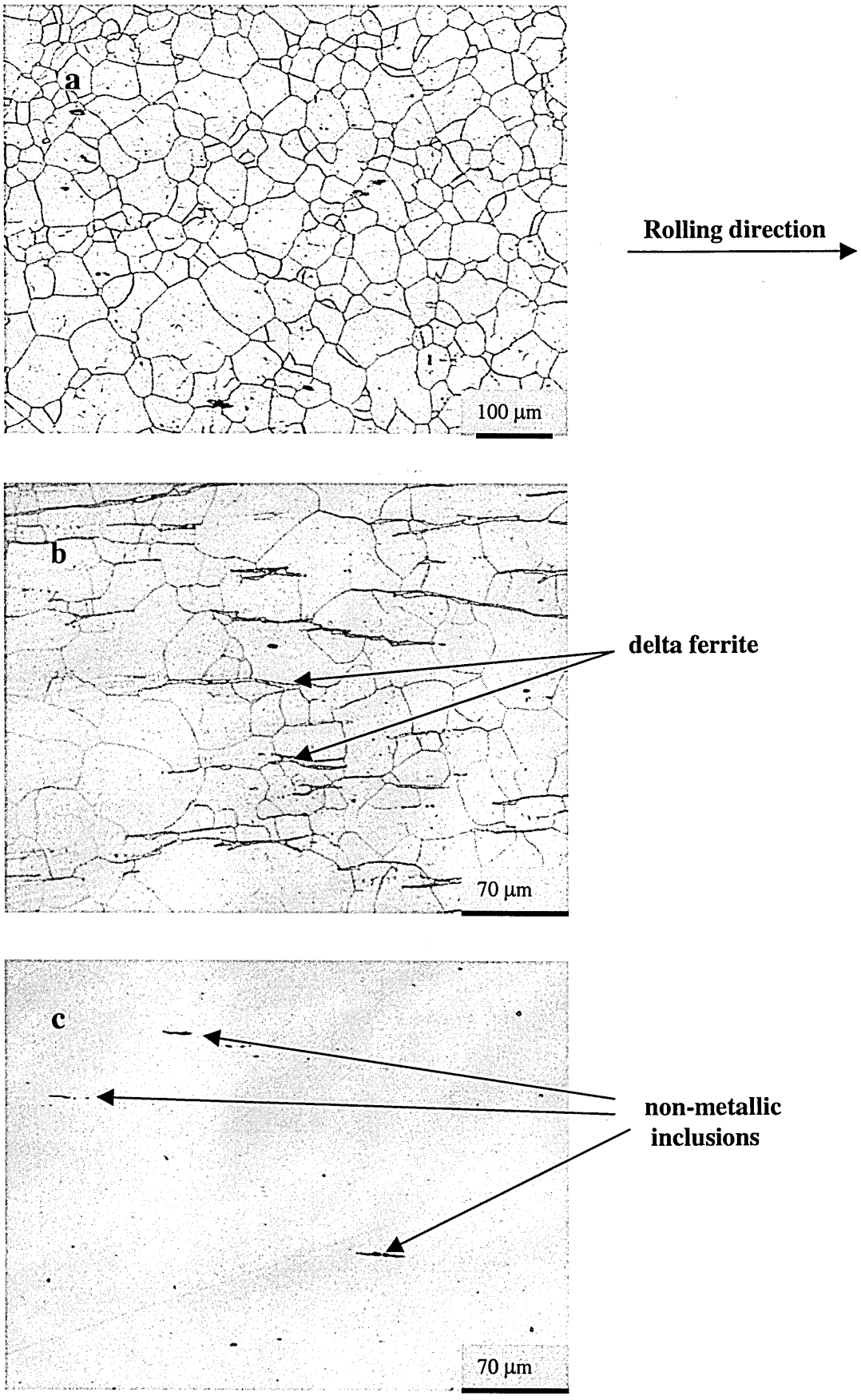

Figure 4.1. Microstructure of the UNS S31603 steel; a). Grain boundaries of the austenitic microstructure, b) delta ferrite (δ-α) along the rolling direction; c). Non-metallic inclusions.

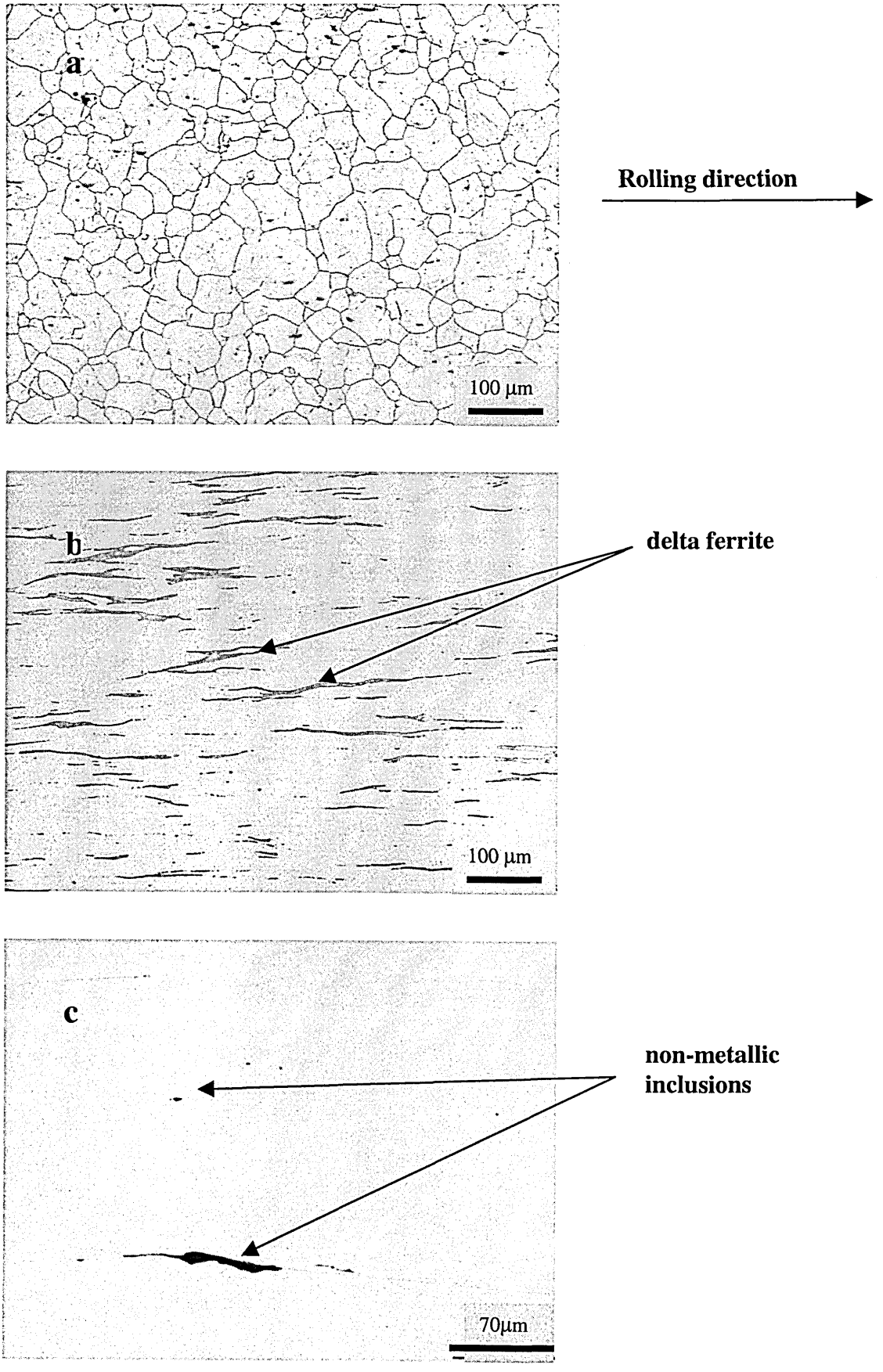

Figure 4.2. Microstructure of the UNS S30400 steel; a). Grain boundaries of the austenitic microstructure, b). delta ferrite (δ-α) along the rolling direction; c). Non-metallic inclusions.

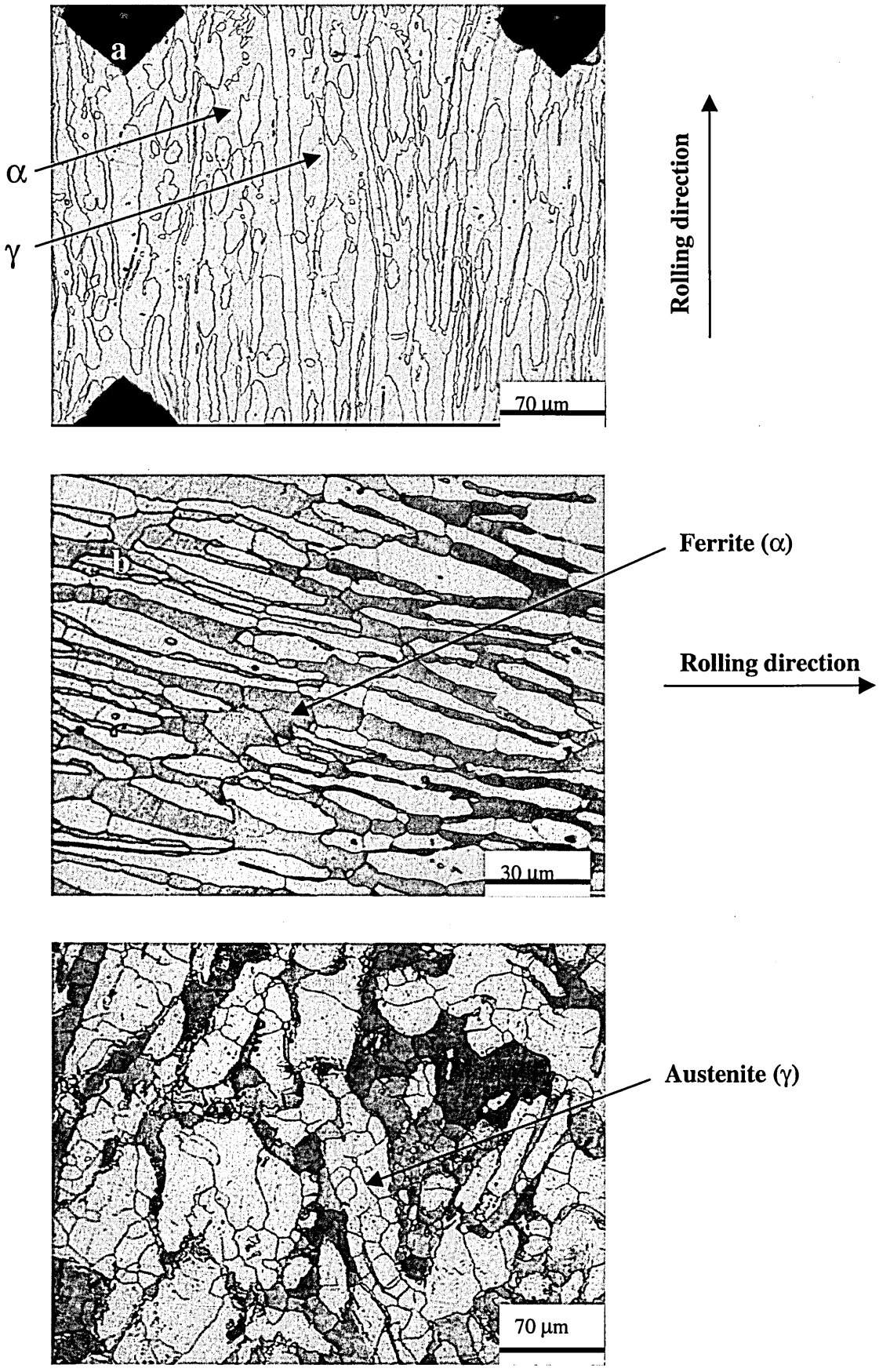

Figure 4.3. Microstructure of the UNS S31803 steel; a) The two phases of the duplex steel, austenite (γ) and ferrite (α). b) The grain boundaries in the ferritic phase c). The grain boundaries in the austenitic phase.

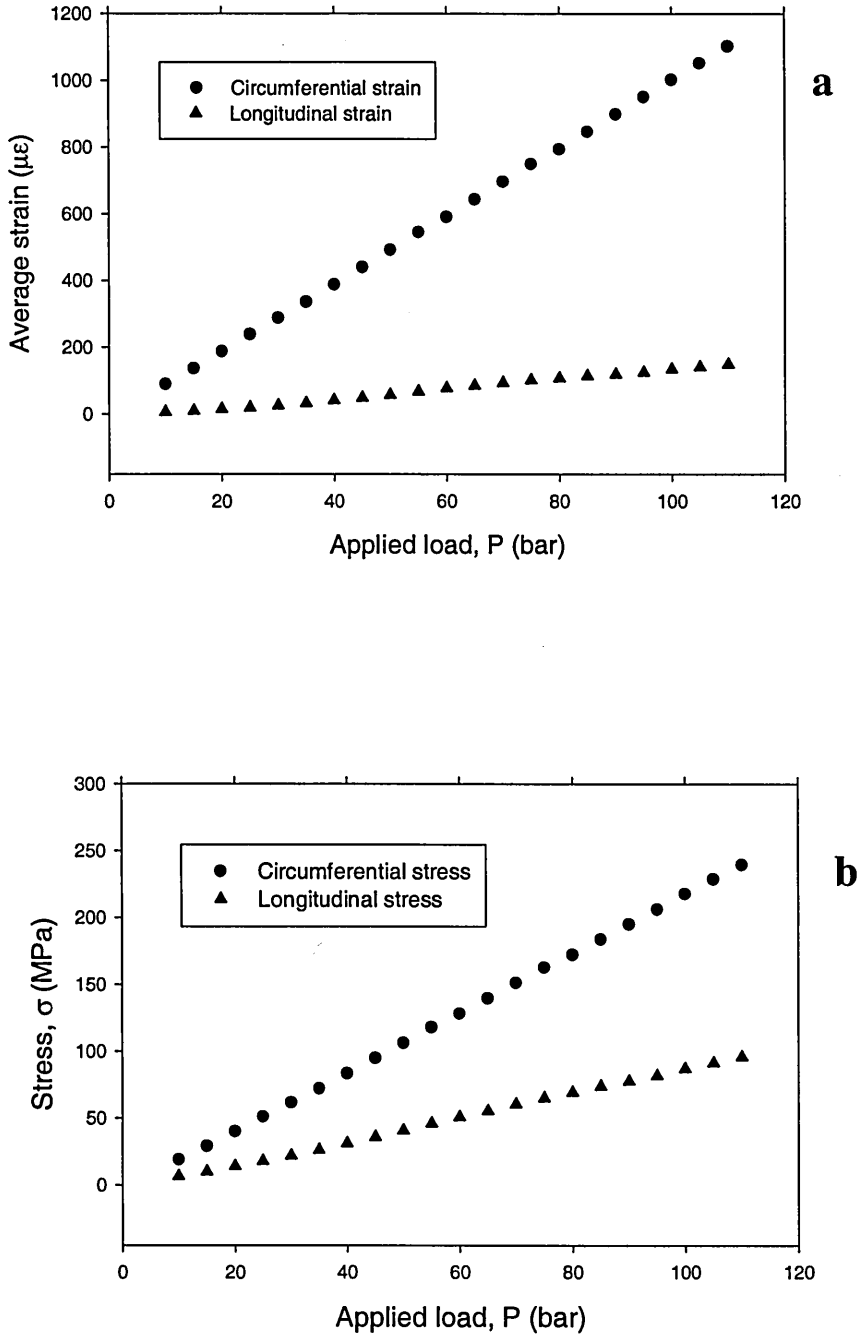

Figure 4.4. Strain and stress induced in the S31603 specimens by the application of pressure by the hydraulic system. a) Strain vs applied pressure and b) Stress vs applied pressure.

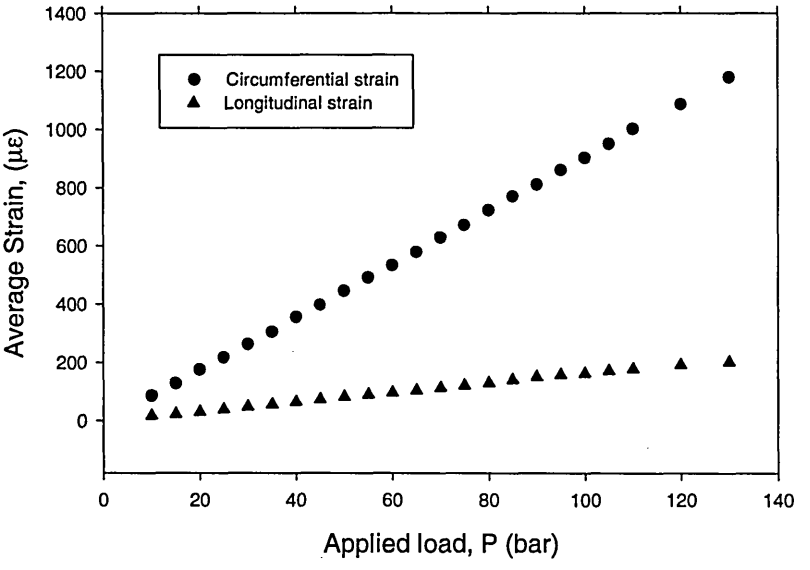

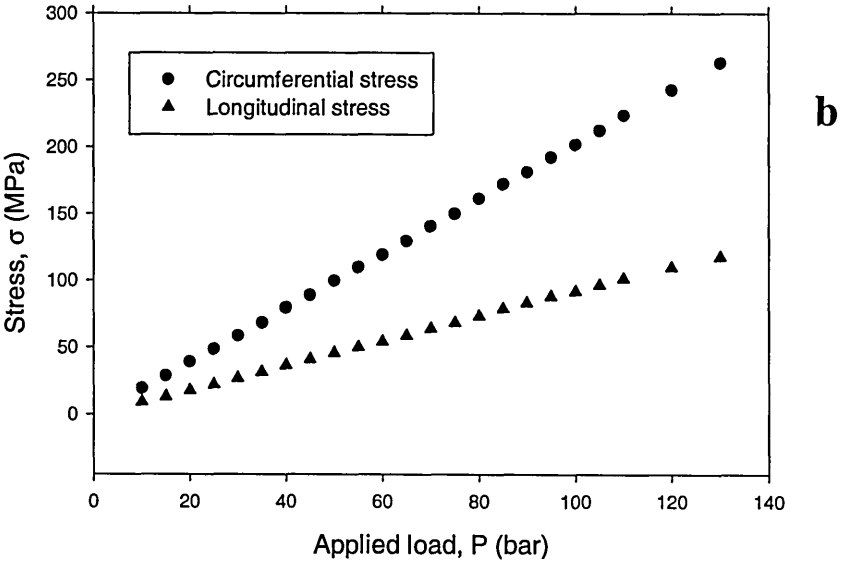

Figure 4.5. Strain and stress induced in the specimen of steel S31603 by the application of pressure by the hydraulic system. a) Strain vs applied pressure and b) Stress vs applied pressure.

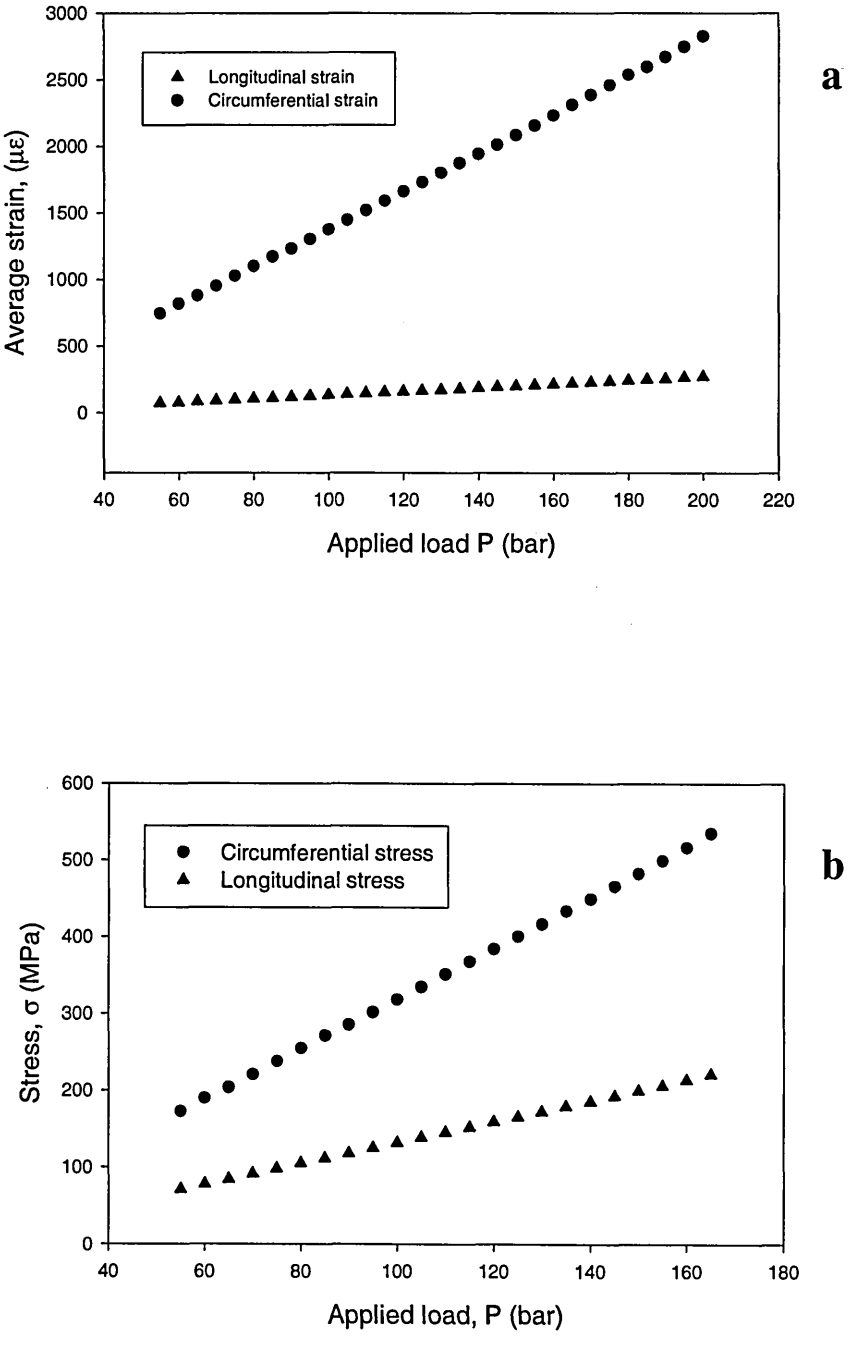

Figure 4.6. Strain and stress induced in the S31803 specimens by the application of pressure by the hydraulic system. a) Strain vs applied pressure and b) Stress vs applied pressure.

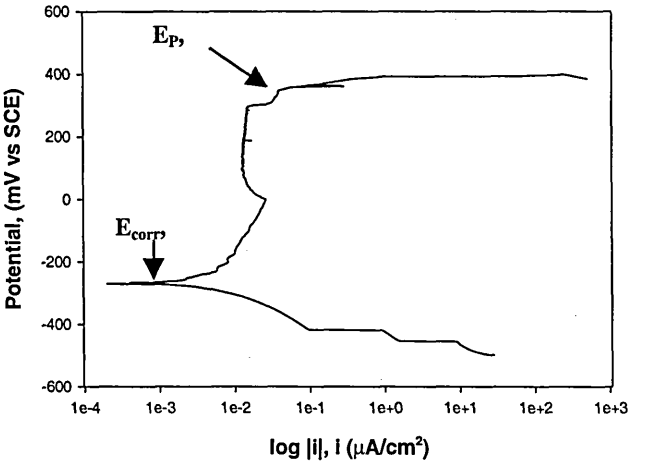

Figure 4.7. Polarisation curve for S31603 steel in artificial seawater, pH 8.2, T=26°C, scan rate 10 mV/min.

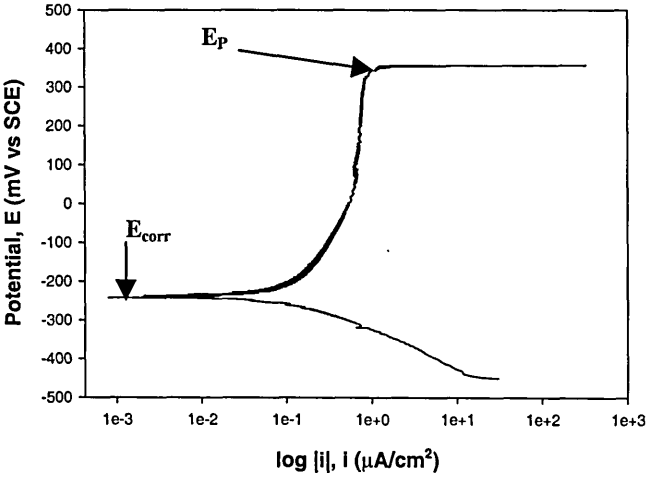

Figure 4.8. Polarisation curve for S30400 steel in artificial seawater, pH 8.2, T=26°C, scan rate 10 mV/min.

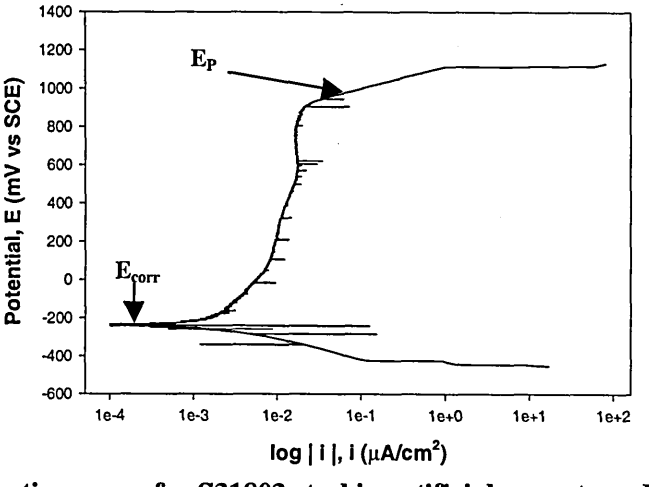

Figure 4.9. Polarisation curve for S31803 steel in artificial seawater, pH 8.2, T=26°C, scan rate 10 mV/min.

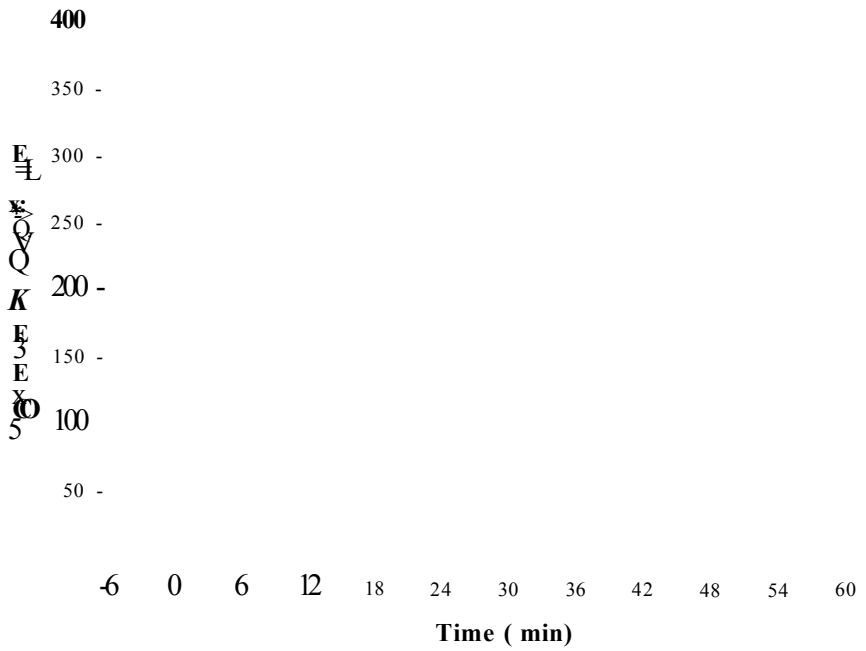

Figure 4.10. Pit depth vs polarisation time for the pre-pitting tests on S31603 steel samples in seawater, (Conditions are given in fig. 3.9).

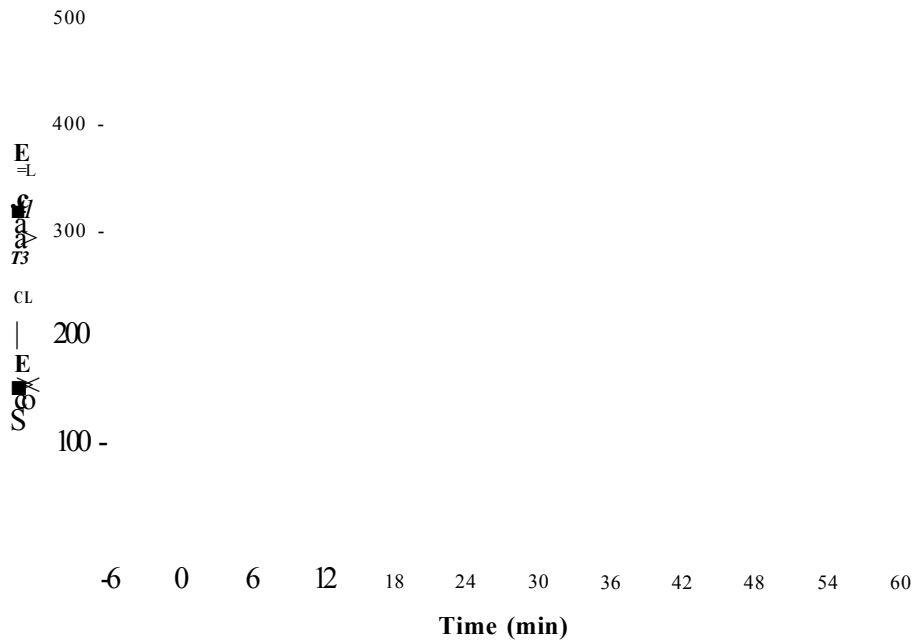

Figure 4.11. Pit depth vs polarisation time for the pre-pitting tests on S30400 steel samples in seawater , (Conditions are given in fig. 3.9).

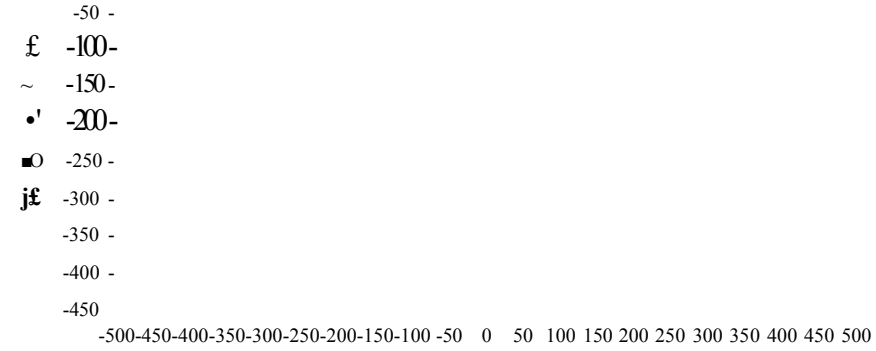

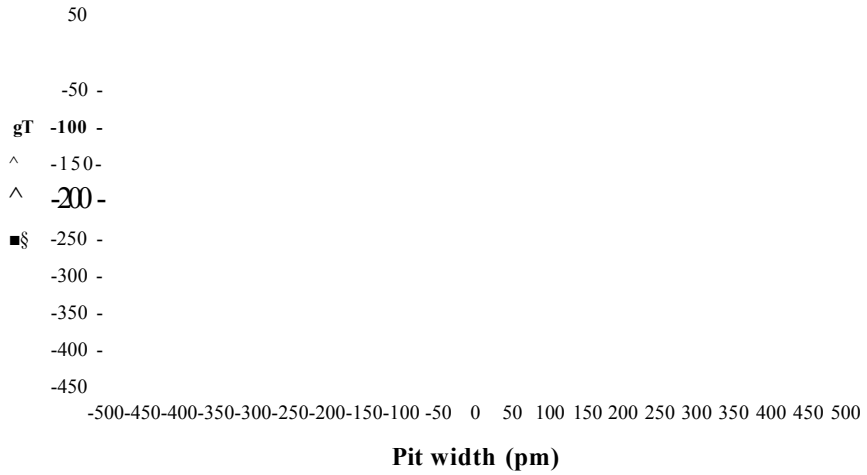

• In Red: minor axis, • In Black: major axis

Figure 4.12. Pit profile for UNS S31603 steel samples polarised for: a) 24 and b) 60 minutes at 280 mV vs SCE under condition of no rotation.

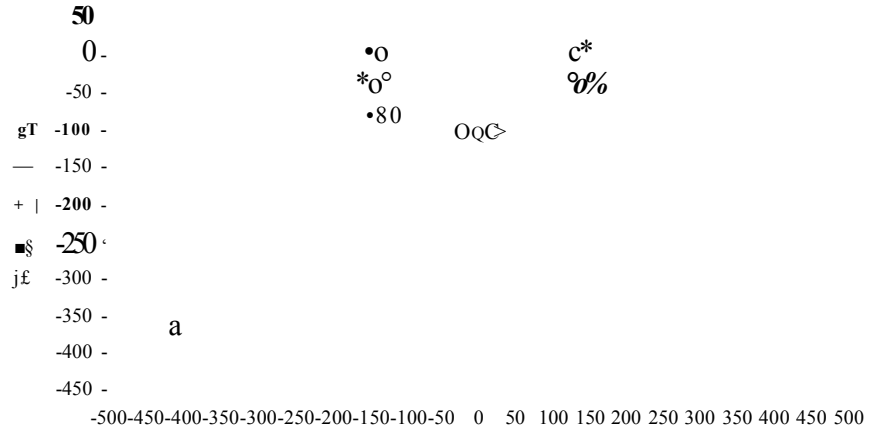

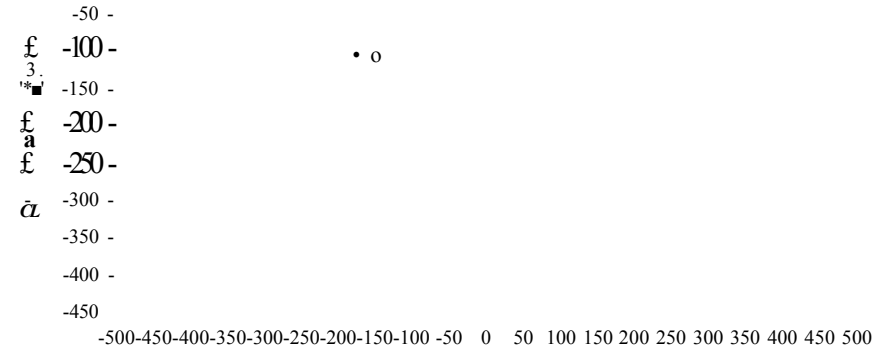

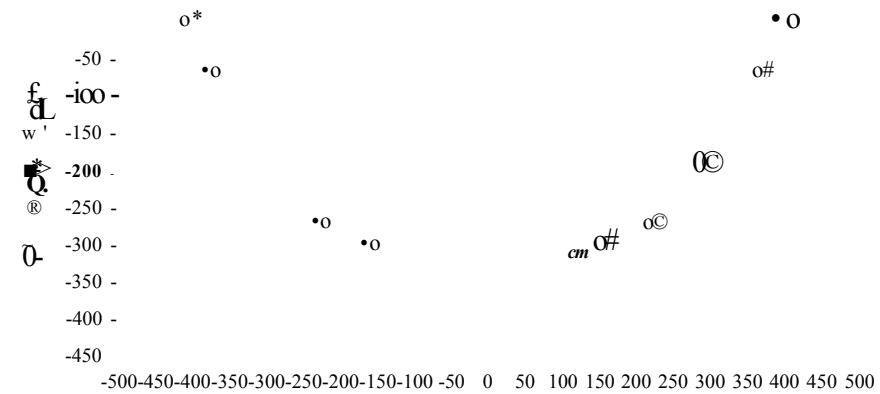

• In Red: minor axis, • In Black: major axis

Figure 4.13. Pit profile for UNS S30400 steel samples polarised for: a) 6, b) 12 and c) 54 minutes at 290 mV vs SCE under condition of no rotation.

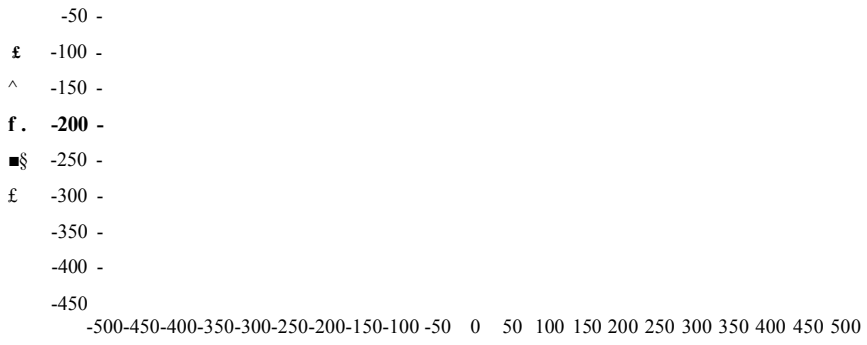

Figure 4.14. Pit profile for cylindrical specimen of S31603 steel polarised 60 min at 290 mV vs SCE and rotating at 100 rpm.

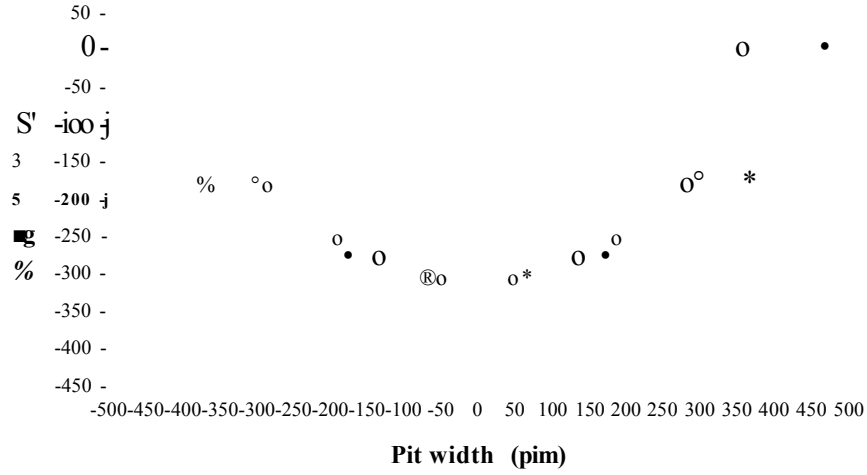

Figure 4.15. Pit profile for cylindrical specimen of S30400 steel polarised 60 min at 290 mV vs SCE and rotating at 100 rpm.

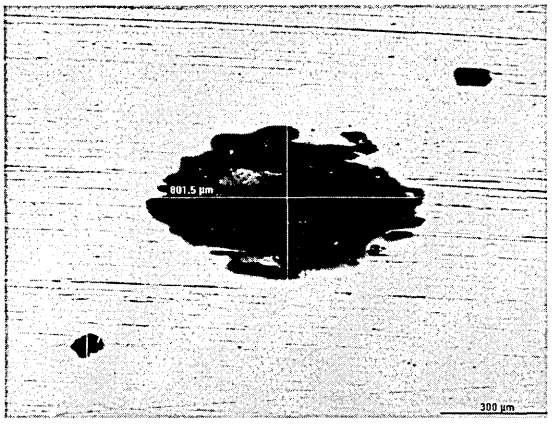

First indentation (not shown)
removed thickness: 0 µm

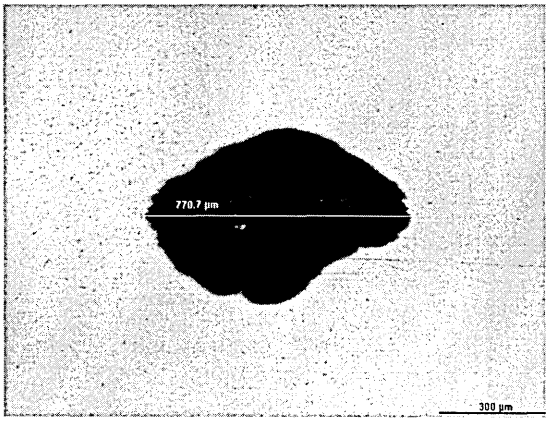

Second indentation (not shown)
removed thickness: 91 µm

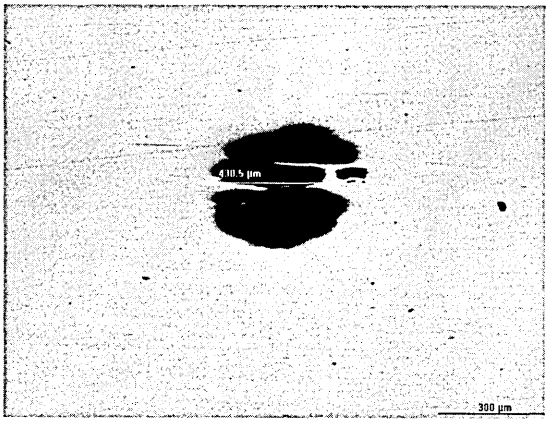

Second indentation (not shown)
removed thickness: 182 µm

Figure 4.16. Sequence of pit depth and width measurements during the material removal procedure on a sample of S31603 steel subjected to anodic polarisation for 36 min at 280 mV vs SCE.

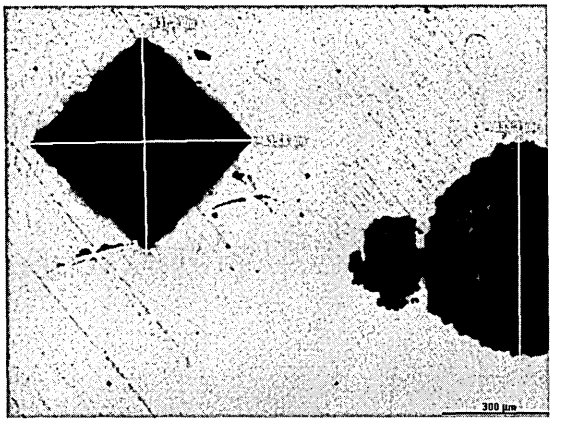

First indentation
removed thickness: 0 μm

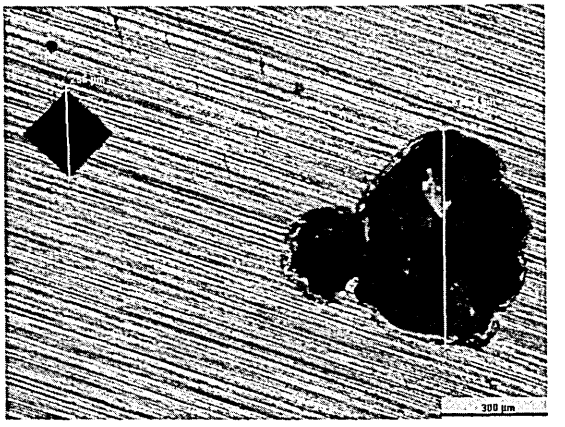

First indentation
removed thickness: 54 μm

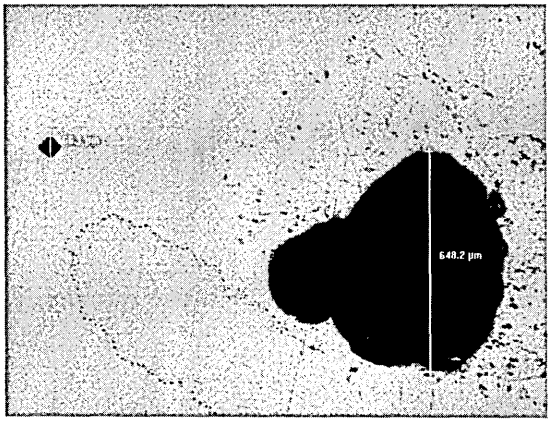

First indentation
removed thickness: 81 μm

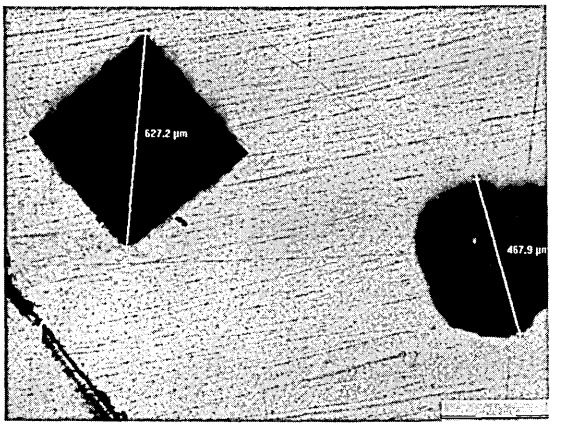

Third indentation
removed thickness: 181 μm

Figure 4.17. Sequence of pit depth and width measurements during the material removal procedure on a sample of S30400 steel subjected to anodic polarisation for 30 min at 290 mV vs SCE.

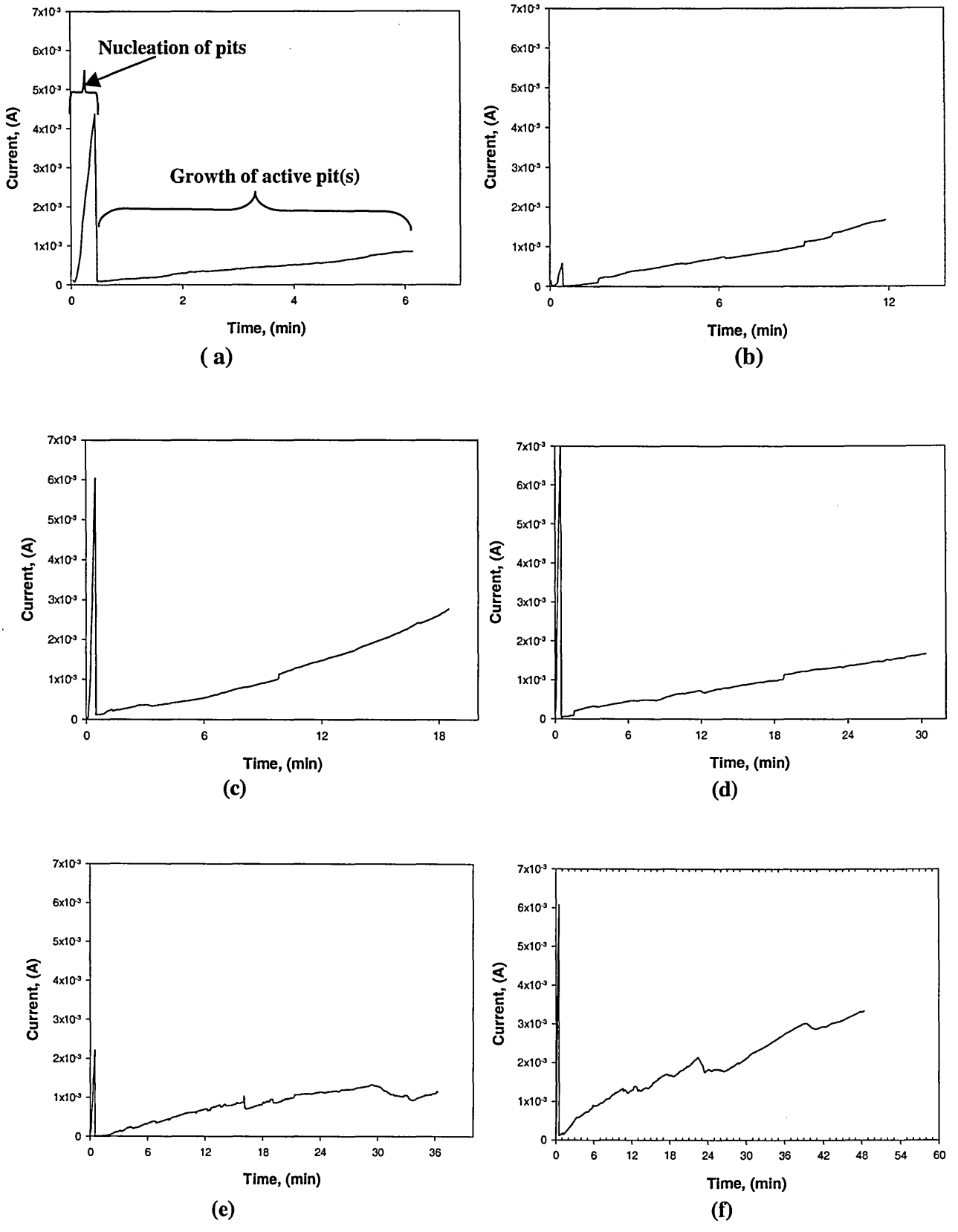

Figure 4.18. Chronoamperometry plots during pit generation on S31603 steel in artificial seawater. Stationary samples polarised: a) 6, b) 12, c) 18, d) 30, e) 36 and f) 48 minutes at 280 mV vs SCE.

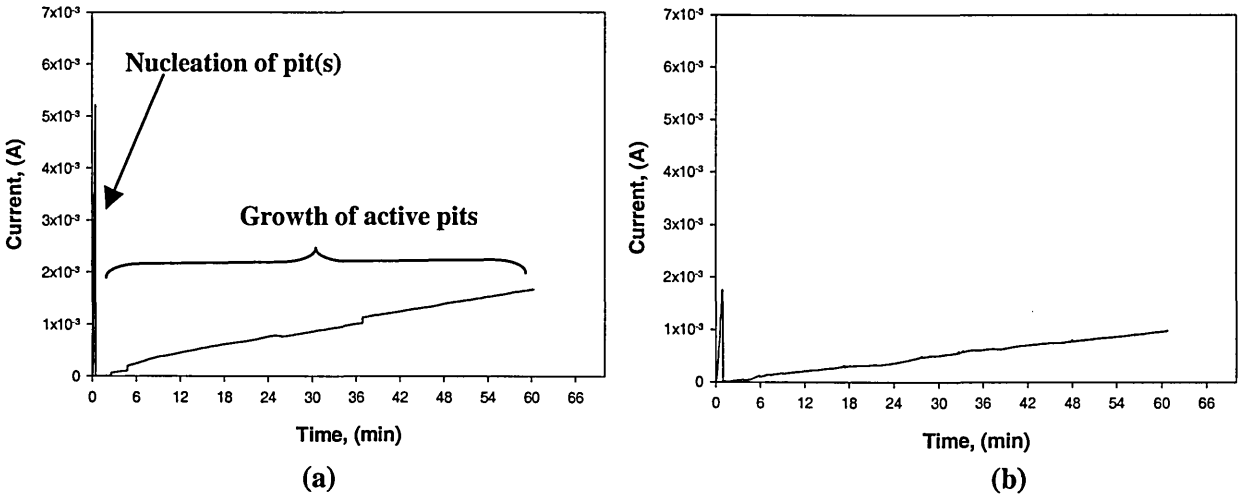

Figure 4.19. Chronoamperometry plots during pit generation on S31603 steel in artificial seawater. Specimens polarised 60 min at 280 mV vs SCE a) stationary and b) rotating at 100 rpm.

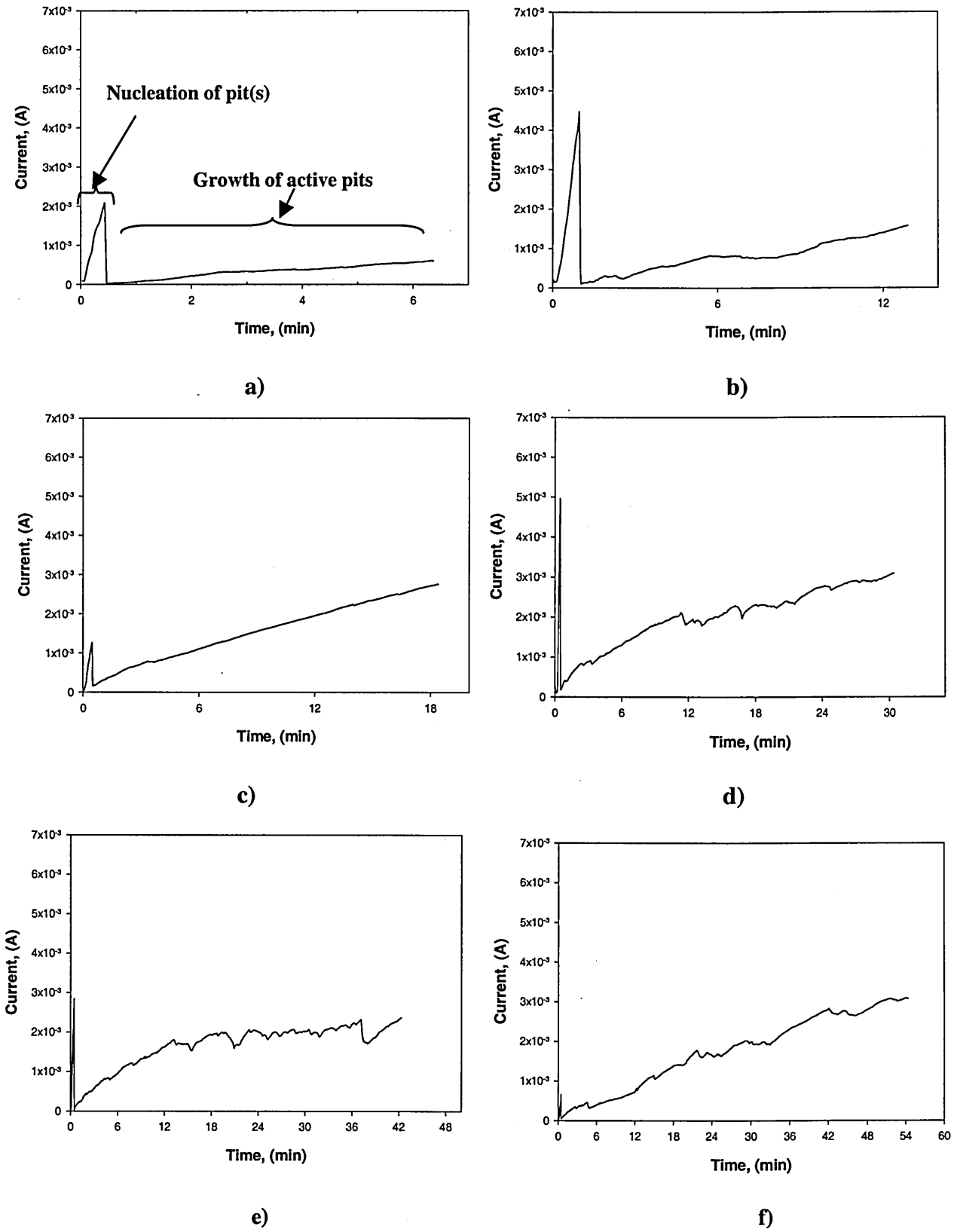

Figure 4.20. Chronoamperometry plots during pit generation on S30400 steel in artificial seawater. Stationary sample polarised: a) 6, b) 12, c) 18, d) 30, e) 42 and f) 54 minutes at 290 mV vs SCE.

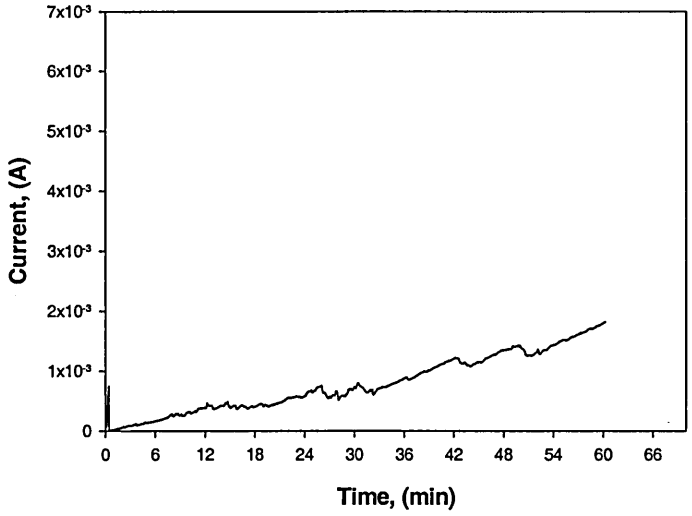

Figure 4.21. Chronoamperometry during pit generation on 304 SS in artificial seawater. Specimen rotating at 100 rpm polarised 60 min at 290 mV vs SCE .

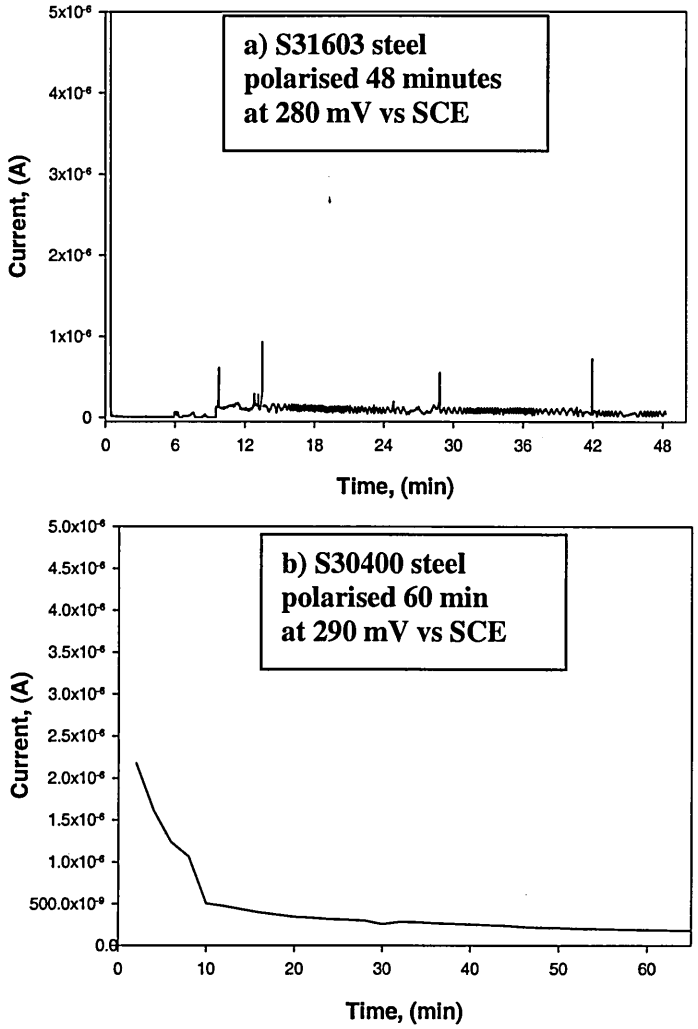

Figure 4.22. Chronoamperometry plots of samples under anodic polarisation in artificial seawater which did not develop pits.

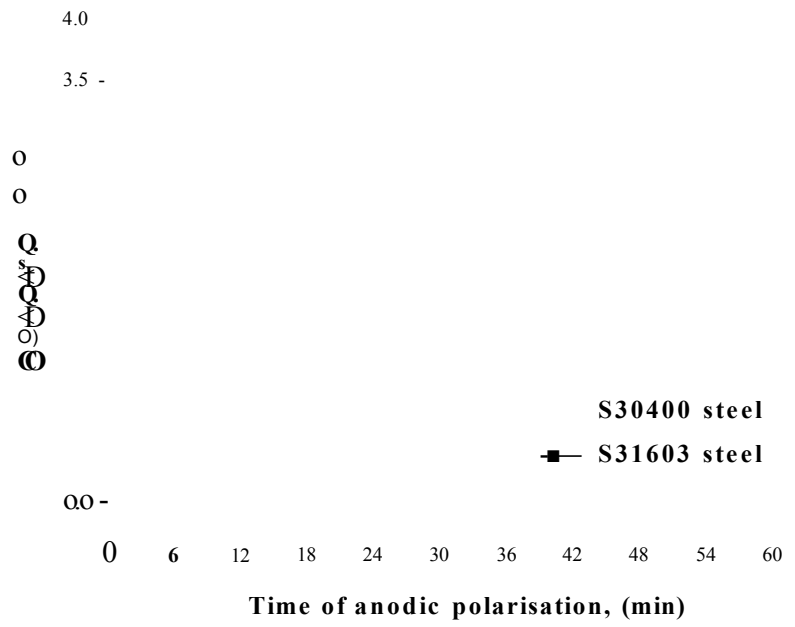

Figure 4.23. a) Quantity of charge per pit as a function of the polarisation time.

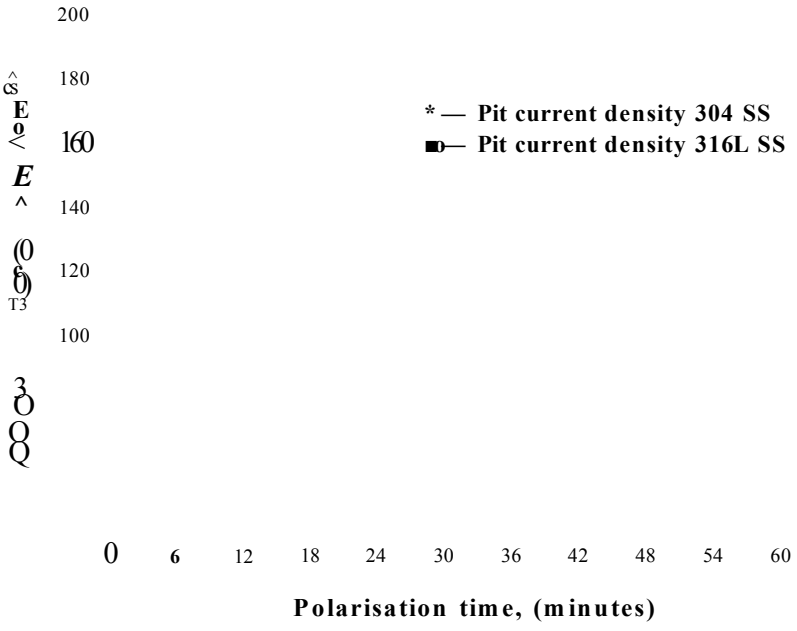

Figure 4.23b) Current density per pit as function of the polarisation time for 304 and 316L SS's obtained from DC measurements.

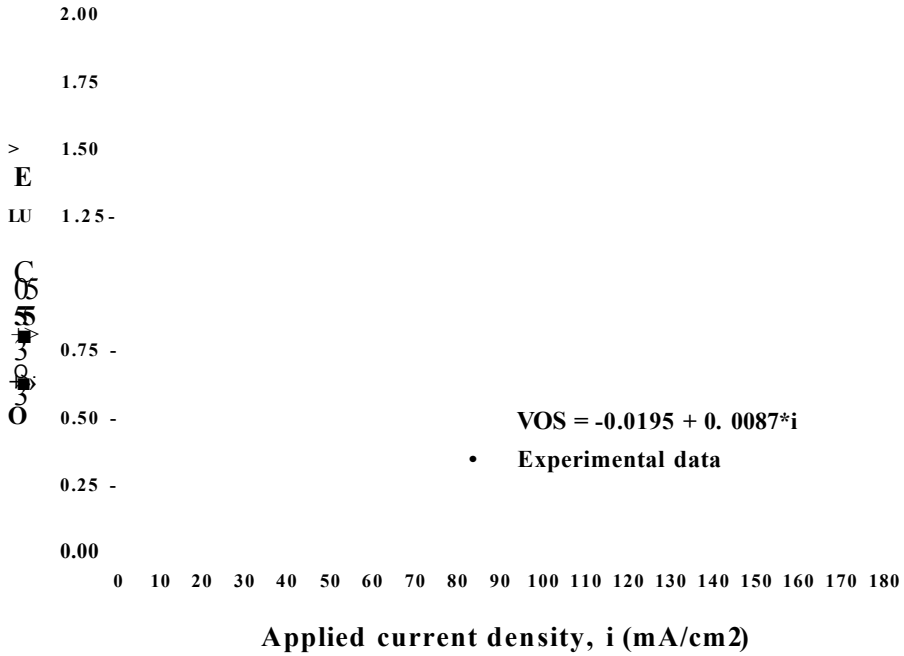

Figure 4.24. Current density - output signal calibration for the SRET measurements using the PIS specimen in synthetic seawater (39 g/I sea salts).

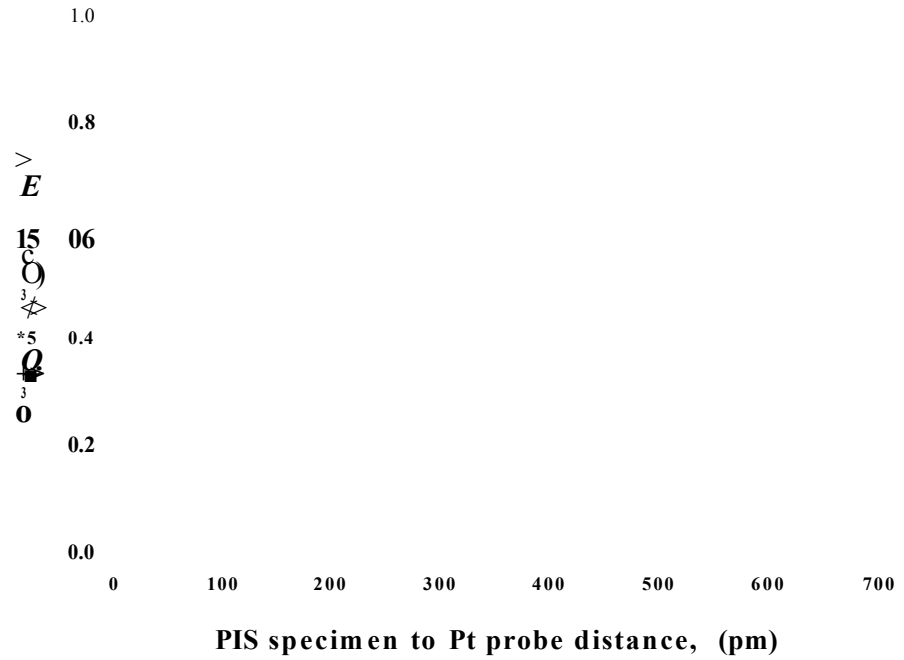

Figure 4.25. Output signal vs Pt probe - PIS distance calibration for an applied current of 25 pA (80 mA/cm2) in synthetic seawater (39 g/1 sea salts).

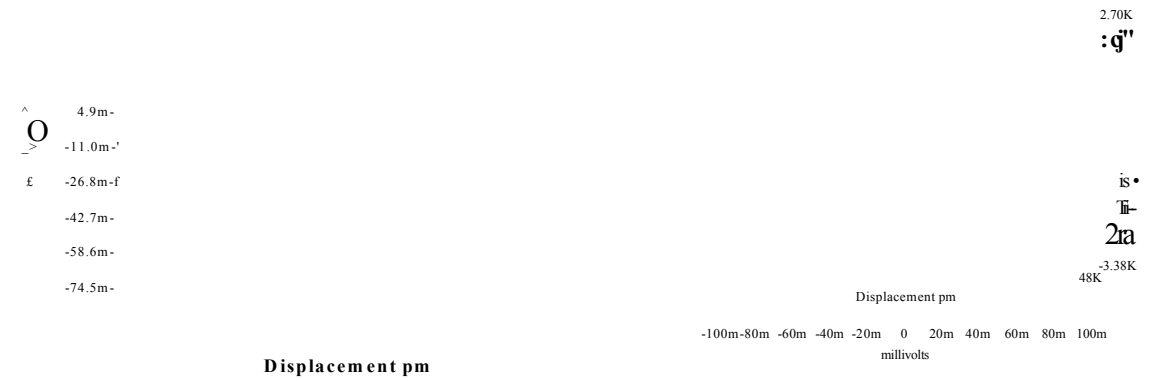

Figure 4.26 Calibration area map and line scans in artificial seawater for an applied current of 2.1 pA, i = 6.4 mA/cm2, Maximum output signal = 0.047 mV.

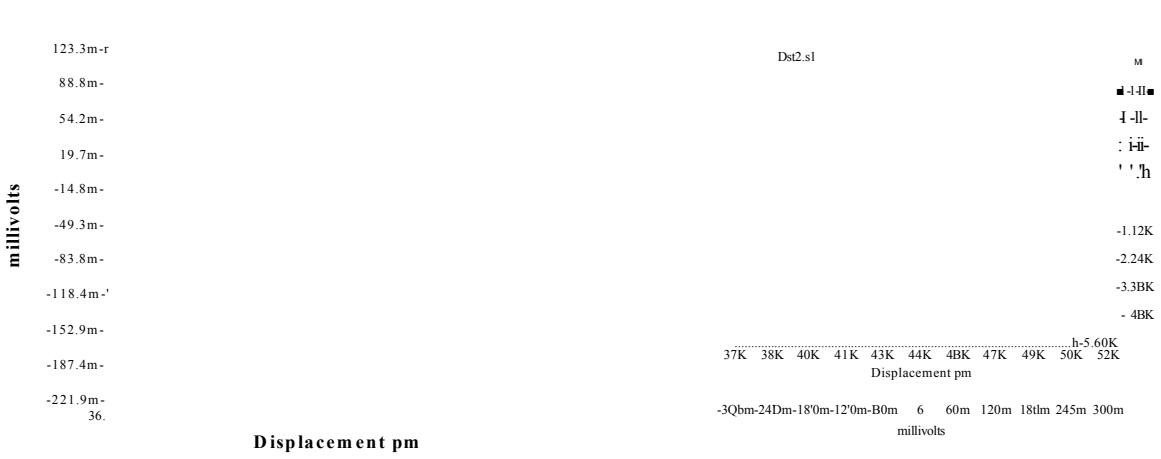

Figure 4.27 Calibration area map and line scans in artificial seawater for an applied current of 4.2 pA, i = 12.8 mA/cm2, Maximum output signal = 0.093 mV.

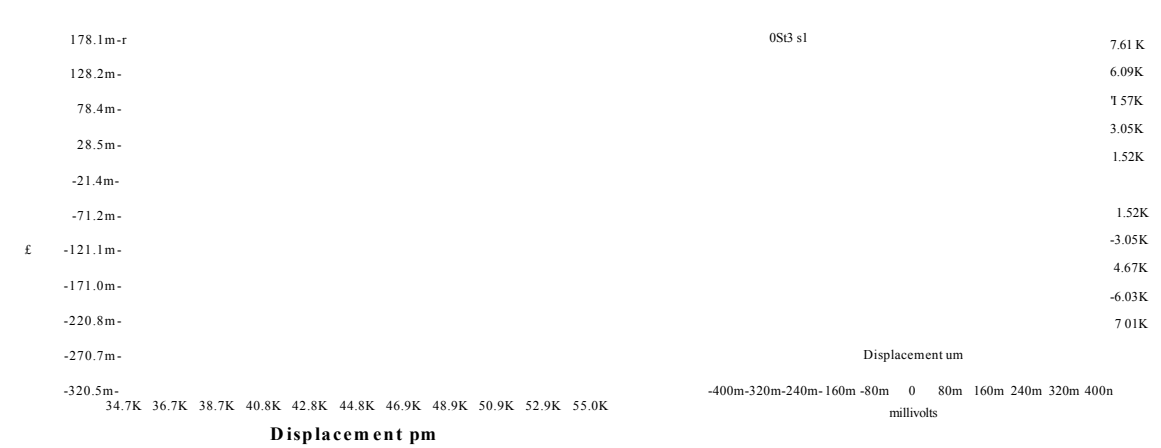

Figure 4.28 Calibration area map and line scans in artificial seawater for an applied current of 6.5 pA, i = 19.76 mA/cm2, Maximum output signal = 0.163 mV.

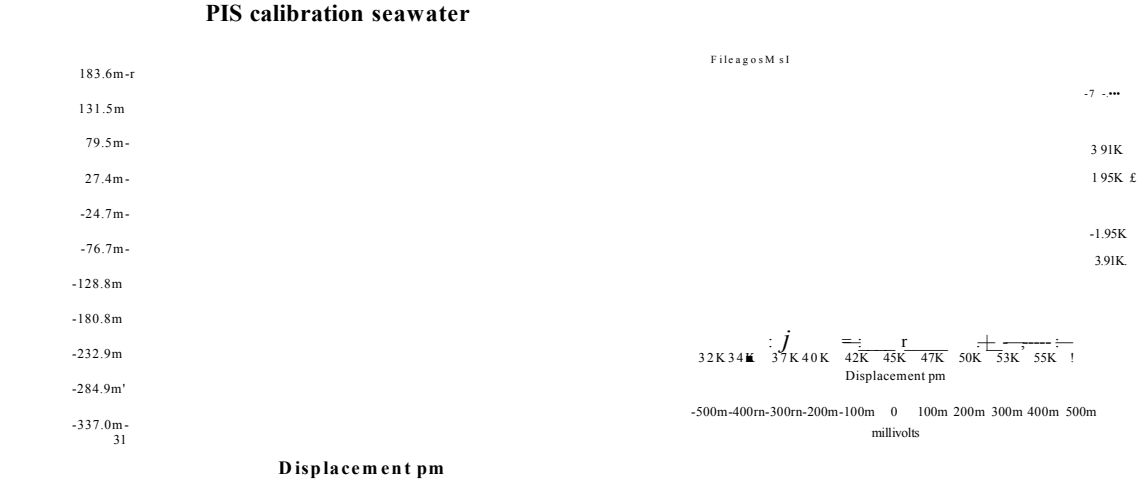

Figure 4.29 Calibration area map and line scans in artificial seawater for an applied current of 8.8 pA, i = 26.8 mA/cm2, Maximum output signal = 0.226 mV.

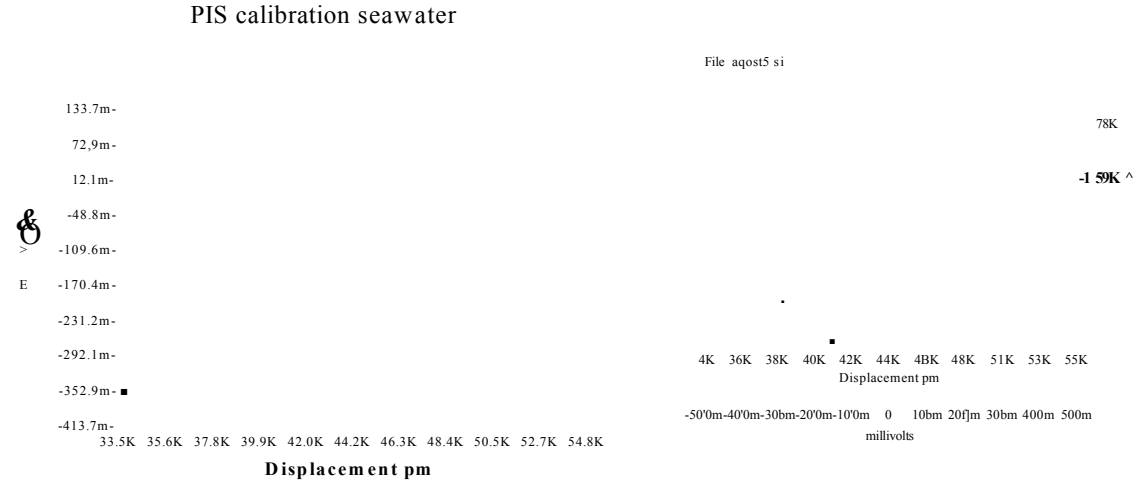

Figure 4.30 Calibration area map and line scans in artificial seawater for an applied current of 11.0 pA, i = 33.8 mA/cm2, Maximum output signal = 0.327 mV.

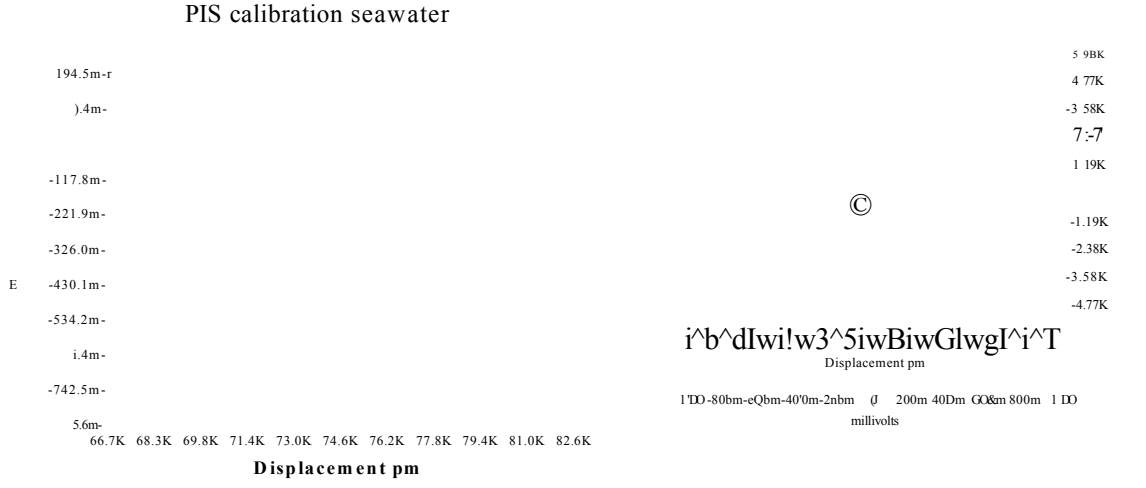

Figure 4.31 Calibration area map and line scans in artificial seawater for an applied current of 27 p.A, i = 85 mA/cm2, Maximum output signal = 0.620 mV.

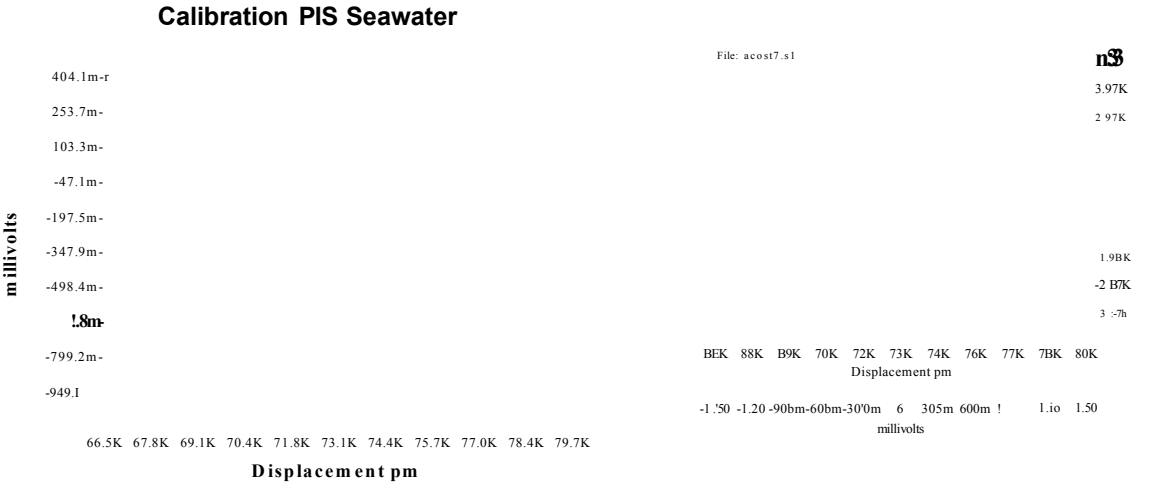

Figure 4.32 Calibration area map and line scans in artificial seawater for an applied current of 55.8 pA, i = 170 mA/cm2, Maximum output signal = 1.02 mV.

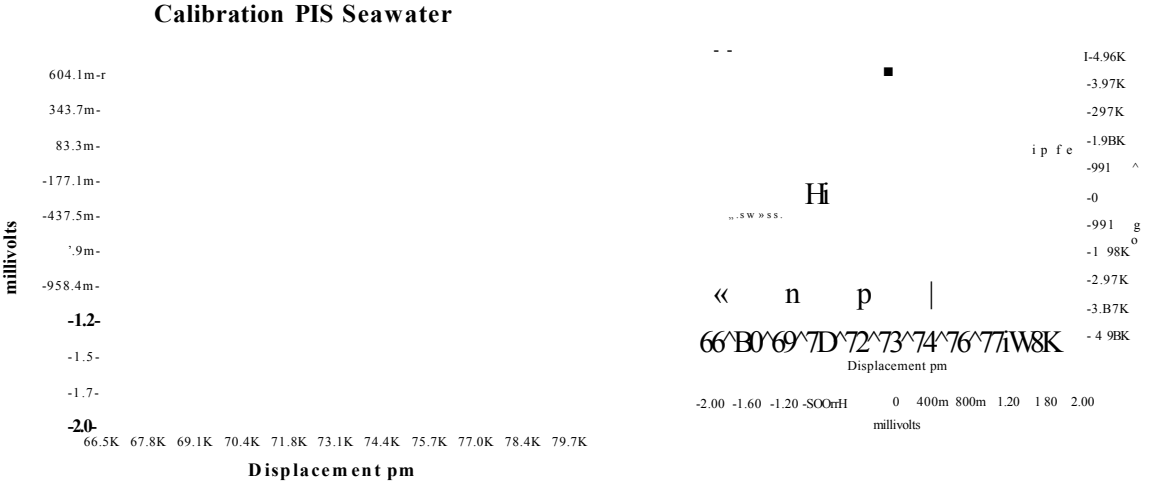

Figure 4.33 Calibration area map and line scans in artificial seawater for an applied current of 84 pA, i = 256 mA/cm2, Maximum output signal = 1.91 mV.

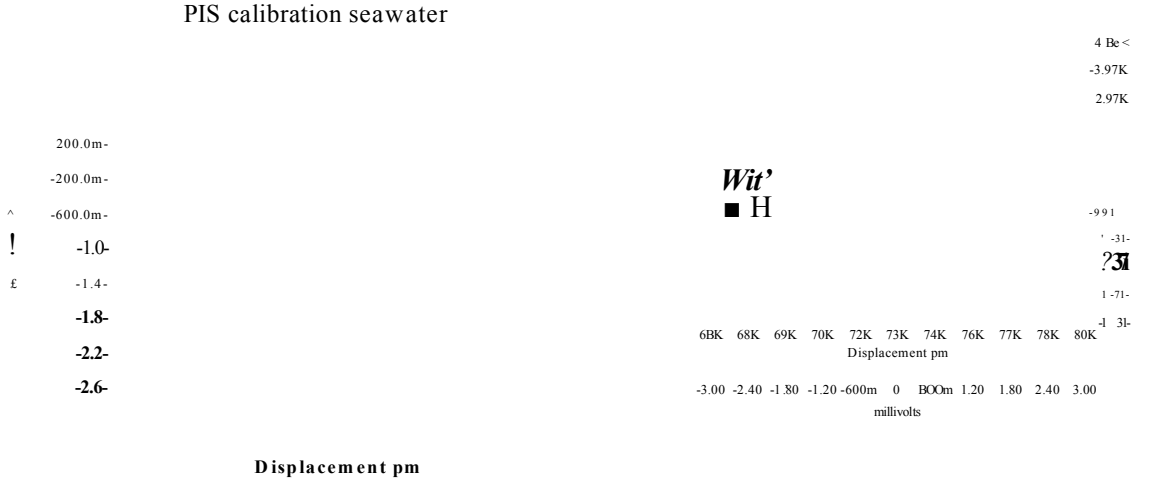

Figure 4.34 Calibration area map and line scans in artificial seawater for an applied current of 111 pA, i = 340 mA/cm2, Maximum output signal = 2.43 mV.

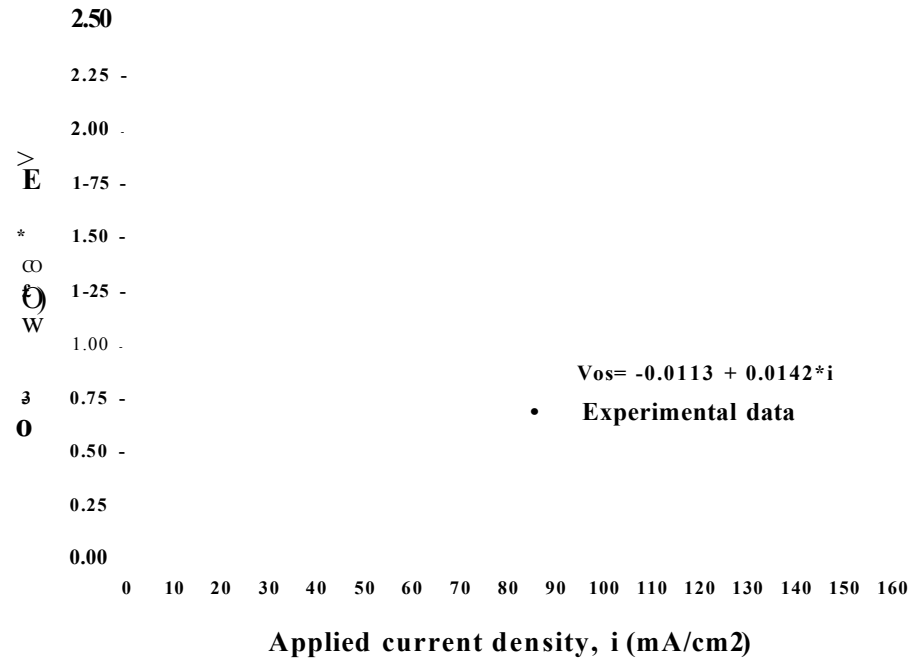

Figure 4.35. Current density - output signal calibration for the SRET measurements using the PIS specimen in 0.05 M FeCl3 solution.

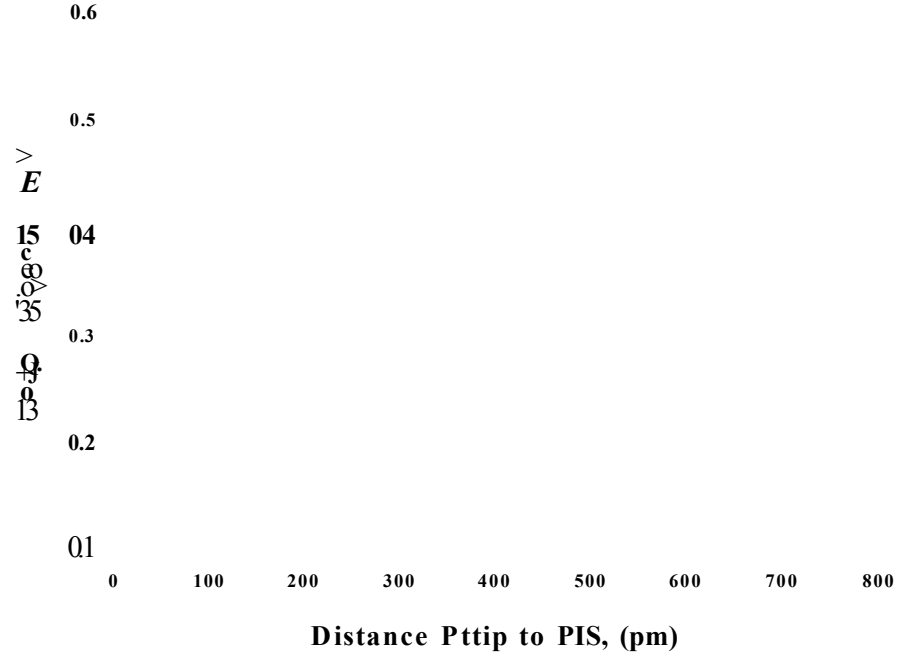

Figure 4.36. Output signal vs Pt probe - PIS distance calibration for an applied current of 10 pA (30.6 mA/cm2) in 0.05 M FeCl3 solution.

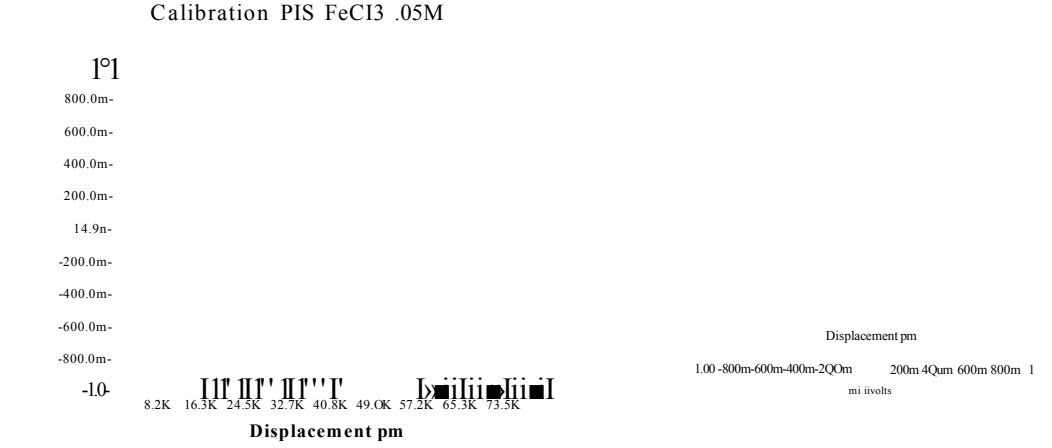

Line scan for an applied current of 2.4 pA (i = 7.34 mA/cm2), maximum output signal: 0.093 mV

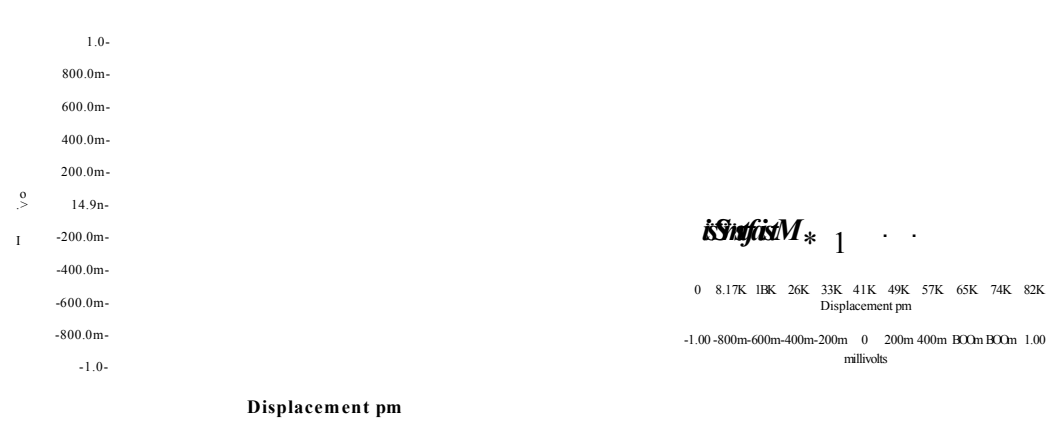

Line scan for an applied current of 4 pA (i = 12.4 mA/cm2), maximum output signal: 0.23 mV

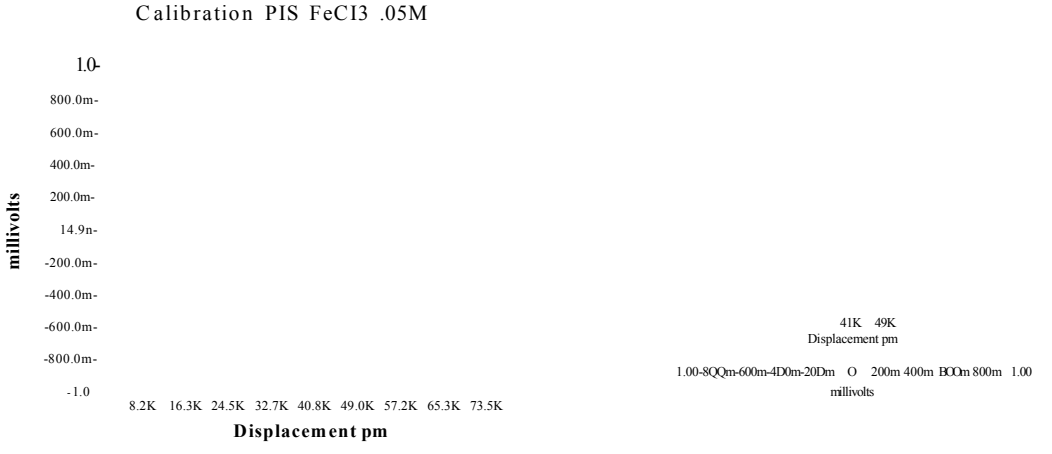

Line scan for an applied current of 13.67 pA (i = 41.8 mA/cm2), maximum output signal: 0.58 mV

Figure 4.37(a) Calibration line scans in FeCl3 solution for different applied current from 2.4 to 13.7 pA.

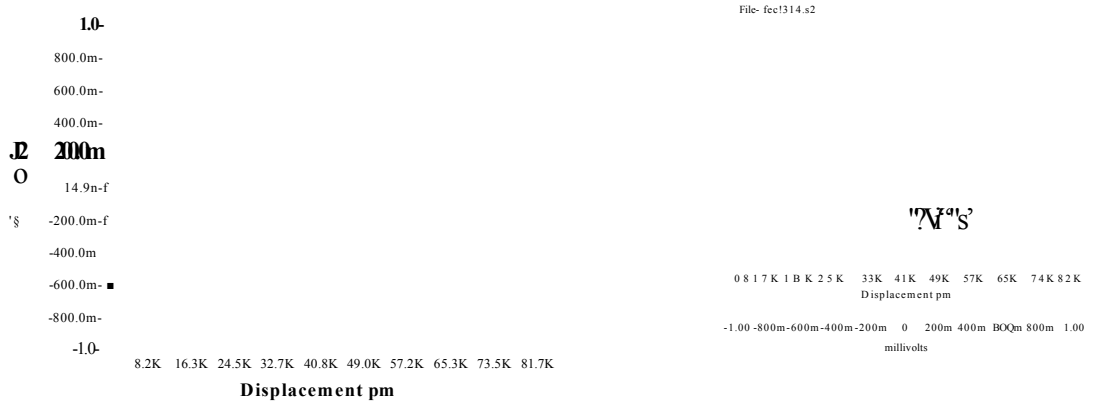

Line scan for an applied current of 23.1 pA (i = 70.58 mA/cm2), maximum output signal: 0.99 mV

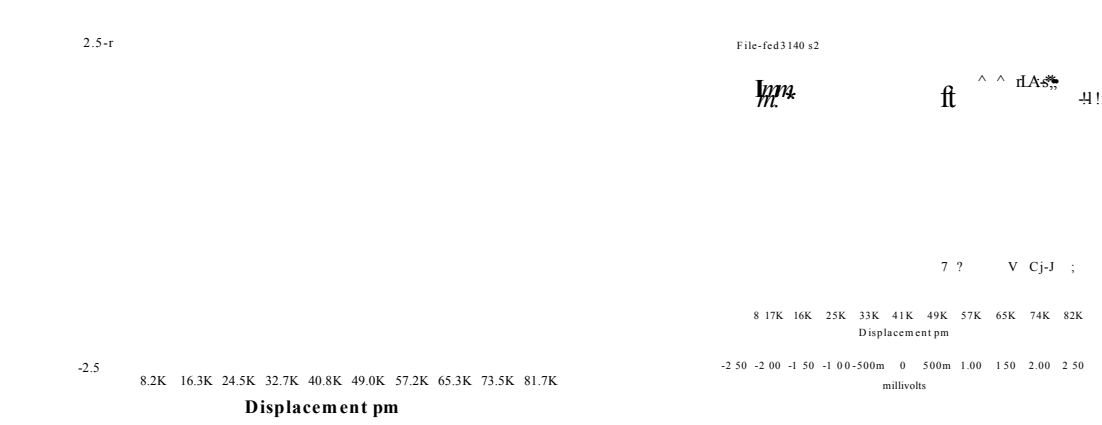

Line scan for an applied current of 34.6 pA (i = 105.8 mA/cm2), maximum output signal: 1.49 mV

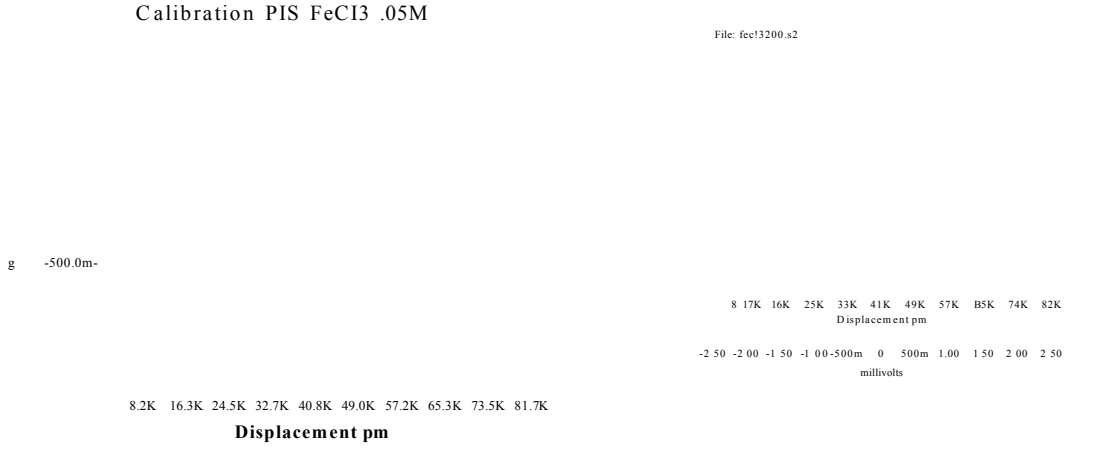

Line scan for an applied current of 46.27 pA (i = 141.5 mA/cm2), maximum output signal: 1.98 mV

Figure 4.37(b) Calibration line scans in FeCl3 solution for different applied current from 23.1 to 46.27 pA.

(a) (b) (c)

Figure 4.38 SRET area maps for specimens of 316L SS in artificial seawater at: a) free corrosion potential (-210 mV vs SCE), b) anodic potential 360 and c) 290 mV vs SCE

(a) (b)

Figure 4.39 SRET area maps for specimens of 304 SS in artificial seawater at: a) anodic potential of 280 and b) anodic potential of 350 mV vs SCE.

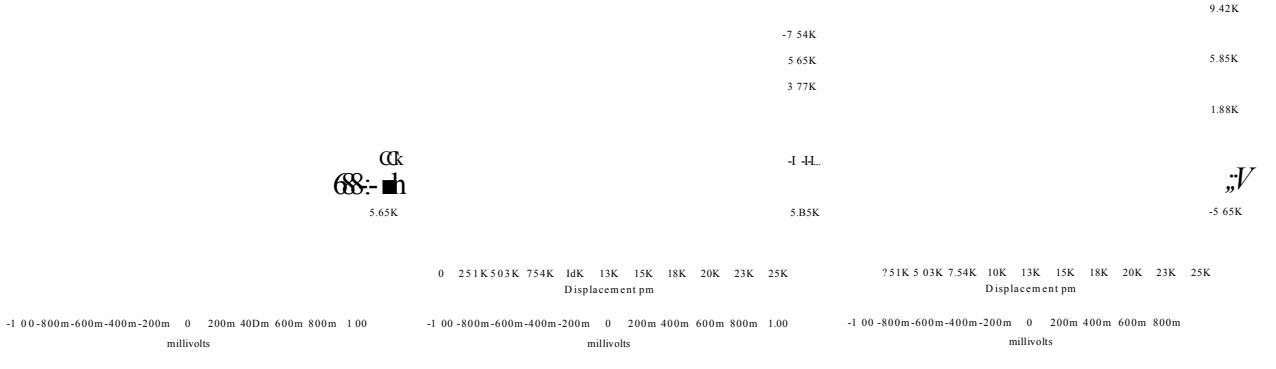

a) b) c)

Figure 4.40 SRET area maps for specimens of Duplex SS in artificial seawater at: a) free corrosion potential (-240 mV vs SCE), b) at an anodic potential of 1170 and c) at 1050 mV vs SCE

5 minutes

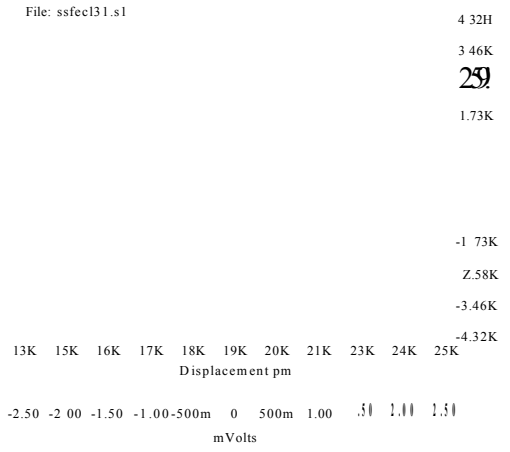

10 minutes

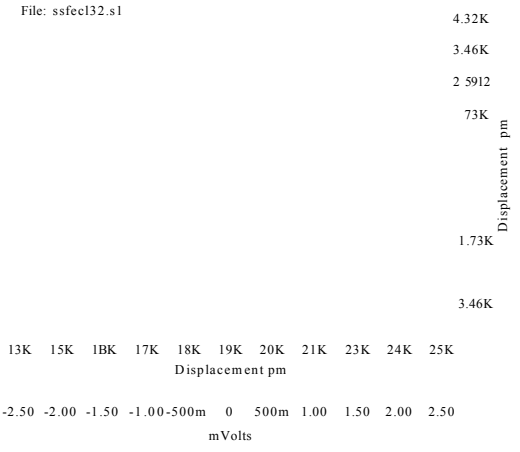

2 0 minutes

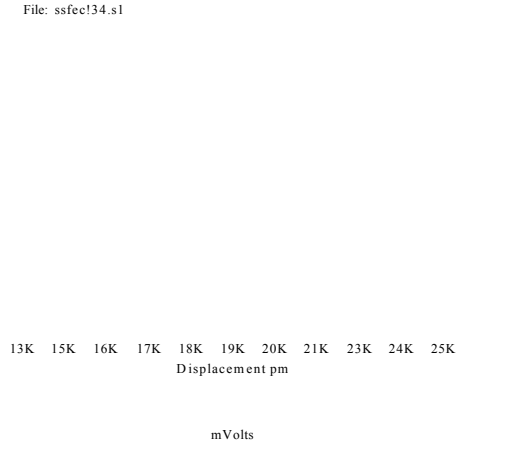

40 minutes

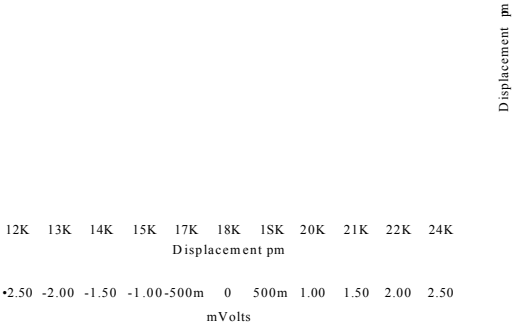

60 minutes

Figure 4.41. SRET area maps for 316L SS in 0.05 M FeCI3 at free corrosion potential after: 5, 10, 20, 40 and 60 minutes immersion

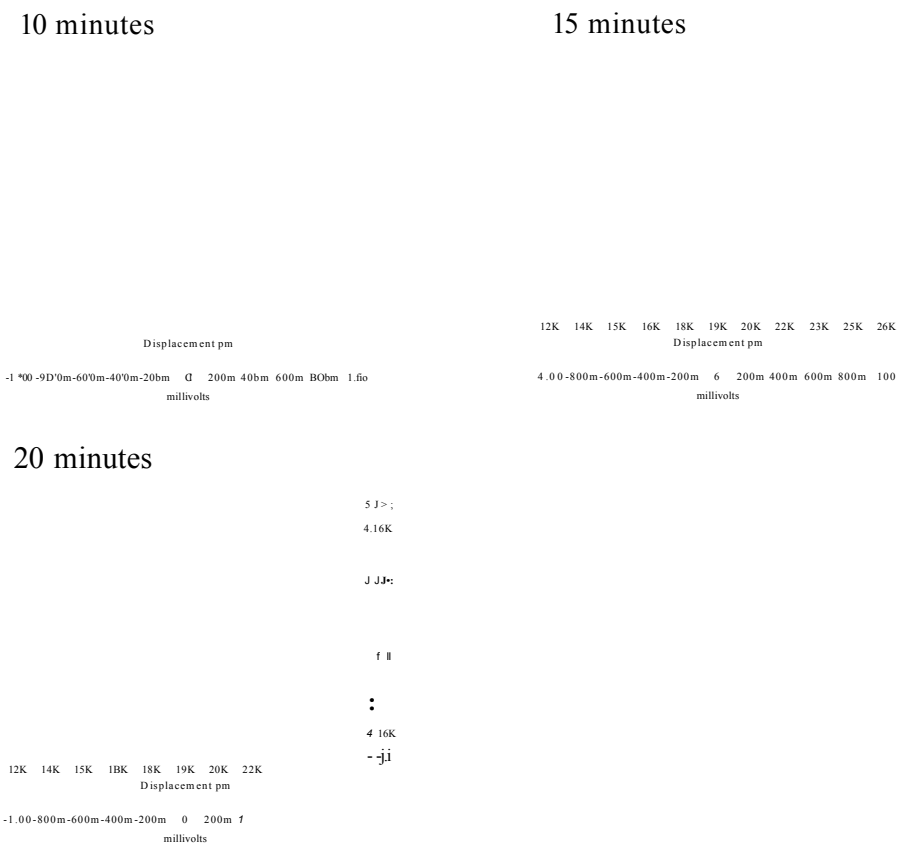

Figure 4.42. Area map scans for specimen of 304 SS in ferric chloride solution 0.05 M after 10,15 and 20 minutes immersion at open circuit potential without stress.

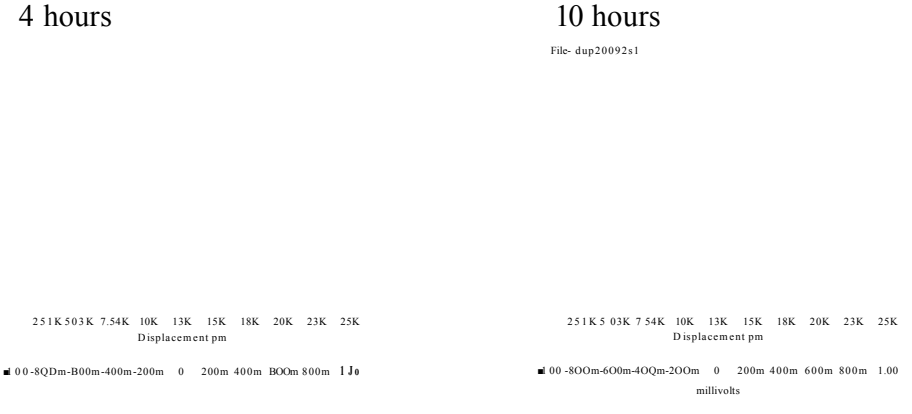

Figure 4.43. Area map scans for specimen of Duplex SS in ferric chloride solution 0.1 M at 4 and 10 hours immersion at open circuit potential without cyclic loading.

3 minutes

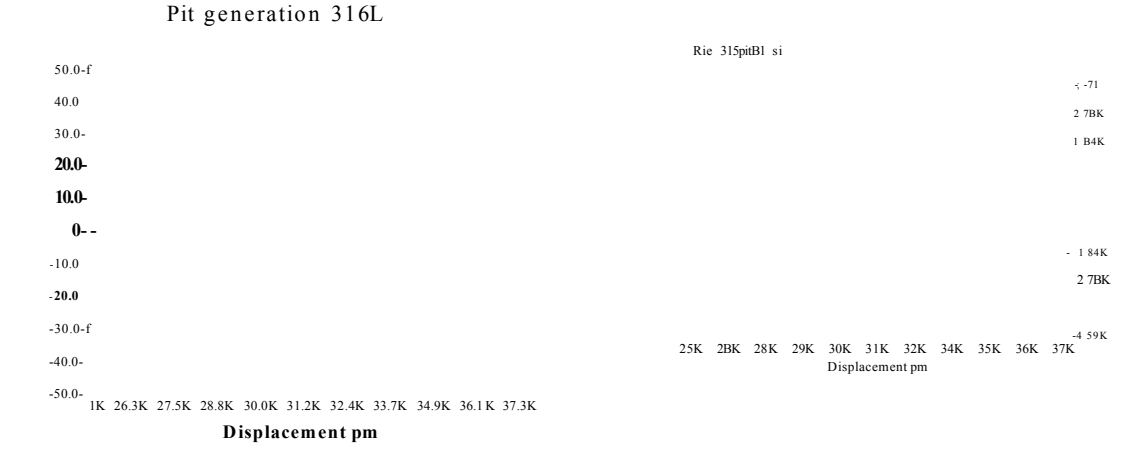

18.5 minutes

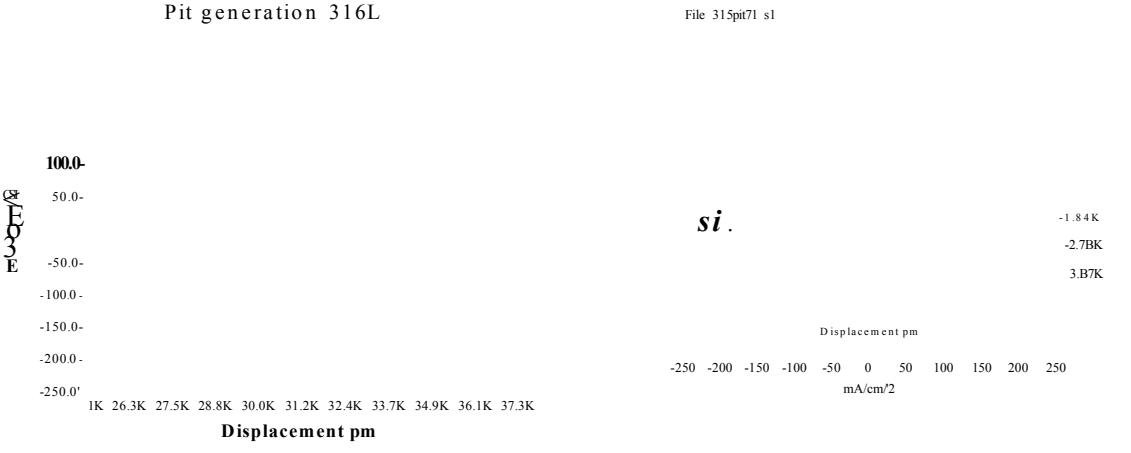

34 minutes

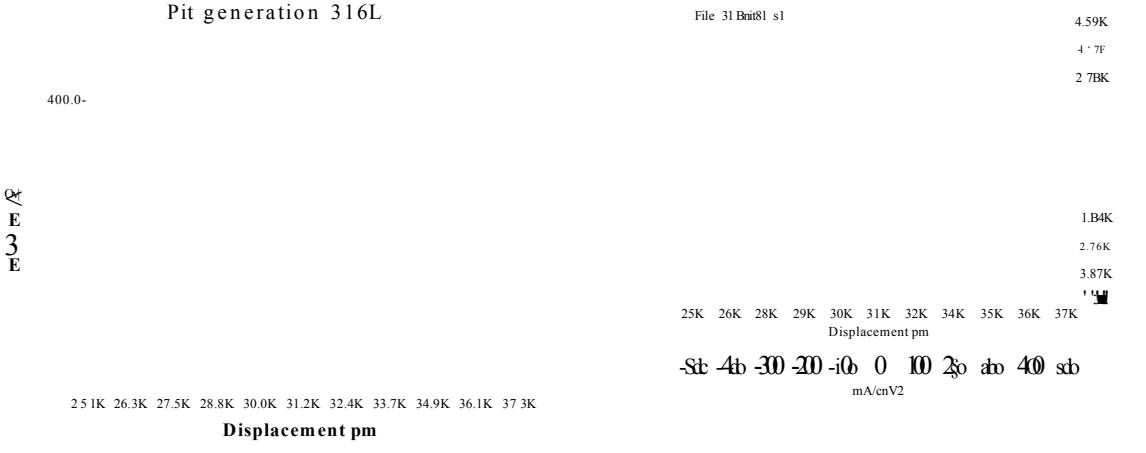

Figure 4.44. SRET measurements during pit generation on 316L specimens polarised at 280 mV vs SCE for 3,18.5, and 34 minutes

54 minutes

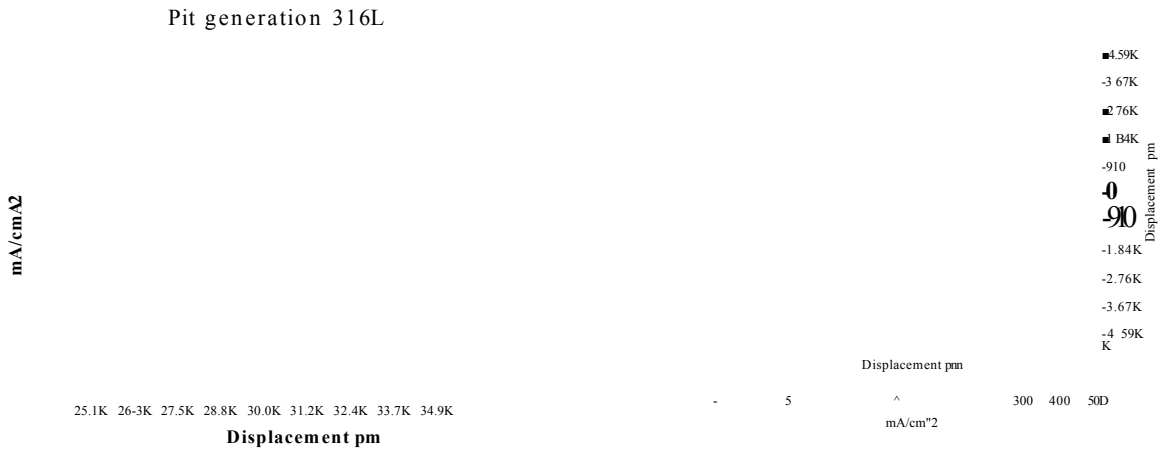

Figure 4.44. (continued) SRET measurements during pit generation on 316L specimens polarised at 280 mV vs SCE for 54 minutes.

2.3 minutes

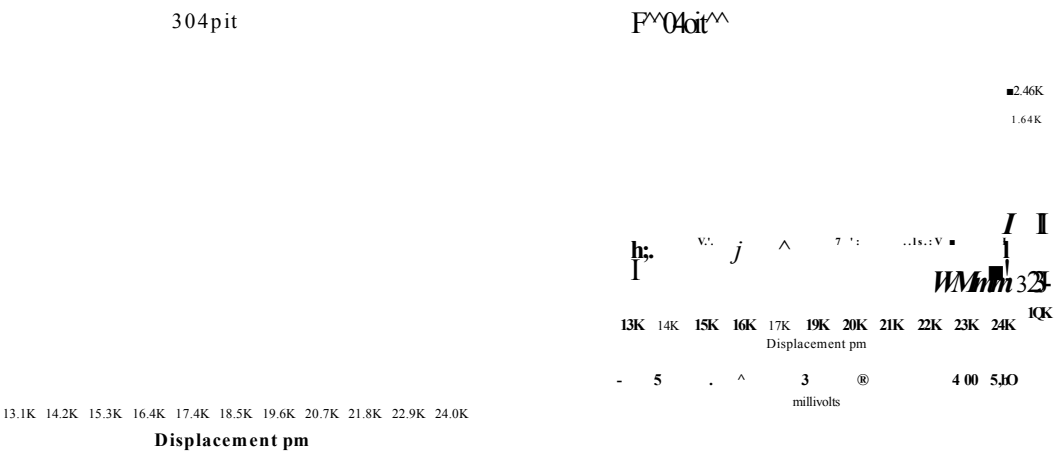

17.5 minutes

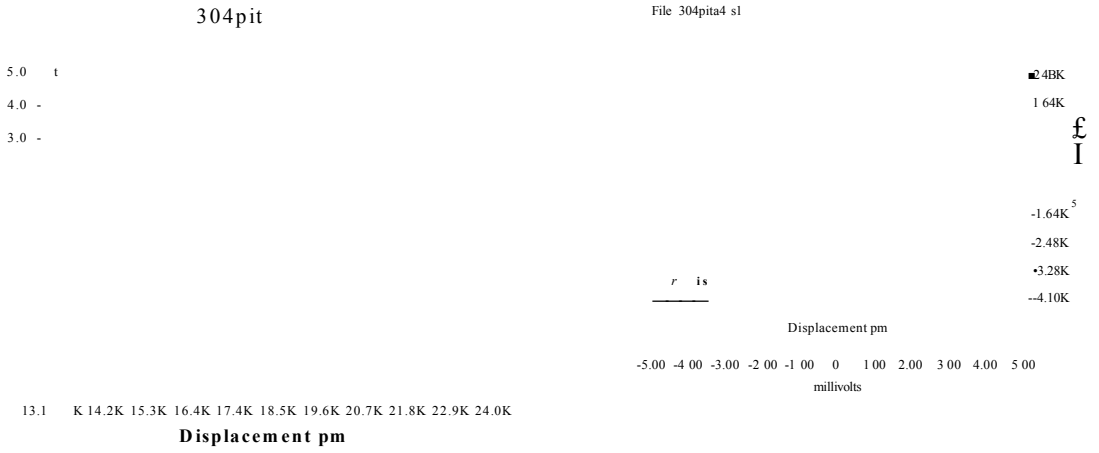

37.5 minutes

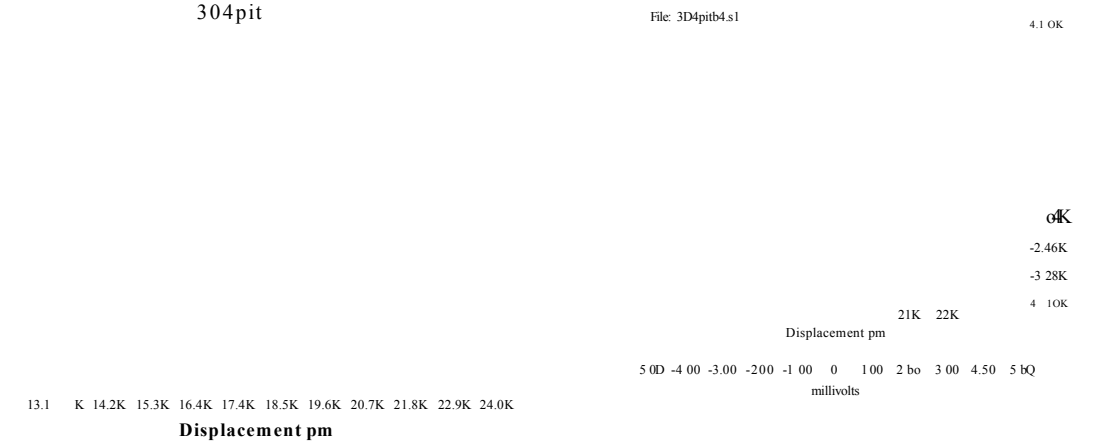

Figure 4.45 SRET measurements during pit generation on 304 SS specimens polarised at 290 mV vs SCE for 2.3,17.5, and 37.5 minutes.

56.5 minutes

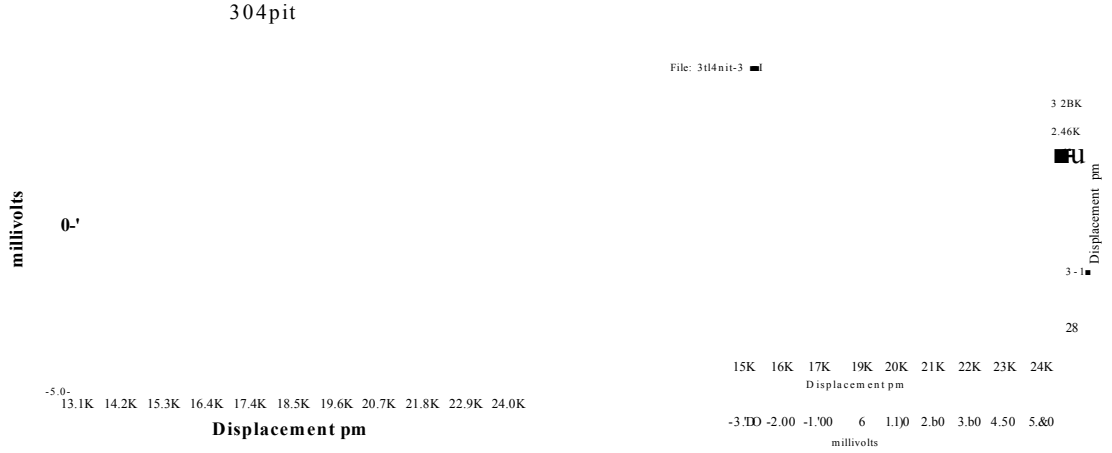

Figure 4.45. (continued) SRET measurements during pit generation on 304 SS specimens polarised at 290 mV vs SCE for 56.5 minutes.

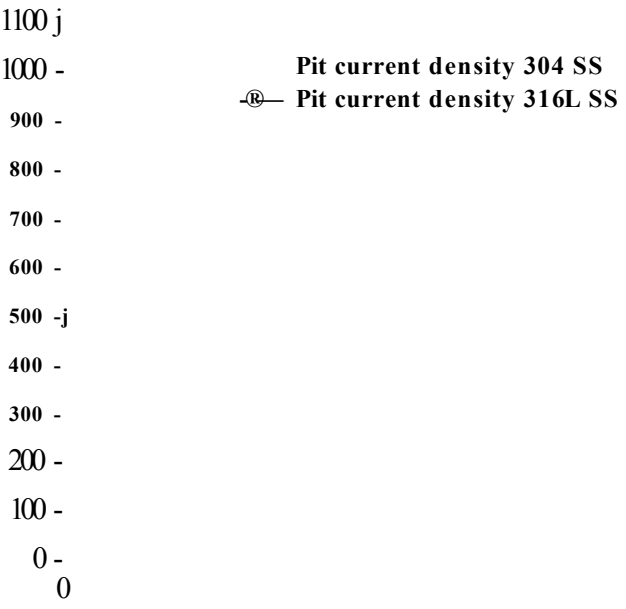

Figure 4.46. SRET localised current density Vs polarisation time for pits generated in 316L and 304 SS's in seawater.

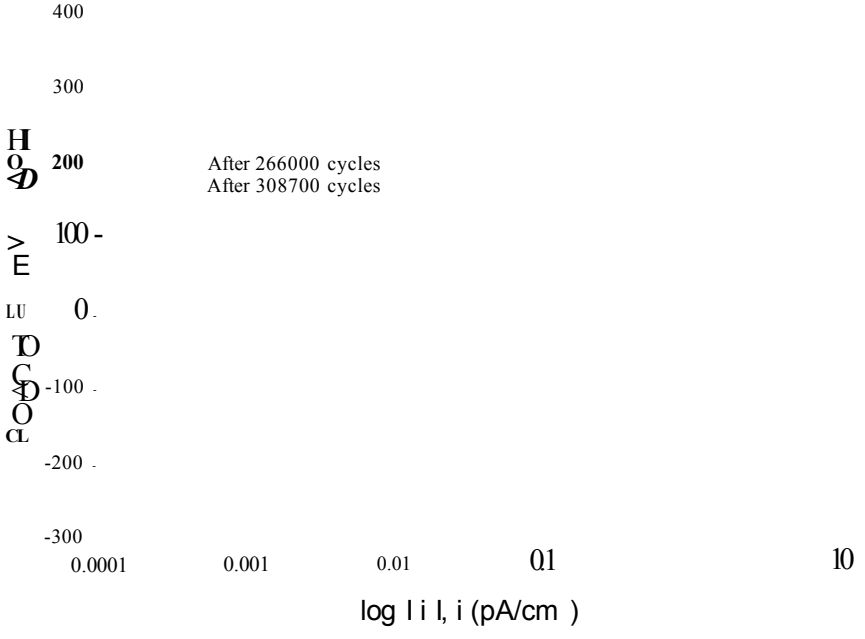

Figure 4.47. Polarisation curves for 316L SS specimen subjected to CF at 106 MPa.

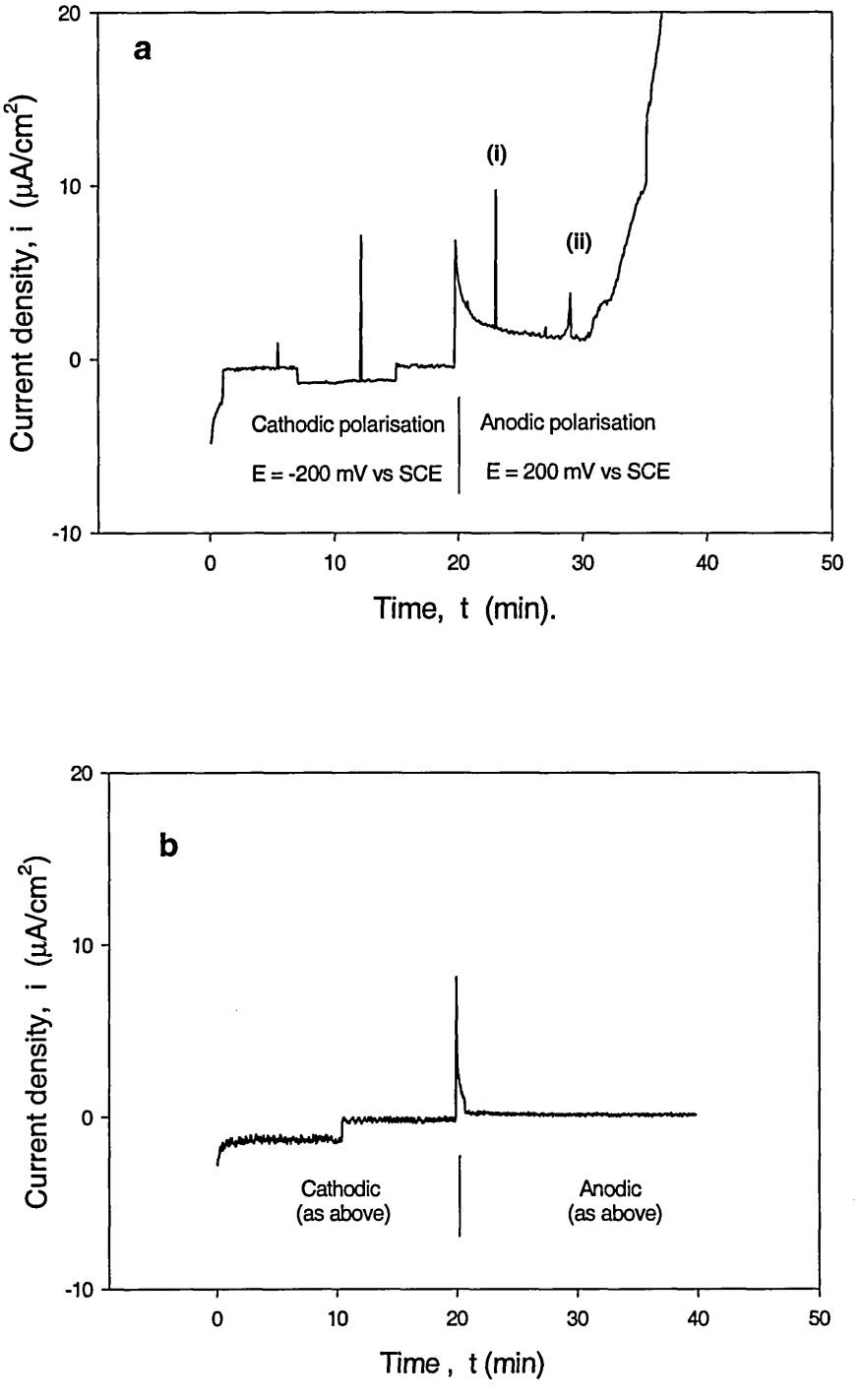

Figure 4.48 Potentiostatic polarisation of 316L SS specimen after 326500 cycles at a cyclic stress of 106 MPa. (a) Immediately after cycling, (b) 30 minutes following (a).

σ_L: Longitudinal stress

σ_C: Circumferential stress

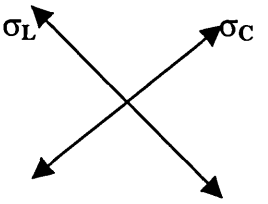

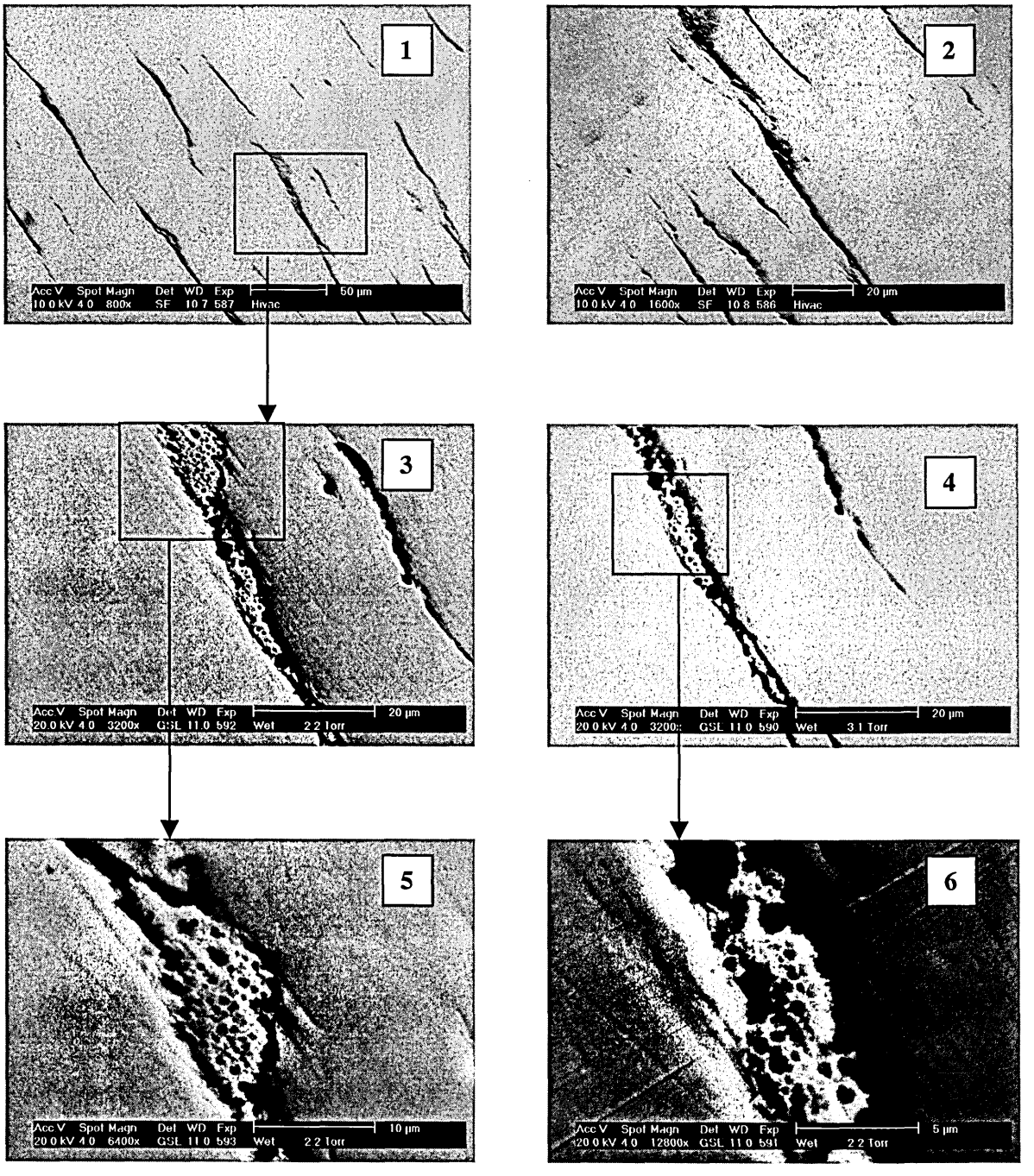

Figure 4.49. SEM analysis of the 316L specimen after 248200 CF cycles in artificial seawater at 106 MPa during which was subjected to anodic polarisation plus 93800 cycles at 172 MPa at free corrosion potential.

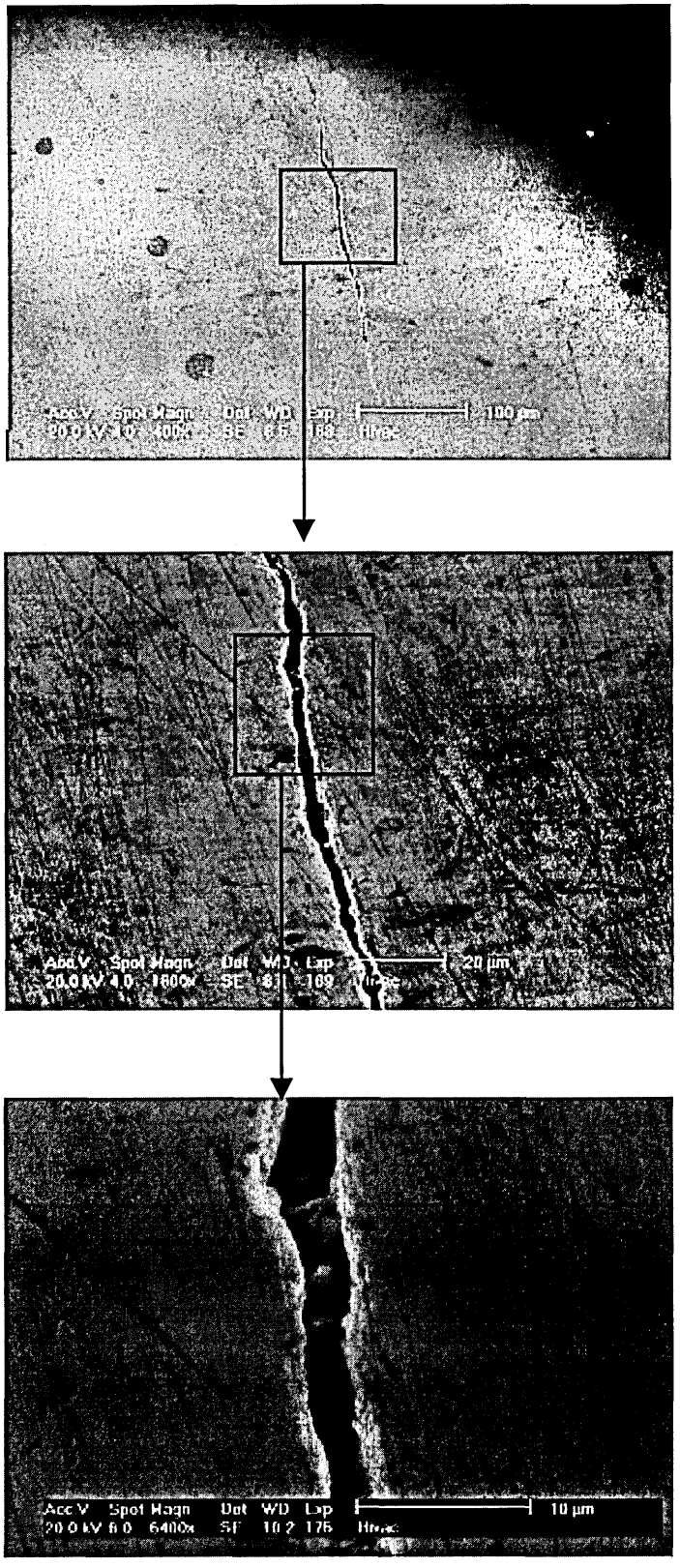

Figure 4.50. SEM images of a 316L SS specimen after failure subjected to CF in artificial seawater at free corrosion potential, applied stress: 260 MPa ($\sigma_{MAX} = 1.10\sigma_{ys}$).

σ_L: Longitudinal stress

σ_C: Circumferential stress

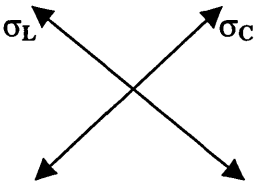

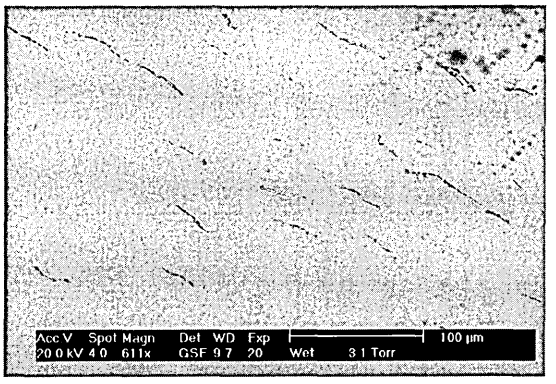

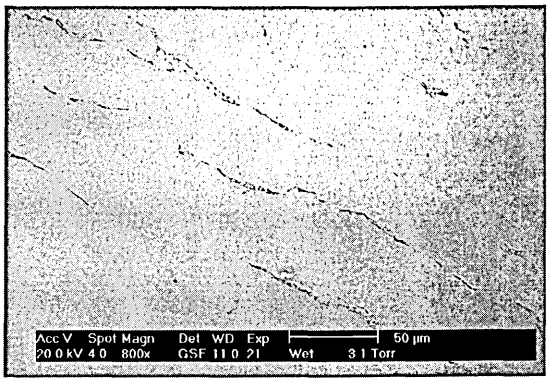

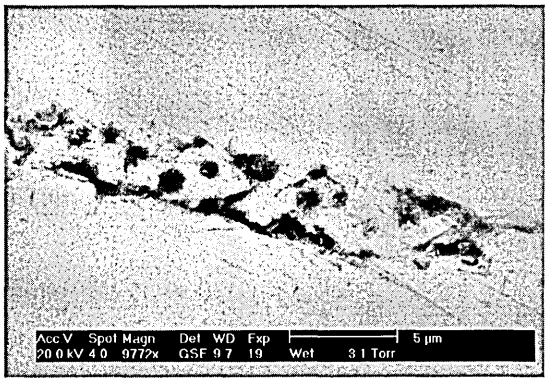

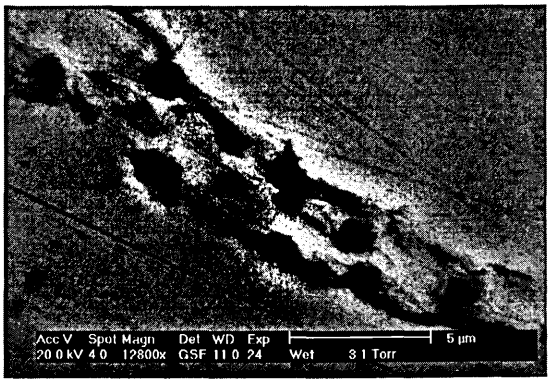

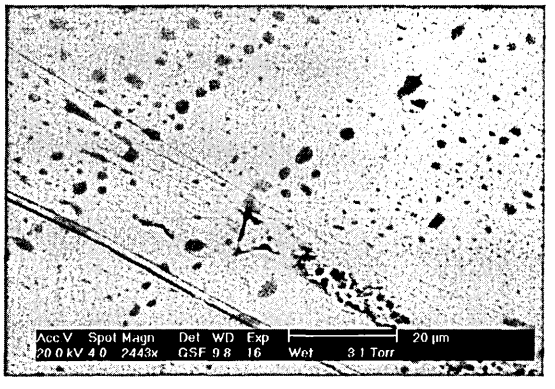

Figure 4.51. SEM analysis of the 304 SS specimen after 28400 CF cycles in artificial seawater at 197 MPa ($\sigma_{MAX} = 0.80\sigma_{ys}$) at free corrosion potential + potentiostatic polarisation at 200 mV vs SCE for periods of 50 minutes.

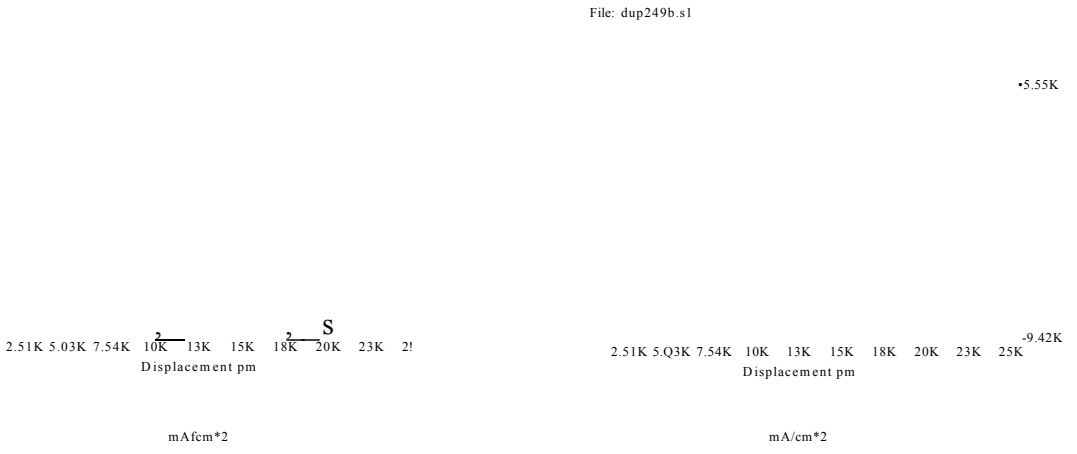

Area map of duplex SS specimen: (a) during polarisation at 1020 mV vs SCE in artificial seawater, and (b) immediately after the polarisation finished.

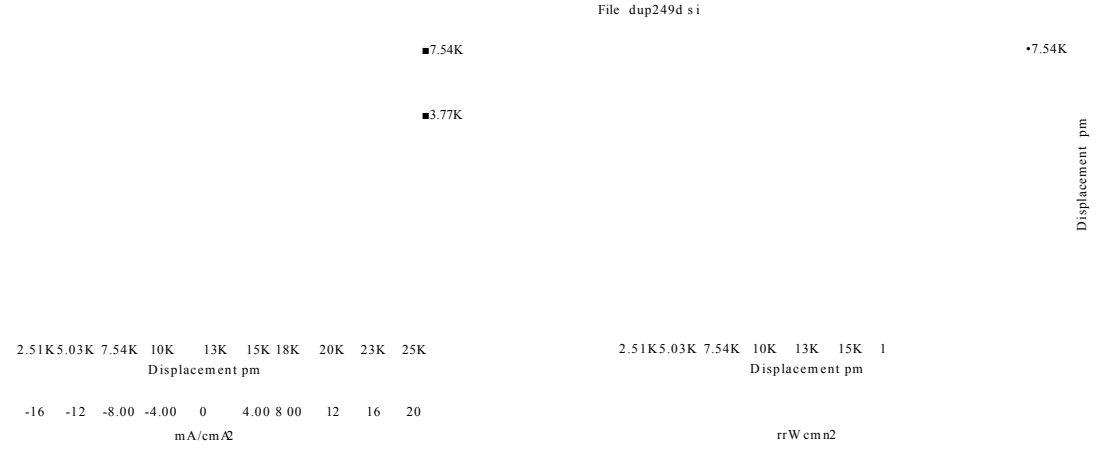

The area map (c) was performed after 1000 cycles at 547 MPa at free corrosion potential. Area map (d) was performed after 2400 cycles at 547 MPa at free corrosion potential.

Figure 4.52. SRET map scans on Duplex SS specimens under CF conditions in artificial seawater.

5 minutes

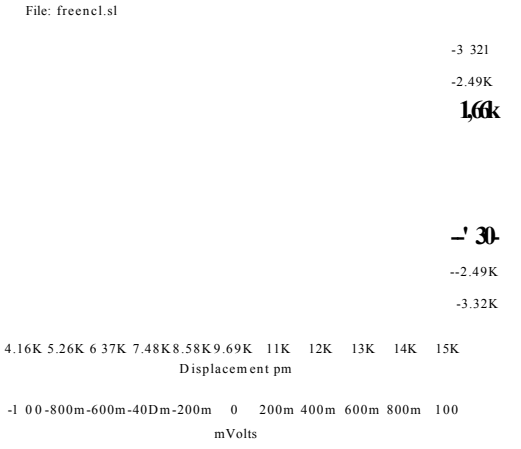

15 minutes

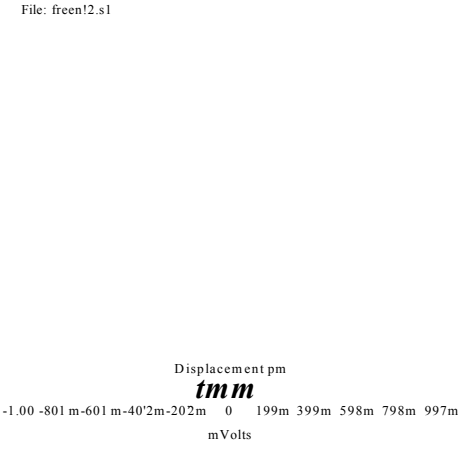

31 minutes

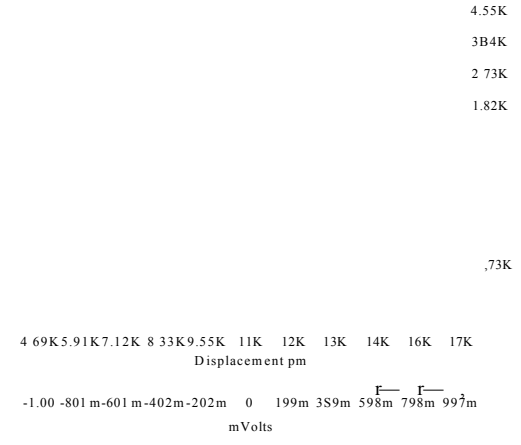

37 minutes

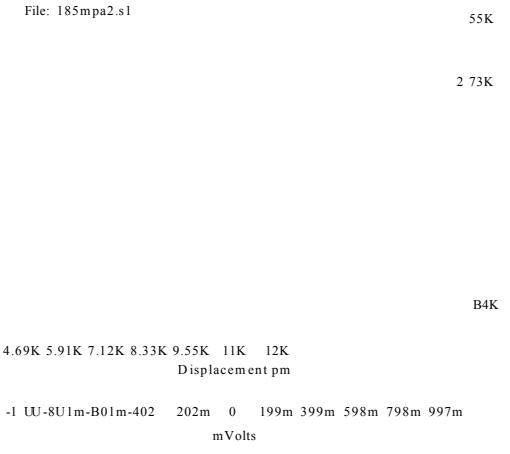

53 minutes

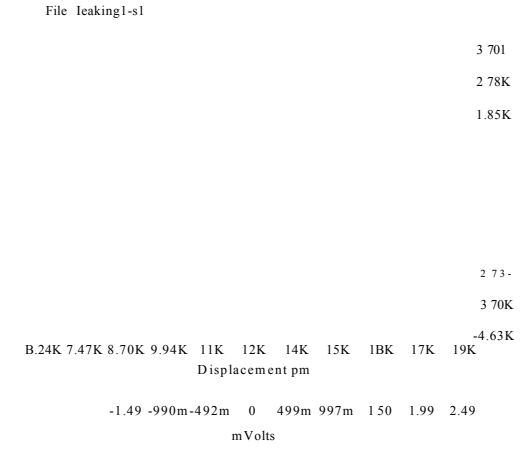

58 minutes

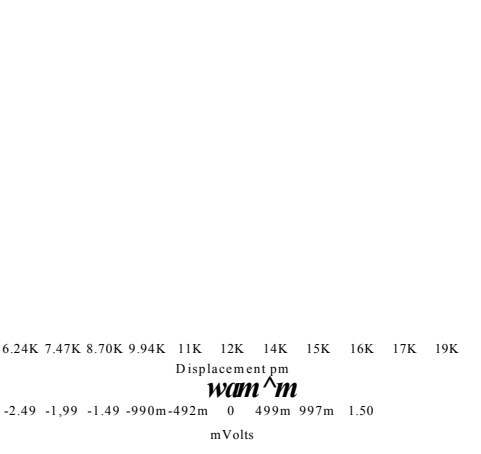

Figure 4.53(a) Area map scans for 316L SS specimen subjected to CF conditions in 0.05 MFeCF solution after 5,15, 31, 37, 53 and 58 minutes immersion.
Note that map scans at 5 and 15 minutes immersion were conducted with no CF loading.

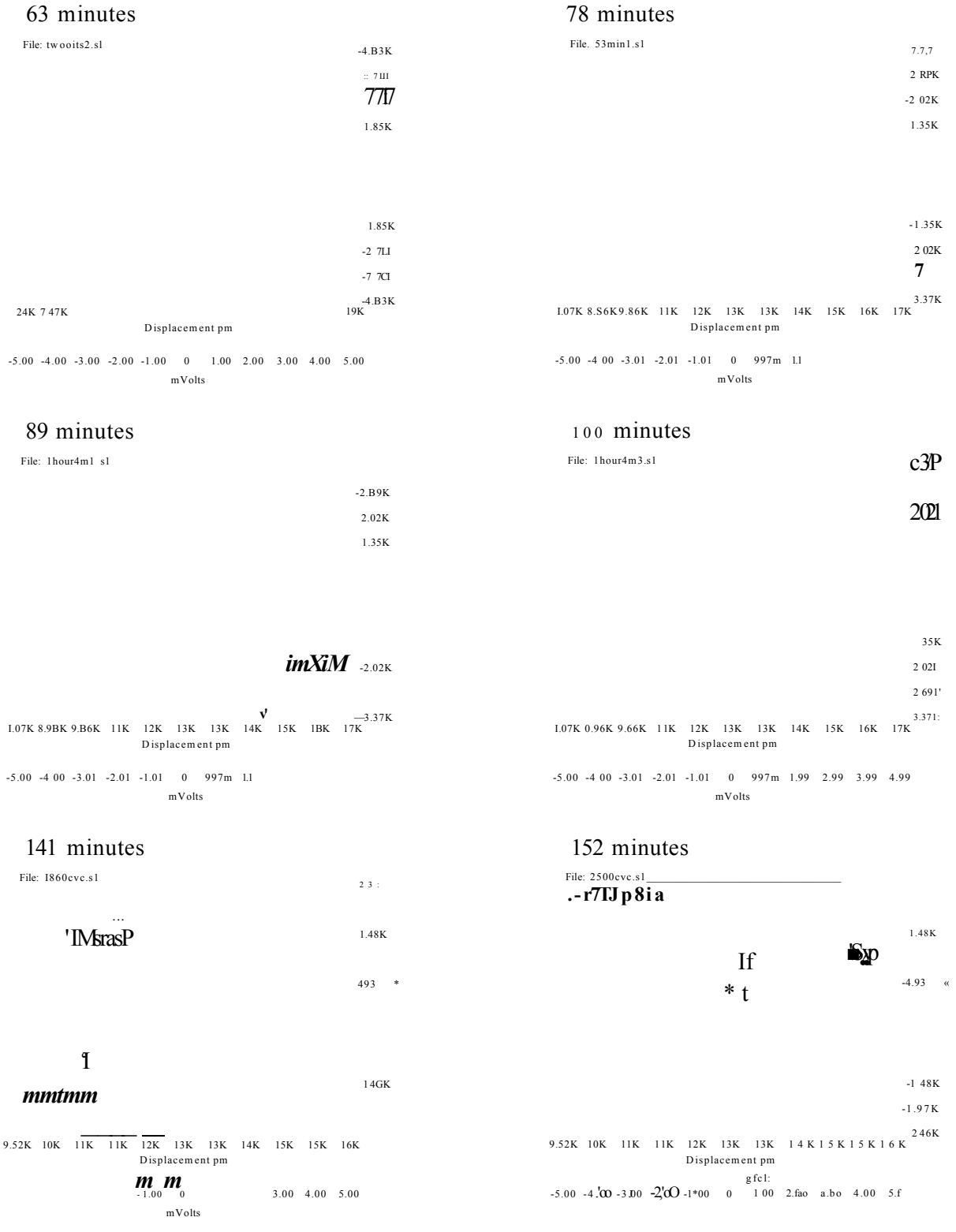

Figure 4.53(b) Area map scans for 316L SS specimen subjected to CF conditions in 0.05 M FeClj solution after 63, 78, 89, 100, 141 and 152 minutes immersion.

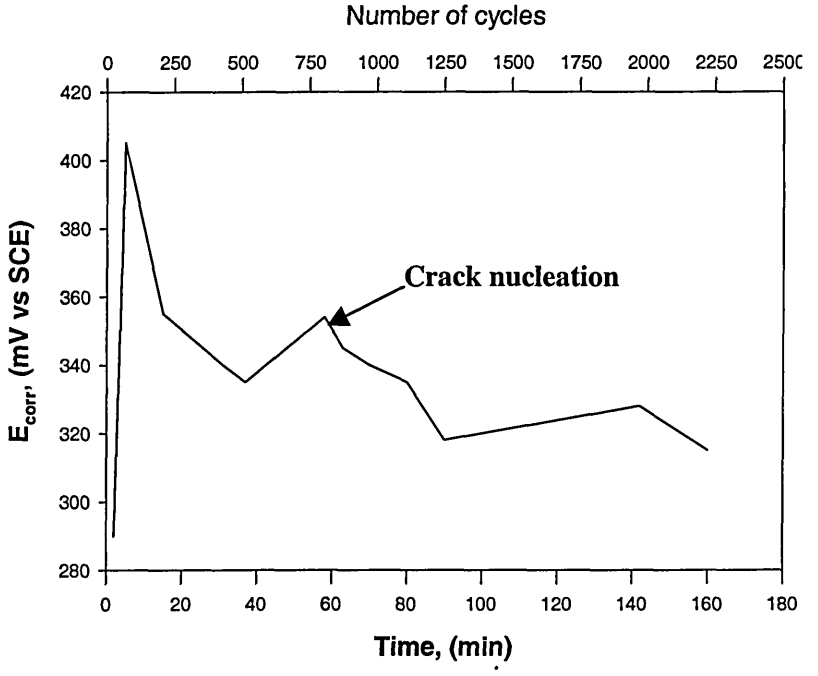

Figure 4.54 Corrosion potential vs time for the specimen of 316L SS immersed in 0.05 M $FeCl_3$ solution subjected to cyclic loading.

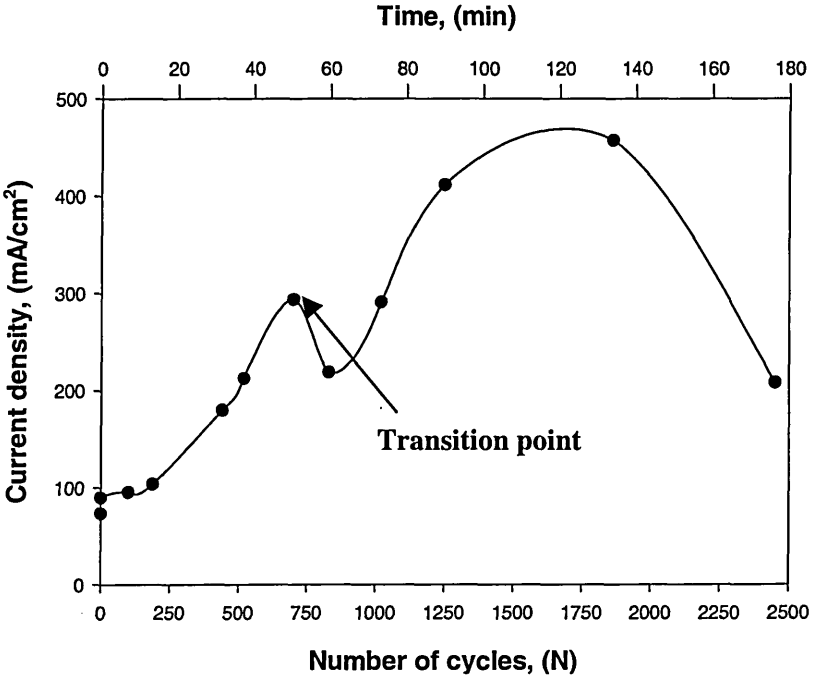

Figure 4.55 Localised current density from pit a vs number of cycles in 0.05 M $FeCl_3$ solution.

17 minutes

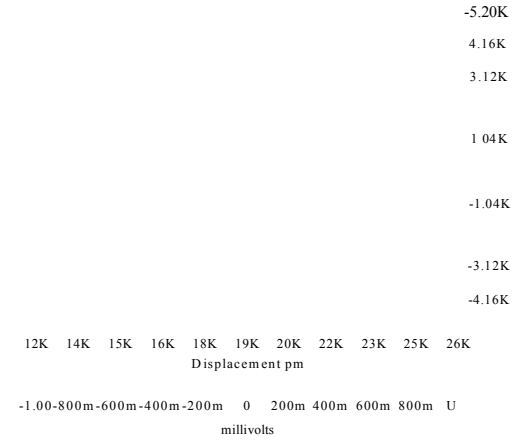

22 minutes

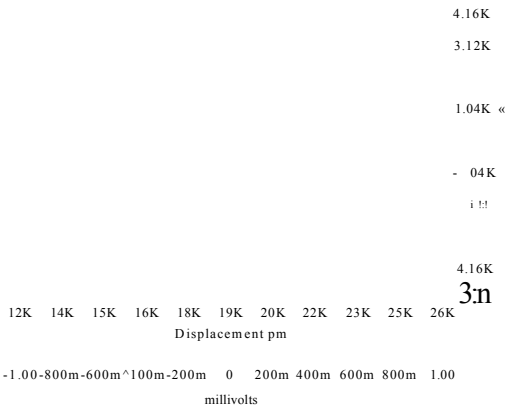

27 minutes

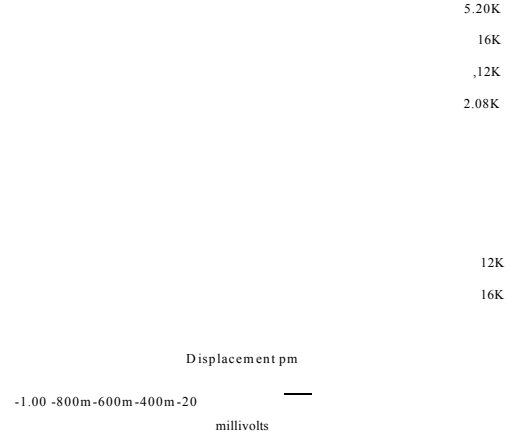

32 minutes

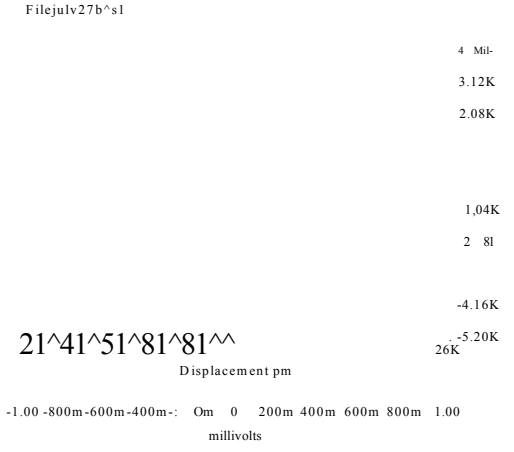

38 minutes

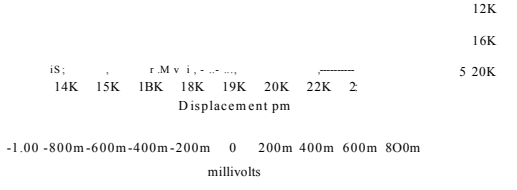

Figure 4.56(a) Area map scans for 304 SS specimen subjected to CF conditions in 0.05 MFeCh solution after 17, 22, 27, 32 and 38 minutes immersion.

48 minutes

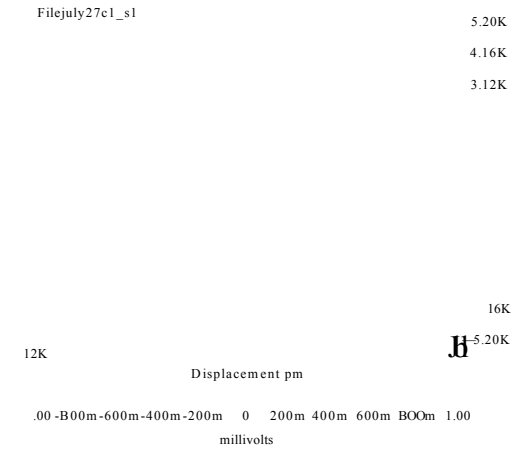

56 minutes

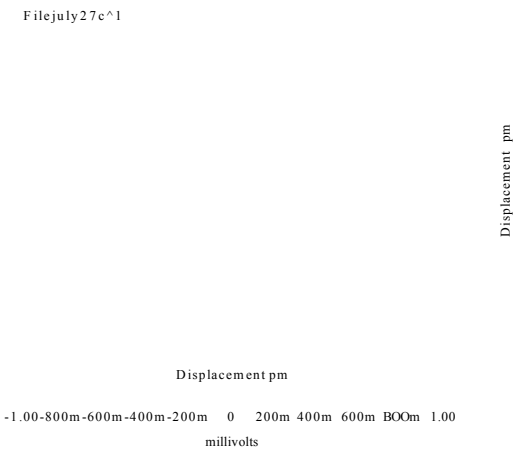

68 minutes

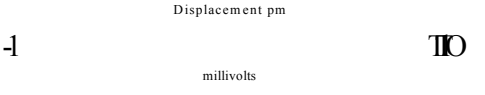

137 minutes

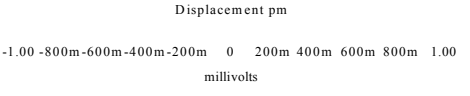

167 minutes

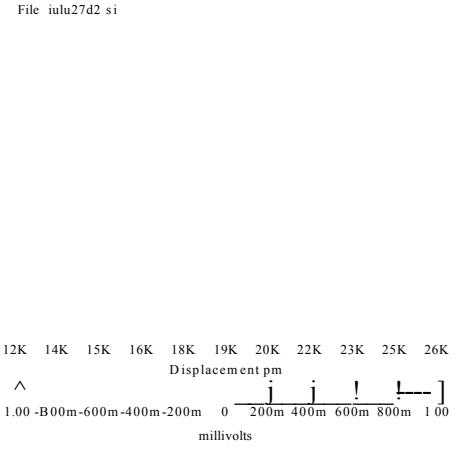

Figure 4.56(b) Area map scans for 304 SS specimen subjected to CF conditions in 0.05 MFeCb solution after 48, 56, 68,137 and 167 minutes immersion.

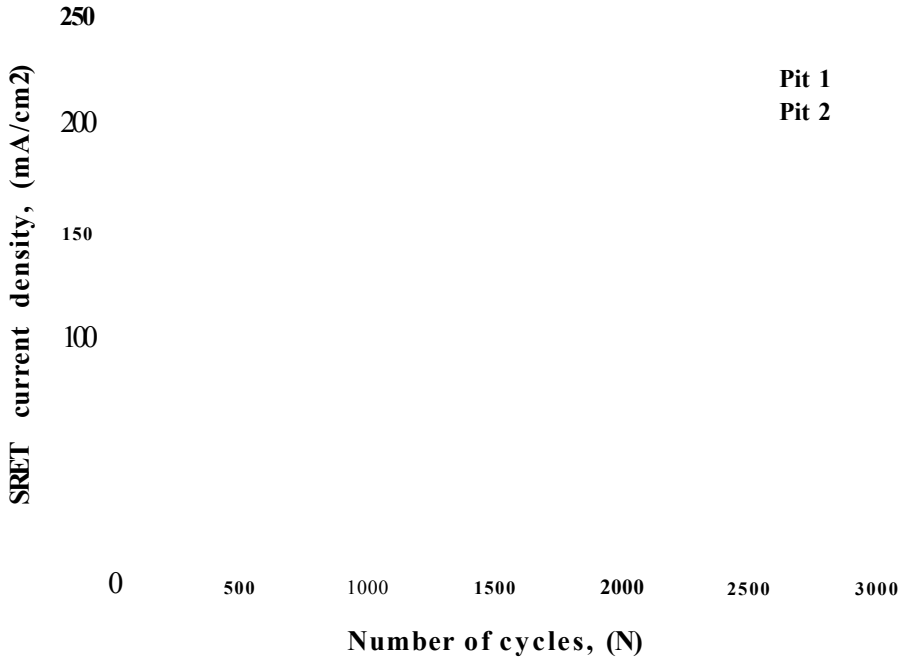

Figure 4.57. Pit current density (from SRET measurements) Vs N for two sites undergoing localised attack on specimens of 304 SS under CF in a solution 0.05 MFeCfj.

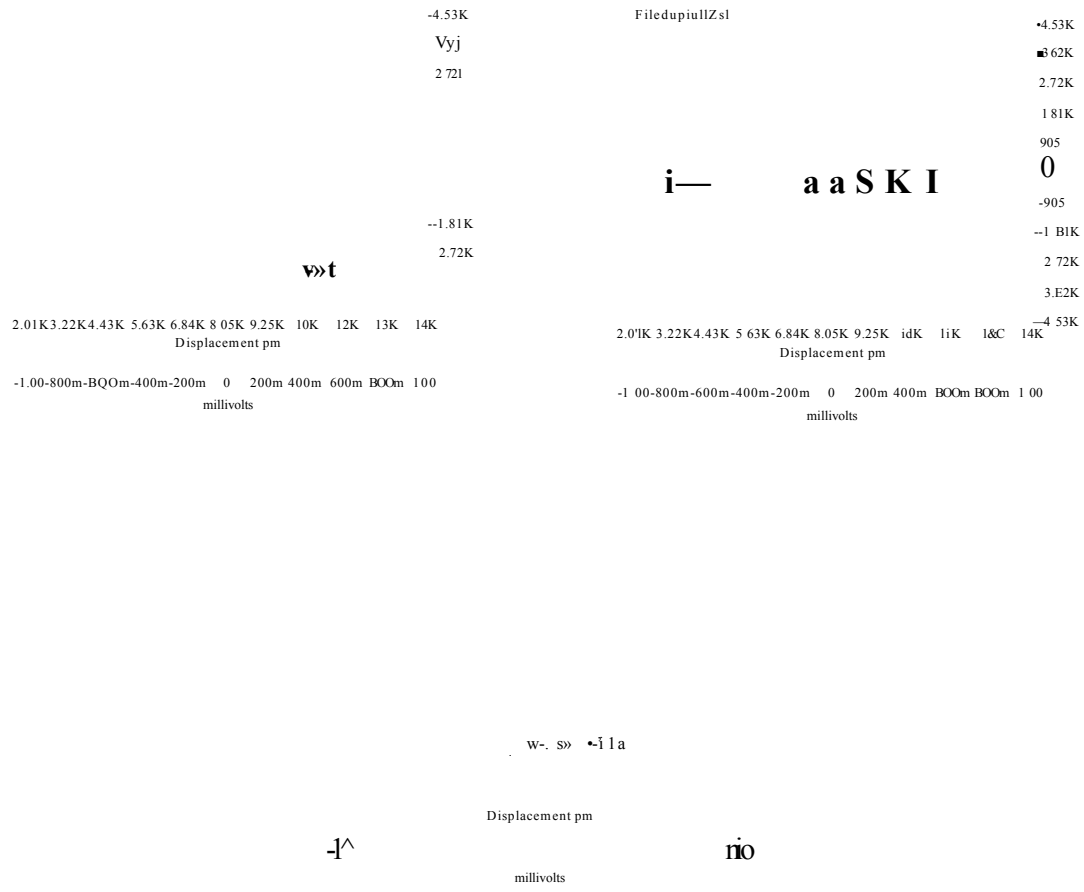

Figure 4.58. SRET map scans for duplex SS in FeCl3 at free corrosion potential after (a) 0, (b) 500 and (c) 9600 cycles at σMAX = 474 MPa, R = 0.

Figure 4.59. SRET map scans for duplex SS in FeCl3 after 5000 cycles at 320 MPa, (a) under anodic polarisation at 1100 mV vs SCE, (b) at free corrosion potential.

Austenite

Ferrite

Figure 5.1. Pitting corrosion of duplex SS at the a-y boundary and subsequent pit propagation at the ferrite phase.

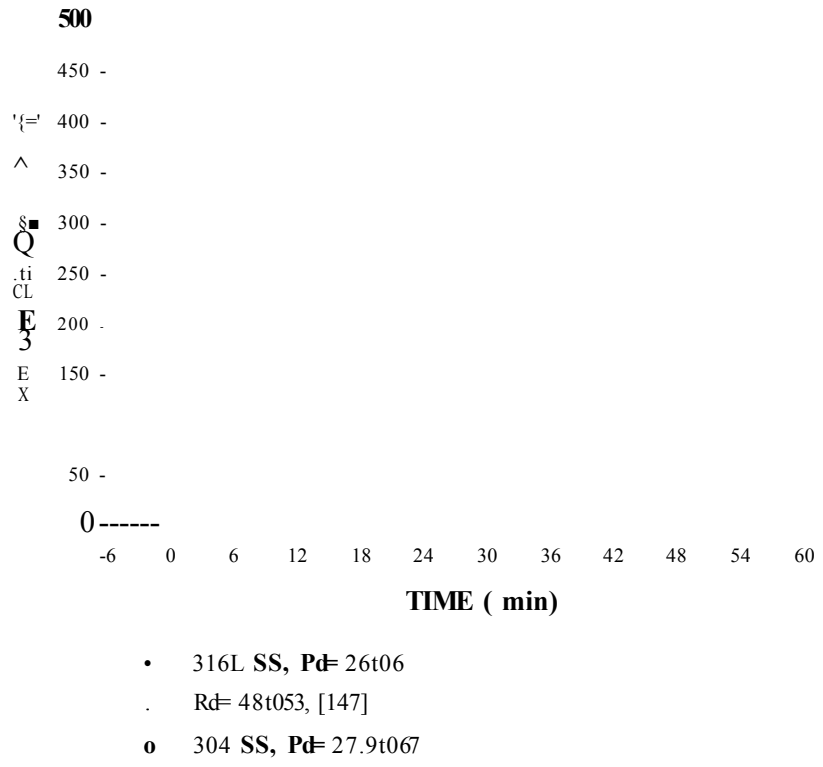

Figure 5.2. Comparison of the pit growth law obtained in the present work with the results obtained in 12 Cr martensitic steel by Zhou et. al. [147]

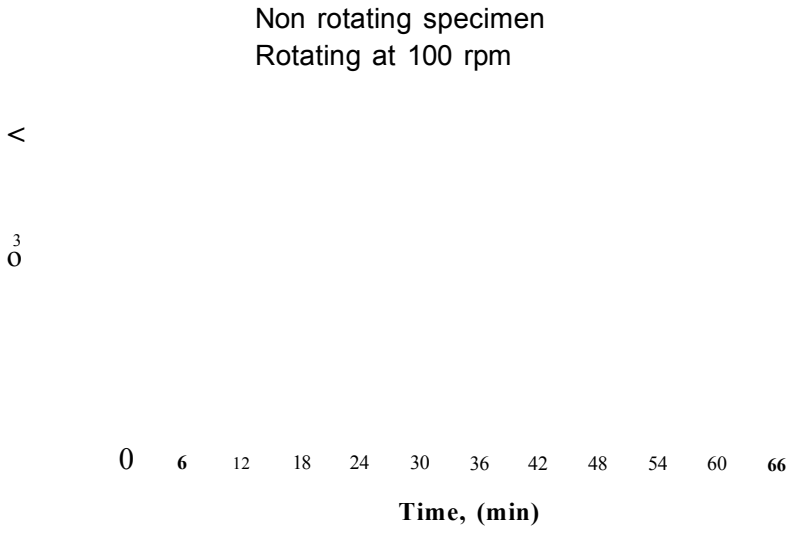

Figure 5.3(a). Chronoamperometries for pit generation on 316L SS specimens polarised 60 minutes at 280 mV vs SCE under non-rotating and rotating conditions.

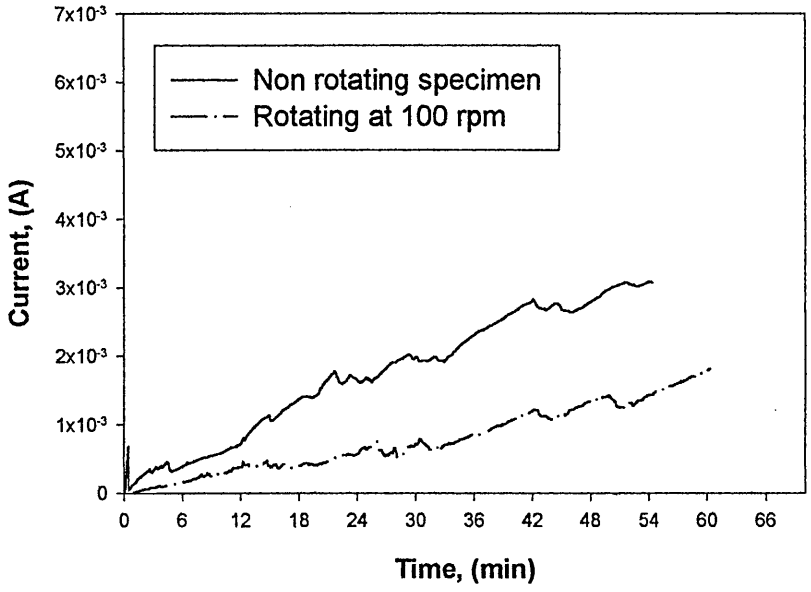

Figure 5.3(b). Chronoamperometries for pit generation on 304 SS specimens polarised 60 minutes at 290 mV vs SCE under non-rotating and rotating conditions.

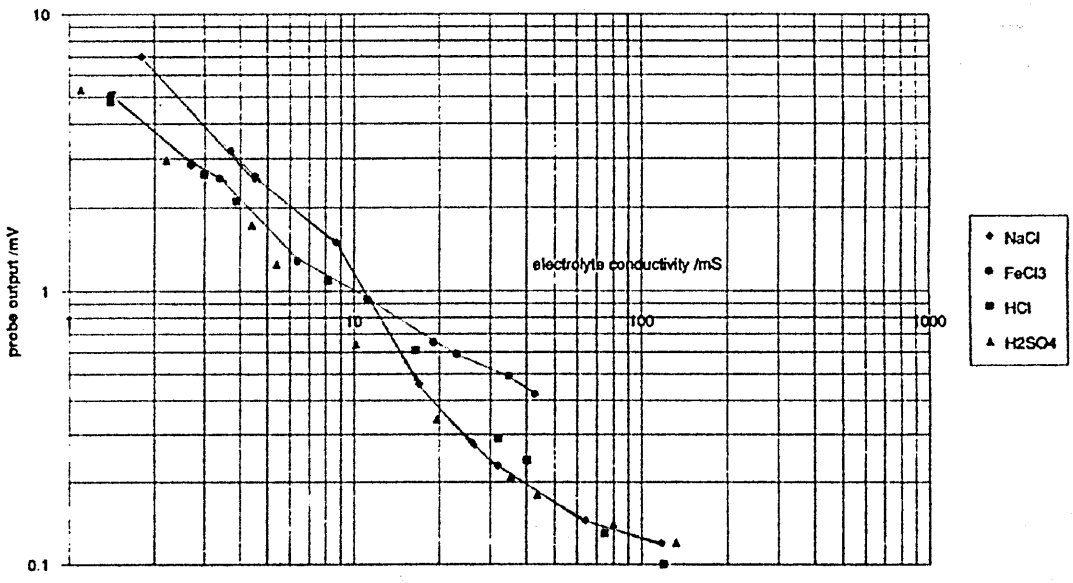

Figure 5.4. Change in output signal as a function of the conductivity for different electrolytes, after [131].

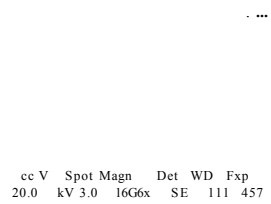

Figure 5.5(a) The position of δ-ferrite in 316L SS (i), and the pattern followed by localised dissolution due to anodic polarisation during CF tests in seawater.

Figure 5.5(b) The position of δ-ferrite in 304 SS (i), and the pattern followed by localised dissolution due to anodic polarisation during CF tests in seawater.